Resonances and Non-Adiabatic Effects in Quantum Dynamics

(Resonances by Complex Methods and the Generalized Multi-Configuration Time-Dependent Hartree Method)

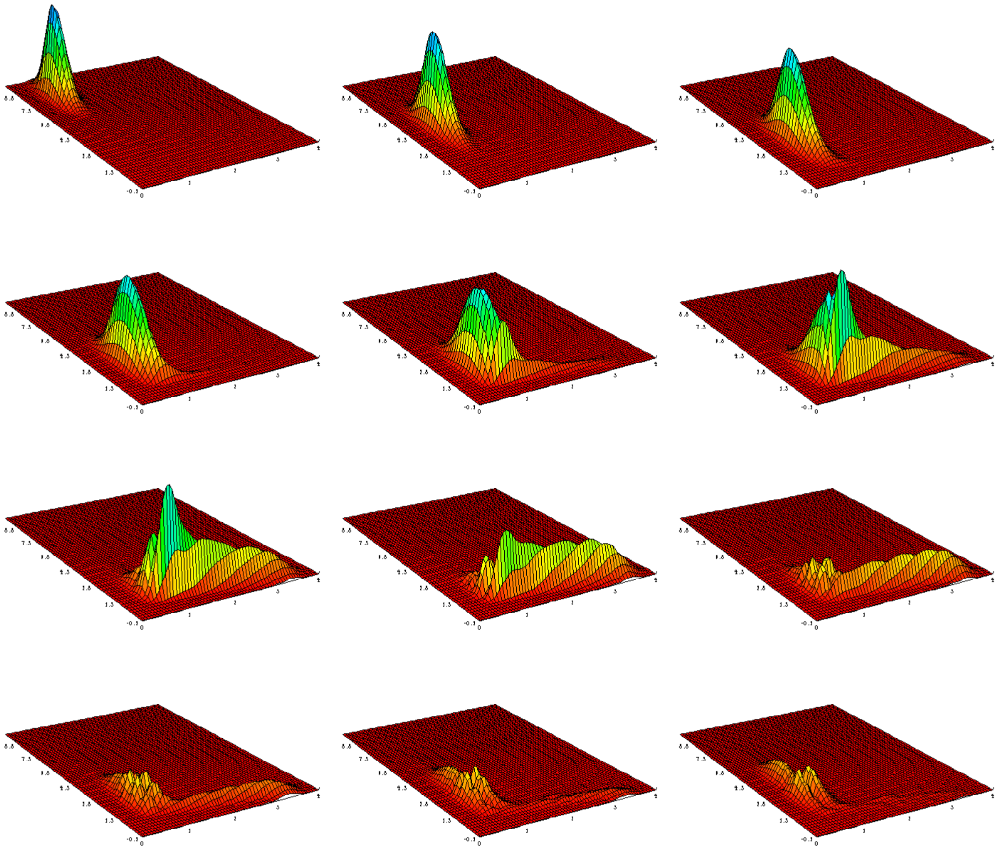

Ph.D. thesis by

Ken Museth

September 7, 1997

Resonances and Non-Adiabatic Effects in Quantum Dynamics

(Resonances by Complex Methods and the Generalized Multi-Configuration Time-Dependent Hartree Method)

Ph.D. thesis by

Ken Museth

September 7, 1997

Department of Chemistry
Faculty of Science
University of Copenhagen
2100 Copenhagen, Denmark

Preface

This thesis, entitled "Resonances and Non-Adiabatic Effects in Quantum Dynamics" (subtitled "Resonances by Complex Methods and the Generalized Multi-Configuration Time-Dependent Hartree Method"), is submitted to the University of Copenhagen in partial fulfillment of the requirements for the Ph.D. degree. The research and work on which this thesis is based was carried out partly at the Department of Theoretical Chemistry, University of Copenhagen, partly at the Laboratoire de Chimie Théorique, Université Paris-Sud, Orsay and finally at the Laboratoire Structure et Dynamique Moléculaires, Université des Sciences et Techniques du Languedoc, Montpellier.

It is with great pleasure that I thank Professor Gert Due Billing, who has acted as my principal supervisor ever since I started at the University of Copenhagen. His scientific achievements and impressive overview has been a tremendous source of inspiration for my own investigations. I have also benefited greatly from his many connections in the scientific community, which has equally been of invaluable importance to the outcome of this project. This is especially directed towards my "French connection", Professor Claude Leforestier, who I have had the distinct pleasure to work with over the last five years. During my many wonderful trips to Paris, and recently Montpellier, Claude has taught me the fine art of grid methods and numerous optimization techniques in molecular quantum dynamics. Over the years he has shown continuous interest and support, and it is true to say that he is the source of inspiration for at least half of the work presented in this thesis. I am also graceful to Victor Sidis and Danielle Grimbert for discussions on the system of H^++O_2, and Nimrod Moiseyev and Hans-Dieter Meyer for useful comments on respectively the numerical complex scaling method and the generalized multi-configuration time-dependent Hartree method presented in this thesis. Finally I wish to extend my thanks to Mads Ipsen, who patiently helped me typesetting this thesis, and Christian Laursen for long discussions on the system of H_2+Cu(100). Last, but by no means least I am very much indebted to my girlfriend Katrine who constantly over the years have made me realize that there is more to life than just science and quantum mechanics.

Survey of the thesis

The contents of this thesis represent my activities during my time of study for the Ph.D. degree. The subject of this project is twofold. First we present a new formulation and numerical studies of non-adiabatic systems in the framework of the multi-configuration time-dependent Hartree (MCTDH) method. Secondly the thesis deals with the description of molecular resonances by complex methods, and we especially focus on the development of the necessary numerical tools for the application of an exact method on systems where no analytical expressions are available for the potential energy function. As such the two topics of this thesis are not related, but as we shall demonstrate they are indeed connected in the sense that all of the systems studied in the thesis turned out to display resonances. For this reason the two topics have been assigned separate parts.

The presented thesis is, in more than one respect, the result of a very *theoretical* study of molecular dynamics. Clearly is does not involve any experimental work whatsoever, and moreover it is based on a wide range of concepts, theorems and numerical techniques used in the study of "exact" quantum dynamics. It is my personal experience that one of the major obstacles faced by many students in learning quantum dynamics at this level of exactness, is their unfamiliarity with many of these concepts and methods. Furthermore, since many of these required concepts and numerical techniques are not discussed in standard textbooks, I have dedicated the first part of this thesis to an introduction to these methods that form the very basis of the work to be presented.

At an early stage of this Ph.D. project I made a fairly definite decision regarding the stylistic form to be used in the presentation of this work. Rather than presenting an abrute series of results and reprints from publications, dominated by discontinuous jumps to literature references, as is "comme il faut" in many Ph.D. thesis, I have rewritten the included papers and in general tried to make the presentation as uniform and independent as possible. Thus, I have aimed at making explanations clear and complete, and most of the derivations are hopefully given with enough detail to make them easy to follow. Also resort to the frustrating phrase "it can be shown that ..." is avoided wherever possible. However, this representation of course entails the risk that what might appear relevant and complicated to me might well be tiresome an trivial to the expert reader, in which case I hope he or she can bear over with my style. This last comment is especially directed towards part I, where some readers perhaps will find the details long and tiresome, yet presumably not trivial. For this same reason the impatient expert reader is encouraged to skip the first part, however at the risk of loosing the coherence of the thesis since extensive reference will be made to this introductory part in the subsequent parts of the thesis.

Below follows a brief outline of the three parts of this thesis. The **first part** includes the chapters:

Chapter 1	Introduction to some basic concepts in quantum scattering. We shall especially focus on the definition of quantum flux and phase shift.
Chapter 2	Many of the central grid methods, numerical optimization techniques and different choices of coordinate systems are introduced.
Chapter 3	The diabatic and adiabatic representations are defined and a simple transformations scheme between the two is outlined.
Chapter 4	Presentation of some important time-dependent propagation techniques.

The **second part** of the thesis deals with the formulation and subsequent testing to the generalized multi-configuration time-dependent Hartree (MCTDH) method, and includes the chapters:

Chapter 5	Introduction to time-dependent self-consistent field methods, and a short presentation of a Gaussian formulation of the MCTDH method.
Chapter 6	Presentation and one-dimensional test of the generalized MCTDH method. This chapter is largely based on reference [1].
Chapter 7	Two-dimensional test of the generalized MCTDH method on the system of H_2+Cu(100). This chapter is largely based on reference [2].
Chapter 8	Discussion and summary for this second part of the thesis.

The **third part** of the thesis concerns the study of molecular resonances using complex methods, and includes the chapters:

Chapter 9	Introduction to resonances and complex methods.
Chapter 10	Study of molecular resonances in the systems of H^++O_2 employing the optical potential method. This chapter is largely based on reference [3].

Chapter 11	Presentation and subsequent test of a new method for numerical complex scaling. This chapter is largely based on reference [4].
Chapter 12	Discussion and summary for this last part of the thesis.

As a closing remark for this short survey of the thesis, I would like to stress that neither me, nor my coworkers, can of course take the credit for the development the MCTDH or the complex coordinate methods. I present extensions, improved formulations and numerical studies of essentially well-established theories, and as such “I built on the shoulders of giants”.

Contents

I Quantum Scattering Theory 1

Part I

Quantum Scattering Theory

1

Introduction

In the past 10-15 years dramatic progress has been achieved in the field of more exact theoretical studies of molecular chemical reactions. This progress is partly due to the emerge of faster super-computers and partly due to the development of new theoretical as well as experimental techniques. The access to fast computers (vector and especially so called massive parallel-computers) have given theoreticians, like myself, a very powerful tool to implement and solve numerical problems on a large scale. This has naturally led to the modern trend in theoretical chemistry where larger and larger systems are studied. Maybe the most important consequence of the improved computer technology is the fact that theoretical chemist are no longer satisfied with merely qualitative models for chemical phenomena. Consequently large efforts have been and continue to be devoted to developing the more exact models to the practical stage where reliable calculations can be carried out for chemical reactions. In addition to this, the publication[5] of epoch-making "state-to-state" (*i.e.* highly detailed) experimental measurements on chemical reactions have undoubtedly motivated many theoreticians to move to more quantitative and exact studies in order to analyze and interpret these experiments. A very good example of this is the recent development of intense laser-fields, which has opened up the exciting prospect of actually controlling chemical reactions on a microscopic level. Thus, the modern trend in theoretical chemistry is to push the methodology and the computers to give a detailed and accurate description of the reaction dynamics in increasingly larger systems.

It is well recognized that quantum mechanical scattering theory provides the most complete and detailed description of atomic and molecular collisions, which are the fundamental microscopic events that underlies a chemical reaction. Thus, the goal of quantum scattering theory is to give a rigorous description of the basic mechanisms for a chemical reaction from a knowledge of forces operating at the atomic and molecular levels. However, usually when we think of a chemical reaction we do not give much thought to the actual intermediate states produced during such a collision. We tend to take the somewhat practical and pragmatic viewpoint of an experimentalist who only want to know how he or she can go from reactants in some initial quantum state, i, to products in a selected final quantum state, f. The motivation for this viewpoint is of course that in the laboratory the measurements are made in the region of space asymptotically far from the target. Hence, it is customary to characterize a specific chemical reaction using the short notation,

$$\mathrm{A} + \mathrm{BC}(i) \xrightarrow{\text{Reaction}} \mathrm{AB}(f) + \mathrm{C} \tag{1.1}$$

where no reference is made to the actual nature of the underlying dynamics. Since the 1960's, when crossed molecular beam experiments had developed to such an extent that it was possible to study such state-to-state reactions, there has been intense interest and effort devoted to the application of quantum scattering theory to these reactions to calculate reliable values for the *differential cross-section*

$$\boxed{\frac{d\sigma_{i\to f}}{d\Omega}(\theta,\phi) \equiv \frac{\text{Outgoing radial flux at } \Omega \text{ per unit solid angle}}{\text{Total incident flux per unit area}} \qquad (1.2)}$$

This quantity, which gives a measure of the probability of producing the state-selected molecule $\mathrm{AB}(f)$ from the reactant molecule $\mathrm{BC}(i)$ at the solid angle $\Omega \equiv (\theta, \phi)$, provides the most detailed quantity that a reaction dynamical experiment can give. As will be emphasized later, this is not to say that modern experiments cannot provide more insight into the underlying dynamics of a chemical reaction than offered by this quantity. It merely points out the important fact that from the knowledge of measured differential cross-sections one can, in principle, reconstruct the intermolecular potentials. Crossed molecular beam experiments enable these differential cross-sections to be fully resolved with respect to θ[1]. Averaging over the scattering angles produce the *integral or total cross-section*

$$\boxed{\sigma_{i\to f}(E) = \int d\Omega \frac{d\sigma_{i\to f}}{d\Omega}(E,\theta,\phi) = \int_0^{2\pi} d\phi \int_{-1}^{1} d(\cos\phi) \frac{d\sigma_{i\to f}}{d\Omega}(E,\theta,\phi) \qquad (1.3)}$$

---

[1] For intermolecular (or isotopic) potentials which depend only on the separation of the two molecules, the scattering is cylindrically symmetric with respect to the axis of the incident beam of molecules in the relative-motion picture. Thus the scattering depends only on the deflection angle θ and not on the azimuthal angle ϕ.

which can, in principle, be measured in less sophisticated bulk experiments. By Boltzmann averaging these integral cross sections over all the possible initial and final states one can next calculate *thermal rate constants* which, in turn, can be measured quite directly in a bulb. Thus, the theory of quantum mechanical scattering, which is the starting point in the derivation of an accurate theory of chemical reaction dynamics, provides a crucial link between the results obtained in detailed state selective molecular beam experiments and thermal average bulb measurements.

As indicated several times above, the rigorous study of chemical reaction dynamics, now a days goes far beyond the simple state-to-state description mentioned so far. The goal of modern quantum scattering theory is not only to give an accurate estimate of detailed quantities like the differential cross-section, eq. (1.2), but also to give a physical insight to the explicit quantum mechanisms, which take us from the reactants to the products. This trend in quantum dynamics is strongly influenced by the resent emerge of the so-called "pump-probe" experiments, where very short laser pulses are used to take "snap-shots" of the chemical reaction as the time evolves. Using this advanced technique, it has now become possible to actually "see" (*i.e.* measure) and test for quantum effects that the theory has predicted for years. Quantum effects have of course always been present in the state-to-state experiments, but they have been "hidden" in the sense that the measurements were not accompanied by a detailed analysis of the quantum system as the actual reaction evolved in time – an examination which often offers an explanation or cause for the explicit quantum effects involved. These quantum effects are typically tunneling, vibrational zero-point energy, classically forbidden transitions, non-adiabatic coupling and the formation of resonances or complexes, some of which will play a central role in this thesis. Consequently, only a full quantum mechanical scattering theory can give a rigorous description of these experiments. This is not meant to imply that it is necessary, or even desirable, to approach all scattering studies in this manner. It is well recognized that if one is interested only in thermal reaction rate constants, then transition-state theory is often adequate. There are also several examples where classical trajectory simulation methods have been applied to describe more detailed state-to-state properties of reactions. Furthermore, there are a variety of approximate quantum mechanical and semi-classical methods (where only some of the degrees of freedom are treated quantum mechanically, the remaining classical) that are satisfactory and useful in various special situations. However, these models are, at least to some extent, approximate and often cannot give complete account for quantum mechanical phenomena encountered in modern experiments, and so only a rigorous quantum scattering calculation is guaranteed to be correct. Hence, it is very important to develop these capabilities to as great an extent as possible in order to be able, in some cases at least, to provide a "completely" reliable theoretical description. Such is the point of view of this thesis.

Throughout the rest of this chapter we are going to introduce some of the central concepts needed for the discussions in the subsequent parts of this thesis. In section 1.1 we will define the important *quantum flux*, entering the definition in eq. (1.2). This concept, which serves as the quantum analog to the classical current of particles, is evidently vital for the studies in part II, and as shown in the last part of section 1.1, it is also useful when studying resonances, which will be the topic of part III. Section 1.2 considers the simple but nevertheless very illustrative case of an elastic scattering and introduces the concept of scattering *phase shift*. This concept will be especially important in part III. However, this section is also included to make a historical connection to the traditional formulation of quantum scattering where reference is only made to the asymptotic states of the system, *i.e.* the initial and final quantum states. Throughout the rest of this thesis we will take a somewhat different viewpoint, in which explicit reference will also be made to the intermediate states produced during the collision.

1.1 Definition of quantum flux

Consider the rate of change of the probability of a particle being in a finite volume V,

$$\begin{aligned}\frac{\partial}{\partial t}P_V(t) &\equiv \frac{\partial}{\partial t}\int_V d^3\vec{r}|\Psi(\vec{r},t)|^2 \\ &= \int_V d^3\vec{r}\left\{\Psi^*(\vec{r},t)\dot{\Psi}(\vec{r},t)+\Psi(\vec{r},t)\dot{\Psi}^*(\vec{r},t)\right\} \\ &= 2\,\mathrm{Re}\int_V d^3\vec{r}\Psi^*(\vec{r},t)\dot{\Psi}(\vec{r},t) \qquad (1.4)\end{aligned}$$

We now insert the celebrated time-dependent Schrödinger equation

$$i\hbar\frac{\partial}{\partial t}\Psi(\vec{r},t)=\widehat{H}\Psi(\vec{r},t)=\left[-\frac{\hbar^2}{2\mu}\widehat{\nabla}^2+V(\vec{r})\right]\Psi(\vec{r},t) \qquad (1.5)$$

into eq. (1.4) and assume that $V(\vec{r})$ is real[2]

$$\begin{aligned}\frac{\partial}{\partial t}P_V(t) &= 2\,\mathrm{Re}\int_V d^3\vec{r}\frac{\Psi^*(\vec{r},t)}{i\hbar}\left(-\frac{\hbar^2}{2\mu}\widehat{\nabla}^2\Psi(\vec{r},t)+V(\vec{r})\Psi(\vec{r},t)\right)\\ &= \mathrm{Re}\left[\frac{i\hbar}{\mu}\int_V d^3\vec{r}\Psi^*(\vec{r},t)\widehat{\nabla}^2\Psi(\vec{r},t)\right] \qquad (1.6)\end{aligned}$$

Next this volume integral is converted to a surface integral by invoking integration by parts[3]

$$\begin{aligned}\int_V d^3\vec{r}\Psi^*(\vec{r},t)\widehat{\nabla}^2\Psi(\vec{r},t) &= \oint_S d^2\vec{e}_r\cdot\Psi^*(\vec{r},t)\widehat{\vec{\nabla}}\Psi(\vec{r},t)\\ &\quad-\int_V d^3\vec{r}\,\widehat{\vec{\nabla}}\Psi^*(\vec{r},t)\cdot\widehat{\vec{\nabla}}\Psi(\vec{r},t) \qquad (1.7)\end{aligned}$$

We note that the last term in eq. (1.7) is real, and thus eq. (1.6) finally reduces to

$$\frac{\partial}{\partial t}P_V(t) = \mathrm{Re}\oint_S d^2\vec{e}_r\cdot\Psi^*(\vec{r},t)\frac{i\hbar}{\mu}\widehat{\vec{\nabla}}\Psi(\vec{r},t) \equiv -\oint_S d^2\vec{e}_r\cdot\vec{\mathbf{j}}\,[\Psi(\vec{r},t)] \qquad (1.8)$$

where we have defined the *non-linear* vector operator

$$\boxed{\vec{\mathbf{j}}\,[\Psi(\vec{r},t)] \equiv \mathrm{Re}\left[\Psi^*(\vec{r},t)\frac{\widehat{\vec{\mathbf{p}}}}{\mu}\Psi(\vec{r},t)\right] \qquad (1.9)}$$

where $\widehat{\vec{\mathbf{p}}} \equiv -i\hbar\widehat{\vec{\nabla}}$ denotes the usual linear momentum operator. The physical interpretation of eq. (1.8) follows immediately when we note that the probability, P_V, can change only by "particles" flowing in or out through the surface S inclosing V, and thus the rhs. of eq. (1.8) must express the total quantum mechanical *flux*. Consequently we can finally identify $\vec{\mathbf{j}}\,[\Psi(\vec{r},t)]$ in eq. (1.9) as the quantum mechanical *flux* density, or probability current density vector, *i.e.* the number of "particles" per unit time that cross a unit surface at the point $\vec{r}$. We can now make the following important conclusions:

---

[2] We shall consider the case with a complex potential later.

[3] In this integral equation and throughout the rest of this chapter we use the notation $\vec{e}_r \equiv \vec{r}/|\vec{r}|$.

- If the wave function is time-independent then so is the flux, *i.e. steady-state flux.*

- Unlike the classical flux ($\vec{\mathbf{j}} = \frac{\vec{p}}{\mu} P_V$) the quantum mechanical flux is a *non-linear* operator giving rise to complicated interference terms between for instance incoming and outgoing parts of the total wave function.

- The flux vector $\vec{\mathbf{j}}$ and the probability density $|\Psi|^2$ satisfy the equation $\partial|\Psi|^2/\partial t$ $+\nabla \cdot \vec{\mathbf{j}} = 0$, which is analogous to the classical equation of continuity[4]. This follows readily[5] by invoking the divergence theorem on eq. (1.8).

- If the wave function is real then $\vec{\mathbf{j}}\,[\Psi(\vec{r}, t)] \equiv 0$. Consequently quantum mechanical scattering necessarily involve *complex* wave functions.

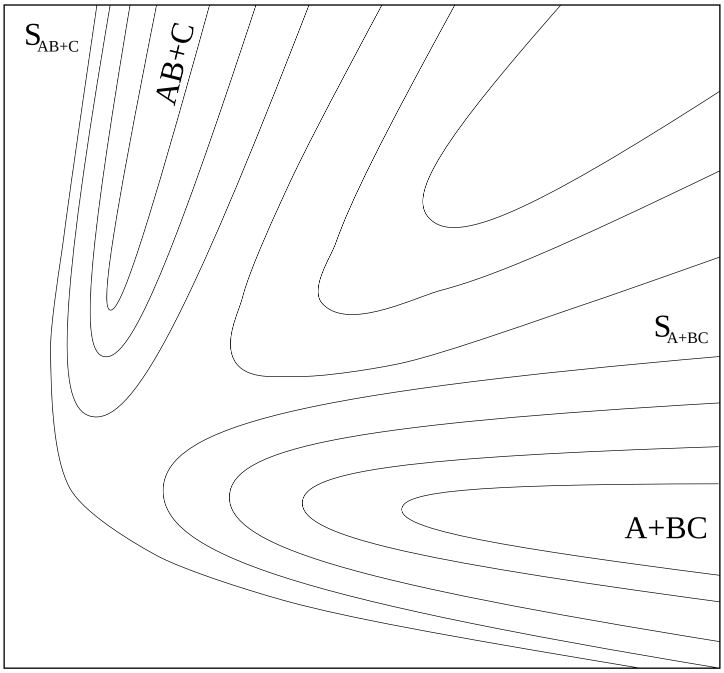

Figure 1.1: Contour-plot of the potential energy surface for a simple three-particle system which is confined to move on a straight line – *i.e.* collinear system. Note the two arrangement channels AB+C and A+BC. The system is enclosed in the box S which is composed of the two parts, $S_{\mathrm{AB+C}}$ and $S_{\mathrm{A+BC}}$, each including one of the channels.

---

[4] The classical *equation of continuity* reads as $\frac{\partial \rho}{\partial t} + \hat{\vec{\nabla}} \cdot \rho\,\vec{v} = 0$ where ρ is the density and $\vec{v}$ the velocity.

[5] First we invoking the divergence theorem, $\int_V d^3\vec{r}\,\hat{\vec{\nabla}} \cdot \vec{\mathbf{j}} = \oint_S d^2\vec{e}_r \cdot \vec{\mathbf{j}}$, and then we make use of the fact that V is arbitrary.

Now, let us shortly consider the very important case when V in eq. (1.5) is not a real potential, but rather a negative imaginary potential (nip), *i.e.* $V \to V_{nip} \equiv -iV$ where $V > 0$. It then follows immediately from eq. (1.6) that the extra term

$$-\frac{2}{\hbar}\,\mathrm{Re}\int_V d^3\vec{r}\,\Psi^*(\vec{r},t)V(\vec{r})\Psi(\vec{r},t) < 0 \tag{1.10}$$

is added to eq. (1.8). Hence we conclude that flux is *removed* from the system when adding a *negative imaginary potential*[6]. This actually forms the basis for several very useful techniques which will play a central role in this thesis. In part II we shall discuss this feature in the context of time-dependent dynamics, and in part III we shall use negative imaginary potentials to locate resonances with.

Let us close this section by considering a simple, but nevertheless typical application of the flux concept, which nicely puts the two topics of this thesis in a perspective. It immediately follows from the definition that

$$P_V(t_1) - P_V(t_0) = -\oint_S d^2\vec{e}_r \cdot \vec{\mathcal{F}}(\vec{r}) \tag{1.11}$$

where we have defined the time-integrated flux $\vec{\mathcal{F}}(\vec{r}) \equiv \int_{t_0}^{t_1} dt\,\vec{\jmath}\,[\Psi(\vec{r},t)]$. Now, imagine that the system under consideration is a simple collinear[7] three-particle system as illustrated in figure 1.1. The two arrangement channels are denoted respectively $\mathrm{A}B + C$ and $\mathrm{A} + BC$, and we note that the surface S enclosing the coordinate space V can be partitioned into two parts, $S_{\mathrm{A}B+C} + S_{\mathrm{A}+BC}$, which include each of the two channels. Next, assume that at $t_0 = 0$ the wave function is normalized, *i.e.* $P_V(0) = 1$, and that after some time, $t_1 = t^*$, the reaction is completed, *i.e.* $P_V(t^*) = 0$. Thus, eq. (1.11) reduces to

$$\int_{S_{\mathrm{AB+C}}} d^2\vec{e}_r \cdot \vec{\mathcal{F}}(\vec{r}) + \int_{S_{\mathrm{A+BC}}} d^2\vec{e}_r \cdot \vec{\mathcal{F}}(\vec{r}) = 1 \tag{1.12}$$

However trivial this equation might appear, it expresses the fundamental concept of conservation of particles (*i.e.* flux), and as will be demonstrated in part II of this thesis it is very useful when testing the numerical implementation of a time-dependent scattering calculation. Nevertheless, important situations may occur

---

[6] These negative imaginary potentials are often also referred to as optical potentials, because they imitate an optical device (*e.g.* particle analyzer) which removes flux from a particle beam.

[7] A collinear reactive system is a system where all the involved particles move on a straight line.

where $P_V(t^*) > 0$, even for large values of t^*, such that eq. (1.12) does not hold[8]. This corresponds to the very interesting case where the system, *i.e.* wave function, is trapped in some intermediate quasi-bound state[9]. The study of the formation of such so-called resonances forms the very basis of part III of this thesis.

1.2 Elastic scattering

In this section we will present a theoretical description of a simple but typical three dimensional scattering experiment. Many of the results derived in this section can be found in standard textbooks, but nevertheless I have decided to include this section for the following reasons: First of all, it is my personal belief and experience that the topic of this section does not receive much attention in quantum scattering courses taught now a days, and as such cannot be considered elementary knowledge. This point is also supported by the fact that many modern textbooks tend to say very little about this topic, or sometimes even completely leave it out. Secondly, this section will establish, at least formally, the significant link between the experimental observations made on dynamical systems (*cf.* eq. (1.2) and (1.3)) and the corresponding theoretical description of it. This thesis strictly considers only the latter class of problems, but for obvious reasons it is very important to establish, or at least point out, this connection between the two very different fields of quantum dynamics. This leads us to the final, and perhaps most importantly, reason for including this section, namely, to give an experimental motivation for the theoretical studies of resonances. So, in a sense this section will also serve as a conceptual toolbox for the introductory discussions in part III.

To keep the notation as simple as possible we are going to restrict ourself to a simple elastic collision, where excitation of internal (*e.g.* vibrational or rotational) degrees of freedom is neglected. Furthermore, we shall only discuss the key features of this dynamical system, and we just note that the generalization of the presented results to non-elastic systems is readily made. Thus, using the notation introduced in eq. (1.1) we have

$$\mathrm{A} + \mathrm{BC}(i) \xrightarrow{\text{Elastic}} \mathrm{A} + \mathrm{BC}(i) \tag{1.13}$$

where A labels the projectile that are scattered by the target BC[10] . Theoretically the two particles are governed by quantum mechanics and the complete system

---

[8] Note that this is of course not in conflict with the law of conservation of particles, it is merely a consequence of $P_V(t^*) > 0$, *i.e.* t^* is not chosen large enough.

[9] For the time being we shall ignore the possibility of the system supporting true bound intermediate states.

[10] We note that in the theorist's eye, there is no distinction between the projectile and the

is therefore best described by a wave function, $\Psi_{\vec{k}}(\vec{r})$. However, to facilitate a physical interpretation we partition $\Psi_{\vec{k}}(\vec{r})$ as

$$\Psi_{\vec{k}}(\vec{r}) = \phi_{\vec{k}}(\vec{r}) + \psi_{\vec{k}}(\vec{r}) \tag{1.14}$$

where $\phi_{\vec{k}}(\vec{r})$ denotes the incident beams wave function and $\psi_{\vec{k}}(\vec{r})$ the scattered wave function. The incident beams wave function, with a constant linear momentum of $\hbar\vec{k}$, is mathematically represented by the plane wave

$$\phi_{\vec{k}}(\vec{r}) = e^{i\vec{k}\cdot\vec{r}} = e^{ikr\cos\theta} \tag{1.15}$$

This wave function is clearly not normalizable in the usual $\mathcal{L}^2(V)$ sense[11], which for the time being we shall just leave as a mathematical curiosity[12]. On physical grounds we will assume that we can write the asymptotic form of the scattered wave function as

$$\lim_{r\to\infty}\left[\psi_{\vec{k}}(\vec{r})\right] = f_E(\theta,\phi)\frac{e^{ikr}}{r} \tag{1.16}$$

This expression states that the scattered wave function has the same shape as the incident wave function (*i.e.* elastic scattering), that the intensity of the scattered beam falls off with the inverse square law, and that the amplitude of the scattered wave, $f_E(\theta,\phi)$, is independent of the details of the experiment. Consequently the asymptotic form of the total wave function is assumed to take the form

$$\boxed{\lim_{r\to\infty}\left[\Psi_{\vec{k}}(\vec{r})\right] = e^{i\vec{k}\cdot\vec{r}} + f_E(\theta,\phi)\frac{e^{ikr}}{r}} \tag{1.17}$$

which can be rearranged to give the formal definition

$$f_E(\theta,\phi) = re^{-ikr}\lim_{r\to\infty}\left[\Psi_{\vec{k}}(\vec{r}) - \phi_{\vec{k}}(\vec{r})\right] \tag{1.18}$$

---

target particle. An experimentalist may however view it differently because the target is usually fabricated from stable, workable, or abundant material, while the beam particle may be rare, unstable or even have an exceedingly short lifetime.

[11] Some times the plane waves are "δ-normalized" leading to the prefactor $(2\pi)^{-3/2}$. However to keep the notation as simple as possible we shall ignore this factor throughout the rest of this section.

[12] Physically this non-normalizability of the plane waves can be understood from the Heisenberg uncertainty principle, $\Delta p\Delta r \geq \frac{\hbar}{2}$. The plane wave has a unique momentum, *i.e.* $\Delta p = 0 \Rightarrow \Delta r \sim \infty$, such that the wave function has a constant (unit) probability amplitude in the configuration space. However disturbing and unphysical this might appear, it is a direct consequence of the fact that we are using a strictly *time-independent* description of a dynamical system which is inherently time-dependent.

This universal amplitude function is referred to as the *scattering amplitude.* Next, using the definition of the differential cross-section, given in eq. (1.2), the expression for the flux-operator derived in the previous section, eq. (1.9), and the asymptotic form listed in eq. (1.17), we obtain the following simple expression for the elastic differential cross-section

$$\boxed{\frac{d\sigma_{el}}{d\Omega}(E,\theta,\phi) = |f_E(\theta,\phi)|^2 \qquad (1.19)}$$

It should be clear from the above that the scattering problem is now reduced to a study of the appropriate boundary conditions of the quantum system, and evidently the scattering amplitude is the central quantity which facilitates an immediate connection to experimental measurements. As a prelude to the derivation of an explicit expression for the elastic scattering amplitude, entering eq. (1.17), we write the plane wave, eq. (1.15) as a "partial wave expansion" [6]

$$\phi_{\vec{k}}(\vec{r}) = 4\pi \sum_{\ell=0}^{\infty} \sum_{m=-\ell}^{\ell} i^{\ell} Y^{*}_{\ell m}(\vec{e}_k) Y_{\ell m}(\vec{e}_r) j_{\ell}(kr) \tag{1.20}$$

where $Y_{\ell m}(\vec{e}_r)$ are spherical Harmonics and $j_\ell(kr)$ are spherical Bessel functions illustrated in figure 1.2. Because the $j_\ell(kr)$'s have the boundary properties[13]

$$j_\ell(kr) = \begin{cases} (kr)^\ell/(2\ell+1)!! & \text{for } kr \to 0 \\ \sin{(kr - \ell\pi)}/kr & \text{for } kr \to \infty \end{cases} \tag{1.21}$$

each Bessel function, $j_\ell(kr)$, has approximately vanishing amplitude when $kr << \ell$ and asymptotically oscillatory behavior for $kr >> \ell$. This should also be visible in figure 1.2. The physical motivation for the expansion in spherical Bessel functions, eq. (1.20), now follows: If the plane wave is incident upon a *finite ranged* potential, $V(r)$, there will always be some partial waves which lie outside of the potential and are therefore unaffected by it. This is simply a consequence of some of the $j_\ell(kr)$'s being essentially zero in the coordinate space in which the potential exists. Thus, if $V(r)$ is finite, then so is the number of scattered partial waves in the sum of eq. (1.20). For the total (distorted) scattering wave function, $\Psi_{\vec{k}}$, we next assume the same form for its partial-wave decomposition, *i.e.* we attempt to write $\Psi_{\vec{k}}$ in a basis-set of spherical Harmonics,

---

[13] Throughout the rest of this section we use the notation $(2\ell+1)!! \equiv 1 \cdot 3 \cdot 5 \cdots (2\ell+1)$.

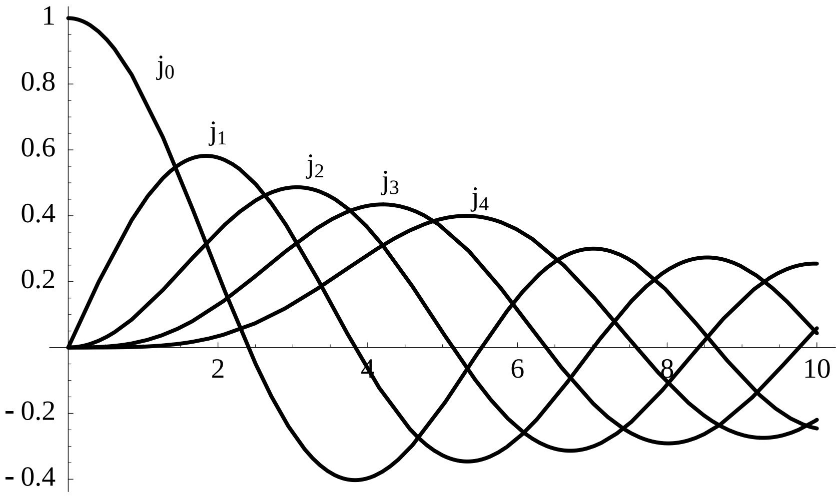

Figure 1.2: Plot of the first five spherical Bessel functions, $j_\ell(kr)$, $\ell = 0, 1, \ldots, 4$. Note that $j_\ell(kr) \approx 0$ for $kr << \ell$ and oscillatory for $kr >> \ell$.

$$\Psi_{\vec{k}}(\vec{r}) = 4\pi \sum_{\ell=0}^{\infty} \sum_{m=-\ell}^{\ell} i^\ell Y^*_{\ell m}(\vec{e}_k) Y_{\ell m}(\vec{e}_r) \frac{u_\ell(kr)}{kr} \tag{1.22}$$

where the radial functions $u_\ell(kr)$ still remain to be defined. To do this we could insert eq. (1.22) into the time-independent Schrödinger equation, which, in spherical center-of-mass coordinates, reads as

$$\widehat{H}\Psi_{\vec{k}}(\vec{r}) = \left[-\frac{\hbar^2}{2\mu r}\frac{\partial^2}{\partial r^2} r + \frac{\widehat{\mathbf{L}}^2}{2\mu r^2} + V(r) \right] \Psi_{\vec{k}}(\vec{r}) \tag{1.23}$$

where $\widehat{\mathbf{L}}^2$ is the total orbital angular momentum. However, before we do this, and attempt to solve the resulting equations for $u_\ell(kr)$ over all the coordinate space, we recall from the introduction that the purpose of this section was merely to establish the theoretical tools needed for the calculation of the differential cross-section. Thus, from eq. (1.19) and (1.18) we see that we actually only need to solve eq. (1.23) in the asymptotic region of r where $V(r) = 0$. The corresponding "free" second-order differential Schrödinger equation[14] has two solutions

$$\left[\frac{d^2}{dr^2}+k^2\right]\begin{Bmatrix}F_\ell(kr)\\ G_\ell(kr)\end{Bmatrix} \;=\; \frac{\ell(\ell+1)}{r^2}\begin{Bmatrix}F_\ell(kr)\\ G_\ell(kr)\end{Bmatrix} \tag{1.24}$$

which are easily expressed in terms of respectively spherical Bessel and Neumann functions[6]

$$F_\ell(kr) \;\equiv\; krj_\ell(kr) \tag{1.25a}$$

$$G_\ell(kr) \;\equiv\; -krn_\ell(kr) \tag{1.25b}$$

We note that $F_\ell(kr)$ is the *regular* solution of eq. (1.24) (*i.e.* non-singular at the origin), and $G_\ell(kr)$ is the corresponding *irregular* (divergent) solution. More specifically we have the boundary behaviors

$$\lim_{kr\to 0}\begin{Bmatrix}F_\ell(kr)\\ G_\ell(kr)\end{Bmatrix}=\begin{Bmatrix}(kr)^{\ell+1}/(2\ell+1)!!\\ (2\ell+1)!!/(kr)^{\ell+1}\end{Bmatrix} \tag{1.26}$$

and

$$\lim_{kr\to\infty}\begin{Bmatrix}F_\ell(kr)\\ G_\ell(kr)\end{Bmatrix}=\begin{Bmatrix}\sin(kr-\ell\pi/2)\\ \cos(kr-\ell\pi/2)\end{Bmatrix} \tag{1.27}$$

At this point it is tempting to assume that since the radial wave function, $u_\ell(kr)$, must always be regular for any finite-ranged non-singular potential, then the irregular $G_\ell(kr)$ solution can be excluded. However this is *not* correct since the two free solutions form a complete set whenever $V(r)=0$, and thus the full wave functions must be a linear combination of the two functions in the region outside the potential's range, say for $r>R$. For reasons that will soon become clear we choose the following combination[15] for the free part of the radial functions

$$u_\ell(kr) \xrightarrow[r>R]{} e^{i\eta_\ell}\left\{\cos(\eta_\ell)\,F_\ell(kr)+\sin(\eta_\ell)\,G_\ell(kr)\right\} \tag{1.28}$$

---

[14] To obtain eq. (1.24) we have first inserted eq. (1.22) into eq. (1.23), with $V(r)=0$, and made use of the fact that the spherical Harmonics are eigenfunctions of the orbital angular momentum, $\widehat{\mathbf{L}}^2 Y_{\ell m}(\vec{e}_r)=\hbar^2\ell(\ell+1)Y_{\ell m}(\vec{e}_r)$. Next we have multiplied the resulting equations by $Y^*_{\ell' m'}(\vec{e}_k)$, integrated over $\vec{e}_k$ (*i.e.* the polar angles defining the direction of the linear momentum) and finally make use of the fact that the spherical Harmonics are orthogonal.

[15] Note that at any case this is a "one-parameter" problem in the sense that if we choose one of the contributions (*e.g.* $G_\ell(kr)$), then the other one ($F_\ell(kr)$) is uniquely determined from the relevant boundary condition on the radial wave function.

where we have introduced the real[16] energy-dependent constant η_ℓ. The physical interpretation of η_ℓ follow immediately if we examine the asymptotic behavior of eq. (1.28)

$$\begin{aligned}\lim_{r \to \infty} u_\ell(kr) &= \exp(i\eta_\ell)\sin(kr - \ell\pi/2 + \eta_\ell) &\text{(1.29a)}\\ &= \frac{1}{2i^{\ell+1}}\left(e^{2i\eta_\ell}e^{ikr} - e^{-ikr}\right) &\text{(1.29b)}\end{aligned}$$

where we have made use of eq. (1.27). Eq. (1.29b) follow by decomposing the sine[17] into the exponentials representing respectively the *outgoing and incoming* waves. Eq. (1.29a) clearly shows that $u_\ell(kr)$ has the same asymptotic form as the free wave, *cf.* eq. (1.21), only with its phase shifted by η_ℓ, which, according to eq. (1.29b), is equivalent to a shift of the outgoing wave's phase by $2\eta_\ell$ relative to the incoming wave. Consequently η_l is referred to as the scattering *phase-shift.* If we next collect eq. (1.20) and (1.21), and eq. (1.22) and (1.29b) we obtain the following asymptotic forms

$$\begin{aligned}\lim_{r\to\infty}\left[\phi_{\vec{k}}(\vec{r})\right] &= \frac{4\pi}{2ikr}\sum_{\ell=0}^{\infty}\sum_{m=-\ell}^{\ell} Y^*_{\ell m}(\vec{e}_k)Y_{\ell m}(\vec{e}_r)(e^{ikr} - e^{-ikr}) &\text{(1.30a)}\\ \lim_{r\to\infty}\left[\Psi_{\vec{k}}(\vec{r})\right] &= \frac{4\pi}{2ikr}\sum_{\ell=0}^{\infty}\sum_{m=-\ell}^{\ell} Y^*_{\ell m}(\vec{e}_k)Y_{\ell m}(\vec{e}_r)(e^{2i\eta_\ell}e^{ikr} - e^{-ikr}) &\text{(1.30b)}\end{aligned}$$

The explicit expression for the *scattering amplitude* next follow immediately from the definition in eq. (1.18)

$$\begin{aligned}f_E(\theta) &= \frac{4\pi}{2ik}\sum_{\ell=0}^{\infty}\sum_{m=-\ell}^{\ell} Y^*_{\ell m}(\vec{e}_k)Y_{\ell m}(\vec{e}_r)(S_\ell - 1) &\text{(1.31a)}\\ &= \frac{1}{k}\sum_{\ell=0}^{\infty}(2\ell+1)P_\ell(\cos\theta)e^{i\eta_\ell}\sin\eta_\ell &\text{(1.31b)}\end{aligned}$$

---

[16] η_l is real as long as only the elastic channel is open. When absorption is included, *i.e.* any process removing flux from the incident channel, then η_ℓ, as defined in eq. (1.28), becomes a complex number with a *positive* imaginary component.

[17] We have made use of the identity

$$e^{i\eta_\ell}\sin(kr - \ell\pi/2 + \eta_\ell) = \frac{e^{2i\eta_\ell}e^{i(kr-\ell\pi/2)} - e^{-i(kr-\ell\pi/2)}}{2i} = \frac{e^{2i\eta_\ell}e^{ikr} - e^{-ikr}}{2i^{\ell+1}}$$

where we have defined the celebrated unitary S-matrix $S_\ell \equiv e^{2i\eta_\ell}$ in eq. (1.31a) and used the following identity to obtain eq. (1.31b)

$$P_\ell(\cos\theta) = P_\ell(\vec{e}_k \cdot \vec{e}_{k'}) = \frac{4\pi}{2\ell+1} \sum_{m=-\ell}^{\ell} Y^*_{\ell m}(\vec{e}_k) Y_{\ell m}(\vec{e}_{k'}) \tag{1.32}$$

where $P_\ell(\cos\theta)$ are Legendre polynomials. According to eq. (1.19) the elastic differential cross section is then simply obtained from the relation $\frac{d\sigma_{el}}{d\Omega}(\theta) = |f_E(\theta)|^2$. Finally, using the definition in eq. (1.3) and the orthogonality relation of the Legendre polynomials[18], the integral cross-section is readily obtained as

$$\sigma_{el}(E) = \frac{4\pi}{k^2} \sum_{\ell=0}^{\infty} (2\ell+1) \sin^2\eta_\ell \tag{1.33a}$$

$$= \frac{\pi}{k^2} \sum_{\ell=0}^{\infty} (2\ell+1) |S_\ell - 1|^2 \tag{1.33b}$$

This finally concludes our brief discussion on introductory quantum scattering, which as mentioned before, provides the formal link to experimental measurements of differential and integral cross-sections.

---

[18] The Legendre polynomials satisfy the orthogonality relation[6]

$$\int_{-1}^{1} dx P_\ell(x) P_{\ell'}(x) = \frac{2}{2\ell+1} \delta_{\ell,\ell'}$$

2

Numerical representations

In this chapter we shall briefly discuss some of the problems and corresponding solutions which I recounted during the numerical formulation of the quantum calculations to be presented in part II and III. However, all of the numerical questions raised in the chapter, and most of the solutions, are quite general in the sense that they are fundamental to every quantum mechanical calculation on a reactive system. In section 2.1 we are going to discuss the so-called coordinate-problem, and in section 2.2 we shall present the concepts, tools and computational techniques used for the numerical representation of the quantum systems that are studied in the subsequent parts of this thesis.

2.1 Coordinates

One of the first major challenges when setting up a reactive quantum calculation is to choose an appropriate set of coordinates in which the corresponding formulation is convenient for the subsequent numerical implementation. In short, the problem is that the coordinates which most conveniently describe the reactants of a chemical reaction are not necessarily particularly convenient for describing the products, and vice versa. Therefore, in order to obtain a complete description of the reactive scattering event, one has either to define a new set of inevitable more complicated coordinates which somehow covers the complete configuration space, or else simply work in an over-complete coordinates space where one simultaneously retain all the convenient sets of coordinates, both for the reactants and the products. The fact that this coordinate problem encumbers quantum calculations so much might at first come as a surprise, since it is well known that classical trajectory calculations on quite complicated reactions have been performed for some time. However, the answer to this enigma is of course straight forward. Quantum mechanical calculations, by virtue of the uncertainty principle, describe all regions of the coordinate space at once, whereas classical trajectory calculations effectively access only a single point in this space at a time. This actually simplifies the classical calculations so much that just about any well defined coordinate system will do.

Below we are going to present three different types of coordinates which will be used in part II and III. These coordinates all have their pros and cons, as we shall soon see, but they are nevertheless the most widely used systems of coordinates in reactive quantum calculations. To keep the notation as simple as possible, we shall continue to use the collinear three particle system, introduced in the previous chapter (*cf.* figure 1.1), as the working example.

2.1.1 Jacobi coordinates

The *Jacobi coordinates* are the natural starting-point for any discussion on coordinates in reactive scattering. Different choices of Jacobi coordinates exist, but common to all of them is that by construction they all lead to a kinetic energy operator without cross-terms. This nice feature of the Jacobi coordinates, and the fact that they are readily generalized to multi-dimensional systems makes them very popular. Especially the so-called *mass-scaled Jacobi coordinates* are convenient as they lead to a very simple form of the kinetic energy operator with only one common mass-factor. Taking the simple collinear three particle reaction as the working example, increments of the reactant and product mass-scaled Jacobi coordinates, (R_a, r_a) and (R_c, r_c), are depicted in figure 2.1. These mass-scaled Jacobi coordinates are defined in terms of the usual (unscaled) atom-diatom displacements, (R'_a, r'_a), as

$$R_a \equiv \alpha_a R'_a \quad \text{and} \quad r_a \equiv \alpha_a^{-1} r'_a \tag{2.1}$$

where the channel-dependent mass-scaling factor α_a reads as

$$\alpha_a \equiv \sqrt{\frac{m_a(m_b+m_c)}{\mu M_{tot}}} \quad \text{where} \quad \mu \equiv \sqrt{\frac{m_a m_b m_c}{M_{tot}}} \tag{2.2}$$

and where M_{tot} is the total mass and μ the three-atom reduced mass. Thus, R_a is a mass-scaled distance between A and the center-of-mass of BC, and r_a is a mass-scaled distance between B and C. It should be clear from figure 2.1 that either set of mass-scaled Jacobi coordinates alone provides a complete description of the collinear coordinate space. However, it should be equally clear that while (R_a, r_a) are better suited for describing translational and vibrational motions in

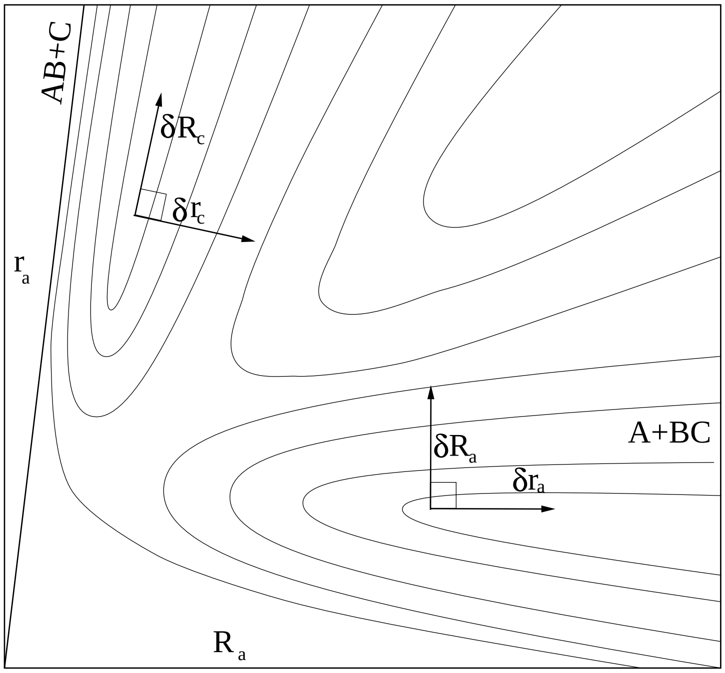

Figure 2.1: Illustration of the increments of the two different sets of mass-scaled Jacobi coordinates, (R_a, r_a) and (R_c, r_c), for a simple collinear atom-diatom reactive system. Asymptotically R describes the translational motion in the corresponding atom-diatom arrangement, and r describes the diatomic vibrations. The axis labels are (R_a, r_a), explicitly defined in eq. (2.1), and the potential contour lines are the same as in figure 1.1.

the A+BC channel, (R_c, r_c) are more appropriate for a corresponding description in the AB+C channel. Consequently it seems natural to simply retain both sets of coordinates at once, using each set for convenience as required. This clearly leads to an over-complete description of the configuration space which result in a potential coupling of the translational and vibrational motions in the different arrangement channels. This non-local coupling between states in the reactant and product channels appear as a type of exchange integrals between basis-functions in different chemical arrangements. These exchange integrals are simply a mathematical manifestation of the interactions which cause the reaction to proceed, and they are quite analogous to electron exchange interactions in LCAO-like quantum chemistry that arise from matrix elements in which the electron coordinates have been exchanged[1]. Thus, the *coordinate-problem*, related to the use of Jacobi coor-

---

[1] In the LCAO-approximation the molecular orbitals for an electron are expanded in atomic orbital basis-functions utilizing the coordinates of the electron with respect to the different nuclear centers. In other words, the central idea in the LCAO model, similar to that of a basis-set expansion in functions expressed in different Jacobi coordinates, is a multi-center expansion.

dinates in reactive scattering, can be solved, but it is nevertheless a complicating feature of these coordinates. Indeed a comprehensive account of such a formulation for the general case of a three-dimensional atom-diatom reaction, was given by Miller[7] as early as in 1969.

2.1.2 Natural collision coordinates

One way to overcome the coordinate problem discussed above is to use *natural collision* coordinates. These coordinates, which were introduced by Marcus[8] more than thirty years ago, are best characterized as a curvilinear reaction coordinate that swings smoothly from the reactant to the product and a perpendicular vibrational coordinate. This is illustrated in figure 2.2 for the collinear case. Here δs is the increment of the translational reaction coordinate s, which asymptotically describes the mass-scaled separation between atom A or C and the pair BC or AB. Different choices of this curvilinear coordinate, s, exist, but the most obvious

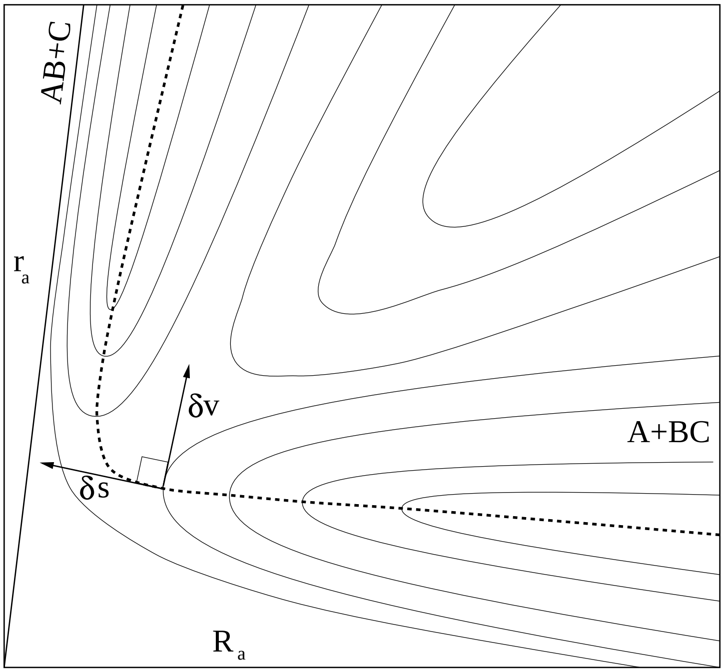

Figure 2.2: Illustration of increments of the natural collision coordinates, (s, v), for the collinear system. The translational reaction coordinate, s, is defined along the minimum energy path, shown as the dashed line going from the reactant to the product arrangement channel. Asymptotically v describes the vibrational motion of the corresponding diatom. The axis labels are the same as in figure 2.1.

one is the reaction-path coordinate which is defined as the minimum-potential-energy path. Like this, the natural collision coordinates have the great advantage of a direct connection to the concept of a reaction path, which we shall utilize in chapter 7. The s coordinate simply follows the reaction path from the entrance channel with minus infinity over the saddle-point, which is defined as the origin, to the exit channel with plus infinity. Similarly, δv is an increment of the vibrational coordinate v, which asymptotically describes a mass-scaled separation of the two atoms in the pair BC or AB. Thus, v denotes the shortest distance from any point in the configuration space to the reaction path, and s denotes the distance along the reaction path to that point. Clearly these natural collision coordinates are convenient in the simple two-channel two-dimensional case exemplified here, but the problem is how to generalize these coordinates to three-dimensional and multi-channel scattering situations. In three dimensions, at each value of the conserved total angular momentum number, the vibrational coordinate, v in figure 2.2, becomes a two-dimensional rot-vibrational surface, which can have quite complicated metric properties, making the internal coordinate somewhat more difficult to define and grasp. Furthermore, in the case of more than two open channel the idea of a well defined reaction path, s, looses its meaning. However, the earliest exact three-dimensional calculations by Kuppermann[9, 10], on the symmetric $H + H_2$ reaction, were actually performed using extensions of these natural collision coordinates. He essentially introduced “matching surfaces” between the three arrangements, but this is clearly a great deal easier to do for the symmetric reaction he studied then it is for anything else. Thus, all in all these coordinates are not very popular in the cases for multi-dimensional or multi-channel systems.

2.1.3 Hyperspherical coordinates

The most annoying feature of natural collision coordinates is probably the need to define matching surfaces between the different arrangements whenever more than one reaction channel is open (*i.e.* energetically allowed). In order to overcome this problem “routinely”, while at the same time retaining many of the advantages that these coordinates do have to offer, one can turn to the so-called *hyperspherical coordinates* which will be the last set of coordinate which we will mention. Hyperspherical coordinates have been defined in several ways in the scientific literature, but characteristic to all of these coordinate systems is that they consist of a *hyper-radius* and a remaining set of *hyper-angles*. The hyper-radius, is a direct measure of the overall extent of the configuration space and plays the role of the reaction coordinate as mentioned above. The hyper-angles define the arrangements of the particle made up by the reactive system. Thus, like for the natural collision coordinates, the major advantage of these hyperspherical coordinates is that they

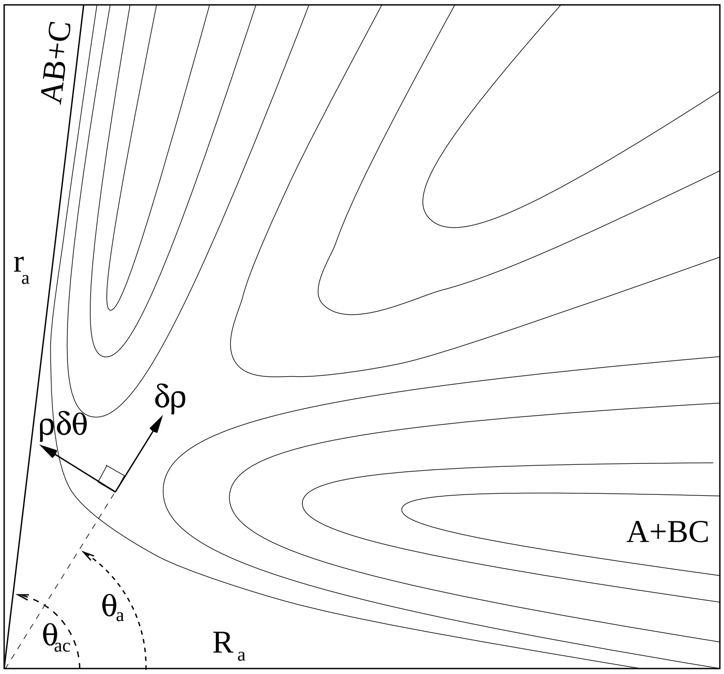

Figure 2.3: Illustration of the hyperspherical collinear Delves coordinates[11]. ρ is the hyper-radius which describes the overall extend of the configuration space, and the hyperangle, θ_a, describe the arrangement of the three particles.

describe the arrangement channels in an equivalent fashion. Once again taking the simple collinear three-particle reaction as the working example we define the hyper-radius, ρ, and the hyper-angle, θ_a as

$$\rho^2 \equiv R_a^2 + r_a^2 \quad \text{and} \quad \theta_{ab} = \tan^{-1}(m_b/\mu) \tag{2.3}$$

where (R_a, r_a) are the mass-scaled Jacobi coordinates, eq. (2.1), and the reduced mass, μ, is define in eq. (2.2). Both coordinates, and their increments are illustrated in figure 2.3. It should be noted that the hyper-radius (as opposed to the hyper-angle) is universal, in the sense that it can equally well be defined in terms of the mass-scaled Jacobi coordinates (R_c, r_c) corresponding to the $\mathrm{AB} + \mathrm{C}$ arrangement. The two possible hyper-angles are in fact related by $\theta_a + \theta_b = \theta_{ab}$ where $\theta_{ab} = \tan^{-1}(m_b/\mu)$ is the *skewing angle* also shown in figure 2.3. While these collinear hyperspherical coordinates, due to Delves[11], are essentially unique, several different possibilities arise when one moves to three dimensions. We shall just mention the symmetric coordinates introduced by Johnson[12–14] as this will be our choice of coordinate in a brief discussion in chapter 8 – or rather a symmetry adapted variant of these. The distinct advantage of these coordinates (which are actually an extension of hyperspherical coordinates due to Smith[15]) is that the five hyper-angles are explicitly subdivided into two sets: Three internal or configuration coordinates, (ρ, θ, ϕ), which determine respectively the size $(\rho \leq 0)$ and shape $(0 \leq \theta \leq \pi/2, 0 \leq \phi < 4\pi)$ of the triangle made up by the three particles, and a set of three external coordinates, (α, β, γ), which are the Euler angles that rotate the space-fixed system into a body-fixed system. Some of the other hyperspherical coordinate systems defined in the scientific literature, simply group the five hyper-angles together on an equal footing. This is for example the case for the, once very popular, hyperspherical coordinates introduced by Morse and Feshbach[16]. The reason why this explicit separation of the coordinates into an internal and external set is so important, is of course that the potential energy is only a function of the internal coordinates. The mapping of the Johnson Hyperspherical coordinates to Cartesian coordinates for a point in the configuration space is particular simple[12]

$$
\begin{aligned}
x &= \rho \sin\theta \cos\phi && (2.4a)\\
y &= \rho \sin\theta \sin\phi && (2.4b)\\
z &= \rho \cos\theta && (2.4c)
\end{aligned}
$$

Thus, (ρ, θ, ϕ) are simply the spherical polar coordinates for a point in the body-fixed frame of reference. If we restrict ourselves to the situation of zero total angular momentum, then the kinetic energy term also depend only on the internal coordinates, and no longer on the orientation angles. Hence, the $J = 0$ three-atom reaction can be formulated in three hyperspherical coordinates which conveniently describe the different arrangement channels in an equivalent fashion.

2.2 Grid methods

Accurate methods and techniques for the numerical representation of quantum systems have been sought since its very inception. Generally speaking, there exist three different types of approaches to this numerical problem in quantum mechanics. The first approach represents the states of the quantum system as ket vectors in the "somewhat abstract" occupation number space. In this so-called *second quantization* of the system, these ket vectors do not contain an explicit reference to any particular basis-set, as is the case in the conventional "first quantization". The reference to a basis-set is instead built into the second quantization operators in such a way that there exist a correlation principle between the first and second quantization[2]. The second quantization formulation is very popular in the field of

---

[2] The form of this correlation depend on the nature of the particles, and for the fermions it is given by the Condon-Slater rules. Thus, a characteristic feature of the second quantization is also that the statistics of the system is build into the formulation itself.

electronic structure theory, but has not received as much attention in scattering calculations. The second type of approach is best characterized as a *state expansion* of wave function in some finite basis-set. Thus, this approach is often referred to as the *finite basis representation* or just FBR in the literature. This technique is very popular in quantum calculation for reasons that will soon become clear. In fact, as we shall see in the next chapter, this approximation actually lies at the very heart of the definition of the electronic potential energy surfaces, which in turn are the starting-point in every scattering calculation. The last approach is to use a discretized representation of the quantum system (*i.e.* the operators and wave functions) on a grid or set of points, which will be the topic of this section. As these *grid methods* form the very basis of all the studies presented in this thesis, we will start out by briefly presenting some of the more important stages in the development of these techniques. This is primarily done to put the important Fourier and DVR methods, to be mentioned below, in perspective.

2.2.1 General collocation methods

Point wise representations of quantum systems actually dates back to the very beginning of quantum mechanics. In the late twenties Hartree[17] and Hylleraas[18] introduced the so-called finite difference method, hereafter denoted FD. In this representation the Schrödinger equation is discretized on a grid as

$$\left[\underline{\underline{\mathrm{T}}} + \underline{\underline{\mathrm{V}}}^D - E\right] \cdot \underline{\Psi} = \underline{0} \tag{2.5}$$

where $\underline{\Psi}$ is the column vector of the amplitudes on the grid, $\underline{\underline{\mathrm{V}}}^D$ is the diagonal matrix representation (denoted by the D) of the local potential in the grid points, and $\underline{\underline{\mathrm{T}}}$ is the (sparse) matrix representation of the non-local kinetic energy operator, obtained from a Taylor series expansion of the latter on the grid. Before the emerge of real super computers in the eighties and massive parallel computers in the nineties, the FD method had not really proved advantageous in more than two dimensions, as a very large number of grid points was necessary to obtain an accurate representation of the kinetic energy term. This problem of representing $\widehat{\mathbf{T}}$ in an accurate way was more or less overcome with the introduction of the *Pseudo-Spectral or collocation methods* in the early eighties. Generally these methods take point of reference in a finite basis representation (FBR) of the kinetic energy operator,

$$\widehat{\mathbf{T}} u_n(x) = \sum_{m=1}^{N} \langle u_m|\widehat{\mathbf{T}}|u_n\rangle u_m(x) \tag{2.6}$$

where we have assumed that the finite basis-set, $\{u_n(x), \quad n = 1, \ldots, N\}$, is orthonormal. The wave function is then expanded in this basis-set, and as in the original FD method the Schrödinger equation is next discretized on a grid to give the very easy handling of the local potential. Thus, at each grid point $\{x_p, \quad p = 1, \ldots, N\}$ we have

$$\sum_{n=1}^{N}\left[\sum_{m=1}^{N}\Big(\langle u_m|\widehat{\mathbf{T}}|u_n\rangle u_m(x_p)\Big) + \left(V(x_p) - E\right) u_n(x_p)\right] C_n = 0 \tag{2.7}$$

where C_n are the expansion coefficients of the wave function, $\Psi(x)$. If we now introduce the *collocation matrix*, $\underline{\underline{\mathrm{R}}}_{pn} \equiv u_n(x_p)$, such that $\underline{\Psi} = \underline{\underline{\mathrm{R}}} \cdot \underline{\mathrm{C}}$, eq. (2.7) can be recast into

$$\begin{aligned}
\left[\underline{\underline{\mathrm{R}}} \cdot \underline{\underline{\mathrm{T}}} + \left(\underline{\underline{\mathrm{V}}}^D - E\underline{\underline{\mathrm{I}}}\right) \cdot \underline{\underline{\mathrm{R}}}\right] \cdot \underline{\mathrm{C}} &= \underline{0} && \text{(2.8a)}\\
\left[\underline{\underline{\mathrm{R}}} \cdot \underline{\underline{\mathrm{T}}} \cdot \underline{\underline{\mathrm{R}}}^{-1} + \underline{\underline{\mathrm{V}}}^D - E\underline{\underline{\mathrm{I}}}\right] \underline{\Psi} &= \underline{0} && \text{(2.8b)}
\end{aligned}$$

where we have obtained the last equation by inserting the unit matrix $\underline{\underline{\mathrm{R}}}^{-1} \cdot \underline{\underline{\mathrm{R}}}$ in front of $\underline{\mathrm{C}}$. Next, multiplying eq. (2.8a) by $\underline{\underline{\mathrm{R}}}^{-1}$ from the left we arrive at the final working equation for the collocation method

$$\boxed{\left[\underline{\underline{\mathrm{T}}} + \underline{\underline{\mathrm{R}}}^{-1} \cdot \underline{\underline{\mathrm{V}}}^D \cdot \underline{\underline{\mathrm{R}}} - E\underline{\underline{\mathrm{I}}}\right] \cdot \underline{\mathrm{C}} = \underline{0} \qquad (2.9)}$$

This equation clearly shows that for an ill-conditioned (*i.e.* singular) collocation matrix, $\underline{\underline{\mathrm{R}}}$, the finite-basis representation of the potential, $\langle u_m|V|u_n\rangle = [\underline{\underline{\mathrm{R}}}^{-1} \cdot \underline{\underline{\mathrm{V}}}^D \cdot \underline{\underline{\mathrm{R}}}]_{mn}$, will be very inaccurate (to say the least). To "routinely" overcome this serious numerical problem of the general collocation scheme one can essentially take two different routes. Noting that the ill-conditioned $\underline{\underline{\mathrm{R}}}$ correspond to a poor choice of the basis-set and grid points, one can try to define a new representation in which these have been optimized for the numerical system at hand. This lead to the so-called discrete variable representations which will be discussed in details soon. Alternatively one can make the collocation matrix unitary, *i.e.* $\underline{\underline{\mathrm{R}}}^{-1} = \underline{\underline{\mathrm{R}}}^{+}$, by ensuring that the FBR functions satisfy the following *discrete*[3] orthogonality (or completeness) relations

$$\sum_{n=1}^{N} u_n^*(x_p) u_n(x_q) = \delta_{pq} \quad \Leftrightarrow \quad \sum_{p=1}^{N} u_n^*(x_p) u_m(x_p) = \delta_{nm} \tag{2.10}$$

---

[3] This is not to be confused with the orthogonality relation $\langle u_m|u_n\rangle = \delta_{mn}$ which we have assumed throughout this discussion.

An example of such a unitary collocation scheme is the celebrated Fourier method which will be the next topic of this section.

2.2.2 The Fourier transform method

Let us next examine a special case of an orthogonal collocation scheme which has become one of the most important numerical techniques in especially time-dependent quantum dynamics. Consider the FBR functions

$$u_n(x) \equiv \frac{1}{\sqrt{N}} \exp[i2\pi k_n x/L] \quad \text{where} \quad \begin{cases} k_n & = n - N/2 \\ n & = 1, \dots, N \end{cases} \tag{2.11}$$

which are clearly orthogonal (but not orthonormal) in the x interval from zero to L. If we now chose a uniform grid, *i.e.* N equally spaced sampling points, $\{x_p = (p-1)\Delta x, \quad p = 1, \dots, N\}$ where $\Delta x \equiv L/N$, we can show the completeness relations

$$\sum_{n=1}^{N} u_n(x_p) u_n^*(x_q) = \frac{1}{N} \sum_{n=1}^{N} \exp[i2\pi k_n (p-q)/N] =$$
$$\frac{1}{N} \exp[i\pi(q-p)] \sum_{n=1}^{N} \exp[i2\pi n(p-q)/N] = \delta_{pq} \tag{2.12}$$

where the last summation can be carried out explicitly because it is a finite trigonometric sum[4]. This is exactly the first of the discrete orthogonality relations in eq. (2.10), and the other one follow immediately from the symmetry between n and p in eq. (2.12). Thus, this is a unitary collocation scheme, with the property that the expansion coefficients of a finite-basis representation,

$$\Psi(x_p) \approx \sum_{n=1}^{N} C_n u_n(x_p) = \frac{1}{\sqrt{N}} \sum_{n=1}^{N} C_n \exp[i2\pi k_n x_p/L] \tag{2.13}$$

---

[4] The case $p-q=0$ is trivial, and for $p \neq q$ it can be shown, using finite sums of trigonometric functions (see paragraph 1.341 eq. (1) and (3) in reference [19]), that

$$\sum_{n=1}^{N} e^{i2\pi nm/N} = e^{i\pi m(N-1)/N} \frac{\sin(\pi m)}{\sin(\pi m/N)}$$

which for $m = p - q$, where $|p-q| \in [1, \dots, N-1]$, is clearly zero.

are simply given by[5]

$$C_n = \sum_{p=1}^{N} \Psi(x_p) u_n^*(x_p) = \frac{1}{\sqrt{N}} \sum_{p=1}^{N} \Psi(x_p) \exp[-i2\pi k_n x_p / L] \tag{2.14}$$

Eq. (2.13) and (2.14) are the discretized analogous to the well-known continuous Fourier transformation,

$$\mathrm{FT}^+[\Psi(k)] \equiv \frac{1}{\sqrt{2\pi}} \int_{-\infty}^{\infty} \Psi(k) e^{\mathrm{i}\,kx}\, dk = \Psi(x) \tag{2.15a}$$

$$\mathrm{FT}^-[\Psi(x)] \equiv \frac{1}{\sqrt{2\pi}} \int_{-\infty}^{\infty} \Psi(x) e^{-\mathrm{i}\,kx}\, dx = \Psi(k) \tag{2.15b}$$

which change a coordinate representation to a momentum representation and vice versa. In quantum mechanics the physical interpretation of the expansion coefficients, C_n, is therefore a discrete representation of the amplitude of the wave function in momentum space. Next we note that,

$$\frac{d^m \Psi(x)}{dx^m} = \frac{1}{\sqrt{2\pi}} \int_{-\infty}^{\infty} \Psi(k) (\mathrm{i}\,k)^m e^{\mathrm{i}\,kx}\, dk \equiv \mathrm{FT}^-[\Psi(k)(\mathrm{i}\,k)^m] \tag{2.16}$$

i.e. $\frac{d^m \Psi(x)}{dx^m}|_{x=x_p}$ is approximated by eq. (2.13) with $C_n \to (\mathrm{i}\,2\pi k/L)^m C_n$, the exceptional importance of this special collocation scheme finally emerge: The kinetic energy operator is local in the momentum representation (as is the case for the potential in the coordinate representation), and the Fourier method facilitates the discrete transformation between the two representations. Kosloff and Kosloff[20] and Feit *et al.*[21] were the first to apply this powerful technique to compute the action of the kinetic energy part of the Hamiltonian. Since then, the Fourier transform method has gained enormous attention and popularity in the area of time-dependent quantum dynamics. This popularity is primarily due to the fast nature of the algorithm used for the numerical implementation of this scheme (hence the name fast Fourier transform or just FFT), which makes it scale semi-linearly, $N \log N$, with the size of the grid, N. Thus, to sum up the FFT method can be viewed as a special case of a unitary collocation scheme, and the equivalence

---

[5] This follow directly from eq. (2.10).

of eq. (2.8b) and (2.9) read as

$$\left[\underline{\underline{\mathrm{R}}}\cdot\underline{\underline{\mathrm{T}}}^{D}\cdot\underline{\underline{\mathrm{R}}}^{+}+\underline{\underline{\mathrm{V}}}^{D}-E\underline{\underline{\mathrm{I}}}\right]\cdot\underline{\Psi}=\underline{0} \tag{2.17a}$$

$$\left[\underline{\underline{\mathrm{T}}}^{D}+\underline{\underline{\mathrm{R}}}^{+}\cdot\underline{\underline{\mathrm{V}}}^{D}\cdot\underline{\underline{\mathrm{R}}}-E\underline{\underline{\mathrm{I}}}\right]\cdot\underline{\mathrm{C}}=\underline{0} \tag{2.17b}$$

Before we proceed further to the last grid method, it is worthwhile to add that in the discrete representation of quantum systems, operators corresponding to physical observables are mapped onto a discrete Hilbert space. Thus, operators in the discrete Hilbert space should satisfy all the quantum mechanical commutation relations obeyed by the corresponding physical observables in the original Hilbert space. Only then does one have a true one-to-one mapping of operators represented in respectively the discrete and the continuous Hilbert space. Kosloff and Kosloff[20] have shown that this is indeed the case with the Fourier discretisation of a wave function which has a finite extent in configuration as well as in momentum space (*i.e.* function is band-limited). This makes the Fourier transform method advantageous over many other methods. However, in situations where the wave function is not periodic or band-limited, one has to employ a semi-local approximation of the kinetic energy operator, which naturally leads us the grid methods to be discussed below.

2.2.3 The Gaussian quadrature

As a prelude for the presentation of the discrete variable representation we shall briefly mention the *Gauss quadrature theorem.* For a more complete discussion on this subject we refer to “Numerical Recipes” by Press *et al.*[22], and the references mentioned therein. The central idea of Gauss quadrature is to discretize an integral through the approximation

$$\int_a^b dx W(x) f(x) \approx \sum_{p=1}^{N} \mathcal{W}_p f(x_p) \tag{2.18}$$

where $f(x)$ is an arbitrary function, $W(x)$ is a known weighting function, $\mathcal{W}_p$ are the associated weights, and x_p are the grid points of the quadrature scheme, also referred to as the abscissas. The fundamental theorem of Gauss quadrature now reads: Given a set of orthogonal polynomial basis-functions

$$\int_a^b dx \mathcal{P}_n^*(x) W(x) \mathcal{P}_m(x) = N_n \delta_{nm}, \quad n, m \in [0, \ldots, N-1] \tag{2.19}$$

where n denotes the polynomial degree and $W(x)$ is a weighting function, it then follows that if x_p and $\mathcal{W}_p$, entering eq. (2.18), are chosen as respectively the N roots of $\mathcal{P}_N(x)$ and the solution to the matrix equation[6]

$$\begin{bmatrix} \mathcal{P}_0(x_1) & \mathcal{P}_0(x_2) & \dots & \mathcal{P}_0(x_N) \\ \mathcal{P}_1(x_1) & \mathcal{P}_1(x_2) & \dots & \mathcal{P}_1(x_N) \\ \vdots & \vdots & \ddots & \vdots \\ \mathcal{P}_{N-1}(x_1) & \mathcal{P}_{N-1}(x_2) & \dots & \mathcal{P}_{N-1}(x_N) \end{bmatrix} \cdot \begin{bmatrix} \mathcal{W}_1 \\ \mathcal{W}_2 \\ \vdots \\ \mathcal{W}_N \end{bmatrix} = \begin{bmatrix} N_0/\mathcal{P}_0^* \\ 0 \\ \vdots \\ 0 \end{bmatrix} \tag{2.20}$$

then eq. (2.19) is exact if the function $f(x)$ can be expressed as a polynomial of degree $\leq 2N-1$. This Gaussian quadrature scheme has proven very useful in many numerical applications, but in the present formulation it suffers from a numerical inconvenience: The scheme has explicit reference to both the abscissas and weights, *cf.* eq. (2.18). The accurate calculation of roots of a polynomial of high order is not always trivial, and eq. (2.20), which generally determines the weights, can be numerically very unstable. The question is now how we can use the Gaussian quadrature scheme to construct a compact collocation method which does not suffer from these problems.

2.2.4 Discrete Variable Representations

In the following we will demonstrate how the discrete variable representation can be derived from the Gaussian quadrature scheme. This DVR method is very central to the work presented in this thesis. In all of the calculations I used one- or two-dimensional DVR formulations, and chapter 11 actually concerns the development of an extension of the DVR method to complex functions, or more correctly the "numerical complex continuation of matrix-elements expressed in a DVR". Therefore I have decided to be more comprehensive in the presentation of this method. The procedure will be as following: First we show a collection of important relations which the DVR scheme satisfy, and then in the end we tie them all together and define the overall scheme. This process might seem a bit lengthy, so I ask the reader to be patient and "hang in there, for the reward is just around the corner".

From the polynomials introduced above we construct the orthonormal functions[7]

$$u_n(x) \equiv \sqrt{\frac{W(x)}{N_n}}\mathcal{P}_{n-1}(x), \quad n = 1, \dots, N \tag{2.21}$$

---

[6] Eq. (2.20) ensures that eq. (2.18) is exact for $f(x) = \mathcal{P}_0^*(x)\mathcal{P}_n(x)$ where $P_0(x)$ is a constant.

[7] Note that these functions are not generally polynomials due to the weighting function $W(x)$.

Using eq. (2.18) we then have the following approximation of a general matrix element

$$\begin{aligned}\langle u_n|f|u_m\rangle &= \int_a^b dx\, u_n^*(x)f(x)u_m(x) \approx \sum_{p=1}^N \frac{\mathcal{W}_p}{N_n}\mathcal{P}_n^*(x_p)f(x_p)\mathcal{P}_m(x_p) \\ &= \sum_{p=1}^N \Omega_p u_n^*(x_p)f(x_p)u_m(x_p) \end{aligned} \tag{2.22}$$

where we have defined the new weights $\Omega_p \equiv \mathcal{W}_p/W(x_p)$. Next setting $f(x) = 1$ in eq. (2.22) and introducing the collocation matrix, $\underline{\underline{\mathrm{R}}}_{pn} \equiv u_n(x_p)$, we obtain the matrix relations

$$\underline{\underline{\mathrm{R}}}^+ \cdot \underline{\underline{\Omega}}^D \cdot \underline{\underline{\mathrm{R}}} = \underline{\underline{1}} \quad \Leftrightarrow \quad \underline{\underline{\mathrm{R}}}^+ = \underline{\underline{\mathrm{R}}}^{-1}\underline{\underline{\Omega}}^{D-1} \tag{2.23}$$

From eq. (2.22) and (2.23) it now follows that

$$\langle u_n|f|u_m\rangle = \left[\underline{\underline{\mathrm{R}}}^+ \cdot \underline{\underline{\Omega}}^D \cdot \underline{\underline{\mathrm{f}}}^D \cdot \underline{\underline{\mathrm{R}}}\right]_{nm} = \left[\underline{\underline{\mathrm{R}}}^{-1} \cdot \underline{\underline{\mathrm{f}}}^D \cdot \underline{\underline{\mathrm{R}}}\right]_{nm} \tag{2.24}$$

which does not depend explicitly on the weights. However, in this form we will have to compute the inverse of the collocation matrix, and so instead we define the *unitary* matrix, $\underline{\underline{\mathrm{U}}}_{pn} \equiv \sqrt{\Omega_p}\underline{\underline{\mathrm{R}}}_{pn}$, *i.e.*

$$\underline{\underline{\mathrm{U}}} = \underline{\underline{\Omega}}^{D\,1/2} \cdot \underline{\underline{\mathrm{R}}} \tag{2.25a}$$

$$\underline{\underline{\mathrm{U}}}^+\underline{\underline{\mathrm{U}}} = \underline{\underline{1}} \tag{2.25b}$$

where eq. (2.25b) follow directly from eq. (2.23) and (2.25a). If we next insert eq. (2.25a) into eq. (2.24) we obtain the very important relation

$$\langle u_n|f|u_m\rangle = \left[\underline{\underline{\mathrm{U}}}^+ \cdot \underline{\underline{\mathrm{f}}}^D \cdot \underline{\underline{\mathrm{U}}}\right]_{nm} = \sum_{p=1}^N \underline{\underline{\mathrm{U}}}^*_{pn} f(x_p)\underline{\underline{\mathrm{U}}}_{pm} \tag{2.26}$$

As a very important special case of this matrix equation we note that

$$\boxed{\underline{\underline{\mathrm{U}}} \cdot \underline{\underline{\mathrm{X}}} \cdot \underline{\underline{\mathrm{U}}}^+ = \underline{\underline{\mathrm{x}}}^D \qquad (2.27)}$$

where we have defined the matrix $\underline{\underline{\mathrm{X}}}_{nm} \equiv \langle u_n|x|u_m\rangle$. From the orthonormal basis-set, $\{u_n(x), \quad n = 1, \ldots, N\}$, we can now define another *orthonormal* basis-set, $\{\mathcal{X}_p(x), \quad p = 1, \ldots, N\}$, by the unitary transformation

$$\mathcal{X}_p(x) = \sum_{n=1}^N \underline{\underline{\mathrm{U}}}^*_{pn} u_n(x) \tag{2.28}$$

which is easily inverted to give

$$u_n(x) = \sum_{p=1}^{N} \underline{\underline{\mathrm{U}}}_{pn} \mathcal{X}_p(x) \tag{2.29}$$

It then follows from eq. (2.28) and (2.26) that

$$\langle \mathcal{X}_p | f | \mathcal{X}_q \rangle = \left[\underline{\underline{\mathrm{U}}} \cdot \underline{\underline{\mathrm{U}}}^{+} \cdot \underline{\underline{\mathrm{f}}}^{D} \cdot \underline{\underline{\mathrm{U}}} \cdot \underline{\underline{\mathrm{U}}}^{+} \right]_{pq} = \underline{\underline{\mathrm{f}}}^{D}_{pq} \equiv f(x_p)\delta_{pq} \tag{2.30}$$

We can now combine eq. (2.25b) and (2.28) to obtain an expression

$$\begin{aligned}
\Psi(x) &= \sum_{n=1}^{N} C_n u_n(x) = \sum_{n=1}^{N} C_n \sum_{p=1}^{N} \underline{\underline{\mathrm{U}}}_{pn} \mathcal{X}_p(x) \\
&= \sum_{p=1}^{N} \sqrt{\Omega_p} \left[\sum_{n=1}^{N} C_n \underline{\underline{\mathrm{R}}}_{pn} \right] \mathcal{X}_p(x) = \sum_{p=1}^{N} \sqrt{\Omega_p} \left[\sum_{n=1}^{N} C_n u_n(x_p) \right] \mathcal{X}_p(x) \\
&= \sum_{p=1}^{N} \sqrt{\Omega}_p \Psi(x_p) \mathcal{X}_p(x)
\end{aligned} \tag{2.31}$$

which has the discrete form

$$\Psi(x_p) = \sum_{p=1}^{N} \sqrt{\Omega}_p \Psi(x_p) \mathcal{X}_p(x_p) \tag{2.32}$$

Noting that the expansion coefficients, $\Psi(x_p)$, in eq. (2.32) are linearly independent we arrive at the result

$$\mathcal{X}_p(x_q) = \Omega_p^{-1/2} \delta_{pq} \tag{2.33}$$

which shows that the function, $\mathcal{X}_p(x)$, has the characteristic “delta-function-like” property to be zero at every grid point different from x_p. This is illustrated in figure 2.6 for a specific choice of the FBR which we will return to shortly.

We are now finally ready to define the overall *discrete variable representation*: The first step is to choose an orthonormal basis-set, $\{u_n(x), \quad n = 1, N\}$ in which the kinetic energy operator is local or at least semi-local, *i.e.* the matrix representation $\langle u_n|\widehat{\mathbf{T}}|u_m\rangle$ is diagonal or very sparse.[8] Next one constructs the symmetric matrix $\underline{\underline{X}}_{nm} \equiv \langle u_n|x|u_m\rangle$ and diagonalize it, and according to eq. (2.27) the eigenvectors define the unitary transformation matrix, $\underline{\underline{U}}$, and the corresponding eigenvalues are the grid points, $\{x_p, \quad p = 1, N\}$, of the DVR scheme.[9] The important point is now that there exist an isomorphism (due to the unitary matrix, $\underline{\underline{U}}$ in eq. (2.28) and (2.29)) between the finite-basis representation (FBR) of $\Psi(x)$ in $\{u_n(x), \quad n = 1, N\}$ and a discrete variable representation (DVR) of Ψ in $\{\mathcal{X}_p(x), \quad p = 1, N\}$. Matrix-elements over functions of the coordinate are by construction diagonal in the DVR (see eq. (2.30)), and eq. (2.26) exactly show us how to approximate the corresponding matrix representation in the FBR to *Gaussian accuracy.* Thus, the equivalents of eq. (2.8b) and (2.9) read as

$$\left[\underline{\underline{U}} \cdot \underline{\underline{T}} \cdot \underline{\underline{U}}^{+} + \underline{\underline{V}}^{D} - E\underline{\underline{I}}\right] \cdot \underline{\bar{\Psi}} = \underline{0} \tag{2.34a}$$

$$\left[\underline{\underline{T}} + \underline{\underline{R}}^{+} \cdot \underline{\underline{V}}^{D} \cdot \underline{\underline{R}} - E\underline{\underline{I}}\right] \cdot \underline{C} = \underline{0} \tag{2.34b}$$

where $\bar{\Psi}_p \equiv \sqrt{\Omega_p}\Psi x_p$, which strictly speaking means that it is not a collocation method in its original sense ($\mathcal{C}_p \neq \Psi x_p$). The DVR basis-set, $\{\mathcal{X}_p(x), \quad p = 1, N\}$, earns its name from the fact that the expansion coefficients of a wave function in this representation correspond to the weighted values of the function at each discrete grid point, as shown in eq. (2.31).

At this point it is very useful to make a comparison of the DVR and the Fourier methods. In the latter one switches back and forth between the momentum and the coordinate representations, in which respectively the kinetic energy operator and the potential is local, and in the DVR scheme one switches back and forth between the FBR and DVR basis-sets in which respectively $\widehat{\mathbf{T}}$ is semi-local and $V(x)$ is local. In the Fourier method the grid is always uniform, whereas in the DVR method one has the liberty to choose the FBR which in turn defines the underlying grid.

The discrete variable representation, just presented, was originally introduced in the area of molecular reaction dynamics by Light and coworkers[23] in the mid-

---

[8] This is the case for most of the orthogonal polynomials due to the existence of simple recurrence relations for the derivatives $u'_n(x)$.

[9] We just note that $\underline{\underline{X}}$ can usually be constructed from analytical expressions due to the characteristic recurrence relations satisfied by $xu_n(x)$.

eighties, and has been very popular in time-dependent as well as time-independent formulations ever since. The success of the DVR method owes to many different factors which we will briefly try to cover now. Although the one-dimensional DVR, described above, is very useful and relatively simple to implement, the use of direct product DVR for multi-dimensional problems is much more advantageous. First, the Hamiltonian matrix in the multi-dimensional DVR is easy to construct as we shall see in both chapter 10 and 11. More importantly this matrix is often very sparse, which leads to a much better scaling of the numerical implementation. In one dimension there are no non-zero matrix elements in the discrete variable representation of the full Hamiltonian (*cf.* eq. (2.34)), and since the rate limiting step in most dynamical calculations is the action of the Hamiltonian on the wave function, corresponding to a matrix-vector multiplication, then the DVR scales like N^2 where N is the dimension of the representation. However, in multi-dimensions $\underline{\underline{\mathrm{H}}}$ will often be very sparse, especially if the kinetic energy operator is separable in the different coordinates, *i.e.*

$$\underline{\underline{\mathrm{H}}}_{pq,p'q'} = \underline{\underline{\mathrm{T}}}^x_{pp'}\delta_{qq'} + \underline{\underline{\mathrm{T}}}^y_{qq'}\delta_{pp'} + V(x_p, y_q)\delta_{pp'}\delta_{qq'} \tag{2.35}$$

Consequently the multi-dimensional DVR scheme scales semi-linearly in the grid-size. In fact Colbert and Miller[24] have shown that in Cartesian coordinates, where $\widehat{\mathbf{T}}$ can always be written as a sum of one-dimensional terms, direct-product multi-dimensional DVR scales like the FFT method, *i.e.* $N \log N$. Even when $\widehat{\mathbf{T}}$ is not separable in the coordinates can the DVR be optimized such that $\underline{\underline{\mathrm{H}}}$ is very sparse. This is done through the successive diagonalization-truncation scheme of Bačić and Light[25], which will be the topic of subsection 2.2.8. For now, we just note that through this truncation-scheme a very compact direct-product basis-set is constructed, *i.e.* N is reduced. As the last important feature of the DVR method we emphasize that this scheme can handle singular terms in the Hamiltonian in a very effective way (*i.e.* analytical) by choosing the ad hoc FBR.

2.2.5 Particle in a box DVR

As a very important special case of a DVR we now briefly present the particle-in-a-box DVR scheme, as this will be the choice of FBR in chapter 10 and 11. We shall adopt a slightly different notation, which will be used throughout part III. For a more complete review of this special DVR we refer to the appendix in reference [24] mentioned above.

Consider a one-dimensional quantum system, with coordinate R restricted to an arbitrary but fixed box. First we note that any physical box can always be shifted without loss of generality. Thus for a given box in the coordinate R - going from *zero* to R_{max} - we can define a FBR basis set of orthonormal particle-in-a-box (PIB) eigenfunctions,

$$\left\{ \langle R|\varphi_n\rangle \equiv \sqrt{\frac{2}{R_{max}}} \sin\left(\frac{n\pi R}{R_{max}}\right), \quad n = 1, 2, \ldots, N_R \right\} \tag{2.36}$$

The N_R roots of $\varphi_{N_R+1}(R)$ in the interval $]\,0;\, R_{max}\,[$

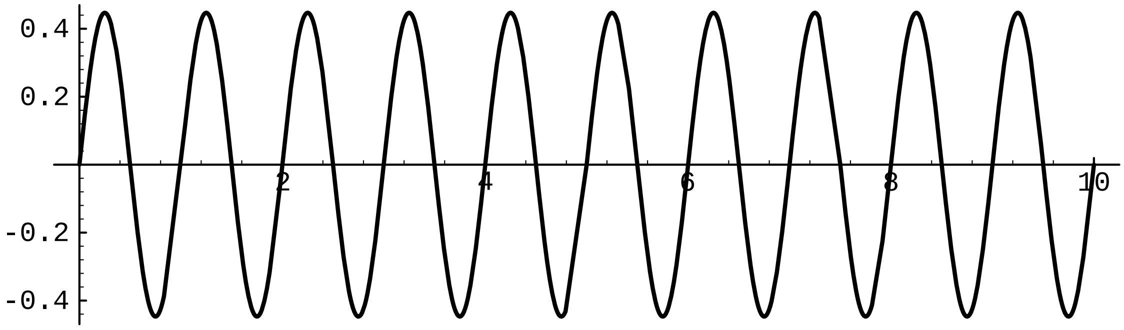

Figure 2.4: Plot of the FBR function $\langle R|\varphi_{20}\rangle$ where $R_{max} = 10$ and $N_R = 30$, *cf.* eq. (2.36).

$$R_p = \frac{R_{max}}{N_R + 1} p \equiv \Delta R\, p, \quad p = 1, 2, \ldots, N_R \tag{2.37}$$

are exactly the abscissas for the DVR associated with this FBR, and the corresponding weights, Ω_p in eq. (2.22), can easily be shown to be the constant ΔR. A plot of one of these simple sin-functions is shown in figure 2.4. The transformation to the DVR, $\{|\mathcal{R}_p\rangle,\ p = 1, N_R\}$, from the FBR, reads as

$$|\mathcal{R}_p\rangle = \sum_{n\,=\,1}^{N_R} U_{pn}|\varphi_n\rangle \tag{2.38}$$

where the *unitary* matrix $\underline{\underline{\mathrm{U}}}$, is given by

$$\underline{\underline{\mathrm{U}}}_{pn} \equiv \langle \mathcal{R}_p|\varphi_n\rangle = \sqrt{\frac{2}{N_R + 1}} \sin\left(\frac{n\pi R_p}{R_{max}}\right) \tag{2.39}$$

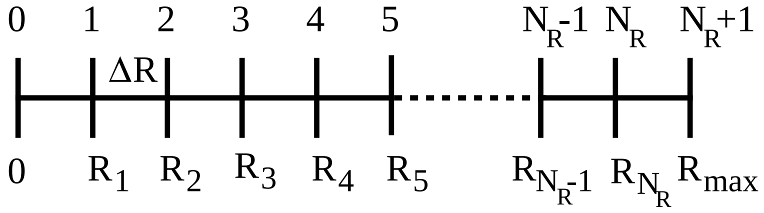

Figure 2.5: Definition of the points in the uniform particle-in-a-box grid. Note that the endpoints are not included in the definition of the points.

It is important to note that the endpoints of the box (*i.e.* 0 and R_{max}) are excluded in the definition of the grid points, see figure 2.5. The reason for this is that every member of the FBR basis set is zero at these points, resulting in zero-columns in $\underline{\underline{U}}$. Thus the matrix expressing the basis set transformation would not be unitary *i.e.* the defined DVR and FBR are not isomorphic. This defines a quadrature scheme of Gaussian accuracy as the described above. In fact, as the expansion functions, eq. (2.36), are periodical, and the underlying grid uniform (*i.e.* evenly spaced), this actually corresponds to the trapezoidal rule. In figure 2.6 one of the members of the DVR basis-set is plotted, note especially the "delta-function"-like behavior as predicted above in eq. (2.33). Within the approximation of the associated quadrature the defined DVR satisfy the following basic relation

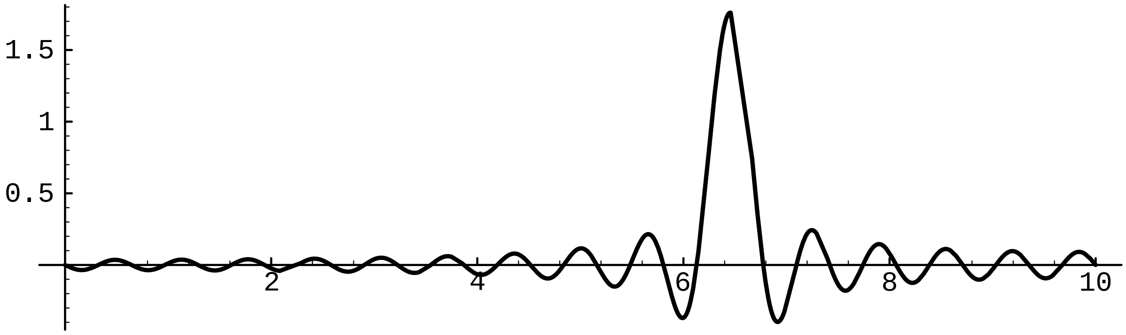

Figure 2.6: Plot of the DVR function $\langle R|\mathcal{R}_{20}\rangle$ with $R_{max} = 10$ and $N_R = 30$, *cf.* eq. (2.36).

$$\langle \mathcal{R}_n \left| V\left(R\right) \right| R_{n'} \rangle = \delta_{nn'} V\left(R_n\right) \tag{2.40}$$

and consequently the potential energy term in the Hamiltonian is simply diagonal in the DVR basis set. Using the analytical expression for the FBR (eq. (10.4)) it is easy to show that the matrix representation of the kinetic energy operator in the DVR basis set reads as

$$\underline{\underline{\mathrm{T}}} = -\frac{\hbar^2}{2\mu}\underline{\underline{\mathrm{U}}} \cdot \underline{\underline{\mathrm{N}}} \cdot \underline{\underline{\mathrm{U}}}^\dagger \tag{2.41}$$

where $\underline{\underline{\mathrm{N}}}_{nn\prime} \equiv -(n\pi/R_{max})^2\delta_{nn'}$ and $\underline{\underline{\mathrm{U}}}$ is defined in eq. (2.39). The evaluation of the matrix elements, T_{pq} in eq. (2.41), thus involve a sum over products of two sin-functions with the premultiplier n^2. After some lengthy algebra (see footnote 20 in reference [24]) one can obtain the following analytical expression for the sum

$$T_{pq} = \frac{h^2(-1)^{p-q}}{4\mu R_{\mathrm{max}}^2} \times \begin{cases} F\left(p-q\right) - F\left(p+q\right) & \text{for } p \neq q \\ \left(2(N_R+1)^2+1\right)/3 - F\left(p+q\right) & \text{for } p = q \end{cases} \tag{2.42}$$

where $F(n) \equiv \sin^{-2}\left(\frac{\pi n}{2(N_R+1)}\right)$.

2.2.6 The HEG method

As pointed out above, the sine-based DVR constitutes a convenient representation for the expansion of a wave function, which is similar in spirit to the very general role played by the plane wave basis-set underlying the FFT scheme. However, for most physical systems, this primitive choice of a basis-set would constitute a poor representation in terms of efficiency. The reason is of course that the DVR basis-set has not been optimized for the numerical problem at hand – or to use a DVR terminology – the grid points have not been chosen so as to reflect the physics of the problem. In other words we would like to have a DVR grid that reflects the topology of the potential energy surface such that the grid is dense in regions where the de Broglie wavelength is small and more sparse elsewhere, see figure 2.7. This problem is actually related to most of the DVR basis-sets we can construct from simple analytical FBR basis-sets considered so fare, unless of course the system is extremely simple. Thus, suppose we have a general FBR basis-set $\{\varphi_n(x)\}$ which may be very complicated but nevertheless constitutes a physically more meaningful representation of the system. The question is now how can we construct a DVR scheme from this FBR basis-set ?

A very simple solution to this numerical problem was proposed more than thirty years ago by Harris, Engerholm and Gwinn[26], and this scheme now goes under the name “the HEG method”. They showed that by substituting $u_n(x) \to \varphi_n(x)$ in eq. (2.26) and (2.27), mentioned above, the desired DVR scheme emerges naturally. Thus, from some arbitrary, but convenient choice of the $\varphi_n(x)$'s, the position matrix, eq. (2.27), is constructed and subsequently diagonalized, which uniquely

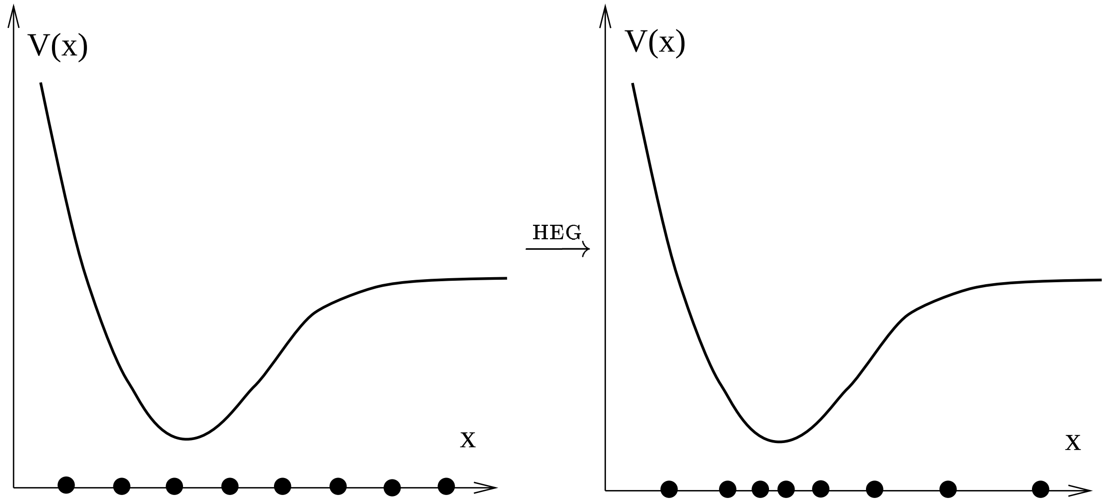

Figure 2.7: Schematic illustration of the HEG scheme, where a DVR grid is constructed which reflects topology of the potential energy surface.

defines a new DVR basis-set according to eq. (2.28) and (2.30). It was later shown by Dickinson and Certain[27], that this method is indeed equivalent to a quadrature scheme of Gaussian accuracy. Thus, the HEG method can also be used to define a numerical quadrature when no analytical expression is known for the FBR functions, $\varphi_n(x)$, or when it is too cumbersome to deal with[10].

2.2.7 Preconditioning and truncation

The next natural question would be, how can we construct the $\{\varphi_n(x)\}$ basis-set which constitutes a physically meaningful representation of the system. In other words, how do we from the knowledge of the full Hamiltonian operator of the system, $\widehat{\mathbf{H}}$, construct a basis-set in which the matrix representation of $\widehat{\mathbf{H}}$ is sparse or almost diagonal ?

The answer to this fundamental question is use *preconditioning* of a primitive basis-set in the leading part of the full Hamiltonian. The central idea is based on the fact that the full Hamiltonian can always the partitioned into a large zero-order term, $\widehat{\mathbf{H}}^0$, and a smaller remainder term $\widehat{\mathbf{h}}$, such that $\widehat{\mathbf{H}} = \widehat{\mathbf{H}}^0 + \widehat{\mathbf{h}}$. The first step is then to setup the matrix representation of $\widehat{\mathbf{H}}^0$ in some primitive but convenient FBR basis-set, *e.g.* the PIB basis-set defined above. This matrix, $\underline{\underline{\mathrm{H}}}^0$, is then diagonalized and the eigenvectors exactly define the $\{\varphi_n(x)\}$ basis-set in

---

[10] Of course we still assume that we can construct the position matrix entering eq. (2.27), for instance by combining a recurrence and orthogonalization relation for the FBR's.

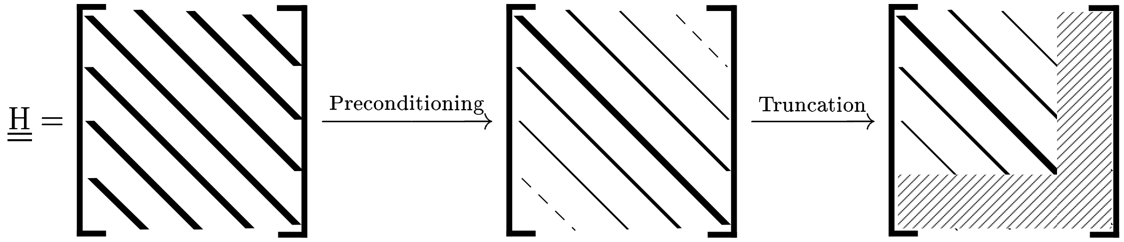

Figure 2.8: Schematic illustration of the two steps in the successive adiabatic reduction scheme.

which $\underline{\underline{H}}$ is close to diagonal, see figure 2.8. By transforming the full Hamiltonian into a more diagonally dominated form, the diagonalization of $\underline{\underline{H}}$, by means of some iterative scheme, will often lead to much faster convergence. However, the advantages of a preconditioning gets ever bigger if we subsequently truncate $\underline{\underline{H}}$, see figure 2.8. Thus, if we are only interested in states of the full system below some threshold energy, E_{thres}, we can reduce the $\{\varphi_n(x)\}$ basis-set size by neglecting the high-energy $\varphi_n(x)$'s with eigenvalues of $\widehat{\mathbf{H}}^0$ larger than E_{thres}. Like this, for a given accuracy on the eigenvalues of $\widehat{\mathbf{H}}$, the combined preconditioning–truncation scheme allows one to reduce the size of the overall working basis-set. The compact $\{\varphi_n(x)\}$ basis-set can then next be used as the input for the HEG scheme mentioned above.

2.2.8 The successive adiabatic reduction method

The last DVR related numerical technique that we shall discuss in this chapter is the very powerful successive adiabatic reduction (SAR) scheme of Bačić and Light[25]. This method can actually be viewed as a sort of generalization of the preconditioning–truncation scheme, just discussed, to multi-dimensional systems. Let us exemplify this method by considering a two-dimensional system depending on the vibrational coordinate r and the translational coordinate R (see for instance figure 10.1). Let us furthermore assume that r describes the fastest or most bound motion in the system. As a prelude to the SAR method we first define some effective translational Hamiltonian, $\widehat{\mathbf{H}}^{eff}(R)$, say along the minimum energy-path in r. We then use this zero-order Hamiltonian to construct a compact FBR basis-set in R, in the way described in the previous subsection, which in turn is used as the input for the HEG method to give the final working DVR basis-set in the translational coordinate, $\{\mathcal{X}_p(R)\}$. The basic idea behind the SAR method is now to expand the full two-dimensional wave function of the system, $\Psi(r, R)$, in a direct product basis-set of the $\mathcal{X}_p(R)$'s and a set of *adiabatic* eigenstates, $\Phi_n(r; R_p)$, with respect to the DVR grid points of the "slow" coordinate, R_p, *i.e.*

$$\Psi(r,R) = \sum_{p,n} C_{p,n}\Phi_n(r;R_p)\mathcal{X}_p(R) \tag{2.43}$$

where the $\Phi_n(r;R_p)$'s are defined as eigenfunctions of the R-fixed Hamiltonian evaluated at the discrete $\{R_p\}$ grid points,

$$\widehat{\mathbf{H}}(r,R_p)\Phi_n(r;R_p) = E_n(R_p)\Phi_n(r;R_p) \tag{2.44}$$

The basis-sets of these vibrationally adiabatic so-called *ray-eigenstates* is next truncated at each R_p by keeping only those states for which the adiabatic energy $E_n(R_p)$ is located below the threshold energy, E_{thres}. All in all this leads to a very compact and convenient adiabatic direct product basis-set in the two coordinates. A plot of the adiabatic energies, $E_n(R_p)$, can give and crude idea of the "non-adiabatic" coupling in the two degrees of freedom, and since these curves can display very complicating topological behavior they are some times given the nickname "spaghetti-curves". We finally note that a basis-sets of "pseudo-diabatic" eigenstates can next be constructed from the re-labeling of the $\Phi_n(r;R_p)$'s according to the avoided crossing of the "spaghetti-curves". Leforestier [28] has recently shown that these "pseudo-diabatic" energy curves provide a very good zero-order description of resonances. The precise definitions of an adiabatic and diabatic representation will exactly be the topic of the next chapter, however this time with respect to the electronic motions.

3

Non-adiabatic dynamics

At the very heart of many ab initio[1] quantum mechanical calculations for molecular systems lies either the Born-Oppenheimer or the adiabatic approximation. The philosophy of these approaches is a separation (complete or partial) of the electronic and nuclear motions, taking point of reference in the large difference in the masses (assumption of infinite nuclear masses). Nevertheless, many chemical reactions involve more than just one (typically the lowest) electronic potential energy surface. Examples of such reactions are electron-transfer and photo-excitation processes which are inherently non-adiabatic, but also more general chemical reactions where more electronic potential energy surfaces are energetically accessible, *i.e.* close in energy. Even apparent single surface problems have due to the geometric phase effects[29–32] turned out to involve the effect of more than one electronic potential energy surface. Solving ab initio quantum mechanical problems for many particle systems in the framework of negligible correlation between the electrons and the nuclei is difficult enough. However, as the experimental measurements get more sophisticated and the available computer resources grow rapidly it is very important to develop the capabilities of the quantum scattering methods which go beyond these approximations to as great an extent as possible in order to be able, in some cases at least, to provide a "completely reliable" theoretical description.

As implied above electronic non-adiabatic transitions occur due to the breakdown of the Born-Oppenheimer approximation (to be define later). In general, one may distinguish between two different forms of electronic non-adiabatic transitions owing to the underlying mechanisms. The first one originates from the radial motion, which in the case of a simple atom-atom collision, arise due to the translational

---

[1] It is a fallacy to put the term ab initio equal to exact in general. Strictly speaking ab initio means "from the beginning", and when used in the context of natural science, it means exact within the framework of a given (non-empirical) model or theory.

motion, and in the more general cases, due to vibrational and angular motions as well. This radial non-adiabatic coupling was first treated by Zener[33], Landau[34] and Stuckelberg[35]. In short they found that the Born-Oppenheimer approximation breaks down when two adiabatic electronic states (to be defined later) of the same symmetry approach each other very closely in energy. The second form of non-adiabatic coupling originates from the rotation of the body fixed axis of the system with respect to an axis fixed in space. This rotational coupling was first discussed by Kronig[36] who found that due to the conservation of the total angular momentum, the transformation from the space fixed to the body fixed frame of reference, additional couplings were introduced between various electronic states. The main difference between the two types of coupling resides in the face that radial coupling may only cause transitions among electronic states of the same symmetry, whereas rotational coupling can mix states of the same and different symmetries.

The subject of the electronic non-adiabatic transitions in atom-molecule collisions has already been reviewed by several authors (*e.g.* [37]), and a complete discussion and derivation of the different non-adiabatic approaches is beyond the scope of this thesis. However, we will present some of the central ideas and concepts, as they will play an important role in especially the second part of this thesis. In order to give a more precise definition of these approximations, we shall consider an N-particle system with g nuclei and $N - g$ electrons. As a prelude to the separation of the nuclear and electronic motions, we introduce a partitioning of the particles in which the labels 1 through g refer to nuclei and the remainder to electrons. Further to simplify the notation we will denote the nuclear coordinates $(\vec{r}_1, \vec{r}_2, \ldots, \vec{r}_g)$ collectively by $\underline{\vec{r}}_{nu}$ and the electronic coordinates $(\vec{r}_{g+1}, \vec{r}_{g+2}, \ldots, \vec{r}_N)$ collectively by $\underline{\vec{r}}_{el}$[2]. To keep things as simple and at the same time general as possible we will conduct the preceding non-adiabatic analysis in a space-fixed frame of reference using simple Cartesian coordinates. Consequently we will not be able to distinguish between the non-adiabatic radial and rotational coupling as mentioned above, but except for the symmetry considerations the two types of coupling are conceptually identical. In reference [38] a more involved derivation is shown in the body-fixed frame of reference using mass-weighted Jacobi coordinates. However, it is the present authors point of view that this additional complication of the system serves no purpose in the present context of merely defining the different non-adiabatic representations. Thus, for the general system in space-fixed coordinates

---

[2] The somewhat bizarre double-vector construction in this notation is used to remind us that it denotes a collection of vectors.

the total non-relativistic Hamiltonian operator, $\widehat{\mathbf{H}}$, reads as

$$\begin{aligned}\widehat{\mathbf{H}}(\underline{\vec{r}}_{el},\underline{\vec{r}}_{nu}) &= \widehat{\mathbf{T}}^{nu}(\underline{\vec{r}}_{nu}) + \widehat{\mathbf{T}}^{el}(\underline{\vec{r}}_{el}) + V^{tot}(\underline{\vec{r}}_{el},\underline{\vec{r}}_{nu}) &\quad (3.1\text{a})\\ &\equiv \widehat{\mathbf{T}}^{nu}(\underline{\vec{r}}_{nu}) + \widehat{\mathbf{H}}^{el}(\underline{\vec{r}}_{el};\underline{\vec{r}}_{nu}) &\quad (3.1\text{b})\end{aligned}$$

where the nuclear and electronic kinetic energy operators respectively read as

$$\begin{aligned}\widehat{\mathbf{T}}^{nu}(\underline{\vec{r}}_{nu}) &= -\sum_{j=1}^{g}\frac{\hbar^2}{2m_j}\nabla^2 &\quad (3.2\text{a})\\ \widehat{\mathbf{T}}^{el}(\underline{\vec{r}}_{el}) &= -\sum_{j=g+1}^{N}\frac{\hbar^2}{2m_j}\nabla^2 &\quad (3.2\text{b})\end{aligned}$$

and the potential energy for the case of Coulomb interaction is defined as

$$V^{tot}(\underline{\vec{r}}_{el},\underline{\vec{r}}_{nu}) = \sum_{\substack{j,k=1\\ j<k}}^{N}\frac{e_j e_k}{4\pi\epsilon_0|\vec{r}_j-\vec{r}_k|} \tag{3.3}$$

The fundamental equation of motion for the complete system is given by the celebrated time-independent Schrödinger equation

$$\widehat{\mathbf{H}}(\underline{\vec{r}}_{el},\underline{\vec{r}}_{nu})\Psi(\underline{\vec{r}}_{el},\underline{\vec{r}}_{nu}) = E\Psi(\underline{\vec{r}}_{el},\underline{\vec{r}}_{nu}) \tag{3.4}$$

where the eigenvalue, E, equals the total energy of the system. From the definition of the electronic Hamiltonian, $\widehat{\mathbf{H}}^{el}$, in eq. (3.1b), we have the additional eigenvalue equation

$$\widehat{\mathbf{H}}^{el}(\underline{\vec{r}}_{el};\underline{\vec{r}}_{nu})\Phi^{el}(\underline{\vec{r}}_{el};\underline{\vec{r}}_{nu}) = \mathcal{E}(\underline{\vec{r}}_{nu})\Phi^{el}(\underline{\vec{r}}_{el};\underline{\vec{r}}_{nu}) \tag{3.5}$$

which has a parametrical dependence[3] on the nuclear configuration, $\underline{\vec{r}}_{nu}$, which is emphasized by the use of a semicolon in the argument list. This equation is often

---

[3] Parametrical dependence of an operator, in the context of quantum mechanics, means that the operator is "local" in the parameters under considerations. Thus, mathematically we can define the term parametrical dependence of an operator $\widehat{\mathbf{O}}(x;y)$, with respect to the variable y, from the relation

$$\int_{-\infty}^{\infty} dy\,\delta(y-y_0)\widehat{\mathbf{O}}(x;y) = \widehat{\mathbf{O}}(x;y_0)$$

where $\delta(y-y_0)$ is a Dirac delta function. For instance, $V(\underline{\vec{r}}_{el},\underline{\vec{r}}_{nu})$, defined in eq. (3.3) is local in both $\underline{\vec{r}}_{el}$ and $\underline{\vec{r}}_{nu}$ whereas $\widehat{\mathbf{T}}^{el}(\underline{\vec{r}}_{el})$ is *not* a local operator in $\underline{\vec{r}}_{el}$, due to the differential operators, entering the eq. (3.2b), which so to speak access the whole configurations space make up by $\underline{\vec{r}}_{el}$. Consequently eq. (3.5) has a parametrical dependence on $\underline{\vec{r}}_{nu}$ and not $\underline{\vec{r}}_{el}$.

referred to as the "clamped nucleus equation" there $\mathcal{E}$ is the electronic energy at the considered nuclear configuration. Generally speaking there now exist two distinct strategies to solve eq. (3.4), the diabatic and the adiabatic, which both lead to so-called close coupled equations in the nuclear coordinates. Both approaches take point of reference in a basis-set expansion of the complete solution to eq. (3.4) in a direct product basis-set of wave functions defined from the clamped nucleus eq. (3.5). This will be the topic of the next two sections.

3.1 The diabatic representation

One of the strategies to solve the full quantum problem of eq. (3.4) is to *fix* the nuclear coordinates $\underline{\vec{r}}_{nu}$ parametrically entering the clamped nucleus eq. (3.5), to a specific reference configuration $\underline{\vec{r}}^{\,0}_{nu} \equiv (\vec{r}^{\,0}_1, \vec{r}^{\,0}_2, \ldots, \vec{r}^{\,0}_g)$, and define a basis-set of orthonormal electronic states, $\left\{\Phi^d_n(\underline{\vec{r}}_{el}; \underline{\vec{r}}^{\,0}_{nu})\right\}$ from the equation

$$\widehat{\mathbf{H}}^{el}(\underline{\vec{r}}_{el}; \underline{\vec{r}}^{\,0}_{nu})\Phi^d_n(\underline{\vec{r}}_{el}; \underline{\vec{r}}^{\,0}_{nu}) = \mathcal{E}_n(\underline{\vec{r}}^{\,0}_{nu})\Phi^d_n(\underline{\vec{r}}_{el}; \underline{\vec{r}}^{\,0}_{nu}) \tag{3.6}$$

These states are called electronically *diabatic*, and it is very important to note that they do not depend explicitly on the nuclear coordinates. If we next, as a first "ansatz", assume this basis-set to be complete in the Hilbert space of the electronic domain, $\mathcal{L}^2(\mathbf{V}_{el})$, which is of course not generally the case for a finite basis-set, then the exact molecular wave function in eq. (3.4) can be expanded as follows

$$\Psi(\underline{\vec{r}}_{el}, \underline{\vec{r}}_{nu}) = \sum_n \Phi^d_n(\underline{\vec{r}}_{el}; \underline{\vec{r}}^{\,0}_{nu})\mathcal{X}^d_n(\underline{\vec{r}}_{nu}) \tag{3.7}$$

where the diabatic nuclear wave functions, $\mathcal{X}^d_n(\underline{\vec{r}}_{nu})$, still remains to be defined. Eq. (3.7) is referred to as the *diabatic representation* of $\Psi(\underline{\vec{r}}_{el}, \underline{\vec{r}}_{nu})$. Inserting this expansion into eq. (3.4) results in

$$\sum_n \left(\widehat{\mathbf{T}}^{el}(\underline{\vec{r}}_{nu}) - E + \widehat{\mathbf{H}}^{el}(\underline{\vec{r}}_{el}; \underline{\vec{r}}^{\,0}_{nu})\right) \Phi^d_n(\underline{\vec{r}}_{el}; \underline{\vec{r}}^{\,0}_{nu})\mathcal{X}^d_n(\underline{\vec{r}}_{nu}) = 0 \tag{3.8}$$

To obtain equations of motion for the diabatic nuclear functions, $\mathcal{X}^d_n(\underline{\vec{r}}_{nu})$, we now proceed along the lines of the so-called close-coupling approach (CC), which is based on a simple technique that we will refer to as the "projection method", where one projects the Schrödinger equation onto (in principle) all the diabatic states. This is done by multiplying eq. (3.8) by all the complex conjugate states,

${\Phi_m^d}^*(\underline{\vec{r}}_{el};\underline{\vec{r}}^0_{nu})$, and integrating over the electronic domain, using the orthonormality relation

$$\int_{\mathbf{V}_{el}} d\underline{\vec{r}}^3_{el}\, {\Phi_m^d}^*(\underline{\vec{r}}_{el};\underline{\vec{r}}^0_{nu})\Phi_n^d(\underline{\vec{r}}_{el};\underline{\vec{r}}^0_{nu}) = \delta_{mn} \tag{3.9}$$

We then obtain the following set of *close-coupled* equations

$$\sum_n \left(\left[\widehat{\mathbf{T}}^{nu}(\underline{\vec{r}}_{nu}) - E \right] \delta_{mn} + \underline{\underline{W}}_{mn}(\underline{\vec{r}}_{nu};\underline{\vec{r}}^0_{nu}) \right) \mathcal{X}_n^d(\underline{\vec{r}}_{nu}) = 0 \tag{3.10}$$

where we have defined the so-called diabatic potential matrix

$$\underline{\underline{W}}_{mn}(\underline{\vec{r}}_{nu};\underline{\vec{r}}^0_{nu}) \equiv \int_{\mathbf{V}_{el}} d\underline{\vec{r}}^3_{el}\, {\Phi_m^d}^*(\underline{\vec{r}}_{el};\underline{\vec{r}}^0_{nu})\widehat{\mathbf{H}}^{el}(\underline{\vec{r}}_{el};\underline{\vec{r}}_{nu})\Phi_n^d(\underline{\vec{r}}_{el};\underline{\vec{r}}^0_{nu}) \tag{3.11}$$

Eq. (3.10) and (3.11) make up the close-coupled working equations in the diabatic representation, and we can immediately make the following characteristic observations:

- The nuclear kinetic energy operator, $\widehat{\mathbf{T}}^{nu}(\underline{\vec{r}}_{nu})$, is *diagonal* in the diabatic representation.

- The diagonal elements of $\underline{\underline{W}}(\underline{\vec{r}}_{nu};\underline{\vec{r}}^0_{nu})$ serve as the *diabatic* potential energy surfaces for the nuclear motion, and the off-diagonal elements are the *diabatic* coupling terms which are directly responsible for the transitions from one diabatic surface to another.

The diabatic approach outlined above is very convenient for practical numerical implementations, but the non-uniqueness of the derived diabatic potentials, due to the arbitrary reference nuclear configuration, $\underline{\vec{r}}^0_{nu}$, entering eq. (3.11), can however be a complicating aspect - as we shall see in the second part of this thesis. Another problem with this approach is that one usually need many diabatic states in the expansion, eq. (3.7), in order to obtain an acceptable representation of the full wave functions. This is of course a direct consequence of the fact that the electronically diabatic states, $\Phi_n^d(\underline{\vec{r}}_{el};\underline{\vec{r}}^0_{nu})$, only contains nuclear information at the fixed point $\underline{\vec{r}}^0_{nu}$. In the following section we will present another approach which tries to solve some of these problems - but as we shall see, just to introduce others.

3.2 The adiabatic representation

An alternative strategy to the solution of eq. (3.4) is to expand $\Psi(\underline{\vec{r}}_{el},\underline{\vec{r}}_{nu})$ in a basis-set of so-called electronically *adiabatic* states

$$\boxed{\Psi(\underline{\vec{r}}_{el},\underline{\vec{r}}_{nu}) = \sum_n \Phi_n^a(\underline{\vec{r}}_{el};\underline{\vec{r}}_{nu})\mathcal{X}_n^a(\underline{\vec{r}}_{nu}) \qquad (3.12)}$$

where $\Phi_n^a(\underline{\vec{r}}_{el};\underline{\vec{r}}_{nu})$ are defined as solutions to the clamped nucleus eigenvalue equation

$$\widehat{\mathbf{H}}^{el}(\underline{\vec{r}}_{el};\underline{\vec{r}}_{nu})\Phi_n^a(\underline{\vec{r}}_{el};\underline{\vec{r}}_{nu}) = \mathcal{E}_n(\underline{\vec{r}}_{nu})\Phi_n^a(\underline{\vec{r}}_{el};\underline{\vec{r}}_{nu}) \qquad (3.13)$$

We note that the adiabatic states (as opposed to the diabatic) depend *parametrically*[4] on the nuclear coordinates, $\underline{\vec{r}}_{nu}$. As in the previous section we have, as a first "ansatz", assumed the basis-set to be complete in the Hilbert space over the electronic domain, $\mathcal{L}^2(\mathbf{V}_{el})$. The expansion in eq. (3.12) is sometimes referred to as the Born-Huang series, and the electronic eigenvalues, $\mathcal{E}_n(\underline{\vec{r}}_{nu})$ define the usual (adiabatic) potential energy surfaces (*e.g.* figure 1.1). To derive close-coupled equations of motion for the functions $\mathcal{X}_n^a(\underline{\vec{r}}_{nu})$ we proceed along the same lines as demonstrated in the previous section, *i.e.* insert eq. (3.12) into eq. (3.4) and multiply it by $\Phi_n^{a\,*}(\underline{\vec{r}}_{el};\underline{\vec{r}}_{nu})$ followed by an integration over the electronic domain. The result read as

$$\boxed{\left(\mathcal{E}_n(\underline{\vec{r}}_{nu}) - E\right)\mathcal{X}_n^a(\underline{\vec{r}}_{nu}) + \sum_n \underline{\underline{\mathrm{T}}}_{mn}(\underline{\vec{r}}_{nu}) = 0 \qquad (3.14)}$$

where we have made use of the orthonormality relation

$$\int_{\mathbf{V}_{el}} d\underline{\vec{r}}_{el}^{3}\,\Phi_m^{a\,*}(\underline{\vec{r}}_{el};\underline{\vec{r}}_{nu})\Phi_n^a(\underline{\vec{r}}_{el};\underline{\vec{r}}_{nu}) = \delta_{mn} \qquad (3.15)$$

and defined the nuclear kinetic matrix elements

$$\underline{\underline{\mathrm{T}}}_{mn}(\underline{\vec{r}}_{nu}) \equiv \int_{\mathbf{V}_{el}} d\underline{\vec{r}}_{el}^{3}\,\Phi_m^{a\,*}(\underline{\vec{r}}_{el};\underline{\vec{r}}_{nu})\widehat{\mathbf{T}}^{nu}(\underline{\vec{r}}_{nu})\left[\Phi_n^a(\underline{\vec{r}}_{el};\underline{\vec{r}}_{nu})\mathcal{X}_n^a(\underline{\vec{r}}_{nu})\right] \qquad (3.16)$$

From these equations we can readily make the following conclusions

---

[4] See footnote 3 on page 43 for a definition of the term parametrical dependence of an operator.

- The *adiabatic* representation of the potential energy surfaces, $\mathcal{E}_n(\underline{\vec{r}}_{nu})$, are by construction diagonal.

- The coupling, responsible for the non-adiabatic transitions between the adiabatic surfaces, are due to the off-diagonal elements of the matrix representation of the nuclear kinetic energy term, eq. (3.16).

In the remaining of this section we are going to explore some of the problems related to the use of the adiabatic representation presented above, which in turn leads up to some very important approximations that will be the topic of the next section.

In order to comment more precisely on the numerical aspects of the adiabatic representation, we now move on at an analysis of the kinetic matrix elements, defined in eq. (3.16), which enter the close-coupled adiabatic working equation listed in eq. (3.14). The explicit form of eq. (3.16) follow immediately from eq. (3.2a)

$$\underline{\underline{\mathrm{T}}}_{mn}(\underline{\vec{r}}_{nu}) = -\sum_{j=1}^{g}\frac{\hbar^2}{2m_j}\int_{\mathbf{V}_{el}} d\underline{\vec{r}}_{el}^{3}\,\Phi_m^{a\,*}(\underline{\vec{r}}_{el};\underline{\vec{r}}_{nu})\nabla_j^2\left[\Phi_n^a(\underline{\vec{r}}_{el};\underline{\vec{r}}_{nu})\mathcal{X}_n^a(\underline{\vec{r}}_{nu})\right] \tag{3.17}$$

To simplify the notations considerably we are going to ignore the arguments, $(\underline{\vec{r}}_{el}, \underline{\vec{r}}_{nu})$, throughout the rest of this section, and furthermore adopt the convenient *bra-ket* notation[5]. Thus, in this compact notation eq. (3.13) and (3.15)

---

[5] First we emphasize that throughout the rest of this chapter the bra-ket notation only denotes integration over the *electronic* coordinates. Next we define the bra-ket notation as a short notation for integrals of the type:

$$\begin{aligned}\langle\Psi|\hat{\mathbf{O}}|\Phi\rangle \equiv \langle\Psi|\hat{\mathbf{O}}[\Phi]\rangle &\equiv \int_{-\infty}^{\infty} dx\,\Big(\Psi^*(x)\hat{\mathbf{O}}\,[\Phi(x)]\Big)\\ &= \int_{-\infty}^{\infty} dx\,\Big(\hat{\mathbf{O}}^*\,[\Phi(x)]\,\Psi(x)\Big)^* \equiv \langle\hat{\mathbf{O}}[\Phi]|\Psi\rangle^*\end{aligned} \tag{3.18}$$

and we note that in the general definition operators always operate to the *right*, and only if the operator happens to be Hermitian - that is if

$$\int_{-\infty}^{\infty} dx\,\Big(\Psi^*(x)\hat{\mathbf{O}}\,[\Phi(x)]\Big) \equiv \int_{-\infty}^{\infty} dx\,\Big(\hat{\mathbf{O}}^*\,[\Psi(x)]\,\Phi(x)\Big) \tag{3.19}$$

can the operator in a bra-ket notation operate *both* to the left or right, *i.e.*

$$\langle\Psi|\hat{\mathbf{O}}|\Phi\rangle \equiv \langle\Psi|\hat{\mathbf{O}}[\Phi]\rangle = \langle\hat{\mathbf{O}}[\Psi]|\Phi\rangle \tag{3.20}$$

simply takes the form

$$(\widehat{\mathbf{H}}^{el} - \mathcal{E}_n)\Phi_n^a = 0 \tag{3.21a}$$

$$\langle\Phi_m^a|\Phi_n^a\rangle = \delta_{mn} \tag{3.21b}$$

Now, using the rule for differentiation of a product-function twice, eq. (3.17) is easily rewritten as

$$\underline{\underline{\mathrm{T}}}_{mn} = -\sum_{j=1}^{g} \frac{\hbar^2}{2m_j} \left(\nabla_j^2\delta_{mn} + \langle\Phi_m^a|\nabla_j^2|\Phi_n^a\rangle + 2\langle\Phi_m^a|\vec{\nabla}_j|\Phi_n^a\rangle \cdot \vec{\nabla}_j\right) \mathcal{X}_n^a \tag{3.22}$$

Inserting this result into eq. (3.14) finally lead to the following adiabatic close-coupled working equations

$$\boxed{-\sum_{j=1}^{g} \frac{\hbar^2}{2m_j} \sum_{n} \left(\nabla_j^2\delta_{mn} + \underline{\underline{\mathcal{T}}}_{mn}^{(j)} + 2\underline{\underline{\vec{\mathcal{T}}}}_{mn}^{(j)} \cdot \vec{\nabla}_j\right) \mathcal{X}_n^a = (E - \mathcal{E}_m)\, \mathcal{X}_m^a \qquad (3.23)}$$

where we have defined the non-adiabatic vector and scalar matrix coupling elements

$$\underline{\underline{\vec{\mathcal{T}}}}_{mn}^{(j)} \equiv \langle\Phi_m^a|\vec{\nabla}_j|\Phi_n^a\rangle \tag{3.24a}$$

$$\underline{\underline{\mathcal{T}}}_{mn}^{(j)} \equiv \langle\Phi_m^a|\nabla_j^2|\Phi_n^a\rangle \tag{3.24b}$$

where $j = 1, 2, \ldots, g$, *i.e.* these elements involve the derivative with respect to the *nuclear* coordinates. As we will clarify now these two types of non-adiabatic coupling elements can cause serious numerical problems in the adiabatic representation. Let us start by examining the vector matrix elements of eq. (3.24a). As a prelude we take the gradient of eq. (3.21a), with respect to the nuclear coordinates, leading to

$$\left(\widehat{\mathbf{H}}^{el} - \mathcal{E}_n\right) \vec{\nabla}_j\Phi_n^a = \left(\vec{\nabla}_j[\mathcal{E}_n] - \vec{\nabla}_j[\widehat{\mathbf{H}}^{el}]\right) \Phi_n^a \tag{3.25}$$

where $j = 1, 2, \ldots, g$. Next we project this equation onto $\langle\Phi_m^a|$, giving

$$\langle\Phi_m^a|\widehat{\mathbf{H}}^{el}|\vec{\nabla}_j\Phi_n^a\rangle - \mathcal{E}_n\langle\Phi_m^a|\vec{\nabla}_j|\Phi_n^a\rangle = \vec{\nabla}_j[\mathcal{E}_n]\langle\Phi_m^a|\Phi_n^a\rangle - \langle\Phi_m^a|\vec{\nabla}_j[\widehat{\mathbf{H}}^{el}]|\Phi_n^a\rangle \tag{3.26}$$

Finally, making use of eq. (3.21b) and the Hermitian[6] property of $\widehat{\mathbf{H}}^{el}$ in the first term of eq. (3.26), it reduces to

$$(\mathcal{E}_m - \mathcal{E}_n)\,\langle\Phi_m^a|\vec{\nabla}_j|\Phi_n^a\rangle = \vec{\nabla}_j[\mathcal{E}_n]\delta_{mn} - \langle\Phi_m^a|\vec{\nabla}_j[\widehat{\mathbf{H}}^{el}]|\Phi_n^a\rangle \tag{3.27}$$

---

[6] See eq. (3.20) in footnote 5 on page 47.

If we first consider the case where $n = m$ we obtain the important result

$$\vec{\nabla}_j[\mathcal{E}_n] = \langle \Phi^a_n | \vec{\nabla}_j[\widehat{\mathbf{H}}^{el}] | \Phi^a_n \rangle \tag{3.28}$$

which is a special case of the famous Hellmann-Feynman theorem

$$\frac{dE_k(\xi)}{d\xi} = \langle \Psi_k(\xi) | \frac{\partial \widehat{\mathbf{H}}(\xi)}{\partial \xi} | \Psi_k(\xi) \rangle \tag{3.29}$$

where $|\Psi_k(\xi)\rangle$ is the k'th eigenstate of $\widehat{\mathbf{H}}(\xi)$, depending on the embedded parameter ξ, with the eigenvalue $E_k(\xi)$. As a prelude to the interpretation of eq. (3.28) we first note that in the adiabatic picture, the $\mathcal{E}_n(\underline{\vec{r}}_{nu})$'s are the potential energy surfaces on which the nuclei moves. Consequently we can think of $\vec{\nabla}_j[\mathcal{E}_n(\underline{\vec{r}}_{nu})]$ as the "adiabatic quantum" *force* felt by the nuclei on surface n. Eq. (3.28) then states that these adiabatic forces on the nuclei are given as the derivative of $\widehat{\mathbf{H}}^{el}$ with respect to the nuclear coordinates averaged over the corresponding electronic adiabatic wave function. The Hellmann-Feynman theorem is clearly an important relation, which we shall actually use in section 9.4, but we have still not gained any information on the elements of eq. (3.24a), as promised.

To do this, we next consider the case where $n \neq m$ in eq. (3.27), that is

$$(\mathcal{E}_m - \mathcal{E}_n)\, \langle \Phi^a_m | \vec{\nabla}_j | \Phi^a_n \rangle = -\langle \Phi^a_m | \vec{\nabla}_j[\widehat{\mathbf{H}}^{el}] | \Phi^a_n \rangle \tag{3.30}$$

If we next make use of the explicit definition of $\widehat{\mathbf{H}}^{el}$, see eq. (3.1b), we finally obtain the important result

$$\langle \Phi^a_m | \vec{\nabla}_j | \Phi^a_n \rangle = (\mathcal{E}_n - \mathcal{E}_m)^{-1} \langle \Phi^a_m | \vec{\nabla}_j[V^{tot}] | \Phi^a_n \rangle, \qquad n \neq m \tag{3.31}$$

This relation reveals the major drawback of the adiabatic representation, namely, that the coupling terms of the type $\langle \Phi^a_m | \vec{\nabla}_j | \Phi^a_n \rangle$ can display very large numerical values in regions where the difference between two adiabatic potential energy surfaces is small. Even worse, these matrix elements may diverge or become discontinuous in polyatomic systems (*i.e.* $N_{nu} \leq 3$) where actual crossing of the adiabatic potential energy surfaces is more likely to occur.

Also the other type of coupling elements, $\langle \Phi^a_m | \nabla^2_j | \Phi^a_n \rangle$, can cause numerical problems. To see why, we first take the gradient of the orthonormality relation of eq. (3.21b), with respect to the nuclear coordinates. This gives

$$\begin{aligned}\langle \vec{\nabla}_j[\Phi^a_m]|\Phi^a_n\rangle + \langle \Phi^a_m|\vec{\nabla}_j[\Phi^a_n]\rangle &= \langle \Phi^a_n|\vec{\nabla}_j[\Phi^a_m]\rangle^* + \langle \Phi^a_m|\vec{\nabla}_j[\Phi^a_n]\rangle \\ &\equiv \underline{\underline{\vec{\mathcal{T}}}}^{(j)*}_{nm} + \underline{\underline{\vec{\mathcal{T}}}}^{(j)}_{mn} = \vec{0}\end{aligned} \tag{3.32}$$

which means that the elements of eq. (3.24a) are skew Hermitian. To obtain a relation for $\underline{\underline{\mathcal{T}}}^{(j)}_{mn}$, we take the gradient of eq. (3.32) once more, leading to

$$\begin{aligned}\langle \nabla^2_j[\Phi^a_m]|\Phi^a_n\rangle + 2\langle \vec{\nabla}_j[\Phi^a_m]|\vec{\nabla}_j[\Phi^a_n]\rangle + \langle \Phi^a_m|\nabla^2_j[\Phi^a_n]\rangle &\equiv \\ \underline{\underline{\mathcal{T}}}^{(j)*}_{nm} + 2\langle \vec{\nabla}_j[\Phi^a_m]|\vec{\nabla}_j[\Phi^a_n]\rangle + \underline{\underline{\mathcal{T}}}^{(j)}_{mn} &= 0\end{aligned} \tag{3.33}$$

This expression clearly shows that the matrix elements, $\underline{\underline{\mathcal{T}}}^{(j)}_{mn}$, are not generally Hermitian or even skew Hermitian. The term "generally" is used because only in a complete adiabatic basis-set, where we can write the resolution of unity as

$$1 = \sum_k |\Phi^a_k\rangle\langle\Phi^a_k| \tag{3.34}$$

do we have

$$\begin{aligned}\underline{\underline{\mathcal{T}}}^{(j)}_{mn} \equiv \langle \Phi^a_m|\vec{\nabla}_j \cdot \vec{\nabla}_j|\Phi^a_n\rangle &= \sum_k \langle \Phi^a_m|\vec{\nabla}_j|\Phi^a_k\rangle \cdot \langle \Phi^a_k|\vec{\nabla}_j|\Phi^a_n\rangle \\ &\equiv \sum_k \underline{\underline{\vec{\mathcal{T}}}}^{(j)}_{mk} \cdot \underline{\underline{\vec{\mathcal{T}}}}^{(j)}_{kn}\end{aligned} \tag{3.35}$$

which is clearly, from eq. (3.32), Hermitian. Thus, the coupling elements of the type, $\langle \Phi^a_m|\nabla^2_j|\Phi^a_n\rangle$, can lead to non-Hermitian matrix expressions, which in turn implies that the S-matrix, defined in section 1.2, is not guaranteed to be unitary. Hence, formally speaking, it is only in the limit of a complete adiabatic basis-set that the number of particles (*i.e.* flux) is conserved. This, and especially the divergent property of the $\langle \Phi^a_m|\vec{\nabla}_j|\Phi^a_n\rangle$ elements (*cf.* eq. (3.31)), are numerically complicating aspects of the adiabatic representation, which often makes the diabatic representation, discussed in the previous section, more popular in terms of actual dynamical calculations. Another route is to introduce approximations to the adiabatic representation, which is the topic of the next section.

3.3 Approximate representations

One obvious way to overcome the problems of divergent and non-Hermitian matrix elements, encountered in the adiabatic representation, is simply to neglect off-diagonal elements of the type $\langle \Phi^a_m|\vec{\nabla}_j|\Phi^a_n\rangle$ and $\langle \Phi^a_m|\nabla^2_j|\Phi^a_n\rangle$, corresponding to using only a single term in the Born-Huang series of eq. (3.12). Eq. (3.23) then reduces to

$$\left(-\sum_{j=1}^{g}\frac{\hbar^2}{2m_j}\left(\nabla_j^2+\underline{\underline{\mathcal{T}}}^{(j)}_{mm}+2\vec{\underline{\underline{\mathcal{T}}}}^{(j)}_{mm}\cdot\vec{\nabla}_j\right)+\mathcal{E}_m-E\right)\mathcal{X}^a_m=0 \tag{3.36}$$

This approach is referred to as the *adiabatic approximation*, as opposed to the "exact" non-adiabatic[7] solution of eq. (3.23). Surely the original motivation for Born and Huang to introduce this approximation was not merely to overcome the numerical problems encountered in the adiabatic representation, but rather to bring eq. (3.23) into a form which could more easily be solved. If we further take the adiabatic states, Φ^a_m, to be real, the term $\vec{\underline{\underline{\mathcal{T}}}}^{(j)}_{mm}$ vanish due to eq. (3.32). In other words, the adiabatic approximation neglects the terms $\langle\Phi^a_m|\vec{\nabla}_j|\Phi^a_n\rangle$, but includes the term $\langle\Phi^a_m|\nabla_j^2|\Phi^a_m\rangle$. However, in the limit of a complete basis, these terms are related through eq. (3.35), and as such it seems unjustifiable to keep $\langle\Phi^a_m|\nabla_j^2|\Phi^a_m\rangle$ but neglect $\langle\Phi^a_m|\vec{\nabla}_j|\Phi^a_n\rangle$. This curiosity of the adiabatic approximation has led theoreticians[8] to the opinion that for some systems the result of neglecting $\langle\Phi^a_m|\nabla_j^2|\Phi^a_m\rangle$ as well as $\langle\Phi^a_m|\vec{\nabla}_j|\Phi^a_n\rangle$ is actually more "justifiable". This is exactly the celebrated *Born-Oppenheimer approximation.* Thus, in this approximation eq. (3.36) simplifies to

$$\left(-\sum_{j=1}^{g}\frac{\hbar^2}{2m_j}\nabla_j^2+\mathcal{E}_m-E\right)\mathcal{X}^a_m=0 \tag{3.37}$$

It is widely believed that the complete decoupling of electronic and nuclear motions, as expressed in eq. (3.37), can be justified by referring to the work presented in a paper[39] by Born and Oppenheimer published in 1927. Nowadays, however, it is more usual to attempt a justification in terms of an approach that was presented first by Born in 1951 and written up in a generally available form by Born and Huang[40] in 1955. Thus, it should be stressed that the Born-Oppenheimer approximation, popularly known as the assumption of infinite nuclear masses, cannot be justified in any simple way in a completely non-classical theory.

---

[7] The term non-adiabatic is clearly a double negative construction, but it is *not* equivalent to diabatic.

[8] My former supervisor, Professor Jan Linderberg, was of this opinion.

3.4 The adiabatic-diabatic transformation

It should be clear from the presentations in the previous sections that both the adiabatic and the diabatic representations have their pros and cons. Thus, it seems desirable to establish a transformation between these two representations and use each one for convenience as required. Such a adiabatic-diabatic transformation has been formulated by Baer[37], which we shall very briefly outline in this section. This is done both for the sake of completion, but especially because we will need this transformation in a discussion in chapter 7. We will simply present this transformation scheme as a recipe, and refer to reference [37] or [41] for the details of the derivation.

For the sake of simplicity we consider a two-dimensional system with the mass-weighted Jacobi coordinates r and R, see subsection 2.1.1. For this simple system the adiabatic and diabatic representations of eq. (3.10) and (3.23) respectively read as

$$\left(-\frac{\hbar^2}{2\mu}\nabla^2 + \underline{\underline{\mathrm{W}}} - E\right)\underline{\mathcal{X}}^d = \underline{0} \tag{3.38a}$$

$$\left(-\frac{\hbar^2}{2\mu}\left(\nabla^2 + 2\vec{\underline{\underline{\mathcal{T}}}}\cdot\vec{\nabla} + \underline{\underline{\mathcal{T}}}\right) + \underline{\underline{\mathrm{V}}} - E\right)\underline{\mathcal{X}}^a = \underline{0} \tag{3.38b}$$

where we have adopted a vector/matrix notation and defined the non-adiabatic coupling matrices of eq. (3.24) where $\vec{\nabla} \equiv [\partial/\partial r, \partial/\partial R]$. Note also that in eq. (3.38a) $\underline{\underline{\mathrm{W}}}$ is the diabatic potential coupling matrix, and in eq. (3.38b) $\underline{\underline{\mathrm{V}}}$ is a diagonal matrix with the adiabatic potentials, $\mathcal{E}_n$, as the elements. Based on simple algebraic arguments and the assumption of a complete adiabatic basis-set (*cf.* eq. (3.34)), Baer shows that a uniform transformation between the two representations exist, *i.e.*

$$\underline{\mathcal{X}}^a = \underline{\underline{\mathrm{A}}} \cdot \underline{\mathcal{X}}^d \tag{3.39a}$$

$$\underline{\underline{\mathrm{W}}} = \underline{\underline{\mathrm{A}}}^+ \cdot \underline{\underline{\mathrm{V}}} \cdot \underline{\underline{\mathrm{A}}} \tag{3.39b}$$

where the unitary transformations matrix, $\underline{\underline{\mathrm{A}}}$, is a solution to the differential equations

$$\left(\vec{\nabla} + \vec{\underline{\underline{\mathcal{T}}}}\right) \cdot \underline{\underline{\mathrm{A}}} = \vec{0} \quad \Leftrightarrow \quad \begin{cases} \partial\underline{\underline{\mathrm{A}}}/\partial r + \underline{\underline{\mathcal{T}}}_r \cdot \underline{\underline{\mathrm{A}}} = 0 \\ \partial\underline{\underline{\mathrm{A}}}/\partial R + \underline{\underline{\mathcal{T}}}_R \cdot \underline{\underline{\mathrm{A}}} = 0 \end{cases} \tag{3.40}$$

The solution of eq. (3.40) can easily be expressed in the following integral equations

$$\begin{aligned}\underline{\underline{\mathrm{A}}}(r,R) = \underline{\underline{\mathrm{A}}}(r_0,R_0) &+ \int_r^{r_0} \underline{\underline{\mathcal{T}}}_r(r,R)\cdot\underline{\underline{\mathrm{A}}}(r,R)dr \\ &+ \int_R^{R_0} \underline{\underline{\mathcal{T}}}_R(r_0,R)\cdot\underline{\underline{\mathrm{A}}}(r_0,R)dR\end{aligned} \tag{3.41}$$

or

$$\begin{aligned}\underline{\underline{\mathrm{A}}}(r,R) = \underline{\underline{\mathrm{A}}}(r_0,R_0) &+ \int_R^{R_0} \underline{\underline{\mathcal{T}}}_R(r,R)\cdot\underline{\underline{\mathrm{A}}}(r,R)dR \\ &+ \int_r^{r_0} \underline{\underline{\mathcal{T}}}_r(r,R_0)\cdot\underline{\underline{\mathrm{A}}}(r,R_0)dr\end{aligned} \tag{3.42}$$

Note especially that if we the define $\underline{\underline{\mathrm{A}}}(r_0,R_0)$ as the unit matrix, the nuclear configuration point, (r_0,R_0), plays the role of the reference point in the diabatic representation, *i.e.* $\vec{\underline{r}}^{\,0}_{nu}$ in eq. (3.11). We now outline the transformation scheme between the two representations.

- From a knowledge of the diabatic representation, *cf.* eq. (3.38a), the adiabatic potentials, $\underline{\underline{\mathrm{V}}}$, and the transformations matrix, $\underline{\underline{\mathrm{A}}}$, are determined from eq. (3.39b). $\vec{\underline{\underline{\mathcal{T}}}}$ is next given as the corresponding solution of eq. (3.40), and finally $\underline{\underline{\mathcal{T}}}$ can be constructed from eq. (3.35),*i.e.* $\underline{\underline{\mathcal{T}}} = [\vec{\underline{\underline{\mathcal{T}}}}]^{\mathrm{T}}\cdot\vec{\underline{\underline{\mathcal{T}}}}$.
- From a knowledge of the adiabatic representation, *cf.* eq. (3.38b), the transformation matrix, $\underline{\underline{\mathrm{A}}}$, is constructed from eq. (3.41) or (3.42). In this equation $\underline{\underline{\mathrm{A}}}(r_0,R_0) = \underline{\underline{1}}$ is chosen as the desired nuclear reference configuration for the corresponding diabatic representation. The diabatic potential energy surfaces are next given by eq. (3.39b).

We furthermore note that by combining the two schemes, outlined above, one can also shift from one diabatic representation to another, simply by choosing a new reference point, (r_0,R_0), in the integration of eq. (3.41) or (3.42). This important feature of the transformation scheme will be mentioned in section 7.1 in the next part of this thesis.

3.4.1 The simple 2-surface case

To illustrate the usefulness of the outlined transformation scheme we close this section with a short study of a simple two-dimensional two-surface system. This is a very typical size of a practical non-adiabatic calculation, and in the context of the present thesis it is of particular interest as this is exactly the size of the system that we shall study in the next part.

Since $\underline{\underline{\mathrm{A}}}$ is orthogonal it can be written as

$$\underline{\underline{\mathrm{A}}} = \begin{bmatrix} \cos\gamma & -\sin\gamma \\ \sin\gamma & \cos\gamma \end{bmatrix} \tag{3.43}$$

where the parameter γ is a function of both r and R. For this two-surface case, $\vec{\underline{\underline{\mathcal{T}}}} \equiv [\underline{\underline{\mathcal{T}}}_r, \underline{\underline{\mathcal{T}}}_R]$, takes the simple form

$$\underline{\underline{\mathcal{T}}}_x = \begin{bmatrix} 0 & \mathcal{T}_x \\ -\mathcal{T}_x & 0 \end{bmatrix} \tag{3.44}$$

where $x = r, R$, and eq. (3.40) simplifies to

$$\frac{\partial \gamma}{\partial x} = \mathcal{T}_x \tag{3.45}$$

$$\gamma(r, R) = \gamma(r_0, R_0) + \int_{r_0}^{r} \mathcal{T}_r(r, R)dr + \int_{R_0}^{R} \mathcal{T}_R(r_0, R)dR \tag{3.46}$$

where $\gamma(r_0, R_0) = 0$ defines the reference configuration in the diabatic representation. Next, from eq. (3.44) it is readily seen that eq. (3.39b) takes the simple form

$$W_{11} = V_1 \cos^2\gamma + V_2 \sin^2\gamma \tag{3.47a}$$

$$W_{22} = V_1 \sin^2\gamma + V_2 \cos^2\gamma \tag{3.47b}$$

$$W_{12} = W_{21} = \tfrac{1}{2}\left(V_2 - V_1\right)\sin 2\gamma \tag{3.47c}$$

Thus, in the simple two-surface two-dimensional case the adiabatic-diabatic transformation scheme, outlined above, is easy to apply.

4

Time-dependent quantum dynamics

The time-dependent formulation of quantum dynamics has over the past decade developed into an extremely important theoretical tool for the description of dynamical processes in the field of chemical physics. In many aspects it is superior and more appealing than the time-independent approach which it superseded. The first important point actually concerns something as "unphysical" as the human intuition. The time-dependent picture of a physical event is much more intuitive than the formally equivalent time-independent, for as put by Kosloff[42] "a cause in the past leading to a result in future is strongly imprinted in human thought". This view-point is always taken in the classical mechanical descriptions, and this analogy has actually been the indirect motivation for the many successful attempts to combined the classical and quantum description in one formulation, which in turn has lead to the semi-classical methods[43]. Thus, an important feature of the time-dependent formulation of quantum dynamics is that one obtains a physical picture of the underlying dynamics, analogous to the classical description, but within the correct quantal framework. For instance, in part II we will show snapshots of the wave packet by plotting probability densities at various stages of the time evolution, and thereby obtain a feel of the dynamical event.

Furthermore, the underlying numerical formulation of the time-dependent wave packet approach is an attractive alternative to that of the time-independent close-coupling method discussed in the previous chapter. Although both formulations are formally equivalent, they are technically and numerically very different, and the former is computationally advantageous for large-scale scattering calculations. In the time-independent formulation the total scattering energy is fixed to a single value, and the wave function is subject to boundary-value-conditions to enforce the correct asymptotic behavior. In contrast, the wave packet in the time-dependent approach is initiated according to a relevant set of initial conditions, and represent a whole spectrum of energies. After a certain time evolution of the system, information is then extracted from this wave packet by projecting it onto individual rot-vibrational product states, or by computing the quantum flux, defined in section 1.1, across a dividing line or surface in the relevant product channels. Thus, in terms of the celebrated S-matrix, introduced in section 1.2, the time-dependent approach solves for different energies a single column of the S-matrix at a time, while the time-independent close-coupled approach solves for the whole S-matrix at a fixed energy in a single calculation. This is one of the reasons why the computational time of each time-dependent calculation scales better than N^2 versus the N^3 scaling of a typical time-independent close-coupled calculation, where$N$ is the total size of the involved basis-sets or grid-points.

Another factor which makes the time-dependent approach so fast and popular is that the explicit propagation in time, of the wave packet, can be accomplished by a variety of very effective numerical schemes developed over the last several years. These propagation methods will be the main topic of this chapter. With the exception of the SOD method, which is included for the sake of completeness, we shall use or refer to all of these methods in the discussions to come in part II and III – some of the discussions will even put the techniques in a context different from the one they will be presented in below. However, nothing is perfect, and the time-dependent approach of course has its limitations where the time-independent description is still superior. The study of molecular resonances in chemical reactions, which will be the topic of part III, are an example of such a case.

4.1 Time propagation

The natural starting point of a discussion on time-dependent propagation methods, is of course the time-dependent Schrödinger equation,

$$i\hbar\frac{\partial}{\partial t}\Psi(x,t) = \widehat{\mathbf{H}}\Psi(x,t) \tag{4.1}$$

where $\widehat{\mathbf{H}}$ is the usual Hamiltonian operator, which, depending on the system it describes, can be either explicitly time-dependent or time-independent, and where $\Psi(\vec{r},t)$ is the corresponding time-dependent wave function, which for reasons that will soon become clear, is often called the wave packet of the system. Recalling the usual time-independent Schrödinger equation, we note that the Hamiltonian operator has two different interpretations in quantum mechanics; it describes both the energy and the time-evolution of the system. Throughout this thesis we will assume that $\widehat{\mathbf{H}}$ is time-independent, which is the case for the closed systems that we shall consider later on. Thus, the formal solution to the first-order differential equation in eq. (4.1) read as

$$\Psi(x,t) \equiv \widehat{\mathbf{U}}(t,t_0)\Psi(x,t_0) = e^{-i\widehat{\mathbf{H}}(t-t_0)/\hbar}\Psi(x,t_0) \tag{4.2}$$

where we have defined the unitary time-evolution operator $\widehat{\mathbf{U}}(t,t_0)$[1]. The central task of this section is to present some of the most important techniques available for the solution of either eq. (4.1) or eq. (4.2). This solution is best accomplished by first representing the wave function on a discrete grid, using one of the grid methods (FD,DVR,FFT) already discussed in section 2.2, and below we will focus on the explicit propagation schemes.

4.1.1 The second-order difference scheme

Perhaps the simplest scheme emerges by approximating the time-derivative of the wave function, entering eq. (4.1), by second-order finite differencing,

$$\frac{\partial}{\partial t}\Psi(x,t) = \frac{\Psi(x,t+\Delta t) - \Psi(x,t-\Delta t)}{2\Delta t} + \mathrm{O}(\Delta t^3) \tag{4.3}$$

Using eq. (4.1), this equation is readily recast into the following iterative expression for a time-increment of the wave function

$$\boxed{\Psi(x,t+\Delta t) = \Psi(x,t-\Delta t) + \frac{2\Delta t}{i\hbar}\widehat{\mathbf{H}}\Psi(x,t) + \mathrm{O}(\Delta t^3)} \tag{4.4}$$

Thus, the wave function obtained by this iterative scheme is correct to the second order in the time-increment, and hence this method is called the second-order difference (SOD) method. This method is clearly extremely easy to implement,

---

[1] Sometimes it is useful to employ a different viewpoint than the one taken in the Schrödinger representation discussed here. In the interaction representation the Hamiltonian is partitioned as $\widehat{\mathbf{H}} = \widehat{\mathbf{H}}^0 + \widehat{\mathbf{V}}$ and the analog of eq. (4.2) reads as $\Psi_I(x,t) = \widehat{\mathbf{V}}_I(t,t_0)\Psi_I(x,t_0)$, where $\widehat{\mathbf{V}}_I(t,t_0) \equiv e^{i\widehat{\mathbf{H}}^0(t-t_0)/\hbar}\widehat{\mathbf{V}}e^{-i\widehat{\mathbf{H}}^0(t-t_0)/\hbar}$ is called the generalized interaction operator. This solution is related to the solution in the Schrödinger representation of eq. (4.2) by the unitary transformation $\Psi_I(x,t) = e^{i\widehat{\mathbf{H}}^0(t-t_0)/\hbar}\Psi(x,t)$. Thus, the Schrödinger representation can be regarded as a special case of the general interaction representation with $\widehat{\mathbf{H}}^0 = 0$, and we just note that the Heisenberg representation emerges when $\widehat{\mathbf{V}} = 0$.

but it suffers from a serious numerical limitation which makes this approach inefficient for especially large-scale calculations. The SOD method requires very small step size, Δt, otherwise the scheme becomes unstable and the solution blows up exponentially. This is a direct consequence of that fact that the corresponding approximated time-evolution operator, $\widehat{\mathbf{U}}(t+\Delta t, t) - \widehat{\mathbf{U}}^{+}(t, t-\Delta t) \approx \frac{2\Delta t}{i\hbar}\widehat{\mathbf{H}}$, is not unitary (*i.e.* norm-conserving) as required by eq. (4.2).

4.1.2 The split-operator method

One way to overcome the numerical problems associated with the SOD method, is to define an approximate evolution operator, $\widehat{\mathbf{U}}(t + \Delta t, t)$, which by construction is unitary. The simplest of these methods split the Hamiltonian as

$$\begin{aligned}
\Psi(x, t+\Delta t) &= e^{-\mathrm{i}\widehat{H}\Delta t/\hbar}\Psi(x,t) \\
&= e^{-\mathrm{i}\widehat{T}\Delta t/2\hbar}e^{-\mathrm{i}\Delta t V/\hbar}e^{-\mathrm{i}\widehat{T}\Delta t/2\hbar}\Psi(x,t) + \mathrm{O}(\Delta t^3) \qquad (4.5\mathrm{a}) \\
&= e^{-\mathrm{i}V\Delta t/2\hbar}e^{-\mathrm{i}\widehat{T}\Delta t/\hbar}e^{-\mathrm{i}V\Delta t/2\hbar}\Psi(x,t) + \mathrm{O}(\Delta t^3) \qquad (4.5\mathrm{b})
\end{aligned}$$

The original formulation of this split-operator method (SO), due to Fleck *et al.*[44], focused on eq. (4.5a) which is referred to as the potential referenced SO, but in this thesis we will make use of the formally identical kinetic referenced SO of eq. (4.5b). The split-operator method has become one of the most popular propagation schemes in medium-sized time-dependent dynamical calculations. This popularity is mainly due to the fact that it enables the actions of the two terms entering the Hamiltonian, $\widehat{\mathbf{H}} = \widehat{\mathbf{T}} + V$, to be evaluated in their respective local representations. This is done by discretizing the wave function on a grid and employing the Fourier transform method of Kosloff and Kosloff[20] for the calculation of the action of the kinetic terms, as discussed in subsection 2.2.2. In subsection 6.2.2 we will outline the explicit procedures involved in a single split-operator propagation for a non-adiabatic system.

Clearly the split-operator method of eq. (4.5) is (like the SOD) only accurate up to second order in Δt, which generally mean that small propagation steps has to be employed. However, recently Bandrauk and Shen[45] have extended this second-order split-operator to make it accurate up to third order in Δt (*i.e.* $\mathrm{O}(\Delta t^4)$), which in turn implies that one can choose larger values of Δt. Thus, this method is actually more computationally effective than the simple second-order SO, even though the action of seven exponential operators has to be computed, using for instance the FFT algorithm. In addition, the phase of the corresponding wave packet is more accurately determined in this approach[45]. However, in the present application of the SO method (see chapter 6 and 7) we are going to calculate the time→energy transform of the wave packet in the discrete time steps ((*cf.* eq. (6.47)), which puts an upper limit to Δt. Consequently we will just employ the simple second-order SO.

4.1.3 The Chebychev polynomial expansion method

Another widely used propagation scheme consist of expanding the evolution operator, $\widehat{\mathbf{U}}(t, t_0)$, in a basis-set of Chebychev polynomials. This method, introduced by Tal-Ezer and Kosloff[46], is also distinguished by its generality in the sense that it is easily adapted to other types of operators depending on the Hamiltonian. (For a more thorough presentation we refer to a review paper by Kosloff[47]). The natural starting point for the presentation is first to outline the way in which Chebychev polynomials are used to expand a simple real function.

Let us consider the expansion of a real function, $f(x)$, in a basis-set of Chebychev polynomials, $\{T_n(x)\}$, defined as

$$T_n(x) = \cos(n \ \arccos(x)), \quad n = 0, 1, 2, \dots \tag{4.6}$$

where x is a real variable confined to the interval $[-1, 1]$. These Chebychev polynomials are orthogonal over the weight function $(1 + x^2)^{-1/2}$[6],

$$\int_{-1}^{1} \frac{T_n(x) T_m(x)}{\sqrt{1 - x^2}} \, dx = \delta_{nm} \frac{\pi}{2} (1 + \delta_{n0}) \tag{4.7}$$

and further satisfy the following characteristic recurrence relation

$$T_{n+1}(x) = 2x T_n(x) - T_{n-1}(x) \tag{4.8}$$

with the initial conditions $T_0(x) = 1$ and $T_1(x) = x$. Consequently, a function $f(x)$, defined in the interval $[-1, 1]$, can be approximated by a finite expansion in Chebychev polynomials in the following way

$$f(x) \approx \sum_{n=0}^{N} A_n T_n(x) \quad \text{where} \quad A_n \equiv \int_{-1}^{1} \frac{f(x) T_n(x)}{\sqrt{1 - x^2}} \, dx \tag{4.9}$$

Now let us return to the problem of expanding a Hermitian operator in a series of Chebychev polynomials. Since the Chebychev polynomials are bound in the interval $[-1,1]$ the first step is to define a renormalized operator by simply shifting its eigenvalue spectra to this range. Let assume that the upper and lower bounds of the spectrum of $\widehat{\mathbf{H}}$ are given by respectively $E_{max} \approx \frac{\hbar^2\pi^2}{2\mu\Delta R^2} + V_{max}$ and $E_{min} \approx V_{min}$. Thus, we define the renormalized operator, α, in the following way

$$\alpha \equiv \frac{\langle E\rangle - \widehat{\mathbf{H}}}{\Delta E/2} \quad \text{where} \quad \begin{cases} \Delta E \equiv E_{max} - E_{min} \\ \langle E\rangle \equiv (E_{max} + E_{min})/2 \end{cases} \tag{4.10}$$

such that $\widehat{\mathbf{H}} = \langle E\rangle - \alpha\Delta E/2$. We can now approximate the evolution operator as

$$\begin{aligned} e^{-i\widehat{\mathbf{H}}t/\hbar} &= e^{-i\langle E\rangle t/\hbar} e^{i\alpha\Delta E t/(2\hbar)} && (4.11a) \\ &\equiv U(\alpha,t) \approx \sum_{n=0}^{N} A_n(t) T_n(\alpha) && (4.11b) \end{aligned}$$

where the time-dependent expansion coefficients in the Chebychev expansion of eq. (4.11b) are obtained as

$$\begin{aligned} A_n(t) &= \frac{2-\delta_{n0}}{\pi} \int_{-1}^{1} \frac{U(\alpha,t)T_n(\alpha)}{\sqrt{1-\alpha^2}}\, d\alpha && (4.12a) \\ &= \frac{2-\delta_{n0}}{\pi} e^{-i\langle E\rangle t/\hbar} \int_{-1}^{1} \frac{e^{i\alpha t\Delta E/(2\hbar)} T_n(\alpha)}{\sqrt{1-\alpha^2}}\, d\alpha && (4.12b) \\ &= \frac{2-\delta_{n0}}{\pi} e^{-i\langle E\rangle t/\hbar} \int_{0}^{\pi} e^{i\cos(\theta)t\Delta E/(2\hbar)} \cos(n\theta)\, d\theta && (4.12c) \\ &= (2-\delta_{n0}) e^{-i\langle E\rangle t/\hbar} i^n j_n(\Delta E t/(2\hbar)) && (4.12d) \end{aligned}$$

The integral in eq. (4.12b) is realized after the substituting $\alpha = \cos(\theta)$, *i.e.* $T_n(\alpha) = \cos(n\theta)$, and eq. (4.12d) follow from the relation[6]

$$\int_0^{\pi} e^{iz\cos(\theta)} \cos(n\theta)\, \theta = \pi i^n j_n(z) \tag{4.13}$$

where $j_n(z)$ are Bessel functions of the first kind (see figure 1.2). The action of the approximated evolution operator on the wave function Ψ is then computed using eq. (4.11b) and (4.12d) and the characteristic recurrence relation (see eq. (4.8))

$$\Psi_{n+1} = 2\frac{\langle E\rangle - \widehat{\mathbf{H}}}{\Delta E/2} \Psi_n - \Psi_{n-1} \tag{4.14}$$

where $\Psi_n \equiv T_n(\alpha)\Psi$.

4.1.4 The Lanczos recursion scheme

The last propagation scheme to be discussed in this section is the Lanczos recursion scheme[48]. The central idea of the Lanczos algorithm is to construct a *compact tridiagonal* matrix representation, $\underline{\underline{\mathrm{H}}}$, of an Hamiltonian operator, $\widehat{\mathbf{H}}$, by means of the following *recursive* definition of an orthonormal basis-set, $\{\Psi_n,\ n = 0, 1, \ldots, M-1\}$,

$$\widehat{\mathbf{H}}\Psi_n = \beta_n\Psi_{n-1} + \alpha_n\Psi_n + \beta_{n+1}\Psi_n \quad \text{where} \quad \begin{cases} \widehat{\mathbf{H}}\Psi_0 & \equiv \alpha_0\Psi_0 + \beta_0\Psi_1 \\ \alpha_n & \equiv \langle\Psi_n|\widehat{\mathbf{H}}|\Psi_n\rangle \\ \beta_{n+1} & \equiv \langle\Psi_{n+1}|\widehat{\mathbf{H}}|\Psi_n\rangle \end{cases} \tag{4.15}$$

such that the tridiagonal matrix representation of $\widehat{\mathbf{H}}$ read as

$$\underline{\underline{\mathrm{H}}} = \begin{bmatrix} \alpha_0 & \beta_0 & 0 & \ldots\ldots\ldots & & & 0 \\ \beta_0 & \alpha_1 & \beta_1 & 0 & \ldots\ldots & & 0 \\ 0 & \beta_1 & \alpha_2 & \beta_2 & 0 & \ldots & 0 \\ \ldots & \ldots & \ldots & \ldots & \ldots & \ldots & \ldots \\ 0 & .. & 0 & \beta_{M-4} & \alpha_{M-3} & \beta_{M-3} & 0 \\ 0 & \ldots & & 0 & \beta_{M-3} & \alpha_{M-2} & \beta_{M-2} \\ 0 & \ldots\ldots & & & 0 & \beta_{M-2} & \alpha_{M-1} \end{bmatrix} \tag{4.16}$$

where M are the number of Lanczos recursions. Note that in eq. (4.15) the initial (Krylov) vector of the recursion, Ψ_0, must be specified. The tridiagonal matrix, $\underline{\underline{\mathrm{H}}}$, can next easily be diagonalized, leading to the $(M \times M)$ eigenvector matrix $\underline{\underline{\mathrm{U}}}$ and the M eigenvalues Λ_n. If we now assume that the system is discretized on a grid of length N, and define the $(N \times M)$ matrix $\underline{\underline{\mathrm{C}}} \equiv [\underline{\Psi}_0, \underline{\Psi}_1, \ldots, \underline{\Psi}_{M-1}]$, the time propagation of the discretized wave function $\underline{\Psi}$ is given by (see eq. (4.2))

$$\underline{\Psi}(t+\Delta t) = \underline{\underline{\mathrm{C}}} \cdot \underline{\underline{\mathrm{U}}} \cdot \exp\left[-\frac{i}{\hbar}\underline{\underline{\Lambda}}\Delta t\right] \cdot \underline{\underline{\mathrm{U}}}^{+} \cdot \underline{\underline{\mathrm{C}}}^{+} \cdot \underline{\Psi}(t) \tag{4.17}$$

The Lanczos scheme is particularly appealing for large systems, as it never requires the explicit knowledge of the large $(N \times N)$ matrix representation of the Hamiltonian directly on the grid. It should be clear from eq. (4.15) that the scheme only needs the *action* of $\widehat{\mathbf{H}}$ on the Ψ_n states, which is much less demanding in terms of computational efforts. Also, the tridiagonal form of the Hamiltonian matrix, eq. (4.16), is computationally very effective because only two vectors, $(\underline{\alpha}, \underline{\beta})$, of dimension M, and three recursion vectors, $(\underline{\Psi}_{n-1}, \underline{\Psi}_n, \underline{\Psi}_{n-1})$, of dimension N, have to be stored in the core memory of the computer.

However, the Lanczos algorithm is not only very useful as a time propagation scheme as shown in eq. (4.17). It is also a very powerful technique to locate eigenvalues and vectors of a large matrix in a narrow window of the spectrum, and it is in fact in this context that we shall refer to the scheme later on. The rate of convergence of a given eigenvalue, Λ_n, is given by the relation

$$\frac{\Lambda_n - \Lambda_{n-1}}{\Lambda_{max} - \Lambda_{min}} \tag{4.18}$$

Hence, the Lanczos algorithm unveil the eigenstates in the sparse part of the spectrum first (*i.e.* at the edges). Also, it can be shown that these eigenvectors display the largest projections onto the initial vector $\underline{\Psi}_0$. Thus, by carefully choosing this initial recursion vector one can selectively tune the Lanczos algorithm to a dynamically relevant part (Krylov subspace) of the whole Hilbert space. As a consequence the order M of the matrix $\underline{\underline{\mathrm{H}}}$ can be chosen in general much smaller than the actual size N of the grid, *i.e.* $M << N$.

Part II

Generalized MCTDH

5

Introduction

The treatment of quantum molecular dynamics is a formidable numerical task when several degrees of freedom and electronic potential energy surfaces have to be considered. The underlying problem is that the numerical effort of most exact calculations, employing grid methods and propagation techniques discussed in part I, scale exponentially with the number of degrees of freedom and surfaces, simply because the basis-set size grows exponentially. Clearly, the higher the dimensionality the more important it becomes to search for optimal basis-sets which with a minimum of functions can represent the total wave function of the system. In the framework of the exact methods this has led to many different strategies, some of which were also discussed in the first part of this thesis (*cf.* chapter 2). However, even with such optimizing schemes, at present time the exact methods are restricted to 3-4 atomic systems and single surface problems. Thus, the need for approximate but still accurate quantum methods exists, and with the recent emerge of detailed experimental studies of large systems (see introduction of chapter 1) this need has gradually increased. One could certainly argue that the desire for such approximate methods has always been present, but it is only with the recent access to powerful computers that very accurate (*i.e.* formally exact) methods has been developed and implemented.

The problem of the unfortunate scaling of the exact multi-dimensional methods is of course related to the fact that one has to compute multi-dimensional matrix-elements of the corresponding representation of the Hamiltonian operator for the system. Thus, if we could somehow avoid having to compute these multi-dimensional matrix-elements, while at the same time retaining the full dimensionality of the system, we would clearly reduce the computational costs. This problem is also encountered in multi-dimensional electronic structure theory, where an approximate solution was first put forward by Hartree and Fock as early as in the late twenties. The central idea was to recast the exact multi-dimensional problem into multiple approximate one-dimensional problems, which in turn are coupled in a self-consistent way. Methods based on this idea are referred to as self-consistent field (SCF) methods since the secular equation in each dimension is solved self-consistently by describing the coupling to the other degrees of freedom through an average field. Hence, to avoid having to compute multi-dimensional integrals for the average field, it is very essential to the SCF approach that the field operator, describing the correlations, is separable in the different degrees of freedom. (We shall elaborate more on this limitation later on).

Common to all the exact quantum approaches mentioned so far in this thesis, is also that the basis-sets (or underlying grids) are static, *i.e.* time-independent. However, in the time-dependent formulation of quantum dynamics, which as discussed in chapter 4 is superior in many ways to the time-independent counterpart, it seems quite natural to introduce a time-dependent basis-set. A fixed static basis-set must cover all the phase space which is accessible by the wave packet during the propagation, whereas the time-dependent basis-set has merely to cover the volume in phase space on which the wave function actually resides at any given time. Hence, if the wave packed remains in some sense localized during the reaction, one would expect the use of a time-dependent basis-set, which so to speak follow the dynamics of the system as time evolves, to be very advantageous.

The combination to these two ideas led to the time-dependent self-consistent field (TDSCF) or time-dependent-Hartree[1] (TDH) approximations, which was first applied to molecular dynamics in the early eighties[49]. In the scientific literature the terminology TDH and TDSCF is often used interchangeably. However, throughout this thesis we shall only use TDSCF for these approximations, and reserve "Hartree" for the exact method to be discussed in chapter 6 and 7. The original formulation of the TDSCF approximation only included a single configuration in the representation of the wave packet (see eq. (5.2) in the next section), and to avoid confusion with the other TDSCF approximation to be discussed in this chapter, we shall use the term single-configuration TDSCF or just SCTDSCF. As will be clarified in the next section, the formulation of dynamical problems in the framework of this SCTDSCF approximation suffered from serious limitations or inaccuracies due to a poor description of the correlation between the different degrees of freedom. Observing that the simple SCTDSCF approach was limited to systems with small correlation Kosloff, Ratner and coworkers [50] proposed a multi-dimensional extension (MCTDSCF), again strongly influenced by the analogous (MCSCF) approach in electronic structure calculations. This approximation has proven useful in many

---

[1] The term time-dependent-Hartree is used rather than time-dependent-Hartree-Fock (known from electronic structure theory), because generally there is no Pauli principle problems involved.

two-dimensional systems, however for three or higher-dimensional problems the exact solution is, in general, not included as the limiting case in the *ansatz* of the multi-configurational representation of the wave function. Using a variational principle, Meyer *et al.*[51] recently presented a special case of a MCTDSCF approximation, which by construction (as will be demonstrated soon), exactly has this desired limiting property. To avoid confusion with the original MCTDSCF approximation this scheme is called the multi-configuration time-dependent Hartree (MCTDH) method. The original formulation of this method is restricted to single surface systems, and the topic of this part of the thesis is the generalization and subsequent evaluation of the MCTDH method to non-adiabatic systems. In the course of deriving the extended MCTDH working equations a new compact notation is also introduced.

The outline of this second part of the thesis is as follows. In the next section we shall briefly discuss the single-configuration TDSCF approximation and its limitations. This is partly done to familiarize the reader with some of the notations and concepts used in the subsequent chapters. Section 5.2 presents a new multi-surface MCTDH scheme employing a non-orthogonal Gaussian basis-set. As will be clarified this scheme turns out to be numerically unstable, and thus this section primely serves as a prelude to the derivations of the generalized MCTDH scheme in chapter 6. In this chapter we also give a simple one-dimensional application, but the real evaluation of the derived MCTDH scheme follows in chapter 7 where it is applied to the two-dimensional two-surface system of H_2 on a copper surface. Finally chapter 8 concludes and briefly outlines the scheme for a three-dimensional application on O_3 where focus is especially given to a new compact basis-set.

5.1 Single-configuration TDSCF

In this section we shortly review the SCTDSCF approximation, first introduced in quantum dynamics by Gerber *et al.*[49] in 1982, and subsequently comment on its strong limitations. Thus, consider a general quantum system with the Hamiltonian

$$\widehat{\mathbf{H}}(x_1, x_2, \ldots, x_N) = \sum_{\kappa=1}^{N} \widehat{\mathbf{h}}_\kappa(x_\kappa) + W(x_1, x_2, \ldots, x_N) \tag{5.1}$$

where N denotes the total number of degrees of freedom. The central *ansatz* of the SCTDSCF approach is now to write the total wave function, $\Psi(x_1, x_2, \ldots, x_N)$, as the *single-configuration* direct product trial function

$$\Psi(x_1, x_2, \ldots, x_N, t) \equiv \phi_1(x_1, t)\phi_2(x_2, t) \cdots \phi_N(x_N, t) \tag{5.2}$$

where the *single particle* functions, $\{\phi_\kappa(x_\kappa, t),\ \kappa = 1, N\}$ are assumed to be normalized at all times t, *i.e.* $\langle\phi_\kappa(t)|\phi_\kappa(t)\rangle = 1$. To simplify the notation we introduce the multi-index $\overline{x} \equiv (x_1, x_2, \ldots, x_N)$ and the short hand bra-ket notation

$$|\Psi\rangle \equiv \prod_{\kappa=1}^{N} |\phi_\kappa\rangle \tag{5.3}$$

We also define the *single-hole* functions $\Psi_{\not\kappa}(x_1, \ldots, x_{\kappa-1}, x_{\kappa+1}, \ldots, x_N)$

$$|\Psi_{\not\kappa}\rangle = \prod_{\substack{\kappa'=1 \\ \kappa' \neq \kappa}}^{N} |\phi_{\kappa'}\rangle \tag{5.4}$$

such that $|\Psi\rangle = |\phi_\kappa\rangle|\Psi_{\not\kappa}\rangle$. Now, inserting the trial function, eq. (5.2), into the time-dependent Schrödinger equation,

$$i\hbar\frac{\partial}{\partial t}\Psi(\overline{x}, t) = \widehat{\mathbf{H}}(\overline{x})\Psi(\overline{x}, t) \tag{5.5}$$

and using dots as a short hand notation for time derivatives, we obtain

$$i\hbar|\dot{\phi}_\kappa\rangle|\Psi_{\not\kappa}\rangle + i\hbar|\phi_\kappa\rangle|\dot{\Psi}_{\not\kappa}\rangle = \left[|\Psi_{\not\kappa}\rangle\widehat{\mathbf{h}}_\kappa + \sum_{\kappa' \neq \kappa}\widehat{\mathbf{h}}_{\kappa'}|\Psi_{\not\kappa}\rangle + W|\Psi_{\not\kappa}\rangle\right]|\phi_\kappa\rangle \tag{5.6}$$

Next we multiply eq. (5.6) by the single-hole functions defined in eq. (5.4), and integrate over all the coordinates *except* x_κ, *i.e.* we multiply eq. (5.6) by $\langle\Psi_{\not\kappa}|$. This gives the following N one-dimensional equations

$$i\hbar|\dot{\phi}_\kappa\rangle = \left[\widehat{\mathbf{H}}_\kappa^{SCF} - i\hbar\langle\Psi_{\not\kappa}|\dot{\Psi}_{\not\kappa}\rangle + \sum_{\kappa' \neq \kappa}\langle\phi_{\kappa'}|\widehat{\mathbf{h}}_{\kappa'}|\phi_{\kappa'}\rangle\right]|\phi_\kappa\rangle \tag{5.7}$$

where we have defined the SCF-Hamiltonian

$$\widehat{\mathbf{H}}_\kappa^{SCF}(x_\kappa) \equiv \widehat{\mathbf{h}}_\kappa(x_\kappa) + W_\kappa^{SCF}(x_\kappa) \tag{5.8}$$

with the average potential or field

$$W_{\kappa}^{SCF}(x_{\kappa}) \equiv \langle \Psi_{\not\kappa} | W | \Psi_{\not\kappa} \rangle \tag{5.9}$$

From eq. (5.7) it should be evident that the new single-particle functions[2]

$$|\Phi_{\kappa}\rangle \equiv |\phi_{\kappa}\rangle \exp\left[\int dt \left(\langle \Psi_{\not\kappa} | \dot{\Psi}_{\not\kappa} \rangle + \frac{i}{\hbar} \sum_{\kappa' \neq \kappa} \langle \phi_{\kappa'} | \widehat{\mathbf{h}}_{\kappa'} | \phi_{\kappa'} \rangle \right)\right] \tag{5.10}$$

satisfy the one-dimensional time-dependent Schrödinger equation

$$\boxed{i\hbar \frac{\partial}{\partial t} |\Phi_{k}\rangle = \widehat{H}_{k}^{SCF} |\Phi_{k}\rangle \qquad (5.11)}$$

Assuming that $W(\overline{x})$, entering eq. (5.11) through eq. (5.9) and eq. (5.8), is separable in the different degrees of freedom[3], it should be clear from the derivations above, that in this approximate SCTDSCF scheme the size of the computational problem increases linearly rather than exponentially with the size of the system. However, the fact that $W(\overline{x})$ is not usually separable gives rise to serious limitations to the approximations represented by eq. (5.11), which in turn makes the SCTDSCF fail in several important situations. Few problems are truly separable, and although some indirect correlations are taken into account, the enforced factorization of the wave function in eq. (5.2) ignores the direct spatial correlations between the single-particle functions. Thus, loosely speaking, this simple SCTDSCF approach neglect, or strongly approximates, the correlations between the one-dimensional subsystems under discussion, and consequently fail when these correlations become important. Hence, the SCTDSCF approximation may significantly distort the dynamics in some systems.

To exemplify this breakdown of the SCTDSCF approximation let us consider a typical case where the one-dimensional adiabatic tunneling of a subsystem (denoted 1) occurs in the presence of a heat bath (*i.e.* thermal environment) represented by the subsystem denoted 2, see figure 5.1. For this system $\phi_1(x_1, t)$ (see eq. (5.2)) has two pronounced peaks centered around the two minima of the left potential energy curve in figure 5.1. However, according to eq. (5.11) the subsystem 2 responds to the average position of subsystem 1. Hence, if the state of subsystem 2 is highly

---

[2] The phase factor in eq. (5.10) is of no importance, and is usually dropped[49].

[3] In section 7.2 we will demonstrate how a general multi-dimensional potential energy function can be approximated as a sum of direct-product functions in the different degrees of freedom.

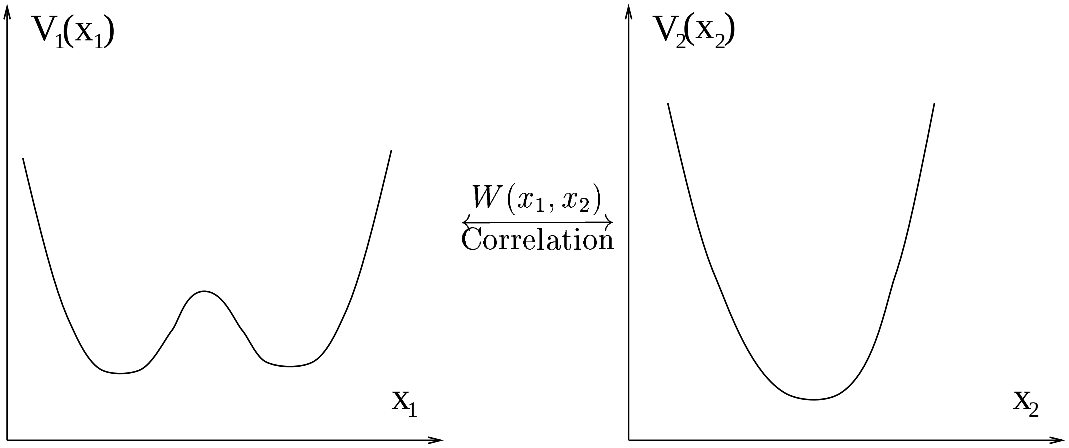

Figure 5.1: Illustration of a typical system for which the SCTDSCF approximation will often give very poor results. The adiabatic potential curves show an example where the tunneling of a system (1) occurs in the presence of a heat bath subsystem (2), represented by a localized oscillator. These potential energy functions enter respectively $\widehat{\mathbf{h}}_1(x_1)$ and $\widehat{\mathbf{h}}_2(x_2)$ in eq. (5.1).

sensitive to the position of subsystem 1, and the time scale associated with the tunneling motion of the latter is slow relative to that of the former, a description based on eq. (5.11) is not valid and will usually fail badly. Thus, the simple SCTDSCF approximation broadly speaking fails because the wave function of the system bifurcates or becomes delocalized, which is not at all unusual in reaction dynamics. For the example just discussed it therefore seems natural instead to represent the subsystem 1 by at least two functions centered around the two minima of the potential curve[4]. Also subsystem 2 can with advantage be represented by more functions, such that the left hand side of eq. (5.2) becomes a sum over several direct products of single-particle functions, or *configurations*, instead of just one. This generally lead to the multi-configuration TDSCF (MCTDSCF) approximations, first introduced to the field of quantum dynamics by Kosloff, Ratner, Miller and many other coworkers around 1987[50, 52]. However, the problem with this approach is that it does not in general have the exact solution as the limiting case as more and more configurations are included in the calculations. By employing a variational principle it is however possible to derive a special type of MCTDSCF scheme which by construction exactly has this desired limiting property. This so-called multi-configuration time-dependent Hartree (MCTDH) method will be the topic of the remaining of this part of the thesis.

---

[4] The left potential energy curve in figure 5.1 may be the lower adiabatic branch obtained by diagonalizing the corresponding two diabatic surfaces. Thus, in this case the two single-particle functions, used to represent subsystem 1, can conveniently be initiated as the diabatic eigenstates.

5.2 Gaussian MCTDH

In this section we are going to present a MCTDH scheme formulated in terms of a non-orthogonal basis-set of Gaussian wave functions. This, still unpublished work, is the result of a close collaboration with G. D. Billing. However, at present time, I have not been able to implement the scheme in a numerically stable form, and as such this project should be considered "work in progress". To some extent this numerical instability was not very surprising as will be discussed more in details below. Consequently, no reliable numerical results will be presented, which also explains for the relatively short discussion of this project. However, as it is formally based on some of the same ideas as the generalized MCTDH scheme, to be thoroughly discussed in the next chapters, this work serves as a good introduction. This is especially true for the variational principle employed in the explicit derivation of the equations of motion. Therefore, we will focus somewhat on the practical aspects of the derivations using the variational principle, which allow us to elaborate less on this particular step in the derivations to be presented in the subsequent chapter.

5.2.1 The numerical scheme

For the sake of simplicity, we shall consider the time propagation of a multi-surface system with only one degree of freedom, R. In a diabatic representation, discussed in section 3.1, the time-dependent Schrödinger equation read as

$$i\hbar\frac{\partial}{\partial t}\Psi_s(R,t) = (\widehat{\mathbf{T}} + V_s(R))\Psi_s(R,t) + \sum_{s'\neq s} W_{s,s'}\Psi_{s'}(R,t) \tag{5.12}$$

where $\widehat{\mathbf{T}} = -\frac{\hbar^2}{2\mu}\frac{\partial^2}{\partial R^2}$ is the usual kinetic energy operator, and the index s refers to the different electronic diabatic potential energy surfaces. For the different surface-functions, $\Psi_s(R,t)$, we introduce the following *multi-trajectory expansion*

$$\Psi_s(R,t) = \sum_{l=1}^{N_s} a_l^s(t)\Phi_l^s(R,t) \tag{5.13}$$

where

$$\Phi_l^s(R,t) \equiv \exp\left[\frac{i}{\hbar}\left\{A_l^s(t)(R-R_l^s(t))^2 + P_l^s(t)\left(R-R_l^s(t)\right) + \gamma_l^s(t)\right\}\right] \tag{5.14}$$

i.e. the surface-functions, $\Psi_s(R,t)$, are expressed in a basis of Gaussian wave packets centered around the trajectories $\{R_l^s(t),\ l = 1,\dots,N_s\}$. The application of Gaussian wave packets (GWP) in dynamical calculations has been pioneered mainly by Heller[53]. Thus, he originally introduced the notation in eq. (5.14) where $A_l^s(t)$ is a width parameter, $P_l^s(t)$ the momentum and $\gamma_l^s(t)$ a phase factor. To maintain the physical interpretation of eq. (5.14) as a semi-classical particle we are going to make two assumptions for the trajectories $\{R_l^s(t),\ l = 1,\dots,N_s\}$. First we assume that they are real and second that they are governed by classical Newtonian mechanics, *i.e.* $\dot{R}_l^s = P_l^s/\mu$. (It can easily be shown from the final equations of motion that this assumptions is strictly only satisfied for a single-term expansion in eq. (5.13)). Consequently the momentum associated to the trajectories, $\{P_l^s(t),\ l = 1,\dots,N_s\}$, are also real. To derive differential equations of motion for the remaining 4 parameters, $\{a_l^s, A_l^s, P_l^s, \gamma_l^s\}$, we apply the Dirac-Frenkel variational principle[54, 55], $\langle\delta\Psi|i\hbar\frac{\partial}{\partial t} - \widehat{\mathbf{H}}|\Psi\rangle = 0$, which in the multi-surface diabatic representation of eq. (5.12) takes the form

$$\langle\delta\Psi_s|(i\hbar\frac{\partial}{\partial t} - \widehat{\mathbf{H}}_s)\Psi_s - \sum_{s'\neq s} W_{s,s'}\Psi_{s'}\rangle = 0 \tag{5.15}$$

where respectively the bra and ket read as

$$\delta\Psi_s = \sum_{l=1}^{N_s}\left\{\frac{\partial\Psi_s}{\partial a_l^s}\delta a_l^s + \frac{\partial\Psi_s}{\partial A_l^s}\delta A_l^s + \frac{\partial\Psi_s}{\partial P_l^s}\delta P_l^s + \frac{\partial\Psi_s}{\partial\gamma_l^s}\delta\gamma_l^s\right\} \tag{5.16}$$

and

$$(i\hbar\frac{\partial}{\partial t} - \widehat{\mathbf{H}}_s)\Psi_s - \sum_{s'\neq s} W_{s,s'}\Psi_{s'} = i\hbar\dot{\Psi}_s - \left(\widehat{\mathbf{T}} + V_s\right)\Psi_s - \sum_{s'\neq s} W_{s,s'}\Psi_{s'} \tag{5.17a}$$

$$= i\hbar\sum_{l=1}^{N_s}\left(\dot{a}_l^s\Phi_l^s + a_l^s\dot{\Phi}_l^s\right) - \sum_{l=1}^{N_s} a_l^s\left(\widehat{\mathbf{T}} + V_s\right)\Phi_l^s - \sum_{s'\neq s}\sum_{l'=1}^{N_{s'}} a_{l'}^{s'} W_{ss'}\Phi_{l'}^{s'} \tag{5.17b}$$

In eq. (5.16), (5.17) and in the remaining of this section, we have, for the sake of simplicity, ignored the arguments R and t. The partial derivatives entering eq. (5.16) are easily obtained using the definitions in eq. (5.13) and (5.14)[5]

$$\frac{\partial \Psi_s}{\partial a_l^s} = \Phi_l^s \tag{5.18a}$$

$$\frac{\partial \Psi_s}{\partial \gamma_l^s} \propto a_l^s \Phi_l^s \tag{5.18b}$$

$$\frac{\partial \Psi_s}{\partial P_l^s} \propto a_l^s (R - R_l^s) \Phi_l^s \tag{5.18c}$$

$$\frac{\partial \Psi_s}{\partial A_l^s} \propto a_l^s (R - R_l^s)^2 \Phi_l^s \tag{5.18d}$$

To obtain auxiliary expressions for the two derivatives entering eq. (5.17b) we once more make use of eq. (5.14)

$$\dot{\Phi}_l^s = \frac{i}{\hbar} \left\{ \dot{A}_l^s (R - R_l^s)^2 + \left(\dot{P}_l^s - 2 A_l^s \dot{R}_l^s \right) (R - R_l^s) + \dot{\gamma}_l^s - P_l^s \dot{R}_l^s \right\} \Phi_l^s \tag{5.19a}$$

$$\widehat{\mathbf{T}} \Phi_l^s = \frac{1}{2\mu} \left\{ 4 A_l^{s2} (R - R_l^s)^2 + 4 A_l^s P_l^s (R - R_l^s) + P_l^{s2} - 2 i \hbar A_l^s \right\} \Phi_l^s \tag{5.19b}$$

According to the Dirac-Frenkel variational principle, eq. (5.15), we finally obtain the equations of motion for the variables $\alpha = \{a, A, P, \gamma\}$ by the stationary conditions

$$\langle \frac{\partial \Psi_s}{\partial \alpha_l^s} | (i\hbar \frac{\partial}{\partial t} - \widehat{\mathbf{H}}_s) \Psi_s - \sum_{s' \neq s} W_{s,s'} \Psi_{s'} \rangle = 0 \tag{5.20}$$

Thus, by successively substituting each of eq. (5.18) and eq. (5.17b) into eq. (5.20) we obtain (after some tedious but simple algebra) two sets of highly non-linear coupled differential matrix-equations. The first set (obtained from eq. (5.20) with $\alpha = a$) is the equation of motion for the expansion coefficients, $a_l^s(t)$ in eq. (5.13),

$$i\hbar \underline{\underline{S}}_s^{(00)} \cdot \dot{\underline{a}}_s = \underline{\underline{H}}_s \cdot \underline{a}_s + \sum_{s'} \underline{\underline{W}}_{ss'}^{(00)} \cdot \underline{a}_{s'} \tag{5.21}$$

where $\underline{a}_s$ denotes the column-vector of the expansion coefficients on surface s. This differential equation is coupled to the second set of equation of motion (obtained

---

[5] The proportionality signs in eq. (5.18b), (5.18c) and (5.18d) are due to the neglect of the prefactor $\frac{i}{\hbar}$ which can be ignored in eq. (5.20).

from eq. (5.20) with $\alpha = \{A, P, \gamma\}$) which describes the time-evolution of the Gaussian wave packet parameters entering the definition in eq. (5.14)

$$\begin{bmatrix} \underline{\underline{\mathrm{M}}}_s^{(00)} & \underline{\underline{\mathrm{M}}}_s^{(01)} & \underline{\underline{\mathrm{M}}}_s^{(02)} \\ \underline{\underline{\mathrm{M}}}_s^{(10)} & \underline{\underline{\mathrm{M}}}_s^{(11)} & \underline{\underline{\mathrm{M}}}_s^{(12)} \\ \underline{\underline{\mathrm{M}}}_s^{(20)} & \underline{\underline{\mathrm{M}}}_s^{(21)} & \underline{\underline{\mathrm{M}}}_s^{(22)} \end{bmatrix} \cdot \begin{bmatrix} \underline{\mathrm{X}}_s^{(0)} \\ \underline{\mathrm{X}}_s^{(1)} \\ \underline{\mathrm{X}}_s^{(2)} \end{bmatrix} = \begin{bmatrix} \underline{\mathrm{Y}}_s^{(0)} \\ \underline{\mathrm{Y}}_s^{(1)} \\ \underline{\mathrm{Y}}_s^{(2)} \end{bmatrix} \tag{5.22}$$

In these two sets of differential equations of motion we have defined the following matrices

$$\left[\underline{\underline{\mathrm{H}}}_s\right]_{kl} = \left[\underline{\underline{\mathrm{S}}}_s^{(00)}\right]_{kl}\left[\underline{\mathrm{X}}_s^{(0)}\right]_l + \left[\underline{\underline{\mathrm{S}}}_s^{(01)}\right]_{kl}\left[\underline{\mathrm{X}}_s^{(1)}\right]_l + \left[\underline{\underline{\mathrm{S}}}_s^{(02)}\right]_{kl}\left[\underline{\mathrm{X}}_s^{(2)}\right]_l + \left[\underline{\underline{\mathrm{V}}}_s^{(00)}\right]_{kl} \tag{5.23a}$$

$$\left[\underline{\underline{\mathrm{S}}}_s^{(pq)}\right]_{kl} \equiv \int_{-\infty}^{\infty} dR\, \{\Phi_k^{s*}(R - R_k^s)^p (R - R_l^s)^q \Phi_l^s\} \tag{5.23b}$$

$$\left[\underline{\underline{\mathrm{M}}}_s^{(pq)}\right]_{kl} \equiv a_k^{s*} a_l^s \int_{-\infty}^{\infty} dR\, \{\Phi_k^{s*}(R - R_k^s)^p (R - R_l^s)^q \Phi_l^s\} \tag{5.23c}$$

$$\left[\underline{\underline{\mathrm{V}}}_s^{(pq)}\right]_{kl} \equiv \int_{-\infty}^{\infty} dR\, \{\Phi_k^{s*}(R - R_k^s)^p V_s (R - R_l^s)^q \Phi_l^s\} \tag{5.23d}$$

$$\left[\underline{\underline{\mathrm{W}}}_{ss'}^{(pq)}\right]_{kl} \equiv \int_{-\infty}^{\infty} dR\, \left\{\Phi_k^{s*}(R - R_k^s)^p W_{ss'} (R - R_l^{s'})^q \Phi_l^{s'}\right\} \tag{5.23e}$$

$$\left[\underline{\mathrm{Y}}_s^{(p)}\right]_l \equiv a_l^{s*} \left\{ \sum_k \dot{a}_k^s \left[\underline{\underline{\mathrm{S}}}_s^{(p0)}\right]_{lk} - \sum_k a_k^s \left[\underline{\underline{\mathrm{V}}}_s^{(p0)}\right]_{lk} - \sum_{s'} \sum_{k'} a_{k'}^{s'} \left[\underline{\underline{\mathrm{W}}}_{s'}^{(p0)}\right]_{lk'} \right\} \tag{5.23f}$$

In the equations above we have furthermore introduced a new set of variables, $X^{(0)}$, $X^{(1)}$ and $X^{(2)}$ defined from the following convenient combinations of the three Gaussian parameters

$$\left[\underline{\mathrm{X}}_s^{(0)}\right]_l \equiv \dot{\gamma}_l^s - \dot{R}_l^s P_l^s - \frac{i\hbar A_l^s}{\mu} + \frac{P_l^{s\,2}}{2\mu} = \dot{\gamma}_l^s - \frac{i\hbar A_l^s}{\mu} + \frac{P_l^{s\,2}}{\mu} \tag{5.24a}$$

$$\left[\underline{\mathrm{X}}_s^{(1)}\right]_l \equiv \dot{P}_l^s - 2\dot{R}_l^s A_l^s + \frac{2A_l^s P_l^s}{\mu} = \dot{P}_l^s \tag{5.24b}$$

$$\left[\underline{\mathrm{X}}_s^{(2)}\right]_l \equiv \dot{A}_l^s + \frac{2A_l^{s\,2}}{\mu} \tag{5.24c}$$

Note that the second equality in eq. (5.24a) and (5.24b) follow from the assumption $\dot{R}_l^s = P_l^s/\mu$ mentioned, in the paragraph below eq. (5.14). Thus, instead for solving directly for the Gaussian parameters, $\{A_l^s, P_l^s, \gamma_l^s\}$, it turns out to be more convenient to introduce the new parameters listed in eq. (5.24). As an additional constraint to the working equations, eq. (5.21) and (5.22), we shall assume that the Gaussian wave packets, defined in eq. (5.14), remain normalized at all times. This is easily shown to give the following requirement for the relation between the imaginary components of the phase and width parameters

$$\mathrm{Im}[\gamma_l^s] = -\frac{\hbar}{4}\ln\left(\frac{2\,\mathrm{Im}[A_l^s]}{\pi\hbar}\right) \tag{5.25}$$

However, in the following we are going to give a somewhat different motivation for this normalization constraint. As mentioned before we assume that the center of the wave packets follow the classical equation of motion, $\dot{R}_l^s = P_l^s/\mu$, where R_l^s is a real function of time, classically known as a trajectory. Consequently $\underline{\mathrm{X}}_s^{(1)}$, defined in eq. (5.24b), is also a real function. However, so far no assumptions have been made for the two other parameters, $\underline{\mathrm{X}}_s^{(0)}$ and $\underline{\mathrm{X}}_s^{(2)}$, and hence in the present form eq. (5.22) is a *complex* matrix-equation. However, if we assume that they are also real, *i.e.* $\mathrm{Im}[\underline{\mathrm{X}}_s^{(0)}] = \mathrm{Im}[\underline{\mathrm{X}}_s^{(2)}] = \underline{0}$, it follows that

$$\left.\begin{array}{l}\mathrm{Im}[\dot{\gamma}_l^s] = \hbar\,\mathrm{Re}\,A_l^s/\mu \\ \mathrm{Im}[\dot{A}_l^s] = -4\,\mathrm{Re}\,A_l^s\,\mathrm{Im}[A_l^s]/\mu\end{array}\right\} \Rightarrow \mathrm{Im}[\dot{\gamma}_l^s] = -\frac{\hbar}{4}\frac{\mathrm{Im}[\dot{A}_l^s]}{\mathrm{Im}[A_l^s]} \tag{5.26}$$

which is exactly the time-derivative of eq. (5.25). Hence, if the Gaussian wave packets are initially normalized, and we assume that $\underline{\mathrm{X}}_s^{(p)}$, $p = 1, 2, 3$ are real column-vectors, it follows from the above analysis that the normalization of the wave packets is maintained as time evolves. This assumption on $\underline{\mathrm{X}}_s^{(p)}$, $p = 1, 2, 3$ significantly simplifies the matrix-equation eq. (5.22), since it splits it into a real and imaginary part. In the remaining of this section we will only focus on the real part of eq. (5.22), corresponding to redefining $\underline{\underline{\mathrm{M}}}_s^{(pq)}$ and $\underline{\mathrm{Y}}_s^{(p)}$ to the real parts of respectively eq. (5.23c) and eq. (5.23f).

At this point it is very important to note that even though the Gaussian basis functions are normalized, they are *not orthogonal*. This, as it turns out, is a very complicating feature of the presented scheme. We shall discuss this problem in more detail in the next subsection, but for now we just note that because the underlying basis-set in this scheme is not by construction orthogonal, the functions may become almost linearly dependent (*i.e.* overlap) as time evolves. Consequently there is no guarantee that the overlap-matrix, $\underline{\underline{\mathrm{S}}}_s^{(00)}$, defined in eq. (5.23b), is not singular, which in turn makes the solution (*i.e.* inversion) of eq. (5.21) numerically very difficult. In order to make it possible to explicitly monitor the numerical scheme for such singularities, we perform a similarity-transformation of eq. (5.21), corresponding a change of basis-set to a orthonormal representation. Thus, we recast eq. (5.21) into the simpler form

$$\boxed{i\hbar\dot{\underline{\mathrm{b}}}_s = \underline{\underline{\mathrm{H}}}'_s \cdot \underline{\mathrm{b}}_s + \sum_{s'} \underline{\underline{\mathrm{W}}}'^{(00)}_{ss'} \cdot \underline{\mathrm{b}}_{s'} \qquad (5.27)}$$

where the matrices, $\underline{\underline{\mathrm{H}}}'_s$ and $\underline{\underline{\mathrm{W}}}'^{(00)}_{ss'}$, and the new expansion coefficients, b^s_l, and its time-derivatives, are defined through the linear transformations

$$\underline{\underline{\mathrm{H}}}'_s \equiv \underline{\underline{\mathrm{D}}}^+_s \cdot \underline{\underline{\mathrm{H}}}_s \cdot \underline{\underline{\mathrm{D}}}_s \qquad \underline{\underline{\mathrm{W}}}'^{(00)}_{ss'} \equiv \underline{\underline{\mathrm{D}}}^+_s \cdot \underline{\underline{\mathrm{W}}}^{(00)}_{ss'} \cdot \underline{\underline{\mathrm{D}}}_{s'} \qquad (5.28a)$$

$$\underline{\mathrm{b}}_s \equiv \underline{\underline{\mathrm{D}}}_s^{-1} \cdot \underline{\mathrm{a}}_s \qquad \Longleftrightarrow \qquad \underline{\mathrm{a}}_s = \underline{\underline{\mathrm{D}}}_s \cdot \underline{\mathrm{b}}_s \qquad (5.28b)$$

$$\dot{\underline{\mathrm{b}}}_s \equiv \underline{\underline{\mathrm{D}}}_s^{-1} \cdot \dot{\underline{\mathrm{a}}}_s \qquad \Longleftrightarrow \qquad \dot{\underline{\mathrm{a}}}_s \equiv \underline{\underline{\mathrm{D}}}_s \cdot \dot{\underline{\mathrm{b}}}_s \qquad (5.28c)$$

The explicit definition of the transformation-matrix $\underline{\underline{\mathrm{D}}}_s$ read as

$$\underline{\underline{\mathrm{D}}}_s \equiv \underline{\underline{\mathrm{U}}}_s \cdot \underline{\underline{\Lambda}}_s^{-1/2} \qquad (5.29a)$$

$$\underline{\underline{\Lambda}}_s \equiv \underline{\underline{\mathrm{U}}}^+_s \cdot \underline{\underline{\mathrm{S}}}^{(00)}_s \underline{\underline{\mathrm{U}}}_s \qquad (5.29b)$$

where, according to eq. (5.29b), the unitary matrix $\underline{\underline{\mathrm{U}}}_s$ and the diagonal matrix $\underline{\underline{\Lambda}}_s$ correspond to respectively the normalized eigenvectors and eigenvalues of the overlap-matrix defined in eq. (5.23b). Clearly, if any of the diagonal elements of $\underline{\underline{\Lambda}}_s$ become zero (or even close to zero), the transformation-matrix $\underline{\underline{\mathrm{D}}}_s$ is singular which in turn means that eq. (5.27) is ill-conditioned. Thus, from a numerical point of view it is more convenient of solve eq. (5.27) than eq. (5.21) since we have a better feel for the nature of the instability. However, it is important to emphasize that we have still not overcome the problem of linear dependence of the underlying basis-set. Another advantage of eq. (5.27) is that we also get an easy measure of the convergence of the scheme. Using the definitions in eq. (5.28) and (5.29), and the hermitian property of $\underline{\underline{\mathrm{H}}}_s$ and $\underline{\underline{\mathrm{W}}}^{(00)}_{ss'}$, it is easily seen that by construction the $\underline{\mathrm{b}}_s$'s satisfy the norm-conservation

$$\frac{\partial}{\partial t} \sum_s \underline{\mathrm{b}}^+_s \cdot \underline{\mathrm{b}}_s = \sum_s \left\{ \dot{\underline{\mathrm{b}}}^+_s \cdot \underline{\mathrm{b}}_s + \underline{\mathrm{b}}^+_s \cdot \dot{\underline{\mathrm{b}}}_s \right\} = 0 \qquad (5.30)$$

Thus, if the calculation is initialized by a single Gaussian wave packet, eq. (5.30) implies that when solving eq. (5.27) for $\underline{\mathrm{b}}_s$ the following simple normalization should be satisfied at any time t

$$\sum_s \sum_{l=1}^{N_s} b^{s*}_l(t) b^s_l(t) = 1 \qquad (5.31)$$

However, as will be clarified in the next subsection, the largest numerical problems actually seemed to be associated to the other matrix equation,eq. (5.22), due the initial conditions of the system.

5.2.2 The numerical implementation

For the numerical implementation I chose the same system as will be studied in detail in section 6.2. Thus, the potential energy functions entering eq. (5.23d), (5.23e) and (5.23f) read as

$$\begin{aligned} V_1(R) &= V_0^1 \exp\left[-2(R - R_{cross})\right] && (5.32a)\\ V_2(R) &= V_0^2 \exp\left[-2(R - R_{cross})\right] + \Delta E && (5.32b)\\ W_{12}(R) &= W_{21}(R) = W_0 \exp\left[-\Delta W (R - R_{cross})^2\right] && (5.32c) \end{aligned}$$

where the values of the parameters are listed in table 6.1. With this convenient choice of the system, the resulting potential matrix-elements can be solved analytically.

The problem of inverting eq. (5.21) has already been discussed above, see text related to eq. (5.27). However, also the second matrix equation of motion, eq. (5.22), causes serious numerical problems, as it is initially singular due to the initial conditions on the expansion coefficients, $a_l^s(t)$, entering the definition in eq. (5.23c). The overall idea behind the Gaussian MCTDH scheme, just presented, is exactly that the system is initiated in a single Gaussian configuration, and then, as time evolves, more and more Gaussian configurations gets occupied. In this way we have a scheme where semi-classical particles, so to speak, are "generated" as needed when the system becomes less and less classical. Actually, it should be stressed that in the limit of an infinite number of Gaussian basis functions, the presented scheme is in principle exact. Thus, only one of the expansion coefficients, $a_l^s(t)$, are nonzero at $t = 0$, which in turn leads to a initially singular $\underline{\underline{\mathrm{M}}}_s^{(pq)}$ matrix in eq. (5.22).

At this point it is important to emphasize that the type of matrix singularity problems mentioned above, has been noted by several authors before, in the context of other time-dependent variational methods, *e.g.* [56–58]. Hence, it seems appropriate to give a more general characteristics of the nature of the underlying problem. In short these problems are caused by a form of over-completeness (*i.e.* linear dependence) of the set of parameters used to represent the overall system. In the present case these parameters are of course $\{a_l^s, A_l^s, P_l^s, \gamma_l^s\}$. The numerical difficulties can thus be traced to the presence of redundant parameters that, roughly speaking, simply duplicates the effect of others. However, the problem cannot be solved merely by reducing the number of parameters, since at different stages of the propagation a different number of parameters are required for an accurate representation of the wave function. Clearly, unless this problem can be solved, the number of parameters that can be included, and thus the accuracy of the variational method, is limited. This effect that the scheme is actually destabilized by increasing the number of parameters in the calculation was exactly observed in the present numerical implementation. With only a single Gaussian wave function in eq. (5.13) (corresponding to a true semi-classical calculation) the scheme was of course completely stable, which was naturally no surprise as the singularities in this case are absent. However, as soon as we included two functions the differential equations became ill-behaved, and as this number was increased we eventually started to get arbitrary results for the norm(*cf.* eq. (5.31)) and energy of the system.

In a paper by Kay[58], this problem of matrix singularities in time-dependent variational methods is exactly addresses. Based on simple linear algebraic arguments he proposes a selective inversion of the matrix equations where the singularity is supposedly handled by ignoring certain elements. However, I did not have much success with this scheme, and to see way we will briefly mention the scheme for the matrix inversion in eq. (5.22). The interested reader is referred to reference [58] for more details. According to Kay a stable inversion is obtained through the approximation

$$\underline{X} \approx \sum_j \beta_j^{-1} \underline{C}_j \cdot \underline{C}_j^+ \cdot \underline{Y} + \sum_r A_r \underline{C}_r \tag{5.33}$$

where $\underline{X}$ and $\underline{Y}$ collectively denote the two columns vectors in eq. (5.22), β_j is the j'th eigenvalue of the $\underline{\underline{M}}$ matrix with the corresponding eigenvector $\underline{C}_j$ and A_j is an *arbitrary* value. In eq. (5.33), the first sum extends over effectively nonzero eigenvalues, $\beta_j >$ cutoff, while the second sum extends over eigenvalues that are effectively zero, $\beta_j <$ cutoff. The problem with this scheme was that the results from the inversion turned out to be very sensitive and dependent on the cutoff value and the arbitrary coefficients A_j. So, all in all it appears that this approach does not solve all the problems with the Gaussian MCTDH scheme, and we conclude that fortunately there is more work to be done.

6
Generalized MCTDH

The quantum dynamical treatment of multidimensional problems is one of the major challenges in theoretical chemistry. As mentioned in the introduction to the previous chapter, the underlying problem is related to the fact that most methods scale with the dimension and the number of degrees of freedom, in an unfortunate fashion. For state-expansion methods it is typically as N^3 where N is the number of quantum states necessary for obtaining convergence. This number usually includes the energetically open states, as well as a good deal of closed ones. In order to reduce the number of states one can relax on the amount of information needed so as to obtain just total, *i.e.* state summed, reaction cross sections or total reaction rates[59–63]. Another avenue is to introduce an approximate description, using approximate wave functions as in the SCTDSCF or MCTDSCF just discussed in section 5.1, mixed quantum-classical methods[64–68] or reduced dimensionality calculations[69–72].

At present exact methods are restricted to treat 3-4 atomic systems and single surface problems. However, many chemical reactions, as those involving ions or open-shell systems, are inherently multi-surface problems. Even apparent single surface problems have due to the geometric phase effects[29–32] turned out to involve the effect of more than one electronic potential energy surface, even for neutral reactions. Considering this complexity, it is obvious that one in most cases has to introduce approximate descriptions where only part of the system is described using "exact" methods. We have already mentioned several of such approximate methods above. Other approaches, which introduces methods for rotational averaged cross-sections and approximate dynamics for part of the system, combined with exact dynamic for the reaction center, have been suggested recently[73].

However, one very interesting recent suggestion is connected to the MCTDH method [51, 74, 75] in which one can optimize the basis-set as a function of time and vary the number of basis-functions according to the coupling. Thus, the method has enough flexibility for dealing with the many different situations encountered in collision theory. In the limit of many basis-functions it is furthermore exact. However, whether it in this limit is more advantageous to use, than other exact methods involving e.g. grid or state-expansion is an open question. In this chapter the method is generalized to multi-surface problems and its performance on a simple model system is investigated.

This chapter, which is largely based on a publication[1] (see A.1 in part IV for the abstract), is organized as follows. In section 6.1 we derive the equations of motion for the generalized MCTDH scheme, using a compact notation. Section 6.2 then presents a numerical study of a simple model system. In subsection 6.2.1 the numerical scheme for the generalized MCTDH method is presented, and in subsection 6.2.2 a numerically exact solution of the non-adiabatic problem is outlined. The numerical results are then reported in subsection 6.2.3, and a comparison of the two methods is subsequently made. Finally section 6.3 concludes and sums up the most important features of the generalized MCTDH method, as compared to the direct method.

6.1 Equations of motion for the Generalized MCTDH scheme

In this section we will derive the nuclear equations of motion for a general non-adiabatic system treated in the MCTDH framework. The single-surface MCTDH scheme originates from Meyer and coworkers[51, 74, 75], and using this work as a starting-point we are able to derive a new set of extended multi-surface working equations. The MCTDH method has been used before to study non-adiabatic processes, like the photodissociation (*i.e.* half-collision) of CH_3I[76–80] and ICN[81], but the employed schemes, as we shall demonstrate, are not as general as the one to be presented in this chapter. The equations of motion are obtained by means of the Dirac-Frenkel variational principle[55], and in the derivations we go somewhat along the same lines as Meyer *et al.*, however with important differences. First of all the explicit derivations are given in more details, and with better motivations, and secondly we will adopt an improved notation. At the end of this section the numerical scheme is commented upon, and we especially emphasize some important differences compared to the original MCTDH scheme.

Let us consider a general system with the time-independent Hamiltonian

$$\widehat{\mathbf{H}}_{tot}(Q,X) = \widehat{\mathbf{T}}_Q + \widehat{\mathbf{T}}_X + V(Q,X) \equiv \widehat{\mathbf{T}}_Q + \widehat{\mathbf{H}}(Q,X) \tag{6.1}$$

where Q and X collectively denote respectively the nuclear and the electronic coordinates. The total wave function is next expressed as the direct product sum

$$\Psi(Q,X,t) = \sum_s \Theta^0_s(X)\Psi_s(Q,t) \tag{6.2}$$

where $\Theta^0_s(X)$ are the usual diabatic electronic states (see section 3.1) defined as eigenfunction of $\widehat{\mathbf{H}}$, introduced in eq. (6.1), with the nuclear reference configuration Q^0. To define the time-dependent nuclear wave functions, $\Psi_s(Q,t)$, we project the total time-dependent Schrödinger equation onto the diabatic electronic states. Thus, we insert the expansion, eq. (6.2), into the time-dependent Schrödinger equation with the Hamiltonian given by eq. (6.1), and multiply it by $\Theta^{0*}_s(X)$ followed by an integrating over all the electronic degrees of freedom. The resulting coupled equations read as

$$\begin{aligned} i\hbar\dot{\Psi}_s(Q,t) &= \left[\widehat{\mathbf{T}}_Q + \langle\Theta^0_s|\widehat{\mathbf{H}}|\Theta^0_s\rangle\right]\Psi_s(Q,t) + \sum_{s'\neq s}\langle\Theta^0_s|\widehat{\mathbf{H}}|\Theta^0_{s'}\rangle\Psi_{s'}(Q,t) \\ &\equiv \widehat{\mathbf{H}}^s\Psi_s(Q,t) + \sum_{s'\neq s} W_{s,s'}(Q)\Psi_{s'}(Q,t) \end{aligned} \tag{6.3}$$

where we have defined the effective nuclear Hamiltonian $\widehat{\mathbf{H}}^s$, on the electronically diabatic surface s, and the coupling elements $W_{s,s'}$, *cf.* eq. (3.10).

Now, let us assume that the system has N nuclear degrees of freedom, *i.e.* $Q \equiv (Q_1,\ldots,Q_N)$, and that $\widehat{\mathbf{H}}^s$, in eq. (6.3), can be separated into an uncorrelated part, given by $\widehat{\mathbf{h}}^s_\kappa$, and a residual correlated part $\widehat{\mathbf{H}}^s_{corr}$

$$\widehat{\mathbf{H}}^s(Q) = \sum_{\kappa=1}^{N} \widehat{\mathbf{h}}^s_\kappa(Q_\kappa) + \widehat{\mathbf{H}}^s_{corr}(Q) \tag{6.4}$$

The fundamental *ansatz* in the multi-configuration time-dependent Hartree scheme (like for the MCTDSCF) is to assume that the total wave function, on a given electronic surface s, can be expressed in the direct product-form[51]

$$\Psi_s(Q,t) = \sum_{j_1=1}^{M_1}\cdots\sum_{j_N=1}^{M_N} A^s_{j_1,\ldots,j_N}(t)\prod_{\kappa=1}^{N}\phi^s_{j_\kappa}(Q_\kappa,t) \equiv \sum_J A^s_J\Phi^s_J \tag{6.5}$$

where $A^s_{j_1,\ldots,j_N}(t)$ denote the expansion coefficients, and $\phi^s_{j_\kappa}(Q_\kappa,t)$ are the so-called *single particle* functions. The M_κ dimensions correspond to the number of configurations included in the expansion of Ψ_s for the different nuclear degrees of freedom,

Q_κ. To simplify the notation considerably we have also in eq. (6.5) introduced the multi-index $J = \{j_1, j_2, \ldots, j_N\}$ and the many-particle *configuration* functions

$$\Phi_J^s \equiv \prod_{\kappa=1}^{N} \phi_{j_\kappa}^s(Q_\kappa, t) \tag{6.6}$$

It is important to note that *both* the expansion coefficients and the single particle functions are time-dependent. To remove this redundancy from eq. (6.5) the following constraints are put on the single particle functions

$$i\hbar\langle\phi_{i_\kappa}^s(t)|\dot{\phi}_{j_\kappa}^s(t)\rangle = \langle\phi_{i_\kappa}^s(t)|\widehat{\mathbf{h}}_\kappa^s|\phi_{j_\kappa}^s(t)\rangle \tag{6.7}$$

where $\widehat{\mathbf{h}}_\kappa^s$ is defined in eq. (6.4). By expanding the time derivative of $\langle\phi_{i_\kappa}^s(t)|\phi_{j_\kappa}^s(t)\rangle$ and using the fact that $\widehat{\mathbf{h}}_\kappa^s$ is Hermitian, it can easily be shown that eq. (6.7) implies that the single particle functions have a constant norm. Hence, if we further assume that the single particle functions are initially normalized, the following normalization applies at *all times*

$$\langle\phi_{i_\kappa}^s(t)|\phi_{j_\kappa}^s(t)\rangle = \delta_{i_\kappa, j_\kappa} \tag{6.8}$$

which, from the definition in eq. (6.6), is readily shown to give the following normalization constraint on the configuration functions

$$\langle\Phi_I^s|\Phi_J^s\rangle = \delta_{I,J} \tag{6.9}$$

The equations of motion for the expansion coefficients, $A_J^s(t)$, and the single particle functions, $\phi_{j_\kappa}^s(Q_\kappa, t)$, are derived from the Dirac-Frenkel variational principle[55], which was already introduced in subsection 5.2.1. Just as then we now take the diabatic viewpoint in which the Dirac-Frenkel variational principle has the from

$$\langle\delta\Psi_s|(i\hbar\frac{\partial}{\partial t} - \widehat{\mathbf{H}}^s)\Psi_s - \sum_{s'\neq s} W_{s,s'}\Psi_{s'}\rangle = 0 \tag{6.10}$$

From the fundamental multi-configuration expansion of eq. (6.5) it immediately follows that the variation of the total single-surface function, Ψ_s, can be expressed as[1]

$$\delta\Psi_s = \sum_J \frac{\partial\Psi_s}{\partial A_J^s}\delta A_J^s + \sum_{j_\kappa} \frac{\partial\Psi_s}{\partial\phi_{j_\kappa}^s}\delta\phi_{j_\kappa}^s \tag{6.11}$$

---

[1] Note that the first sum in eq. (6.11) is over a multi-index, $J = \{j_1, j_2, \ldots, j_N\}$, whereas the last sum is actually a double summation since $\sum_{j_\kappa} \equiv \sum_{\kappa=1}^{N}\sum_{j_\kappa=1}^{M_\kappa}$.

Next we substitute eq. (6.11) into eq. (6.10) and make use of the fact that the Dirac-Frenkel variational principle assumes stationary conditions with respect to all of the involved parameters (*i.e.* for all of the variations δA^s_J and $\delta\phi^s_{j_\kappa}$). This result in the following two important conditions on the single-surface wave functions

$$\langle \frac{\partial \Psi_s}{\partial A^s_J} | (i\hbar \frac{\partial}{\partial t} - \widehat{\mathbf{H}}_s)\Psi_s - \sum_{s' \neq s} W_{s,s'}\Psi_{s'} \rangle = 0, \qquad \text{for all } J \qquad (6.12a)$$

$$\langle \frac{\partial \Psi_s}{\partial \phi^s_{j_\kappa}} | (i\hbar \frac{\partial}{\partial t} - \widehat{\mathbf{H}}_s)\Psi_s - \sum_{s' \neq s} W_{s,s'}\Psi_{s'} \rangle = 0, \qquad \text{for all } j_\kappa \qquad (6.12b)$$

which in turn form the very starting point for the derivations of the working equations for the generalized MCTDH scheme. However, before we proceed, we will introduce a useful notation that will help us simplify these derivations considerably.

Consider first the so-called *single-hole* functions[74]

$$\begin{aligned} \Psi^s_{i_\kappa}(Q_{\{\not\kappa\}}, t) &= \sum_{j_1=1}^{M_1} \cdots \sum_{j_{\kappa-1}=1}^{M_{\kappa-1}} \sum_{j_{\kappa+1}=1}^{M_{\kappa+1}} \cdots \sum_{j_N=1}^{M_N} A^s_{j_1,\ldots,j_{\kappa-1},i_\kappa,j_{\kappa+1},\ldots,j_N}(t) \\ &\quad \times \prod_{\substack{\kappa'=1 \\ \kappa' \neq \kappa}}^{N} \phi^s_{j_{\kappa'}}(Q_{\kappa'}, t) \equiv \sum_{J\{\not\kappa\}} A^s_{i_\kappa, J\{\not\kappa\}} \Phi^s_{J\{\not\kappa\}} \end{aligned} \qquad (6.13)$$

where we have introduced the new multi-index $J\{\not\kappa\} \equiv \{j_1, \ldots, j_{\kappa-1}, j_{\kappa+1}, \ldots, j_N\}$. Thus, throughout the rest of this chapter the $\{\not\kappa\}$-single-hole-index collectively denotes all the nuclear degrees of freedom *except* Q_κ. Using this new notation, we can derive a set of important auxiliary relations which will make the subsequent derivation of the generalized equations of motion for the single-particle functions much easier. We first note that Ψ_s can be expressed as

$$\Psi_s = \sum_{j_\kappa} \Psi^s_{j_\kappa} \phi^s_{j_\kappa} = \sum_{j_\kappa} \sum_{J\{\not\kappa\}} A^s_{j_\kappa, J\{\not\kappa\}} \Phi^s_{J\{\not\kappa\}} \phi^s_{j_\kappa} \qquad (6.14)$$

Using the definition in eq. (6.6) it immediately follows that

$$\begin{aligned} \Phi^s_J &= \phi^s_{j_\kappa} \Phi^s_{J\{\not\kappa\}} & (6.15a) \\ \dot{\Phi}^s_J &= \sum_{\kappa} \dot{\phi}^s_{j_\kappa} \Phi^s_{J\{\not\kappa\}} & (6.15b) \end{aligned}$$

These relations can be used to show the constraint for the configuration functions, corresponding to eq. (6.7),

$$\begin{aligned} i\hbar\langle\Phi^s_I|\dot{\Phi}^s_J\rangle &= i\hbar\sum_\kappa\langle\Phi^s_{I\{\not\kappa\}}|\Phi^s_{J\{\not\kappa\}}\rangle\langle\phi^s_{i_\kappa}|\dot{\phi}^s_{j_\kappa}\rangle && \text{(6.16a)} \\ &= \sum_\kappa\langle\Phi^s_{I\{\not\kappa\}}|\Phi^s_{J\{\not\kappa\}}\rangle\langle\phi^s_{i_\kappa}|\widehat{\mathbf{h}}^s_\kappa|\phi^s_{j_\kappa}\rangle && \text{(6.16b)} \\ &= \langle\Phi^s_I|\sum_\kappa\widehat{\mathbf{h}}^s_\kappa|\Phi^s_J\rangle && \text{(6.16c)} \end{aligned}$$

Next we note that equivalent relations exist for the single-hole configuration functions,

$$\begin{aligned} \langle\Phi^s_{I\{\not\kappa\}}|\Phi^s_{J\{\not\kappa\}}\rangle &= \delta_{I\{\not\kappa\},J\{\not\kappa\}} && \text{(6.17a)} \\ i\hbar\langle\Phi^s_{I\{\not\kappa\}}|\dot{\Phi}^s_{J\{\not\kappa\}}\rangle &= \langle\Phi^s_{I\{\not\kappa\}}|\sum_{\kappa'\neq\kappa}\widehat{\mathbf{h}}^s_{\kappa'}|\Phi^s_{J\{\not\kappa\}}\rangle && \text{(6.17b)} \end{aligned}$$

Now let us return to the problem of deriving the equations of motion for the generalized MCTDH scheme, using the Dirac-Frenkel variational conditions in eq. (6.12). From eq. (6.5) and eq. (6.14) it immediately follows that the partial derivatives in the bra-notations, entering eq. (6.12), can be expressed as respectively

$$\begin{aligned} \frac{\partial\Psi_s}{\partial A^s_J} &= \Phi^s_J && \text{(6.18a)} \\ \frac{\partial\Psi_s}{\partial\phi^s_{j_\kappa}} &= \Psi^s_{i_\kappa} && \text{(6.18b)} \end{aligned}$$

To derive the equations of motion for the expansion coefficients, A^s_J, we simply substitute eq. (6.18a) into eq. (6.12a)[2] and make use of eq. (6.3), (6.4), (6.5) and (6.9). The result is

$$\begin{aligned} i\hbar\dot{A}^s_J &= \langle\Phi^s_J|\left\{\widehat{\mathbf{H}}^s_{corr}|\Psi_s\rangle + \sum_{s'\neq s}W_{s,s'}|\Psi_{s'}\rangle\right\} && \text{(6.19a)} \\ &= \sum_I A^s_I\langle\Phi^s_J|\widehat{\mathbf{H}}^s_{corr}|\Phi^s_I\rangle + \sum_{s'\neq s}\sum_I A^{s'}_I\langle\Phi^s_J|W_{s,s'}|\Phi^{s'}_I\rangle && \text{(6.19b)} \end{aligned}$$

---

[2] Note that this corresponds to multiplying eq. (6.3) by ${\Phi^s_J}^*$, followed by an integration over *all* the nuclear coordinates, Q.

We will comment on this equation later when we have derived the last set of equations which together with eq. (6.19b) make up the working equations for the presented generalized MCTDH scheme.

We are now finally ready to begin the derivations of the equation of motion for the single-particle functions. Contrary to those of the expansion coefficients, A^s_J (*cf.* eq. (6.19b)) the derivations to be presented below involve a lot of tedious algebraic manipulations. However, as the resulting equations have never been presented in the literature before, we found it appropriate to include some of the details of the explicit derivation. Thus, if the reader, for some reason, is not interested in these details, he or she is encouraged to move on to eq. (6.25).

As a prelude, we make use of eq. (6.4), (6.5) and (6.14) to rewrite eq. (6.3) as

$$\begin{aligned} i\hbar\dot{\Psi}_s &= i\hbar\sum_J \dot{A}^s_J \Phi^s_J + i\hbar\sum_{j_\kappa}\left\{\Psi^s_{j_\kappa}\dot{\phi}^s_{j_\kappa} + \sum_{J\{\cancel{\kappa}\}} A_{j_\kappa,J\{\cancel{\kappa}\}}\dot{\Phi}^s_{J\{\cancel{\kappa}\}}\phi^s_{j_\kappa}\right\} \\ &= \sum_{j_\kappa}\left\{\Psi^s_{j_\kappa}\widehat{\mathbf{h}}^s_\kappa + \sum_{J\{\cancel{\kappa}\}} A^s_{j_\kappa,J\{\cancel{\kappa}\}}\Big(\sum_{\kappa'\neq\kappa}\widehat{\mathbf{h}}^s_{\kappa'}\Big)\Phi^s_{J\{\cancel{\kappa}\}}\right\}\phi^s_{j_\kappa} \\ &\quad + \widehat{\mathbf{H}}^s_{corr}\Psi_s + \sum_{s'\neq s} W_{s,s'}\Psi_{s'} \end{aligned} \tag{6.20}$$

To explicitly derive the equations of motion for the single-particle functions, $\phi^s_{j_\kappa}$, we substitute eq. (6.18b) and (6.20) into the Dirac-Frenkel variational condition of eq. (6.12b) [3]. This gives

$$\begin{aligned} & i\hbar\sum_{j_\kappa}\left\{\langle\Psi^s_{i_\kappa}|\Psi^s_{j_\kappa}\rangle\dot{\phi}^s_{j_\kappa} + \sum_{I\{\cancel{\kappa}\},J\{\cancel{\kappa}\}} A^s_{i_\kappa,I\{\cancel{\kappa}\}}A^s_{j_\kappa,J\{\cancel{\kappa}\}}\langle\Phi^s_{I\{\cancel{\kappa}\}}|\dot{\Phi}^s_{J\{\cancel{\kappa}\}}\rangle\phi^s_{j_\kappa}\right\} \\ &= \sum_{j_\kappa}\left\{\langle\Psi^s_{i_\kappa}|\Psi^s_{j_\kappa}\rangle\widehat{\mathbf{h}}^s_\kappa + \sum_{I\{\cancel{\kappa}\},J\{\cancel{\kappa}\}} A^s_{i_\kappa,I\{\cancel{\kappa}\}}A^s_{j_\kappa,J\{\cancel{\kappa}\}}\langle\Phi^s_{I\{\cancel{\kappa}\}}|\sum_{\kappa'\neq\kappa}\widehat{\mathbf{h}}^s_{\kappa'}|\Phi^s_{J\{\cancel{\kappa}\}}\rangle\right\}\phi_{j^s_\kappa} \\ &\quad + \langle\Psi^s_{i_\kappa}|\left\{\widehat{\mathbf{H}}^s_{corr}|\Psi_s\rangle + \sum_{s'\neq s} W_{s,s'}|\Psi_{s'}\rangle\right\} - i\hbar\sum_J \dot{A}^s_J\langle\Psi^s_{i_\kappa}|\Phi^s_J\rangle \end{aligned} \tag{6.21}$$

---

[3] This corresponds to projecting eq. (6.20) onto the single-hole functions $\langle\Psi^s_{i_\kappa}|$ or equally multiplying eq. (6.20) by eq. (6.13) followed by an integration over all the nuclear coordinates *except* Q_κ.

Next we substitute $\dot{A}_J^s$ in the last term of eq. (6.21) by eq. (6.19a) and make use of eq. (6.17) to reduce it. The result read as

$$\begin{aligned}
i\hbar \sum_{j_\kappa} \langle \Psi^s_{i_\kappa} | \Psi^s_{j_\kappa} \rangle \dot{\phi}^s_{j_\kappa} &= \sum_{j_\kappa} \langle \Psi^s_{i_\kappa} | \Psi^s_{j_\kappa} \rangle \widehat{\mathbf{h}}^s_\kappa \phi^s_{j_\kappa} + \langle \Psi^s_{i_\kappa} | \left\{ \widehat{\mathbf{H}}^s_{corr} | \Psi_s \rangle + \sum_{s' \neq s} W_{s,s'} | \Psi_{s'} \rangle \right\} \\
&\quad - \left\{ \sum_J \langle \Psi^s_{i_\kappa} | \Phi^s_J \rangle \langle \Phi^s_J | \right\} \left\{ \widehat{\mathbf{H}}^s_{corr} | \Psi_s \rangle + \sum_{s' \neq s} W_{s,s'} | \Psi_{s'} \rangle \right\} \qquad (6.22) \\
&\equiv \sum_{j_\kappa} \langle \Psi^s_{i_\kappa} | \Psi^s_{j_\kappa} \rangle \widehat{\mathbf{h}}^s_\kappa \phi^s_{j_\kappa} + \left\{ \langle \Psi^s_{i_\kappa} | - \widehat{\mathbf{O}}^s_{i_\kappa} \right\} \left\{ \widehat{\mathbf{H}}^s_{corr} | \Psi_s \rangle + \sum_{s' \neq s} W_{s,s'} | \Psi_{s'} \rangle \right\}
\end{aligned}$$

where we have defined $\widehat{\mathbf{O}}^s_{i_\kappa} \equiv \sum_J \langle \Psi^s_{i_\kappa} | \Phi^s_J \rangle \langle \Phi^s_J |$. Using eq. (6.5), (6.13) and (6.17), $\widehat{\mathbf{O}}^s_{i_\kappa}$ can next be simplified to:

$$\begin{aligned}
\widehat{\mathbf{O}}_{i_\kappa} &\equiv \sum_{j_\kappa} \sum_{J\{\cancel{\kappa}\}} \sum_{I\{\cancel{\kappa}\}} A^s_{i_\kappa, I\{\cancel{\kappa}\}} \langle \Phi^s_{I\{\cancel{\kappa}\}} | \Phi^s_{J\{\cancel{\kappa}\}} \rangle | \phi^s_{j_\kappa} \rangle \langle \phi^s_{j_\kappa} | \langle \Phi^s_{J\{\cancel{\kappa}\}} | \\
&= \left\{ \sum_{j_\kappa} | \phi^s_{j_\kappa} \rangle \langle \phi^s_{j_\kappa} | \right\} \left\{ \sum_{J\{\cancel{\kappa}\}} A^s_{i_\kappa, J\{\cancel{\kappa}\}} | \Phi^s_{J\{\cancel{\kappa}\}} \rangle \right\} \\
&= \left\{ \sum_{j_\kappa} | \phi^s_{j_\kappa} \rangle \langle \phi^s_{j_\kappa} | \right\} \langle \Psi^s_{i_\kappa} | \equiv \widehat{\mathbf{P}}^s_\kappa \langle \Psi^s_{i_\kappa} | = \langle \Psi^s_{i_\kappa} | \widehat{\mathbf{P}}^s_\kappa \qquad (6.23)
\end{aligned}$$

where $\widehat{\mathbf{P}}^s_\kappa \equiv \sum_{j_\kappa} | \phi^s_{j_\kappa} \rangle \langle \phi^s_{j_\kappa} |$ is the time-dependent projection operator onto the space spanned by the single-particle functions in the coordinate Q_κ on the electronic surface s. The last commutation relation in eq. (6.23) follow directly from the definition of the single-hole functions. If we finally back-substitute eq. (6.23) into eq. (6.22) we obtain the following equation of motion for the single-particle functions.

$$\begin{aligned}
i\hbar \sum_{j_\kappa} \langle \Psi^s_{i_\kappa} | \Psi^s_{j_\kappa} \rangle \dot{\phi}^s_{j_\kappa} &= \sum_{j_\kappa} \langle \Psi^s_{i_\kappa} | \Psi^s_{j_\kappa} \rangle \widehat{\mathbf{h}}^s_\kappa \phi^s_{j_\kappa} + \left\{ 1 - \widehat{\mathbf{P}}^s_\kappa \right\} \\
&\quad \times \sum_{j_\kappa} \left\{ \langle \Psi^s_{i_\kappa} | \widehat{\mathbf{H}}^s_{corr} | \Psi^s_{j_\kappa} \rangle \phi^s_{j_\kappa} + \sum_{s' \neq s} \langle \Psi^s_{i_\kappa} | W_{s,s'} | \Psi^{s'}_{j_\kappa} \rangle \phi^{s'}_{j_\kappa} \right\} \qquad (6.24)
\end{aligned}$$

This equation is readily inverted to give the final equations of motion for the single-particle functions,

$$i\hbar\dot{\underline{\phi}}^{s}_{\kappa} = \widehat{\mathbf{h}}^{s}_{\kappa}\underline{\phi}^{s}_{\kappa} + \langle\underline{\underline{1_{\mathrm{s}}}}\rangle^{-1}_{\{\not\kappa\}}\left(1-\widehat{\mathbf{P}}^{s}_{\kappa}\right)\left(\langle\underline{\underline{\widehat{\mathbf{H}}^{\mathrm{s}}_{\mathrm{corr}}}}\rangle_{\{\not\kappa\}}\underline{\phi}^{s}_{\kappa} + \sum_{s'\neq s}\langle\underline{\underline{\mathrm{W}_{\mathrm{s,s'}}}}\rangle_{\{\not\kappa\}}\underline{\phi}^{s'}_{\kappa}\right) \tag{6.25}$$

where we have adopted a vector/matrix notation with $\underline{\phi}^{s}_{\kappa} \equiv [\phi^{s}_{1_\kappa}, \phi^{s}_{2_\kappa}, \ldots, \phi^{s}_{M_\kappa}]^{\mathrm{T}}$. Along the same lines as Meyer *et al.*[51, 74] we have furthermore introduced the time-dependent mean-field *operators*,

$$\left[\langle\underline{\underline{\widehat{\mathbf{H}}^{\mathrm{s}}_{\mathrm{corr}}}}\rangle_{\{\not\kappa\}}\right]_{i_\kappa,j_\kappa} \equiv \langle\Psi^{s}_{i_\kappa}|\widehat{\mathbf{H}}^{s}_{corr}|\Psi^{s}_{j_\kappa}\rangle \tag{6.26a}$$

$$\left[\langle\underline{\underline{\mathrm{W}_{\mathrm{s,s'}}}}\rangle_{\{\not\kappa\}}\right]_{i_\kappa,j_\kappa} \equiv \langle\Psi^{s}_{i_\kappa}|W_{s,s'}|\Psi^{s'}_{j_\kappa}\rangle \tag{6.26b}$$

$$\left[\langle\underline{\underline{1_{\mathrm{s}}}}\rangle_{\{\not\kappa\}}\right]_{i_\kappa,j_\kappa} \equiv \langle\Psi^{s}_{i_\kappa}|\Psi^{s}_{j_\kappa}\rangle = \sum_{I\{\not\kappa\}} A^{s*}_{i_\kappa,I\{\not\kappa\}}A^{s}_{j_\kappa,I\{\not\kappa\}} \tag{6.26c}$$

where the bra-ket notation is to be understood as an integration over all the degrees of freedom *except* Q_κ. Note especially the simple expression for the unit mean-field "operator", eq. (6.26c), due to the orthonormality of the single-hole configuration functions, eq. (6.17a). The diagonal element $[\langle\underline{\underline{1_{\mathrm{s}}}}\rangle_{\{\not\kappa\}}]_{i_\kappa,i_\kappa}$ display the population of the single-particle function ϕ_{i_κ}, and thus it is denoted the *density matrix*.

Eq. (6.19b) and eq. (6.25) make up the total working equations for the presented generalized MCTDH scheme. In the equation of motion for the A^{s}_{J}-coefficients, eq. (6.19b), only the correlation part of the Hamiltonian and the non-adiabatic coupling terms enter. $\widehat{\mathbf{H}}^{s}_{corr}$ describes the correlation among the different configurations on a single electronic surface, and $W_{s,s'}$ contains the non-adiabatic coupling terms which are responsible for the transitions from one diabatic potential surface to another. Eq. (6.25) further contains the single-particle Hamiltonians, $\widehat{\mathbf{h}}^{s}_{\kappa}$, that propagates the single-particle functions into the same Hilbert space as time evolves. The $(1-\widehat{\mathbf{P}}^{s}_{\kappa})$ operator in front of the second term of eq. (6.25) assures that the correction to the single-particle functions, due to correlation and non-adiabatic coupling, is added from the Hilbert space which is *orthogonal* to this space. It should also be emphasized that in the MCTDH scheme the non-correlated single-particle Hamiltonians, first introduced in eq. (6.4), are chosen somewhat arbitrarily. This adds a very important technical degree of freedom to the scheme, corresponding to a "restricted freedom" when choosing the initial single-particle functions. Thus, in general the single-particle functions do not have any physical significance, and consequently single-particle properties can not directly be calculated. However, by diagonalizing the density matrix, defined in eq. (6.26c), one can uniquely define a set of single-particle functions. These, so-called natural single-particle functions, have physical significance and can, as we will demonstrate in the next chapter, be used to evaluate the overall convergence with respect to a given number of single-particle functions employed in the scheme. This approach actually resembles the construction of natural orbitals in electronic structure theory.

Next we note that if we especially choose $\widehat{\mathbf{h}}^s_\kappa = 0$ and employ a large enough basis-set, *i.e.* $\widehat{\mathbf{P}}^s_\kappa \equiv \sum_{j_\kappa} |\phi^s_{j_\kappa}\rangle\langle\phi^s_{j_\kappa}| = 1$, the single-particle functions become time-independent, while eq. (6.19b) stays unchanged (except that now $\widehat{\mathbf{H}}^s_{corr} = \widehat{\mathbf{H}}^s$). This is precisely the equations of motion for the numerically exact solution of the non-adiabatic problem using a conventional time-independent state-expansion. Thus, we make the very important observation that the given generalized MCTDH scheme includes the exact solution as a limited case.

Now, we comment on the multi-dimensional integrals entering eq. (6.19b) and eq. (6.25) as respectively the time-dependent mean-field operators and matrix elements over $\widehat{\mathbf{H}}^s_{corr}$ and $W_{s,s'}$. As discussed in section 2.2, the normal procedure for evaluating multi-dimensional integrals of these types would be as follows: First one defines a set of orthonormal ad hoc basis-sets in each of the nuclear degrees of freedom (*e.g.* particle in a box basis-sets). These basis functions define an ad hoc discrete variable representations (DVR) in each dimension in the usual way. However, since they are chosen somewhat arbitrarily they do not reflect the physics of the system. In other words we would like to construct a set of DVR grids, in each dimension, that reflects the topology of the involved potential energy surfaces, such that the grids are dense in regions where the de Broglie wavelength is small and more sparse elsewhere. For a simple single-surface problem, as considered by Meyer and coworkers[51, 74, 75], one would normally employ the optimizing scheme[82] based on the HEG method[26] discussed in detail in subsection 2.2.6. To repeat, in this scheme one first constructs sets of eigenfunctions of zero-order Hamiltonians, which in this case would be the single-particle operators. Each of these basis-sets, expressed in the ad hoc basis, are then truncated according to the collision energy. The resulting compact basis-sets are then used to construct new "physically meaningful" DVR basis-sets by diagonalizing the position operator. The eigenfunctions define sets of compact DVR basis-sets where the corresponding eigenvalues are the optimized grid points. This is a very powerful scheme for constructing optimized compact DVR basis-sets in single-surface problems, and in the next part of this thesis we shall use it extensively. However, in the present context, the single-particle operators, $\widehat{\mathbf{h}}^s_\kappa$, defined in the generalized MCTDH scheme, refer to different potential energy surfaces, and therefore a naive application of the HEG scheme would result in many different DVR grids in each coordinate. Consequently, the non-adiabatic coupling elements, entering eq. (6.19b) and eq. (6.25), could not be handled numerically within the same DVR-scheme. Thus, it is not clear how one should construct a *unique* optimized DVR scheme in each of the nuclear degrees of freedom. All this is of course not an artifact of the generalized MCTDH scheme itself, but simply a consequence of the complexity of multi-surface systems. However, it means that a great computational/numerical advantage of the MCTDH scheme has been lost in the course of generalizing it to non-adiabatic systems.

Finally we comment of the previous schemes used in the literature to study non-adiabatic processes in the framework of the MCTDH method [76–81]. In the work presented in reference [76–78] the same single-particle functions are used for all the electronic states, whereas we use a separate set for each of the surfaces (hence the index s on $\phi^{s}_{j_\kappa}(Q_\kappa, t)$). Thus, they simply use one of the coordinates, Q_κ in eq. (6.5), as a grid-less coordinate for the electronic state. Fang *et al.*[79–81] derive an non-adiabatic scheme for explicitly a two-surface two-dimensional system, which as we will show in the next chapter actually corresponds to the special case of $\widehat{\mathbf{h}}_\kappa \equiv 0$ in our general multi-surface multi-dimensional scheme. Thus, the scheme of Fang *et al.* is not just a special case of our general scheme, it is actually also less effective as it does not correspond to an interaction representation, where a zero-order Hamiltonian is defined in each degree of freedom.

6.2 Numerical calculations on a model system

In this section we present a numerical study of a simple non-adiabatic model system conducted in the framework of the generalized MCTDH approach presented in the previous section. The results are subsequently compared to numerically exact calculations employing a Split-operator propagation scheme. Finally convergence and consumed CPU-time for the two schemes are compared.

The system of choice is a simple one-dimensional two-surface model that can easily be solved numerically exact. The coupled nuclear equations, eq. (6.3), read as

$$i\hbar \begin{bmatrix} \dot{\Psi}_1(x,t) \\ \dot{\Psi}_2(x,t) \end{bmatrix} = \begin{bmatrix} \widehat{\mathbf{T}} + V_1(x) & W(x) \\ W(x) & \widehat{\mathbf{T}} + V_2(x) \end{bmatrix} \cdot \begin{bmatrix} \Psi_1(x,t) \\ \Psi_2(x,t) \end{bmatrix} \tag{6.27}$$

where $\widehat{\mathbf{T}} = -\frac{\hbar^2}{2\mu}\frac{\partial^2}{\partial x^2}$ and the potential energy curves and the non-adiabatic coupling term are taken to be

$$
\begin{aligned}
V_1(x) &= V_0^1 \exp\left[-2(x - x_{cross})\right] & (6.28a)\\
V_2(x) &= vV_0^2 \exp\left[-2(x - x_{cross})\right] + \Delta E & (6.28b)\\
W(x) &= W_0 \exp\left[-\Delta W (x - x_{cross})^2\right] & (6.28c)
\end{aligned}
$$

x_{cross} denotes the crossing point of the two diabatic potential energy curves, ΔE is the asymptotic splitting of the curves and $\{V_0^1, V_0^2, W_0, \Delta W\}$ are parameters of respectively the two surfaces and the non-adiabatic Gaussian coupling term, W. The employed numerical values of these potential parameters are listed in table 6.1, and a plot of $V_1(x)$, $V_2(x)$ and $W(x)$, and the corresponding adiabatic curves, is shown in figure 6.1.

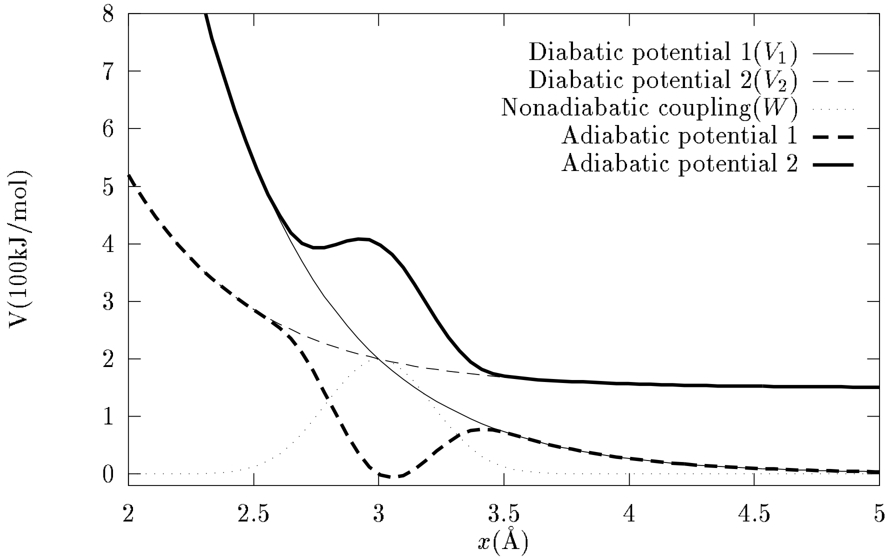

Figure 6.1: Plot of the different potential energy curves mentioned in the text.

In both of the numerical schemes we adapt the usual wavepacket formulation of a scattering experiment [53]. Thus, the system is started on the lowest electronic surface, $V_1(x)$, by initiating the wave function as

$$
\begin{aligned}
\Psi_1(x, t=0) &= \left[\frac{2x_1}{\pi(x_1^2 + x_2^2)}\right]^{1/4} \exp\left[-\frac{(x - x_0)^2}{x_1 - ix_2} - ik_0 x\right] & (6.29a)\\
\Psi_2(x, t=0) &= 0 & (6.29b)
\end{aligned}
$$

where we have defined the constants $x_1 = (2\Delta x_0)^2$ and $x_2 = 2(x_0 - x_{foc})/k_0$. Eq. (6.29a) is nothing but a normalized Gaussian wavepacket, centered around

k_0, with the additional property that it has its minimum width, Δx_0, at x_{foc}, different from the initial starting point x_0 [53, 83]. If we then fix x_{foc} as the classical turning-point on $V_1(x)$, we have reduced the interference problems that occur where part of the wavepacket reaches the end of the grid while a significant part of the wave function is still in the reaction zone. However, the use of a focusing wavepacket, alone, is not sufficient to avoid artificial boundary effects in most computationally realistic calculations. Consequently we will have to use additional numerical techniques to further minimize the artifacts inevitably following the use of a finite basis expansion of the wave function. Thus, both schemes make use of absorbing boundary conditions, in the form of a negative imaginary potential (NIP), but as we shall see the two implementations are very different.

6.2.1 Model study of the generalized MCTDH

First we note that because the considered system is one-dimensional there is no residual correlation term in the Hamiltonian, *i.e.* $\widehat{\mathbf{H}}^s_{corr} = 0$ in eq. (6.4). Thus, eq. (6.19b) for the model system reduces to

$$i\hbar\frac{d}{dt}A^1_i(t) = \sum_j \langle\phi^1_i|W|\phi^2_j\rangle A^2_j(t) \tag{6.30a}$$

$$i\hbar\frac{d}{dt}A^2_i(t) = \sum_j \langle\phi^2_i|W|\phi^1_j\rangle A^1_j(t) \tag{6.30b}$$

For the single-particle functions we are going to make an assumption previously make by Jäckle and Meyer[75] in a single-surface calculation on the collinear $H + H_2 \rightarrow H_2 + H$ reaction (see equation (14) and (17) in this reference). The assumption is to neglect the mean-field operator (here $W(x)$) such that eq. (6.25) simplifies to

$$i\hbar\frac{\partial}{\partial t}\phi^s_i(x,t) = \widehat{\mathbf{h}}^s\phi^s_i(x,t) \qquad (s = 1, 2) \tag{6.31}$$

As noted in reference [75], this can in certain situations (like the present) lead to a faster scheme. Actually this is equivalent to assuming that $\widehat{\mathbf{P}}^s_\kappa \equiv \sum_{j_\kappa} |\phi^s_{j_\kappa}\rangle\langle\phi^s_{j_\kappa}| \approx 1$ in eq. (6.25). This, in turn corresponds to the exact limit of the MCTDH scheme, which is exactly what we want the study[4]. Next we define the single-particle Hamiltonians as

$$\widehat{\mathbf{h}}^s = \widehat{\mathbf{T}} + V_s(x) \qquad (s = 1, 2) \tag{6.32}$$

---

[4] If we, on the other hand, did not make this assumption, it is easy to show that with one single-particle function we would just return to the original set of coupled equations, given in eq. (6.30). A direct solution of eq. (6.30) is however the topic of the next subsection.

Now, if we initiate the single-particle functions as eigenfunctions of respectively $\widehat{\mathbf{h}}^1$ and $\widehat{\mathbf{h}}^2$, the single-particle constrain, eq. (6.16) and eq. (6.9), is trivially fulfilled, and the solution to eq. (6.31) simply reads as

$$\phi_i^s(x,t) = e^{-iE_i^s t/\hbar}\phi_i^s(x,0) \qquad (s=1,2) \tag{6.33}$$

where E_i^1 and E_i^2 are eigenvalue number i of respectively $\widehat{\mathbf{h}}^1$ and $\widehat{\mathbf{h}}^2$. Thus, the propagation of the single-particle functions is now trivial, and we are left with eq. (6.30) as the working equation. To numerically integrate this equation we next employ an ad hoc basis. We use the following normalized particle-in-a-box basis-set

$$\left\{\varphi_n\left(x\right) \equiv \sqrt{\frac{2}{x_{max}}}\sin\left(\frac{n\pi x}{x_{max}}\right) \qquad n=1,\ldots,N\right\} \tag{6.34}$$

where the domain of interest for the coordinate is assumed to be scaled to the interval $x \in]0;x_{max}[$. As discussed in subsection 2.2.5, this FBR is isomorphic to a DVR basis-set, $\{|x_p\rangle,\ p=1,N\}$, with the underlying uniform grid $\{x_p = p\Delta x\ p = 1,N\}$ and the constant weight $\mathcal{W} = \Delta x = x_{max}/(N+1)$. On this grid eq. (6.30) takes the form

$$\begin{aligned}
\frac{d}{dt}A_i^1(t) &= -\frac{i\Delta x}{\hbar}\sum_{j,p}\phi_i^{1*}\left(x_p,t\right)W\left(x_p\right)\phi_j^2\left(x_p,t\right)A_i^2(t) && \text{(6.35a)}\\
\frac{d}{dt}A_i^2(t) &= -\frac{i\Delta x}{\hbar}\sum_{j,p}\phi_i^{2*}\left(x_p,t\right)W\left(x_p\right)\phi_j^1\left(x_p,t\right)A_i^1(t) && \text{(6.35b)}
\end{aligned}$$

As mentioned above $\{\phi_i^1\}$ and $\{\phi_i^2\}$ are defined as eigenfunctions of the single-particle Hamiltonians. Hence, the single-particle functions, eq. (6.33), are initialized on the grid as

$$\phi_i^s\left(x_p,0\right) = \Delta x^{-1/2}\underline{\underline{\mathrm{U}}}^s_{p,i} \qquad (s=1,2) \tag{6.36}$$

where the unitary $\underline{\underline{\mathrm{U}}}^s$-matrices, defined in eq. (2.39), respectively diagonalize $\widehat{\mathbf{h}}^1$ and $\widehat{\mathbf{h}}^2$ expressed in the DVR, $\{|x_p\rangle,\ p=1,N\}$. The initialization of the A-coefficients follow immediately from the initial conditions of the wavepacket discussed in the previous subsection (eq. (6.29)). Thus, we write

$$\begin{aligned}
A_i^1(0) &= \sqrt{\Delta x}\sum_p \Psi_1\left(x_p,0\right)\underline{\underline{\mathrm{U}}}^1_{p,i} && \text{(6.37a)}\\
A_i^2(0) &= 0 && \text{(6.37b)}
\end{aligned}$$

where $\Psi_1\left(x_p,0\right)$ is defined in eq. (6.29a). The numerical values of $A_i^1(0)$ can also be used to truncate $\{\phi_i^1\}$, which in turn defines the number of single-particle functions included for both surfaces. Eq. (6.35) can now be integrated in time using *e.g.* a predictor-corrector scheme. However, as some of the wavepacket reaches the end of the grid it is reflected back into the reaction region, thus causing significant inaccuracies. The reason for this is of course that in the present formulation the wave function is assumed to be zero at the boundary, *i.e.* we have effectively placed an infinite wall at x_{max}. The standard way of treating this difficulty is to employ an absorbing boundary condition by adding to the Hamiltonian a negative imaginary short-range potential in the asymptotic region of the grid [84]. Many different types of NIP's have been suggested in the literature, [85–87], but common to all of them is that they are not, strictly speaking, perfect absorbers in the whole energy domain represented by the wavepacket. We choose a simple linear "ramp-potential"

$$V_{nip}(x) = \begin{cases} -iV_{\max}\frac{x-x_{nip}}{x_{\max}-x_{nip}}, & x_{nip} \le x \le x_{\max}, \\ 0, & \text{otherwise}, \end{cases} \tag{6.38}$$

where x_{nip} and $V_{\max}$ are parameters to be fitted to the scattering experiment at hand. It is important to note that we cannot simply redefine the single-particle Hamiltonians to include the NIP, as this will produce single-particle functions that grow exponentially with time, because of complex eigenvalues entering eq. (6.33). Thus, instead we will have to redefine the A-coefficients after each time-step to include the damping factor of the NIP. Using the terminology of the split-operator method, presented in subsection 4.1.2, this amounts to multiplying the wave function by $\exp[-i\Delta t V_{nip}/\hbar]$, thus redefining the A-coefficients as

$$\begin{aligned} A_i^{s,nip}(t) &\rightarrow \langle\phi_i^s|\Psi_s^{nip}\rangle \approx \langle\phi_i^s|e^{-i\Delta t V_{nip}(x_p)/\hbar}|\Psi_s\rangle \\ &\approx \Delta x \sum_{j,p} A_j^s(t)\phi_i^{s*}(x_p,t)\, e^{-i\Delta t V_{nip}(x_p)/\hbar}\phi_j^s(x_p,t) \end{aligned} \tag{6.39}$$

after each successful propagation of eq. (6.35) by the time-step Δt.

6.2.2 Numerically exact calculations

To obtain a numerically exact solution of the coupled time-dependent Schrödinger equation, see eq. (6.27), we employ the Split operator method [44], discussed in subsection 4.1.2. Thus, to propagated the wave function a time-step Δt, we use the non-adiabatic equivalent of eq. (4.5b), which reads as

$$\underline{\Psi}(x,t+\Delta t) = \exp\left[-i\underline{\underline{V}}\Delta t/2\hbar\right]\exp\left[-i\hat{\underline{\underline{\mathbf{T}}}}\Delta t/\hbar\right]\exp\left[-i\underline{\underline{V}}\Delta t/2\hbar\right]\underline{\Psi}(x,t) \tag{6.40}$$

In this operator matrix equation $\underline{\Psi}$ is a column vector, $[\Psi_1,\Psi_2]^T$, $\hat{\underline{\underline{\mathbf{T}}}}$ is a 2×2 diagonal matrix with the kinetic energy operator in the diagonal and $\underline{\underline{V}}$ is defined as

$$\underline{\underline{\mathrm{V}}}(x) = \begin{bmatrix} V_1(x) - iV_{nip}(x) & W(x) \\ W(x) & V_2(x) - iV_{nip}(x) \end{bmatrix} \tag{6.41}$$

where the individual potentials are given in eq. (6.28) and eq. (6.38). Note that in this scheme we have simply included the NIP in the definition of the two potential energy surfaces. To evaluate the action of $\exp\left[-i\underline{\underline{\mathrm{V}}}\Delta t/2\hbar\right]$, operating on the wave function, it is necessary to make a unitary transformation to the adiabatic representation in which eq. (6.41) is diagonal. At first sight this might seem impossible since $\underline{\underline{\mathrm{V}}}$ is not strictly Hermitian, and thus the spectral theorem can not directly be applied. However, given that we add the same NIP to the two surfaces, it is easy to see that any unitary matrix that diagonalizes the potential energy matrix without the NIP's will also diagonalize eq. (6.41). Hence, if we discretize eq. (6.40) and eq. (6.41) on an equidistant grid $\{x_p = p\Delta x,\ p = 1, N\}$, we can for each grid point, x_p, construct a symmetric matrix $\underline{\underline{\mathrm{U}}}(x_p)$ such that $\underline{\underline{\Lambda}} = \underline{\underline{\mathrm{U}}}^{\mathrm{T}} \cdot \underline{\underline{\mathrm{V}}} \cdot \underline{\underline{\mathrm{U}}}$, where $\underline{\underline{\Lambda}}$ is diagonal with the elements Λ_1 and Λ_2. Then the effect of applying the potential operator, entering eq. (6.40), is evaluated according to the expression

$$\exp\left[-i\underline{\underline{\mathrm{V}}}\Delta t/2\hbar\right] = \underline{\underline{\mathrm{U}}} \cdot \begin{bmatrix} \exp\left[-i\Lambda_1\Delta t/2\hbar\right] & 0 \\ 0 & \exp\left[-i\Lambda_2\Delta t/2\hbar\right] \end{bmatrix} \cdot \underline{\underline{\mathrm{U}}}^T \tag{6.42}$$

After the action of this (coordinate-local) operator onto the wave function, we have to apply the kinetic energy operator $\exp\left[-i\hat{\underline{\underline{\mathrm{T}}}}\Delta t/\hbar\right]$, see eq. (6.40). The effect of applying this differential operator is easily calculated by transforming the wave function from the coordinate grid-representation to a momentum grid-representation by means of a Fourier transformation. To return to the coordinate representation we next perform an inverse Fourier transformation of the wave function, and finally to complete the Split propagation by Δt we act the potential energy operator, eq. (6.42), once more onto the result.

6.2.3 Numerical results for the two schemes

The numerical schemes presented in the two previous subsections were implemented in FORTRAN 77 on a super-scalar vector computer. The integration of eq. (6.35) was carried out by employing a predictor-corrector scheme of variable-order (up to $11'th$ order), and the action of the kinetic energy operator on the discretized wave function was calculated using a FFT algorithm, see subsection 2.2.2. To extract information from the calculations on the transition probabilities among the two surfaces we evaluated the quantum flux, F, of the wave functions. In section 1.1

we defined the flux operator in coordinate space (see eq. (1.9)), which is readily recast to the following momentum representation,

$$F_s(k,t) = \frac{\hbar k_s}{\mu}\left|\Psi_s^+(k,t)\right|^2 \qquad (s=1,2) \tag{6.43}$$

where $k_1 = k$, $k_2 = \sqrt{k^2 - 2\mu\Delta E/\hbar^2}$ and

$$\Psi_s^+(k,t) = \frac{1}{\sqrt{2\pi}}\int_{-\infty}^{\infty} dx \exp\left[ikx\right]\Psi_s(x,t) \tag{6.44}$$

The transition probability from the initial state was then obtained as the ratio between the outgoing fluxes and the initial incoming flux:

$$P_s(k) = \frac{F_s(k,t^*)}{F_0(k,0)} \qquad (s=1,2) \tag{6.45}$$

where the initial incoming flux, $F_0(k,0)$, can be obtained analytically by inserting eq. (6.29a) into eq. (6.44):

$$F_0(k,0) = \frac{\hbar k \Delta x_0}{\mu}\sqrt{\frac{2}{\pi}}\exp\left[-2\Delta {x_0}^2(k-k_0)^2\right] \tag{6.46}$$

However, to directly calculate $F_s(k,t^*)$ in eq. (6.45), we would have to use a grid large enough that at a certain time, t^*, all of the wavepacket was well outside the region of reaction *and* the domain of definition of the NIP. The solution is instead to use the time/energy Fourier transform, $\Psi_s^+(x,E)$, defined as

$$\Psi_s^+(x,E) = \frac{1}{\sqrt{2\pi}}\int_{-\infty}^{\infty} dt \exp\left[iEt/\hbar\right]\Psi_s(x,t) \tag{6.47}$$

rather than the space/momentum transform, $\Psi_s^+(k,t)$. One can then show the simple relation (see appendix in reference [88])

$$\Psi_s^+(x,E) = \frac{\mu}{\hbar k}e^{-ikx}e^{iEt^*/\hbar}\Psi_s^+(k,t^*) \tag{6.48}$$

Inserting this expression and eq. (6.46) into eq. (6.45) we finally obtain

$$P_s(k) = \frac{\hbar^2 k k_s \left|\Psi_s^+\left(x^*, \hbar^2k^2/2\mu\right)\right|^2}{\Delta x_0 \mu^2 \exp\left[-2\Delta {x_0}^2(k-k_0)^2\right]} \tag{6.49}$$

We then choose $x^* < x_{nip}$ and calculate the time/energy transform of the wave functions, eq. (6.47), as a discrete sampling after each time-step Δt. Next, recalling the discussion on conservation of flux in section 1.1 (see eq. (1.12)), we note that the relation $P_1(k) + P_2(k) = 1$, can then be used as a measure of convergence as a function of k (in the neighborhood of k_0). The total transition probabilities are obtained from the ratio between the total fluxes, *i.e.*

$$P^s_{tot}(k_0) = \frac{\hbar^2}{k_0 \mu^2} \int\limits_{-\infty}^{\infty} dk k^2 k_s \left| \Psi_s^+ \left(x^*, \hbar^2 k^2 / 2\mu \right) \right|^2 \tag{6.50}$$

where we have used that the total flux of the Gaussian wavepacket is simply given by $\hbar k_0/\mu$. Again the sum from the two surfaces should give unity. As yet another measure of the overall convergence we use the fact that both numerical schemas are energy-conserving. (This follows formally from the Dirac-Frenkel variational principle and the fact that the Split operator is unitary outside the NIP). From eq. (6.29a) we obtain $\langle k^2 \rangle = k_0^2 + \frac{1}{x_1}$ which immediately leads to the following expression for the time-independent mean-energy

$$\langle E \rangle = \frac{\hbar^2}{2\mu} \langle k^2 \rangle = \frac{\hbar^2}{2\mu} \left(k_0^2 + \frac{1}{4 \Delta x^2} \right) \tag{6.51}$$

This number was then compared to $\langle \Psi_1 | h_1 | \Psi_1 \rangle + \langle \Psi_2 | h_2 | \Psi_2 \rangle + 2 \operatorname{Re} \left[\langle \Psi_1 | W | \Psi_2 \rangle \right]$ as a functions of time for the two schemes.

Below in table 6.1 we have listed the values of the parameters that were fixed throughout the calculation presented in this section.

In figure 6.2 the transition probability, $P_2(k)$, is shown as a function of the wave vector, $k = \sqrt{2\mu E/\hbar}$. These probabilities were obtained by 7 MCTDH calculations with 400 grid points and different values of $k_0 = (30, 35, 40, 45, 50, 55, 60)$. The convergence was of the order of 10^{-5} with the split operator method employing 750 grid points. Figure 6.2 shows Stückelberg oscillations [35] above the threshold energy, $\Delta E = 1.5 \cdot 100\,\mathrm{kJ/mol} \sim k = 27\text{Å}^{-1}$, and a very narrow peak at $k = 45\text{Å}^{-1}$ corresponding to $E = 4 \cdot 100\,\mathrm{kJ/mol}$. The oscillations occur because the system has a turning-point and thus interference will take place when the system follow the different possible paths leading to the upper surface. The peak at $E = 4{\cdot}100\,\mathrm{kJ/mol}$ is an interesting indication of the formation of a resonance, which is actually the topic of the next part of this thesis. Thus, here we see a nice example of the connection between the two topics studied in this thesis. A closer inspection of the adiabatic potential energy curves, see figure 6.1, exactly shows a well on the upper surface at this value of the energy, which suggests that the system is trapped

Table 6.1: Numerical values of the parameters fixed in the calculations. The numbers are reported in molecular units (see appendix A in reference [89]).

Parameters	MCTDH[f]	Common	Split[g]
μ(au)		1.0	
x_{min}(Å)		0.0	
x_{max}(Å)		18.0	
Propagation:			
x^*(Å)[a]		10.0	
$\Delta t(10^{-14}$s)	0.005[b]		0.002[b]
time-steps	4000[b]		15000[b]
Precision	10^{-6}[c]		—[d]
Gaussian wavepacket:			
x_0(Å)		10.0	
x_{foc}(Å)		3.0	
Δx_0(Å)		0.25	
Potentials:			
x_{cross}(Å)		3.0	
V_0^1(100kJ/mol)		2.0	
V_0^2(100kJ/mol)		0.5	
ΔE(100kJ/mol)		1.5	
W_0(100kJ/mol)		2.0	
ΔW(Å^{-2})		11.09	
x_{nip}(Å)		13.5[e]	
V_{max}(100kJ/mol)		0.30[b]	

[a] The time sampling of the wave function at this grid point (see eq. (6.47), eq. (6.48) and eq. (6.49)) was not started before the wavepacket was moving out of the reaction region.

[b] This parameter is actually a functions of k_0, but the listed value was typical for most calculations.

[c] Input-parameter to the variable order predictor-corrector routine.

[d] The Split operator method does not offer any control over the precision in the time-propagation.

[e] This corresponds to a NIP which is defined on the last 25% of the grid-points.

[f] Generalized MCTDH as described in subsection 6.2.1.

[g] Split-operator scheme, employing the FFT algorithm, as described in subsection 6.2.2.

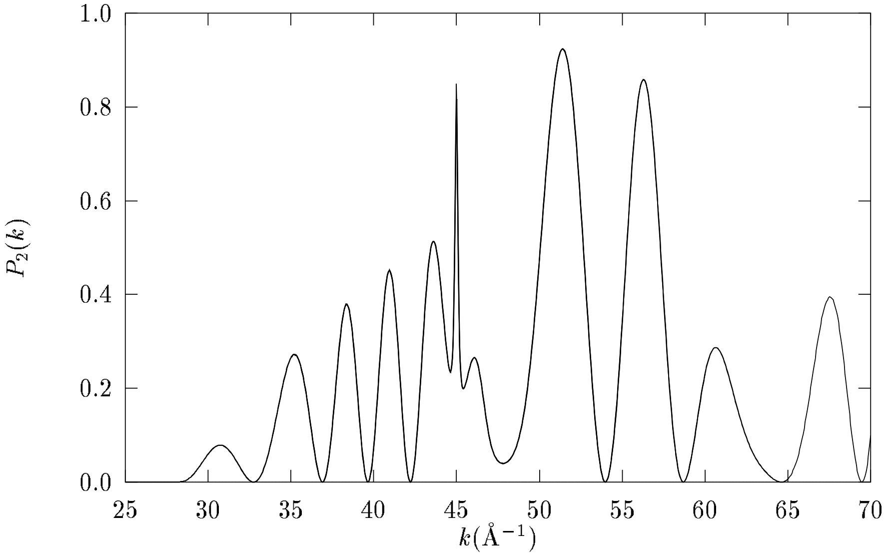

Figure 6.2: The probability for transition from the initial state on the lower surface to a final state on the upper surface is shown as a function of the wavenumber. The results were obtained by the generalized MCTDH scheme, using seven different values of k_0.

on the upper adiabatic surface for a short time before it tunnels out. This, as we shall see in the next part, correspond to the formation of a shape resonance. The exact position and life-time of the resonance can be calculated using the "complex scaling of a DVR"-method, suggested recently by Museth *et al.* [4]. This we will demonstrate in chapter 12.

In table 6.2 and 6.3 we have listed the convergence for the total transition probabilities for respectively the Split operator and the MCTDH method. In all the calculations k_0, in eq. (6.50), was fixed to 3500kJ/mol and the remaining parameters as listed in table 6.1. Due to the fact that the NIP was not a perfect absorber in all of the energy domain represented by the wavepacket, reflection was inevitable and consequently convergence below 10^{-5} could not be obtained as a result of merely increasing the grid size. Table 6.2 shows that the Split operator method needs more than 750 grid points to ensure a convergence of the order of 10^{-5}. Given that the most time-consuming step in the Split operator scheme is the one-dimensional FFT-call, we would expect the CPU-time to scale as $N \log N$, where N denotes the size of the grid. If we take an initialization-time into account, this characteristic semi-linear time-dependence is confirmed by the second column in table 6.2. Table 6.3 clearly shows that the MCTDH method needs much less points, than the direct method, to achieve the same convergence, which is due to the fact that in the MCTDH method the basis-sets are optimized as a function of

Table 6.2: Convergence of the total transition probabilities in the Split operator method. In all the tabulated calculations the initial Gaussian wavepacket was centered at $k_0 = 35(\text{Å}^{-1})$.

Grid size (N)	$P_1(k_0)$	$P_2(k_0)$	$P_1(k_0) + P_2(k_0)$	CPU sec.	MFLOP[a]
200	0.54052	0.09937	0.63989	9.0	117
300	0.86115	0.13876	0.99991	12.3	119
400	0.86138	0.13857	0.99996	15.6	116
500	0.86139	0.13858	0.99997	19.5	120
750	0.86140	0.13858	0.99998	32.2	111
1000	0.86140	0.13858	1.00000	37.9	121

[a] Million floating point operations pr. second on a single CPU of a Cray C92 (peak performance is approximately 900 MFLOP).

Table 6.3: Convergence of the total transition probabilities in the generalized MCTDH scheme. In all the tabulated calculations the initial Gaussian wavepacket was centered at $k_0 = 35(\text{Å}^{-1})$.

Grid size (N)	M[a]	$P_1(k_0)$	$P_2(k_0)$	$P_1(k_0) + P_2(k_0)$	CPU sec.	MFLOP[b]
200	200	0.15772	0.01767	0.17536	196	468
250	250	0.87679	0.12320	0.99998	227	490
300	300	0.86122	0.13879	1.00000	303	476
400	200	0.85919	0.14067	0.99986	142	455
400	267	0.86113	0.13887	0.99999	247	438
400	400	0.86140	0.13858	1.00000	505	477

[a] Number of single-particle functions included in the calculation.

[b] Million floating point operations pr. second on a single CPU of a Cray C92 (peak performance is approximately 900 MFLOP).

time, *i.e.* they follow the dynamics of the system as time evolves. Still, the number of employed single-particle functions is relatively high, which is of course due to the very simple form assumed for these functions. However, it should be emphasized that the simple time-dependence of the single-particle functions (see eq. (6.33)) is not trivial in the sense that it deals with the numerically difficult rapid oscillations of the functions in an ad hoc way. Thus, if we had ignored this time-dependence, and assumed a completely static form of the single-particle functions, we would have to employ approximately as many functions as grid-points in the FFT scheme.

Table 6.3 shows that the full convergence is obtained with 400 only grid-points and single-particle functions, and an acceptable precision remains when the former is truncated by a factor of $\frac{2}{3}$. However, it is equally clear from table 6.3 that the MCTDH scheme is approximately 10 times slower than the simple Split operator method, even though the code ran 4-5 times faster on the same vector-computer. This was of course a bit disappointing, but considering the complexity of the MCTDH approximation - even for an as simple problem as the considered - it was not surprising. It is difficult to make any conclusive remarks on the large difference in the MFLOP performances of the two codes. However, it appears that the predictor-corrector algorithm is more vectorized than the FFT. Finally we note that the MCTDH method scales almost quadraticly with the dimensions, if we take a certain initialization-time for the scheme into account. However, if we allow for a smaller convergence by truncating the single-particle basis-sets, table 6.3 shows an almost linear dependence of the CPU-time.

6.3 Conclusions

It is evident from the results presented in the previous section that for simple non-adiabatic systems the generalized MCTDH method is not the method of choice - especially not when one seeks numerically exact results. As expected from the equations of motion for the MCTDH scheme, it is perfectly capable of producing these exact results with a relatively small grid, but the cost in terms of CPU-time is very large. Even in the approximate domain, the direct Split operator method converges much faster - in spite of the fact that it uses twice as many grid-points and 2-3 times as many time-steps. One major drawback of the generalized MCTDH scheme was pointed out in section 6.1; the presented numerical scheme, unlike the original MCTDH scheme, does not allow for the direct construction of an optimized DVR, using the HEG-scheme. Consequently the definition of the ad hoc basis-set is very critical for the overall numerical performance of the scheme. In the calculations presented in the previous section we used a basis-set of particle in a box functions, *i.e.* we used a uniform DVR-grid that does not reflect the underlying physics of the problem. It is possible that we could have chosen a better ad hoc basis for this concrete study, but the general problem of optimizing and truncating the basis-sets and grids this still remains to be solved for multi-surface systems.

However, it is very important to emphasize that the considered model-system is very simple, and therefore the use of an approximate method like, the generalized MCTDH, may not prove advantageous as compared to more direct numerically exact methods. The conclusion is clear for very simple non-adiabatic systems, but it is likely that the picture will change when more complexity is added to the system. The distinct advantage of the MCTDH scheme is exactly connected with the large flexibility of the scheme to deal with complicated situations encountered in complex collision experiments. One can vary the number of basis-functions according to the correlation and non-adiabatic coupling as time evolves, and the numerical scheme scales almost linearly with the number of surfaces and degrees of freedom (see reference [74]) - and these features have not yet been exploited. Thus, a study of a multi-surface system with more degrees of freedom is required to give any conclusive evaluation of the presented generalized MCTDH scheme. This is exactly the topic of the next chapter.

7

MCTDH on non-adiabatic H_2+Cu

The overall motivation of the work to be presented in this chapter is twofold (see A.2 in part IV for the abstract). First of all we want to test the generalized MCTDH scheme, derived in the previous chapter, on a two-dimensional two-surface reactive system. Secondly we want to investigate the non-adiabatic effects involved in the dynamical process of dissociation of hydrogen on a copper surface. However, it is very important to emphasize that in the context of this thesis the first motivation carries by fare the greatest weight, and as such the specific system, studied below, is of less importance. This point is furthermore stressed by the fact that the potential energy surfaces, on which the calculations were based, are probably not very reliable. As will be clarified in the next section, improvements can be made on these surfaces, which we plan to do in the very near future. Thus, in this chapter we shall mainly focus on the implementation and performance of the generalized MCTDH scheme, and only comment briefly on the physical interpretations of the actual numerical results obtained.

The chapter is organized as follows. In section 7.1 we define the system to be studied below, *i.e.* the electronic potential energy surfaces of H_2+Cu(100). Next, in section 7.2, we present a simple scheme which is used to express these potential energy surfaces in a direct product form in the two coordinates. Section 7.3 then outlines the overall scheme for the MCTDH calculations, based on the equations of motion derived in section 6.1. Thus, whenever possible, reference will be made to the previous chapter, and we shall only focus on the new features of the scheme which are relevant in the present context. This is also true for section 7.4, where we briefly comment on the implementation of the split-operator scheme, previously discussed in subsection 6.2.2. The numerical results for the two schemes are next presented in section 7.5, and finally we draw the conclusions in section 7.6.

7.1 The electronic potential energy surfaces

As stressed in the introduction to this chapter the aim of the presented work is primarily to study the generalized MCTDH scheme on a non-adiabatic two-dimensional system. As such, "any" dynamical system would do, but instead of choosing a well-studied non-adiabatic benchmark system, I decided to test it on a set of potential energy surfaces which have recently been calculated by other members of our group. Using the EDIM methodology, C. Laursen and G. D. Billing have constructed the two lowest diabatic potential energy surfaces for the reaction of molecular hydrogen on a copper(100) surface. However, before we could use the surfaces for the dynamical simulations, some additional manipulations had to be made. Thus, except for the simple adjustments of the surfaces, to be described below, I did not have any part in the explicit calculations of these surfaces. As such, my insight into the details of the approximations behind the calculations of these surfaces is very limited, and hence I will only give a short comment below.

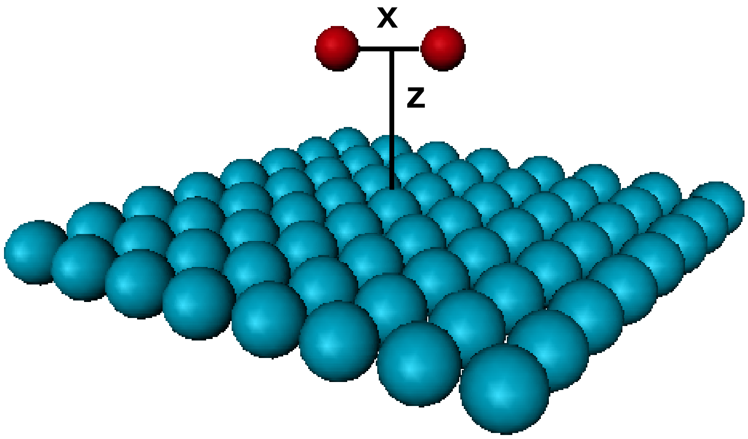

Figure 7.1: Schematic illustration of the two coordinates for the H_2+Cu system, which are treated fully quantum mechanically in the presented study.

The system under consideration is the dynamical process of dissociation of hydrogen on a metallic copper(100) surface. The calculations, to be presented, include the two lowest diabatic electronic surfaces, which are constructed from an EDIM-potential suggested by Truong *et al.*[90]. The dynamics is confined to a two-dimensional treatment for the reactive subsystem by quantizing the vibrational coordinate, x, and the translational coordinate, z, see figure 7.1. Thus, we assume the metallic surface to be static in the sense that no degrees of freedom for the (134) copper atoms are included, *i.e.* no phonon excitation. (We expect to include this additional degree of freedom in a future study). Contributions from H $\sim$ H interactions (covalent bonds) are described by the well established diatom in molecule (DIM) methodology, and the interactions of H $\sim$ Cu are evaluated using DIM and the embedded atom method (EAM)[91]. From this, two analytical diabatic surfaces result, which are "empirically" parameterized by 8 parameters. These parameters are next fixed by a non-linear least squares fit to the lowest adiabatic total energy ab initio calculations (DFT-GGA) due to Wiesenekker *et al.*[92]. A contour plot of this lowest adiabatic surface is shown in figure 7.2.

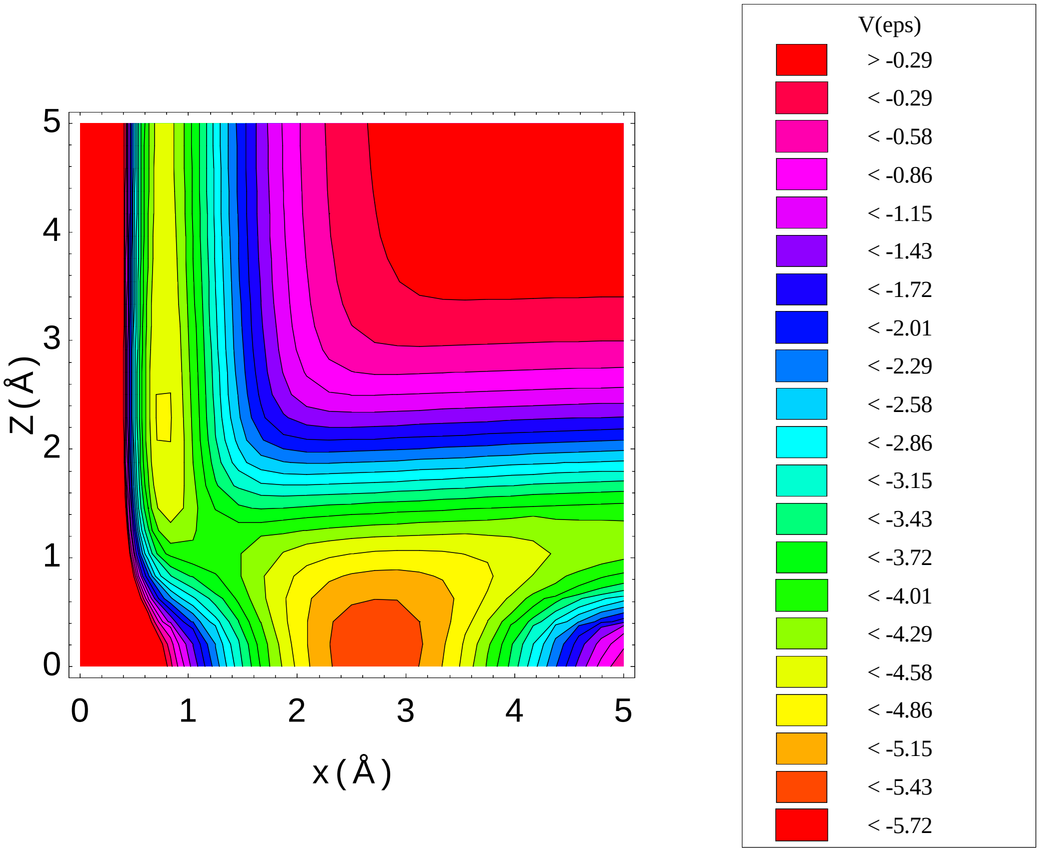

Figure 7.2: Contour plot of the lower adiabatic surface of H_2+Cu(100), due to Wiesenekker *et al.*[92].

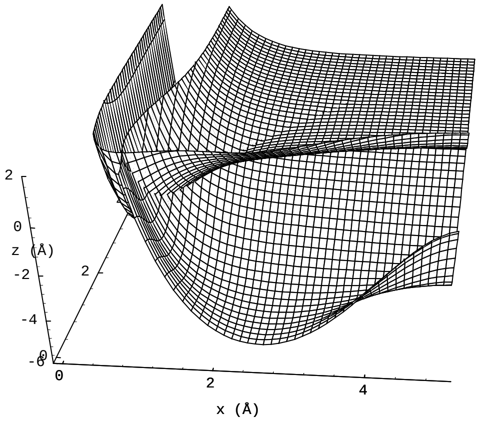

Figure 7.3a: Plot of the "original" two lower diabatic surfaces of H_2+Cu(100), due to Laursen and Billing.

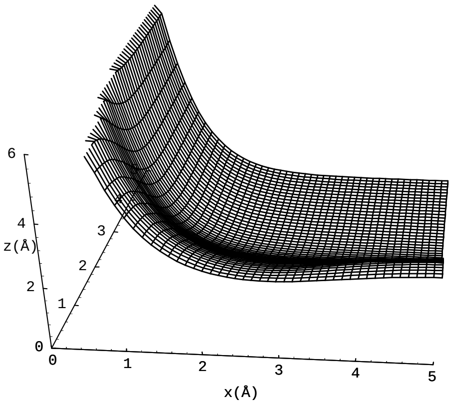

Figure 7.3b: Plot of the non-adiabatic coupling term corresponding to the surfaces shown in figure 7.3a.

All in all this lead to the diabatic potential energy surfaces shown in figure 7.3a and figure 7.3b. It should be clear from these surfaces that they do not correlate with respectively molecular and atomic hydrogen, but rather some combination of the two. (The non-adiabatic coupling in figure 7.3b is constant but non-zero in the incoming channel). This is simply a consequence of the EDIM formulation for the surfaces. However, we would like to initiate the dynamical calculations on the lower diabatic surface in a vibrational eigenstate of free H_2 asymptotically fare from the Cu(100) surface. Thus, it is necessary to shift to another diabatic representation which has the "correct" asymptotic behavior.

The formally correct procedure for such a change to a new diabatic representation was outlined in section 3.4, based on the adiabatic-diabatic transformation scheme of Baer[37]. To repeat, one first has to shift to the adiabatic representation, with the corresponding two unique surfaces defined as

$$V_1 = \frac{1}{2}\left(W_{11} + W_{22} + \sqrt{(W_{11} - W_{22})^2 + 4W_{12}^2}\right) \tag{7.1a}$$

$$V_1 = \frac{1}{2}\left(W_{11} + W_{22} - \sqrt{(W_{11} - W_{22})^2 + 4W_{12}^2}\right) \tag{7.1b}$$

Next, eq. (3.46) is integrated with $\gamma(x_0, z_0) = 0$, where the new diabatic reference configuration, (x_0, z_0), is taken to be a point in the incoming channel of figure 7.2, corresponding to a system of molecular hydrogen asymptotically separated from the copper surface.

However, we choose, as a first ansatz, a more "quick and dirty" approach to this change of reference configuration in the diabatic representation. We simply assumed (*i.e.* guesses) a form of the diabatic coupling potential, $W_{12}(x,z)$, and solved eq. (7.1) for the corresponding diabatic potentials,

$$\begin{aligned} W_{11} &= \tfrac{1}{2}\left(V_1 + V_2 \pm \sqrt{(V_1 - V_2)^2 - 4W_{12}^2}\right) && (7.2a) \\ W_{22} &= \tfrac{1}{2}\left(V_1 + V_2 \mp \sqrt{(V_1 - V_2)^2 - 4W_{12}^2}\right) && (7.2b) \end{aligned}$$

The correct sign in eq. (7.2) is determined from the crossing of the new diabatic surfaces, which in turn can the be deduced from a simple maximum-overlap criteria of the corresponding eigenvectors which diagonalizes $\underline{\underline{W}}$ to give $\underline{\underline{V}}$.

In view of the correct procedure, outlined in section 3.4, this approach is clearly very approximate in nature, and the success of this scheme is of course entirely based on the reliability of the assumed diabatic coupling potential. Thus, in general results obtained from calculations on these new diabatic surfaces should be treated with great caution. However, in the spirit of merely testing the convergence and overall numerical performance of the generalized MCTDH scheme, this approximation is very convenient as it is quickly implemented, stable and moreover allow us to easily modify the system to introduce different quantum effects. Thus, by changing the coupling emphasis can be put on effects like tunneling, non-adiabatic transition and resonances formation. So, all in all this system should be considered merely a model-system for the H_2+Cu(100) reaction, derived from the lowest adiabatic ad initio surface.

For the diabatic coupling term, W_{12}, we assumed a simple Gaussian coupling, which is convenient as it is flexible and at the same time involves a minimum of parameters. In stead of defining this Gaussian coupling directly in the Jacobi coordinates, (x,z), we found it more realistic to use a set of natural collision coordinates, discussed in detail in subsection 2.1.2. Thus, we assumed

$$W_{12}(s,v) = W_{21}(s,v) \equiv A \exp\left[-4\ln 2\left((s/\Delta s)^2 + (v/\Delta v)^2\right)\right] \qquad (7.3)$$

where s is the intrinsic reaction coordinate interconnecting the two minima on either side of the saddle point (see figure 7.5), and v is the perpendicular vibrational coordinate. In eq. (7.3) A is an amplitude parameter and $(\Delta s, \Delta v)$ are the full widths at half maxima in the two directions. The reaction coordinate s, which was explicitly defined from a standard minimum energy path scheme employed on the lowest adiabatic surface, is shown in figure 7.4. Figure 7.5 shows the corresponding minimum energy profile of $V_1(s)$, leading from the gas-phase to dissociation on the

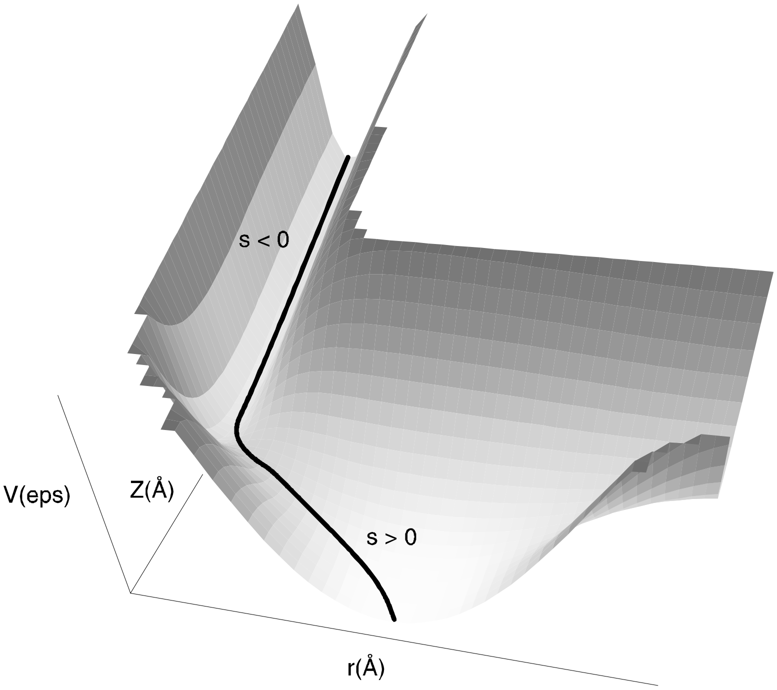

Figure 7.4: Plot of the minimum energy path (thick line) on the lower adiabatic surface.

metallic surface. Note especially the two minima on either side of the saddle point, corresponding to respectively physisorption and chemisorption wells. The relation between the two sets of coordinates, (x, z) and (s, v), is as follows: v denotes the shortest distance from any point (x, z) to the reaction path, and s denotes the distance along the reaction path to that point.

With the parameters, entering eq. (7.3), fixed as $A = 3.4$, $\Delta s = 0.7$ and $\Delta v = 0.6$, figure 7.6a shows a plot of the approximated coupling potential. The corresponding diabatic energy surfaces, derived from eq. (7.2), is next shown in figure 7.6b. Note that for this particular choice of W_{12}, the resulting diabatic surfaces do actually not cross, but rather approach each other in the saddle point. Thus, in this simple case the correct sign in eq. (7.2) is always the lower one. This non-crossing feature of the produced diabatic surfaces is to be considered an artifact of the approximated coupling. It should also be noted that the square root, entering the analytical expression for the diabatic surfaces, eq. (7.2), puts some constraints on the explicit values of the coupling parameters, $(A, \Delta s, \Delta v)$. Especially one has to be careful that the coupling does not extent into the region of configuration space with large values of both (x, z), since here the two adiabatic surfaces meet, *i.e.* $|V_1 - V_2| \to 0$.

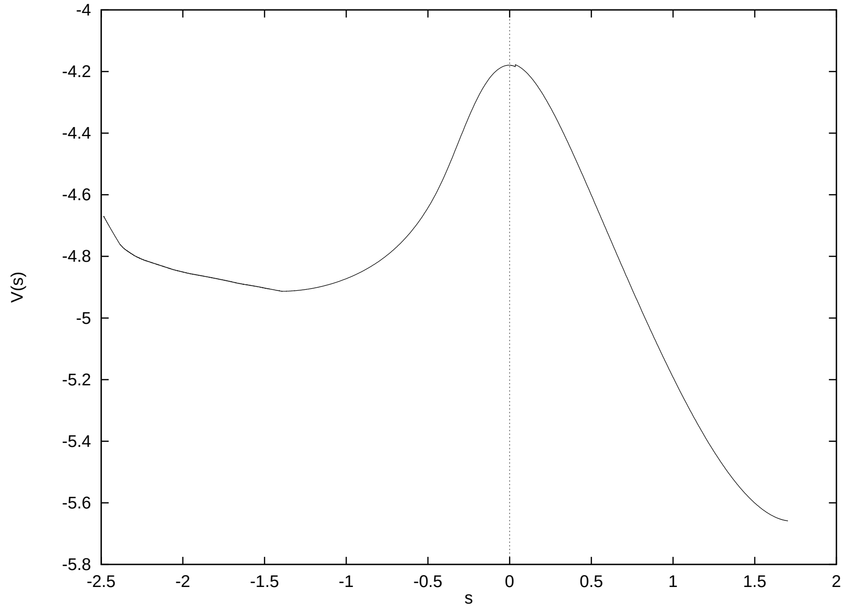

Figure 7.5: Minimum energy profile of the lowest adiabatic surface leading from the gas phase to dissociation on the metallic surface. Note the two minima on either side of the saddle point, corresponding to respectively physisorption and chemisorption wells.

7.2 Direct-product representation of the potentials

As was already pointed out in the previous chapter, one of the major limitations of the MCTDH method, is the underlying assumption of a separable form of the Hamiltonian operator for the total system. To exploit the central advantage of the MCTDH method, it is of course necessary to avoid the computation of multi-dimensional integrals. This can in turn only be accomplished if the full Hamiltonian can be expressed as a linear combination of a *limited* set of products of single-particle operators. This is usually fulfilled by the correlated part of the Hamiltonian, $\widehat{\mathbf{H}}^{s}_{corr}$, due to the separability of the kinetic energy terms[1]. However, this is in general not the case for the diabatic potential energy terms, $W_{s,s'}$, entering eq. (6.25). Thus, to obtain this desired product representation of the potential energy surfaces we employ an approximate scheme due to Jäckle and Meyer[75, 93]. The method is largely based on the *Approximations theorem* by Schmidt[94], which defines a procedure for the optimal approximation of a symmetric function in two variables by a sum of functions of one variable. We first review the general multi-

---

[1] This does of course depend on the choice of coordinates used for the representation of the kinetic energy operator.

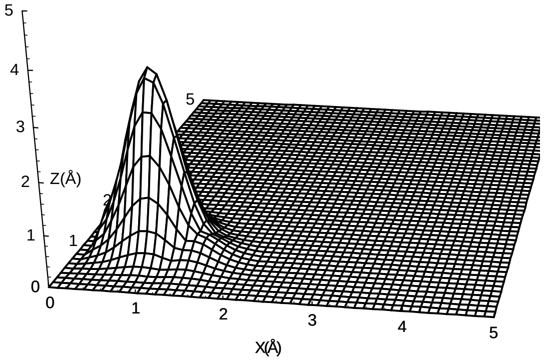

Figure 7.6a: Plot of the Gaussian coupling-term, defined in eq. (7.3).

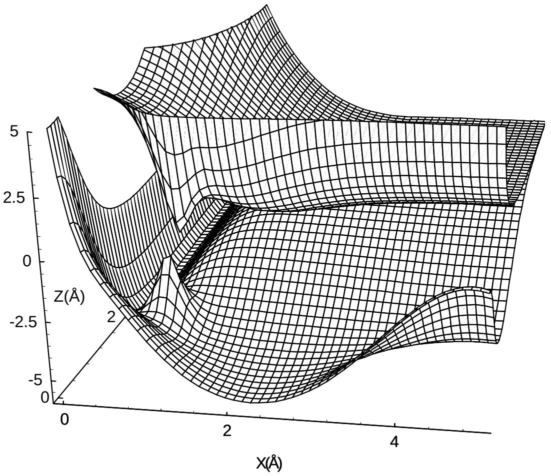

Figure 7.6b: Plot of the lower and upper diabatic surface.

dimensional scheme, and subsequently apply it to the two-dimensional system of H_2+Cu.

The approximation is based on the concept of density matrices, already discussed in section 6.1. The potential is first discretized on a product grid

$$W\left(R^1_{i_1}, R^2_{i_2}, \dots, R^N_{i_N}\right) \equiv W_{i_1,i_2,\dots,i_N} \tag{7.4}$$

where $\{R^\kappa_{i_\kappa},\ i_\kappa = 1,\dots,N_\kappa\}$ denote the grid points in the κ'th degree of freedom. Next, we define the symmetric *potential density matrices*, $\underline{\underline{\rho}}^\kappa$

$$\rho^\kappa_{nm} \equiv \sum_{i_1}^{N_1}\cdots\sum_{i_{\kappa-1}=1}^{N_{\kappa-1}}\sum_{i_{\kappa+1}=1}^{N_{\kappa+1}}\cdots\sum_{i_N=1}^{N_N} W_{i_1,\dots,i_{\kappa-1},n,i_{\kappa+1},\dots,i_N}\, W_{i_1,\dots,i_{\kappa-1},m,i_{\kappa+1},\dots,i_N} \tag{7.5}$$

and determine their orthonormal eigenvectors, $\underline{V}^\kappa_j$, as well as their corresponding eigenvalues, λ^κ_j. In reference [93] they are denoted respectively the natural potentials and natural weights. It is important to note that the natural weights are assumed to be in decreasing order, *i.e.* $\lambda^\kappa_j \geq \lambda^\kappa_{j+1}$. To employ the same notation as Jäckle and Meyer[75, 93] we also define $V^\kappa_j(R^\kappa_{i_\kappa}) \equiv [\underline{V}^\kappa_j]_{i_\kappa}$. The idea is now to approximate the potential as

$$W\left(R^1_{i_1}, R^2_{i_2}, \dots, R^N_{i_N}\right) \approx \sum_{i_1}^{n_1}\cdots\sum_{i_N=1}^{n_N} C_{i_1,\dots,i_N}\, V^1_{i_1}(R^1_{i_1})\cdots V^N_{i_N}(R^N_{i_N}) \tag{7.6}$$

where $\{n_\kappa,\ \kappa = 1,\ldots,N\}$ are the expansion orders in the different degrees of freedom, and where the expansion coefficients, $C_{i_1,\ldots,i_N}$ are determined from the expression

$$C_{i_1,\ldots,i_N} \equiv \sum_{i_1=1}^{N_1} \cdots \sum_{i_N=1}^{N_N} W_{i_1,\ldots,i_N}\, V^1_{i_1}(R^1_{i_1}) \cdots V^N_{i_N}(R^N_{i_N}) \tag{7.7}$$

Note especially that eq. (7.6) is exact if $\{n_\kappa\} \to \{N_\kappa\}$. In reference [93] Jäckle and Meyer proceed to define an iterative procedure where the expansion coefficients, $C_{i_1,\ldots,i_N}$, and the natural potentials, $\underline{V}^\kappa_j$, entering eq. (7.6), are improved to give a better product representation of the potential. They define the *modified density matrices*, $\underline{\underline{\tilde{\rho}}}^\kappa$, as

$$\tilde{\rho}^\kappa_{nm} \equiv \sum_{i_1}^{n_1} \cdots \sum_{i_{\kappa-1}=1}^{n_{\kappa-1}} \sum_{i_{\kappa+1}=1}^{n_{\kappa+1}} \cdots \sum_{i_N=1}^{n_N} C_{i_1,\ldots,i_{\kappa-1},n,i_{\kappa+1},\ldots,i_N}\, C_{i_1,\ldots,i_{\kappa-1},m,i_{\kappa+1},\ldots,i_N} \tag{7.8}$$

where $1 \leq n_\kappa, m_\kappa \leq N_\kappa$. Thus, in contrast to eq. (7.5) the upper limits of the summations are the expansion orders, $\{n_\kappa\}$, and not the number of grid points $\{N_\kappa\}$. (Note that if $\{n_\kappa\} \to \{N_\kappa\}$ in eq. (7.8) then $\tilde{\rho}^\kappa_{nm} \to \delta_{nm}\lambda^\kappa_n$). The modified density matrices are next diagonalized,

$$\underline{\underline{\tilde{\rho}}}^\kappa_{diag} = \underline{\underline{U}}^{\kappa\ T} \cdot \underline{\underline{\tilde{\rho}}}^\kappa \cdot \underline{\underline{U}}^\kappa \tag{7.9}$$

and the orthogonal matrices, $\underline{\underline{U}}^\kappa$, are used to define the new potential vectors, $\underline{\tilde{V}}^\kappa_j$, as

$$\underline{\underline{\tilde{V}}}^\kappa \equiv \underline{\underline{V}}^\kappa \cdot \underline{\underline{U}}^\kappa \tag{7.10}$$

where $\underline{\underline{\tilde{V}}}^\kappa \equiv [\underline{\tilde{V}}^\kappa_1, \ldots, \underline{\tilde{V}}^\kappa_{N_\kappa}]$ and $\underline{\underline{V}}^\kappa \equiv [\underline{V}^\kappa_1, \ldots, \underline{V}^\kappa_{N_\kappa}]$. Finally the new expansion coefficients, $\tilde{C}_{i_1,\ldots,i_N}$, are constructed from eq. (7.7) with $V^\kappa_{i_\kappa}(R^\kappa_{i_\kappa}) \to \tilde{V}^\kappa_{i_\kappa}(R^\kappa_{i_\kappa})$. The idea is now to repeat these iterative steps (eq. (7.8), (7.9), (7.10) and (7.7)) until convergence is reached, *i.e.* until the transformation matrices in eq. (7.10) are sufficiently close to a unit matrix. This scheme was used to approximate the two-dimensional diabatic potential energy surfaces of H_2+Cu, shown in figure 7.6. In figure 7.7 plots of the deviation for different approximations of the lower diabatic surface are shown. The approximations employed expansion orders, (n_x, n_z), of respectively $(3,4)$, $(5,6)$ and $(7,9)$. The maximum value of the corresponding

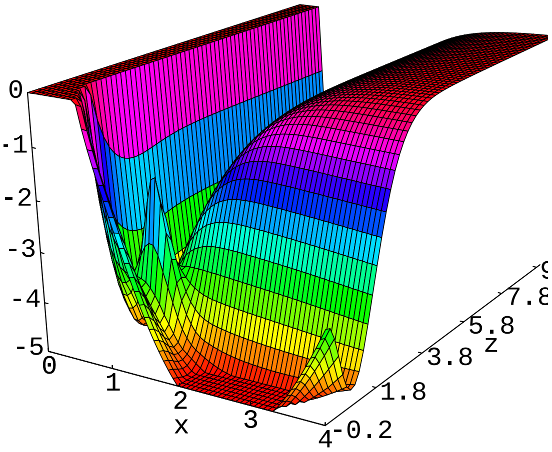

Figure 7.7a: Plot of the lower diabatic surface.

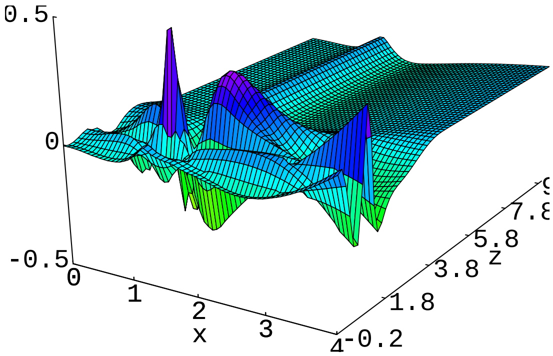

Figure 7.7b: Plot of the difference between figure 7.7a and the approximated surface employing 3 functions in x and 4 in z.

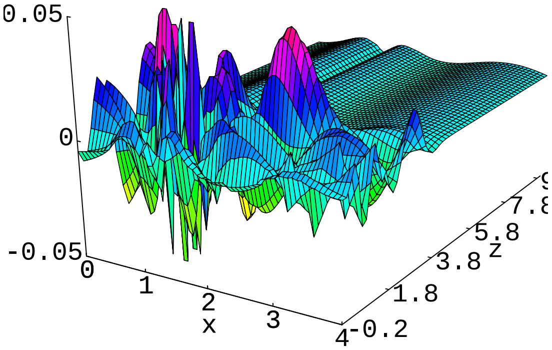

Figure 7.7c: Plot of the difference between figure 7.7a and the approximated surface employing 5 functions in x and 6 in z.

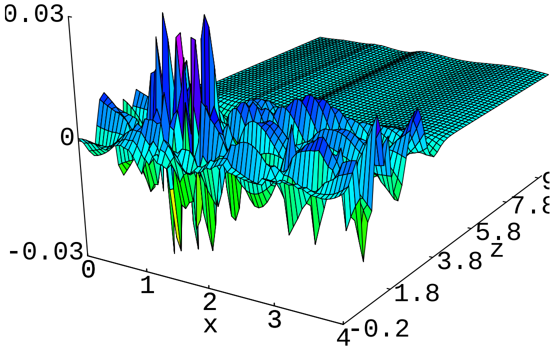

Figure 7.7d: Plot of the difference between figure 7.7a and the approximated surface employing 7 functions in x and 9 in z.

deviations are shown to be respectively 0.5, 0.05 and 0.03. In view of the approximate nature of the diabatic coupling, *cf.* eq. (7.3), and hence also the two diabatic potentials, I found the precision with $n_x = 5$ and $n_z = 6$ to be sufficient in all the calculations. Furthermore, the numerical work in the implementation of the generalized MCTDH scheme, to be presented in the next section, scales exponentially with the expansion orders, such that the small improvement obtained by increasing (n_x, n_z) is largely outweighed by the numerical penalty. It should also be noted that I found the optimizing scheme of Jäckle and Meyer[93], outlined above, to be useless in the present context, the reason being an extremely slow convergence. Actually, after 20 iterations, involving CPU demanding matrix constructions (eq. (7.8)) and diagonalizations (eq. (7.9)), the approximation employing $(n_x = 5, n_z = 6)$ only improved by a factor of 10^{-6}. However, it is possible that the scheme will converge faster in more dimensions.

7.3 Implementation of the MCTDH scheme

In this section we briefly outline the numerical scheme for the non-adiabatic MCTDH study of H_2+Cu(100). The details of the multi-dimensional non-adiabatic MCTDH scheme was presented in the previous chapter, and hence we shall only focus on the new features, and give extensive reference to especially section 6.1. Furthermore, many of the numerical techniques employed in the explicit implementation are the same as for the simple one-dimensional study outlined in section 6.2.

Before we present the equations of motion for the single-particle functions we define the single-particle operators

$$\widehat{\mathbf{h}}^s_x = -\frac{\hbar^2}{2\mu}\frac{\partial^2}{\partial x^2} + W_{11}(x, z_0) \tag{7.11a}$$

$$\widehat{\mathbf{h}}^s_z = -\frac{\hbar^2}{2m}\frac{\partial^2}{\partial z^2} \tag{7.11b}$$

where $s = 1, 2$, $\mu = m_{\mathrm{H}}/2$, $m = 2m_{\mathrm{H}}$, and z_0 is fixed asymptotically fare from the metallic surface. This is, as we shall see, a very convenient choice as it will allow us to initiate the single-particle functions as respectively vibrational eigenfunctions of the H_2 molecule in x and a free translational particle in z. The single-surface and two-surface correlation terms are next defined as

$$\widehat{\mathbf{H}}^1 = W_{11}(x, z) - W_{11}(x, z_0) + V^1_{opt}(x) + V^1_{opt}(z) \tag{7.12a}$$

$$\widehat{\mathbf{H}}^2 = W_{22}(x, z) - W_{11}(x, z_0) + V^2_{opt}(x) + V^2_{opt}(z) \tag{7.12b}$$

$$W = W_{12}(x, z) \tag{7.12c}$$

where V^s_{opt} are absorbing potentials in the different coordinates. It is very important to note that even though these optical potentials are strictly single-particle operators, they cannot be included in the definitions of the single-particle operators of eq. (7.11). The reason for this is that in the derivation of the generalized MCTDH scheme the single-particle operators, $\widehat{\mathbf{h}}^s_\kappa$, are assumed to be *Hermitian.* If this is not the case, then the single-particle function will not stay orthogonal as time evolves, *i.e.* eq. (6.8) and (6.9) does not hold. (In the previous chapter we redefined the expansion coefficients to include the absorbing properties, *cf.* eq. (6.39), thereby leaving the single-particle operators Hermitian). In this study we choose a more effective exponential form of the optical potential, as compared to the simple linear potential employed in the one-dimensional calculations (see eq. (6.38)). This allowed us to use a smaller grid in the two-dimensions, which in the present context is of great importance. The explicit form of the optical potentials read as

$$V^s_{opt}(R) = \begin{cases} 0 & \text{for} \quad R_{min} \leq R \leq R_{opt} \\ -iAN \exp\left[-2\frac{R_{max}-R_{opt}}{R-R_{opt}}\right] & \text{for} \quad R_{opt} < R \leq R_{max} \end{cases} \tag{7.13}$$

where $s = 1, 2$, $R = x, z$ and N is a normalization constant found numerically to be 13.22. The absorbing properties of this potential has been investigated thoroughly by Vibók and Balint-Kurti, and in reference [87] they have tabulated optimized values for the parameter A and the range of definition, $\Delta R_{opt} \equiv R_{max} - R_0$, for a given energy domain. As a last comment we also note that the correlating potentials of eq. (7.12) are not the pure diabatic potentials due to the zero-order term $W_{11}(x, z_0)$. This actually means that the two-particle potentials have a more smooth topological behavior, which in turn results in a better product representation when employing the scheme outlined in the previous section.

The working equations for a two-dimensional two-surface system are readily derived from eq. (6.19b) and eq. (6.25). Below we just give the equations of motion for the single-particle functions in the x coordinate, and the corresponding equations in the other coordinate are simply obtained by interchanging x and z. The equations for the time-dependent expansions coefficients (eq. (6.19b)) read as

$$\begin{aligned} i\hbar\dot{A}^s_{i_x i_z} &= \sum_{j_x=1}^{M^s_x}\sum_{j_z=1}^{M^s_z}\langle\phi^s_{i_x}|\langle\phi^s_{i_z}|\widehat{\mathbf{H}}^s|\phi^s_{j_z}\rangle|\phi^s_{j_x}\rangle A^s_{j_x j_z} \\ &+ \sum_{j'_x=1}^{M^{s'}_x}\sum_{j'_z=1}^{M^{s'}_z}\langle\phi^s_{i_x}|\langle\phi^s_{i_z}|W|\phi^{s'}_{j'_z}\rangle|\phi^{s'}_{j'_x}\rangle A^{s'}_{j'_x j'_z} \end{aligned} \tag{7.14}$$

where $(s, s') = (1, 2)$ or $(2, 1)$. Using eq. (6.25) it is easy to show that the equations of motion for the single-particle functions read as

$$i\hbar|\dot{\phi}^s_{i_x}\rangle = \widehat{\mathbf{h}}^s_x|\phi^s_{i_x}\rangle + \sum_{k_x=1}^{M^s_x}\langle 1\rangle^{-1}_{i_x k_x}\cdot\left\{|\tilde{\phi}^s_{k_x}\rangle - \sum_{l_x=1}^{M^s_x}\langle\phi^s_{l_x}|\tilde{\phi}^s_{k_x}\rangle|\phi^s_{l_x}\rangle\right\} \tag{7.15}$$

where we have defined the correlated single-particle functions

$$|\tilde{\phi}^s_{k_x}\rangle \equiv \sum_{j_x=1}^{M_x^s} \langle \widehat{\mathbf{H}} \rangle_{k_x j_x} |\phi_{j_x}\rangle + \sum_{j'_x=1}^{M_x^{s'}} \langle W \rangle_{k_x j'_x} |\phi^{s'}_{j'_x}\rangle \tag{7.16}$$

and the mean-field operators

$$\langle 1^s \rangle_{i_x k_x} \equiv \sum_{i_z=1}^{M_z^s} A^{s*}_{i_x i_z} A^s_{k_x i_z} \tag{7.17a}$$

$$\langle \widehat{\mathbf{H}}^s \rangle_{k_x j_x} \equiv \sum_{k_z=1}^{M_z^s} \sum_{j_z=1}^{M_z^s} A^{s*}_{k_x k_z} A^s_{j_x j_z} \langle \phi^s_{k_z} | \widehat{\mathbf{H}}^s | \phi^s_{j_z} \rangle \tag{7.17b}$$

$$\langle W \rangle_{k_x j'_x} \equiv \sum_{k_z=1}^{M_z^s} \sum_{j'_z=1}^{M_z^{s'}} A^{s*}_{k_x k_z} A^{s'}_{j'_x j'_z} \langle \phi^s_{k_z} | W | \phi^{s'}_{j'_z} \rangle \tag{7.17c}$$

Using the simple relation (see eq. (7.14))

$$\langle \phi^s_{l_x} | \tilde{\phi}^s_{k_x} \rangle = i\hbar \sum_{k_z=1}^{M_z^s} A^{s*}_{k_x k_z} \dot{A}^s_{l_x k_z} \tag{7.18}$$

eq. (7.15) can also be recast into the form

$$i\hbar |\dot{\phi}^s_{i_x}\rangle = \widehat{\mathbf{h}}^s_x |\phi^s_{i_x}\rangle + \sum_{k_x=1}^{M_x^s} \langle 1^s \rangle^{-1}_{i_x k_x} \cdot \left\{ |\tilde{\phi}^s_{k_x}\rangle - i\hbar \sum_{l_x=1}^{M_x^s} \sum_{k_z=1}^{M_z^s} A^{s*}_{k_x k_z} \dot{A}^s_{l_x k_z} |\phi^s_{l_x}\rangle \right\} \tag{7.19}$$

In this form the analogy to the working equations previously used by Fand and Guo[79] is immediately apparent. For the two-dimensional MCTDH treatment of the photodissociation of ICN, they employed an expression equivalent to eq. (7.19) with $\widehat{\mathbf{h}}^s_x \equiv 0$. Even though the difference might seem marginal, it is fare from trivial. The present formulation, with $\widehat{\mathbf{h}}^s_x \neq 0$, can be interpreted as a more general interaction representation of the equations due to Fang and Guo. Since the computation of the mean-fields of eq. (7.17) requires a much greater computational effort in comparison to the simple calculation of the single-particle operators acting on the single-particle functions, a splitting of the Hamiltonian, according to eq. (7.19), should result in a decrease in the computational effort. For a simple two-dimensional single-surface calculation this has been confirmed by Jäckle and Meyer[75]. Furthermore, as noted above, the separation of a zero-order term from the potential energy functions generally lead to smoother surfaces, which in turn result in fewer terms in the product representations. This too will speed up the computation of the mean-field operators. Thus, for instance when computing the mean-field operator entering eq. (7.17b),

$$\begin{aligned}\langle\phi^1_{k_z}|\widehat{\mathbf{H}}^1|\phi^1_{j_z}\rangle \approx &\sum_{i_x=1}^{n_x}\sum_{i_z=1}^{n_z} C_{i_x i_z} V_{i_x}\langle\phi^1_{k_z}|V_{i_z}|\phi^1_{j_z}\rangle \\ &+ V^1_{opt}(x)\delta_{k_z j_z} + \langle\phi^1_{k_z}|V^1_{opt}(z)|\phi^1_{j_z}\rangle\end{aligned} \tag{7.20}$$

the natural potentials, $\{V_{i_x}(x), V_{i_z}(z)\}$, are obtained from the product representation of $W_{11}(x,z) - W_{11}(x,z_0)$, *cf.* eq. (7.6), leading to smaller expansion orders, (n_x, n_z), than for the corresponding representation of $W_{11}(x,z)$. The action of $\widehat{\mathbf{T}}$, entering the single-particle operators, is easily evaluated using a one-dimensional FFT algorithm.

As in the previous chapter we employ a particle-in-a-box DVR scheme in both coordinates. Using the uniform transformations, defined in subsection 2.2.5, the vibrational eigenfunctions of $\widehat{\mathbf{h}}^s_x$ are computed, and they serve as the initial functional form of the single-particle functions $\{\phi^s_{i_x}(x,t=0)\ i_x = 1, M^s_x\}$. As a prelude for the initialization of the translational single-particle functions in z we first define the functions

$$\{(z-z_0)^\alpha\Psi_1(z,t=0) \quad \alpha = 0,1,\ldots,M^s_z - 1\} \tag{7.21}$$

where $\Psi_1(z,t=0)$ is the focusing Gaussian wave function defined in eq. (6.29a). These functions are then orthogonalized by the well-known Gram-Schmidt orthonormalization scheme and properly normalized. It should be noted that the prefactors $(z-z_0)^\alpha$, as oppose to just z^α, are used in order to obtain a numerically stable Gram-Schmidt orthonormalization for large values of α, *i.e.* $M^s_z > 5$. The precision of the Gram-Schmidt scheme can further be improved by iteratively repeating the orthonormalization. For $M^s_z = 7$, 10 iterations was enough the ensure a precision of 10^{-9}. All in all this defines the orthogonal single-particle functions $\{\phi^s_{i_z}(z,t=0)\ i_z = 1, M^s_z\}$ with the built in feature that only $\phi^1_1(z,t=0)$ is initially populated, *i.e.*

$$A^s_{i_x,i_z}(t=0) \equiv \delta_{i_x,n}\delta_{i_z,1}\delta_{s,1} \tag{7.22}$$

where n defines the initial vibrational mode of the H_2 molecule. From the definition of the density matrices in eq. (7.17a) it should be clear that the initial condition of eq. (7.22) lead to singularities. These inherited initial value singularities are exactly the same ones that cost us tremendous numerical problems in the Gaussian

MCTDH scheme, presented in section 5.2. However in contrast to those singularities, the present singularities can be removed by a simple regularization scheme. We defined the regularized "pseudo-inverse" of the density matrix as

$$\underline{\underline{\langle 1^s \rangle}}^{-1} = \left(\underline{\underline{\langle 1^s \rangle}} + \epsilon \underline{\underline{1}} \right)^{-1} \tag{7.23}$$

where ϵ is a small number, typically in the order of 10^{-6}. Other more sophisticated regularization schemes can be employed (see *e.g.* equation (20) in reference [74]), but I found the simple procedure of eq. (7.23) to work well in the present study. Finally, the temporal propagation of the expansion coefficients in eq. (7.14) and the single-particle functions in eq. (7.15) is carried out by a variable-order (up to 11) predictor-corrector scheme.

7.4 Implementation of the split-operator scheme

The present implementation of the split-operator scheme, initially presented in subsection 4.1.2, goes along the same lines as outlined in subsection 6.2.2. Thus, we employ the split-operator defined in eq. (6.40), with the modifications $\widehat{\mathbf{T}} = \widehat{\mathbf{T}}_x + \widehat{\mathbf{T}}_z$ and

$$\underline{\underline{\mathrm{V}}}(x,z) = \begin{bmatrix} W_{11}(x,z) + V_{opt}(x) + V_{opt}(z) & W_{12}(x,z) \\ W_{12}(x,z) & V_{22}(x) + V_{opt}(x) + V_{opt}(z) \end{bmatrix} \tag{7.24}$$

where V_{opt} are the optical potentials defined in eq. (7.13). The action of the kinetic energy operator is evaluated by a two-dimensional FFT algorithm. The total wave function is initiated on the direct-product grid as a vibrational eigenfunction of the H_2 molecule in x, times a Gaussian wave function in z, *i.e.* a product of eigenfunctions for the single-particle operators defined in eq. (7.11). This corresponds to the initial condition of a free hydrogen molecule incident upon a metallic copper surface.

7.5 Numerical results

To extract informations from the two different types of calculations, outlined above, we evaluate the flux of the two-dimensional wave functions. However, unlike in the simple one-dimensional study, presented in the previous chapter, it is only physically meaningful to calculate the momentum-resolved reaction probabilities in the incoming arrangement channel. Due to the cut-off of the diabatic potentials for relatively small values of x (*cf.* figure 7.6), we can only define well behaved asymptotic states in the z direction, corresponding to free molecular hydrogen in some vibrational eigenstate incident upon the metallic copper surface. (The outgoing channel in z on the upper electronic surface, corresponding to free atomic H incident upon Cu(100), is *closed* for all the energy domains investigated in this study). Thus, in the outgoing reactive channels in x, describing dissociated hydrogen on copper, we compute the total outgoing flux of the wave function over a dividing line at x^*, placed immediately after the reaction barrier, see figure 7.5. Hence we cannot distinguish between chemisorbed H_2 on Cu(100) and dissociated hydrogen on copper. From the discussion in section 1.1 it follows that the total reaction probability can be calculated as

$$P_x^s(k_0) = \int_0^{t_{max}} dt \int_{z_{min}}^{z_{max}} dz\, \mathbf{j}_x \left[\Psi^s(x^*, z, t)\right] \tag{7.25}$$

where $\mathbf{j}_x \left[\Psi_{n_0}^s(x^*, z, t)\right]$ is the quantum flux in the x direction on surface $s = 1, 2$ of the total wave function at the point (x^*, z), see definition in eq. (1.9). In the incoming arrangement channel in z we calculate the momentum-resolved reflection probabilities in much the same way as outline in the introduction of subsection 6.2.3. However, the following modifications are made primarily because of the additional channel-index, n, describing the vibrational mode of the H_2 molecule. Eq. (6.43) now read as

$$F_{n_0\to n}(k, t) = \frac{\hbar k_{n_0\to n}}{m} \left|\Psi_{n_0\to n}(k, t)\right|^2 \tag{7.26}$$

where $k_{n_0\to n} = \sqrt{k^2 - 2m(E_n - E_{n_0})/\hbar^2}$ and n_0 denotes the initial vibrational quantum number. Since the outgoing arrangement channel in z on the upper surface is closed for all the energy domains investigated in this study, the surface index 1 and arrangement index z are implicit in eq. (7.26) and throughout the rest of this discussion. As a prelude for the calculation of $\Psi_{n_0\to n}(k, t)$, we project the total wave function onto the vibrational eigenfunctions of H_2 at the dividing line through z^*, *i.e.*

$$\Psi_{n_0\to n}(z^*, t) \equiv \int_{x_{min}}^{x_{max}} dx\, \phi_n(x, 0) \Psi_{n_0}(x, z^*, t) \tag{7.27}$$

where $\phi_n(x, 0)$ in the MCTDH formulation are the initial single-particle functions in the x coordinate. As in eq. (6.47) we next perform the time/energy Fourier transform of these functions,

$$\Psi_{n_0\to n}(z^*, E) = \frac{1}{\sqrt{2\pi}} \int_0^{t_{max}} dt\, \exp\left[iEt/\hbar\right] \Psi_{n_0\to n}(z^*, t) \tag{7.28}$$

where $E = E_n + \frac{k^2\hbar^2}{2m}$. Finally, using the equivalent of eq. (6.48), the momentum-resolved reflection probabilities read as

$$P_{n_0\to n}(k) = \frac{\hbar^2 k k_{n_0\to n} |\Psi_{n_0\to n}(z^*, E)|^2}{\Delta z_0 m^2 \exp\left[-2\Delta {z_0}^2 (k-k_0)^2\right]} \tag{7.29}$$

and the total probabilities are given by

$$P^{tot}_{n_0\to n}(k_0) = \frac{\hbar^2}{k_0 m^2} \int_0^{k_{max}} dk\, k^2 k_{n_0\to n} |\Psi_{n_0\to n}(z^*, E)|^2 \tag{7.30}$$

In table 7.1 we have listed the numerical values of the parameters fixed in the generalized MCTDH and split-operator calculations. Like in the previous chapter all the numbers and results presented in this chapter are reported in molecular units[2]. Throughout the rest of this chapter we will denote the molecular energy unit (100 kJ/mol $\approx$ 1 eV) by ϵ. As noted in the table the numerical values of some of the parameters are actually dependent on the initial choice of the energy, *i.e.* k_0 and n_0, but the range of values are nevertheless typical.

Let us start by discussing some of the features and results obtained for the dynamical system of H_2+Cu(100) itself. Figure 7.8 shows a plot of the fully converted reflection probability obtained from eq. (7.29) with $n = n_0 = 1$, *i.e.* the vibrational ground state. The plot shows that for k values below 15Å^{-1}, corresponding to approximately 0.2ϵ, the hydrogen molecule bounces back from the copper surface, without any vibrational excitation. This is in good agreement with the hight of the reaction barrier of approximately 0.4ϵ, see figure 7.5, and the fact that $E_2 - E_1 = 0.77\epsilon - 0.26\epsilon = 0.51\epsilon >> 0.2\epsilon$ as measured from the bottom of the lower surface at z_0. However, it is a bit disappointing to observe that for energies just above the barrier ($k \approx 20\text{Å}^{-1}$) the system reacts 100%, corresponding to all of the hydrogen adsorbing on the copper surface. This is not observed experimentally, where the dissociation probability saturates at a value less than 1. This, we think, is the indication of a true non-adiabatic process, and the fact that we do not observe this saturation in the present non-adiabatic study is most probably because of a poor assumption for the form of the non-diabatic coupling surface, eq. (7.3). This is confirmed by the fact that for energies above the barrier, we found that only about 10% of the wave packet resides on the upper surface for approximately 20 Fs (see figure 7.12 later), which on a time scale of 300 Fs, for the direct reaction, is very little. (See also figure 7.18 at the end if this section). Thus,

---

[2] The molecular units of energy, mass, length and time are respectively 100 kJ/mol $\approx$ 1 eV, 1 amu, 1Å and 10^{-14} s = 10 Fs. In these units $\hbar$ has the value 0.06350781278 (see appendix A in reference [89] for the numerical values of other physical constants).

Table 7.1: Numerical values of the parameters fixed in the calculations. The numbers are reported in molecular units (see footnote 2 on page 119).

Parameters	MCTDH[h]	Common	Split[i]
Grids:			
x_{min}(Å)		0.0	
x_{max}(Å)		4.0	
N_x[a]		64	
z_{min}(Å)		-0.2	
z_{max}(Å)		10.0	
N_z[a]		128	
Propagation:			
x^*(Å)		2.0	
z^*(Å)[b]		8.0	
$\Delta t(10^{-14}\mathrm{s})$[a]	0.005		0.002
Precision	10^{-6}[c]		—[d]
Gaussian wavepacket:[e]			
z_0(Å)		8.0	
z_{foc}(Å)		1.2	
Δz_0(Å)		0.5	
Coupling potential:[f]			
A(100kJ/mol)		3.4	
Δs(Å)		0.7	
Δv(Å)		0.6	
Optical potentials:[g]			
x_{opt}(Å)		2.2	
A_x(100kJ/mol)		0.5[a]	
z_{opt}(Å)		8.2	
V_z(100kJ/mol)		0.5[a]	

[a] This parameter is actually dependent on the initial energy of the system, but the listed value was typical for most calculations.

[b] The time sampling of the wave function along this line (see eq. (7.27) and (7.28)) was not started before the wavepacket was moving out of the reaction region.

[c] Input-parameter to the variable order predictor-corrector routine.

[d] The Split operator method does not offer any control over the precision in the time-propagation.

[e] See eq. (6.29a)

[f] See eq. (7.3)

[g] See eq. (7.13)

[h] Generalized MCTDH as described in section 7.3.

[i] Split-operator scheme, employing the FFT algorithm, as described in section 7.4.

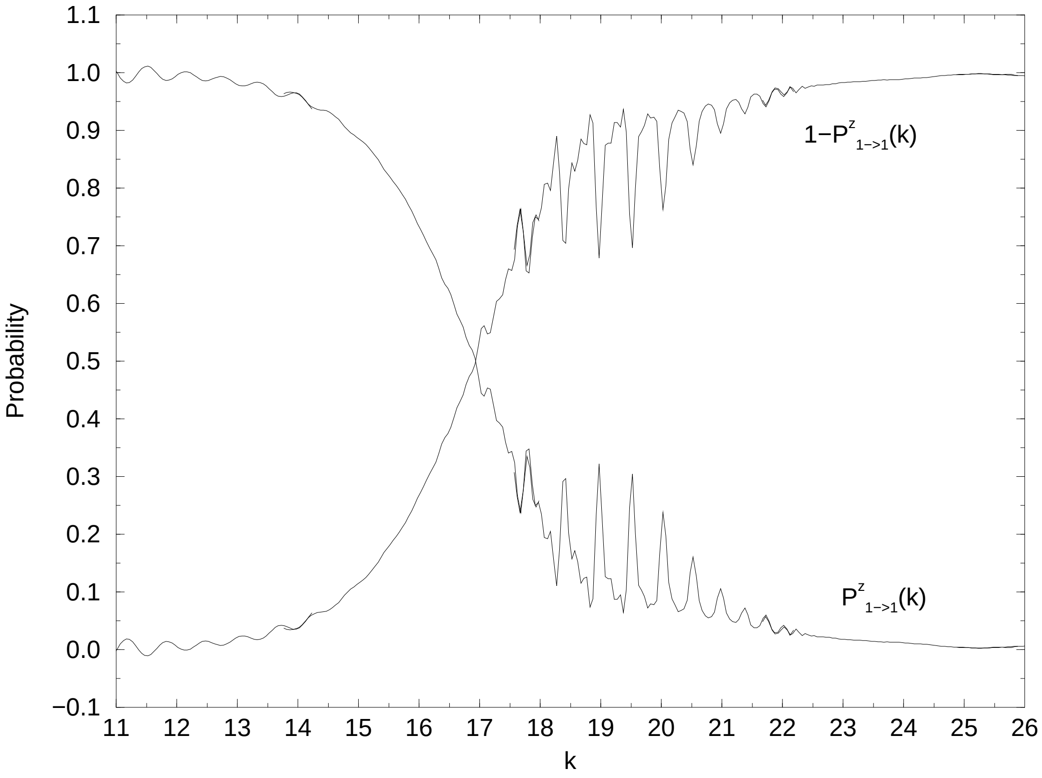

Figure 7.8: Plot of the fully converted reflection probability $P^z_{1\to 1}(k)$.

it seems that the non-adiabatic coupling in the present approximated formulation has been underestimated.

However, a very interesting feature of figure 7.8 are the structures around $k = 20\text{Å}^{-1}$, indicating the formation of quasi-bound *resonance* states, corresponding to physisorption of H_2 in the well just before the reaction barrier, see figure 7.5. This is confirmed by plots of the probabilities density for the two-dimensional wave function for times larger than 200 Fs, see figure 7.16 and 7.17 at the end of this section. The characterization and study of such resonance states is exactly the topic of the next part of this thesis, but for now we shall just think of them as quasi-bound states in which the system is trapped for a considerable amount of time. As such, the formation of resonances in the present dynamical study constitutes a tedious numerical problem because the propagation times had to be considerably prolonged. Hence, in order to obtain the fully converted probabilities shown in figure 7.8, the calculations around $k = 20\text{Å}^{-1}$ were propagated to 750 Fs, *i.e.* the computational times were more than doubled.

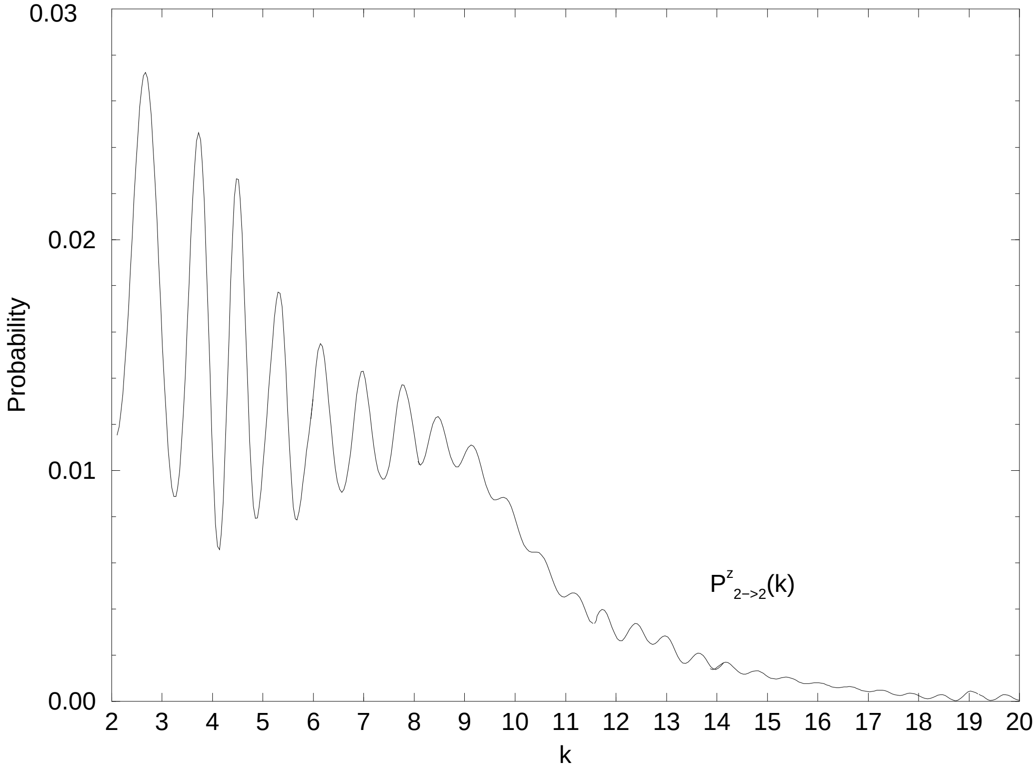

Figure 7.9: Plot of the fully converted reflection probability $P^z_{2\to 2}(k)$.

Figure 7.9 shows a plot of the fully converted reflection probability obtained from eq. (7.29) with $n = n_0 = 2$, *i.e.* the first excited vibrational state. The plot shows almost complete dissociation for all values of k, which is in agreement with the available energy ($> E_2 - E_1 = 0.51\epsilon$) and the hight of the barrier ($\approx 0.4\epsilon$). The structures for low k are possibly due to the formation for resonances, but this is difficult to confirm visually due to the very low amplitudes.

Now, let us return the main topic of this chapter namely the test of the generalized MCTDH scheme outlined in section 7.3. In figure 7.10 the convergence of $P_{1\to 1}(k)$ for 6 MCTDH calculations, employing respectively $(2, 3, 4, 5, 6, 7)$ single-particle functions in both coordinates, is shown against the "exact" results using the split-operator scheme. The different probability curves are all obtained from a single calculation with $k_0 = 20\text{Å}^{-1}$, such that only results in the neighborhood of this value should be considered reliable. It should also be noted that the propagation times were fixed to 300 Fs in all the calculations, which explains for the missing structures when compared to figure 7.8. Thus, the calculations only show

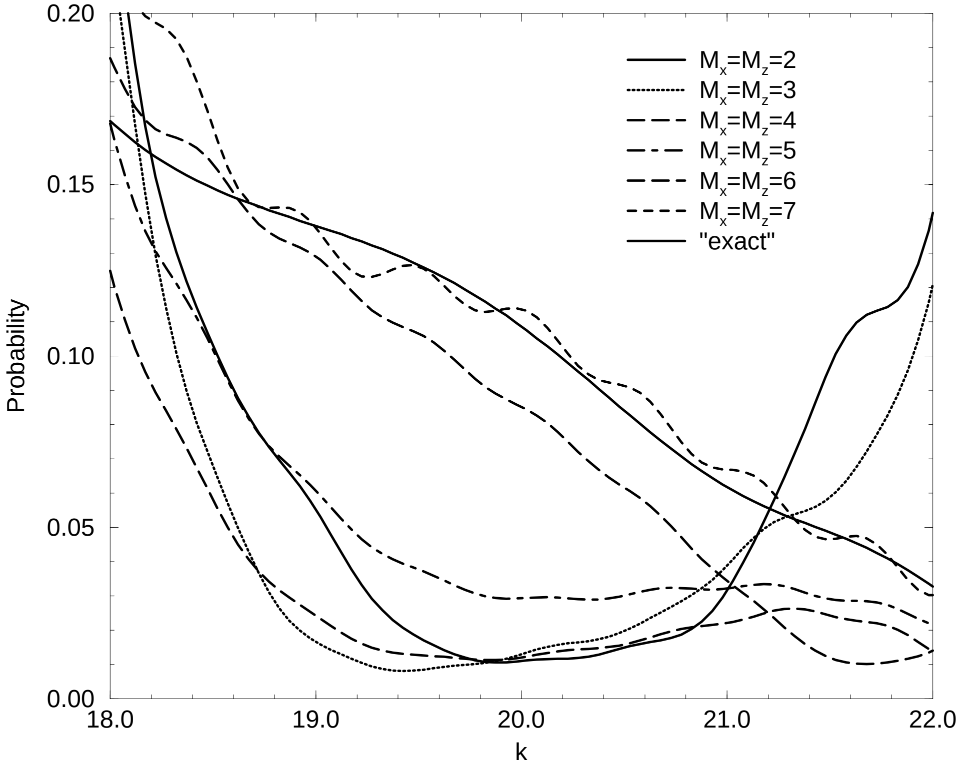

Figure 7.10: Plot of the convergence of $P_{1\to1}(k)$ for 6 MCTDH calculations, employing respectively $(2, 3, 4, 5, 6, 7)$ single-particle functions in both coordinates, shown against the "exact" results using the split-operator scheme.

the direct dissociation probabilities. As will become clear later, this was done to significantly reduce the computational times. The curves show a clear convergence to the "exact" result as expected. The MCTDH calculations, employing less than 6 single-particle functions in the two coordinates, show too high reactivity, but with $M_x = M_z = 6$ the right behavior of the probability curve is observed, and with 7 functions the probability is almost converted.

Table 7.2 shows a list of the total probabilities in the different arrangement channels, for the calculations depicted in figure 7.10. These number were obtained using eq. (7.25) and (7.30). The table also lists the total CPU times, times pr. propagation step and the performance of the FORTRAN code in megaflops. The same convergence is observed in this table for the total reaction probabilities, as was seen for the energy-resolved probabilities in figure 7.10. It is however disappointing to see that at no level of approximation does the MCTDH scheme offer a computational advantage over the direct split-operator scheme – at least not in terms of CPU time. This, we think this is primarily due to the superiority of the simple two-dimensional FFT algorithm over the relative complexity of the MCTDH scheme employing a slow predictor-corrector propagation. However, as will be argues below, it is very important to emphasize that the MCTDH calculations could have been significantly improved by allowing for less single-particle functions on the upper surface. Even more speed-up would result from a flexible implementation of the MCTDH scheme where single-particle functions were added as needed during the time propagation itself. Finally it should be noted that the MCTDH code still needs to be further optimized for the vector computer. The table also shows an exponential growth in the amount of computational work, as the number of employed single-particle functions are increased. This exponential scaling of the MCTDH scheme in the number of single-particle functions has been predicted by Manthe *et al.*[74]. In this reference they also argue that the scheme should feature a favorable semi-linear scaling in the number of degrees of freedom, which we can however not see any clear evidence for. Only in the very approximate limit, employing less that 4 single-particle functions, does the MCTDH scale better than the split-operator scheme, when going from one to two dimensions (*cf.* table 6.2 and 6.3). Considering the reservations concerning the insufficient implementation of the MCTDH code, it is difficult to make any clearcut conclusions based on the CPU times listed in table 7.2, however is seems inevitable to say that the present MCTDH implementation does not seem to be the method of choice for a system like the one studies here.

In figure 7.10 and table 7.2 we examined the convergence of the MCTDH scheme by a direct comparison to the exact solution of the split-operator method. This is of course the obvious way to examine the convergence, but the MCTDH actually offers another type of "self control" which does not refer to other calculations, and as such can be very useful when exact results cannot be produced. As discussed in detail in section 6.1, one can define a unique set of natural single-particle functions by diagonalizing the density matrices (see eq. (7.17a)), and the resulting eigenvalues, called natural weights, are a direct measure of the population of the corresponding natural single-particle functions. In figure 7.11 we have shown a plot of $\log[\Lambda^1_{i_z}(t)]$ where $\Lambda^1_{i_z}(t)$ is the natural weight of single-particle function i_z on the lower surface at time t. The plot clearly shows that the contribution from the added single-particle functions gradually decreases, and it is interesting to see that at no time does single-particle function number 7 contribute to the total wave function by more than a factor of one thousandth. The plot also gives a very interesting picture of when the different single-particle functions actually contribute during the dynamical event, and it is clear that this is mainly when the wave packet crosses the barrier after 120 Fs. This characteristic feature could be exploited in the numerical

Table 7.2: Convergence of the total reaction probabilities in the different channels of H_2+Cu, as a function of the number of employed single-particle functions in the MCTDH scheme. All the tabulated calculations were initiated in the vibrational ground state of the hydrogen molecule, and with a kinetic energy corresponding to $k_0 = 20(\text{Å}^{-1})$. The calculations were all propagated to 300 Fs, at which time the direct scattering was over. It should also be noted that the MCTDH code has not yet been fully optimized, and as such the reported CPU times for these calculations are temporary.

M[a]	$P_z^1(k_0)$[b]	$P_x^1(k_0)$	$P_x^2(k_0)$	$P_{tot}(k_0)$[c]	$P_0(k_0)$[d]	time[e]	time/step[f]	MFLOP[g]
2	17.31	51.09	0.22	68.62	31.38	1168	0.19	220
3	14.12	84.62	0.41	99.15	0.85	2181	0.36	281
4	3.17	93.33	0.47	96.97	3.03	5863	0.98	309
5	4.68	91.22	0.46	96.36	3.64	10482	1.74	326
6	8.77	88.39	0.45	97.61	2.39	17105	2.85	349
7	11.04	82.63	0.45	94.12	5.88	26253	4.37	379
split[c]	10.92	82.24	0.43	93.59	6.41	1116	0.08	323

[a] Number of single-particle functions in both coordinates, *i.e.* $M = M_x = M_z$.

[b] $P_z^2(k_0)$ was constantly found to be zero.

[c] $P_{tot}(k_0) \equiv P_z^1(k_0) + P_x^1(k_0) + P_x^2(k_0)$

[d] $P_0(k_0) \equiv 100 - P_{tot}(k_0)$, *i.e.* a measure of physisorption.

[e] Total CPU time in seconds.

[f] CPU time pr. propagation step.

[g] Million floating point operations pr. second on a single CPU of a Cray C92 (peak performance is approximately 900 MFLOP).

[h] Results obtained from the split-operator scheme.

implementation, by gradually switching on the single-particle functions as needed in the calculation. We expect that this could give a significant speed-up of the MCTDH scheme. Note also that after the crossing of the barrier, the sum-curve dramatically decreases to a value below zero, which is due to the absorption of the wave packet by the optical potential in the exit channel. It is equally evident from this figure why less than 6 single-particle functions give so poor results. Finally, we note that the minimum value of $\Lambda^1_{i_z}(t)$ is introduced by the regularization scheme defined in eq. (7.23).

In figure 7.12 we have shown a logarithmic plot of the natural weights for the single-particle function in the z coordinate on the upper surface. This plot shows the same characteristic time-evolution of the contributions from the different single-particle functions as depicted in figure 7.11. However, two features are unique for this plot.

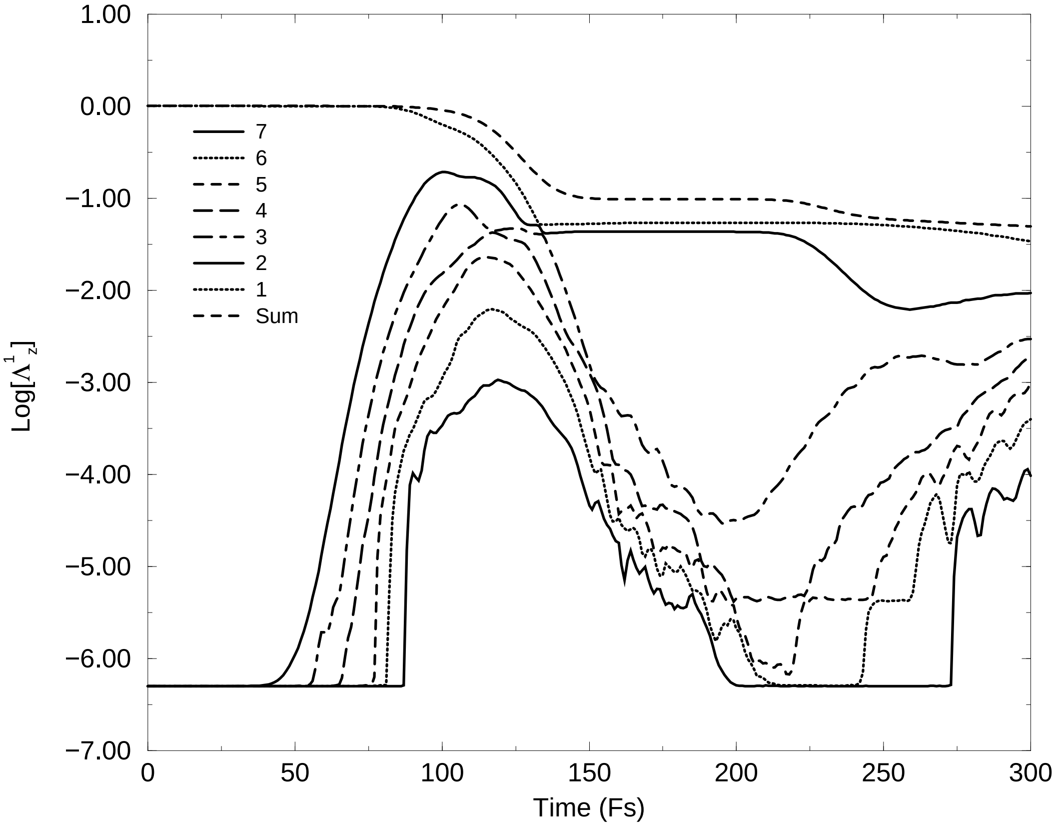

Figure 7.11: Logarithmic plot of the natural weights for the single-particle function in the z coordinate on the lower surface.

First of all we observe that very little (maximum 10%) of the wave packet actually populates the upper diabatic surface. As mentioned above, this can explain for the saturation of the reaction probability at unity, which in turn is an indication of an underestimated non-adiabatic coupling due to a poor approximation of W_{12} through eq. (7.3). The other interesting observation that can be made from this plot is that the contributions from the 3-4 lowest curves are virtually zero, which of course suggests that we could have done with only 3 single-particle functions in this degree of freedom. Thus, this could also be exploited in the code leading to yet another significant reductions of the computational efforts.

On the last few pages of this chapter we have shown a series of "animations" of the dynamical reaction of H_2+Cu(100). The series of plots, figure 7.13 to figure 7.16, show the probability densities of the lower wave function as a function of time obtained from MCTDH calculations employing respectively 2, 3, 5 and 7 single-

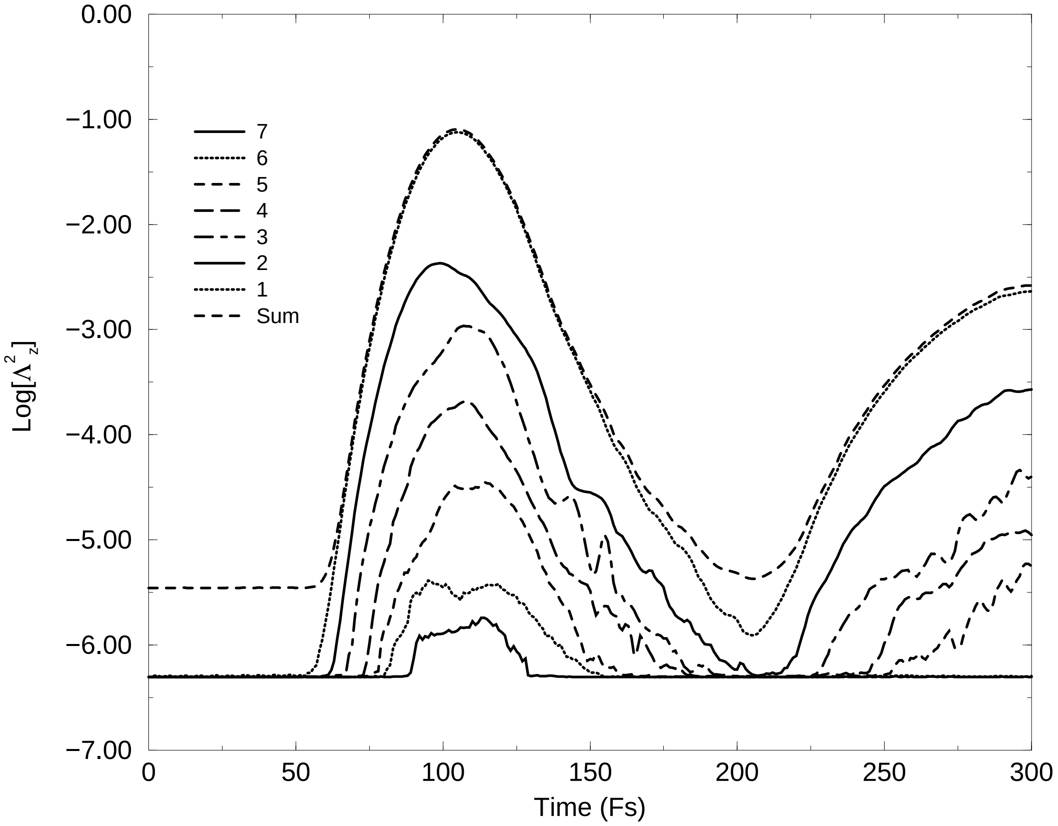

Figure 7.12: Logarithmic plot of the natural weights for the single-particle function in the z coordinate on the upper surface.

particle functions in the two coordinates. These plots should be compared to figure 7.17 showing the corresponding results for the split-operator method. In all the depicted calculations the system was initiated in the vibrational ground state and with $k_0 = 20\text{Å}^{-1}$. The plots show a clear convergence to the exact wave function as the number of single-particle functions are increased. Note also the formation of a vibrationally excited quasi-bound resonance state at $t = 250$Fs and $t = 300$Fs. This is especially clear in figure 7.16 and 7.17. Finally figure 7.18 shows plots of the probability densities on the upper diabatic surface, and it seems evident from these figures that in the present approximate formulation of the potentials the non-adiabatic transition is very limited.

7.6 Conclusion

First of all we stress that the potential energy surfaces, on which the work presented in this chapter was based, are by construction very approximate. Consequently we have refrained from drawing too drastic conclusions on the dynamical system of molecular hydrogen on a copper (100) surface, and instead focused on the implementation and performance of the generalized MCTDH scheme. A clear indication of the insufficiency of the employed diabatic surfaces is the observation that for energies above the reaction barrier the collision leads to complete dissociation of H_2, which suggests that the non-adiabatic coupling in the present formulation is underestimated. However, as one very interesting feature of the studies system, we found evidence for the formation of resonance states, corresponding to physisorption of H_2 on the Cu(100) surface. In future work we plan to improve the surfaces by employing the correct adiabatic-diabatic transformation scheme, outlined in section 3.4, and furthermore include phonon excitation in the metallic surface in order to get a more realistic description of Cu(100).

The main objective of the work presented in this chapter was to study the two-dimensional two-surface implementation of the generalized MCTDH scheme, derived in the previous chapter. As fare as this objective is concerned the project was a success, in the sense that we have demonstrated that the generalized MCTDH scheme does indeed converge to the “exact” solution as more and more single-particle functions are employed in the calculations. We also emphasize that the numerical implementation was found to be fairly simple and stable, suggesting that the extension to more degrees of freedom will be equally simple. However, we cannot hide the disappointment in discovering that the MCTDH scheme was actually much slower than the direct solution employing the split-operator scheme. We have pointed out several obvious way to significantly improve the numerical performance of the MCTDH code, basically related to a more effective and flexible implementation of a dynamical truncated basis-set, but it is probably unrealistic to think that this will improve the MCTDH scheme to the extend that it can actually outperform the direct methods in the exact limit. Thus, at best we can conclude that the generalized MCTDH scheme, in this work, seems most advantageously geared for the approximate limit of description, event though it does indeed offer the exact solution as well. If we however, for the sake of the argument, ignore these obvious insufficiencies of the presented implementation of the MCTDH scheme, we seem to be in the same situations as in the conclusion of the previous chapter where we had to resort to the frustrating phrase “it is possible that going to larger dimensionality will change this picture”.

(a) $T = 0\,\mathrm{Fs}$

(b) $T = 50\,\mathrm{Fs}$

(c) $T = 100\,\mathrm{Fs}$

(d) $T = 120\,\mathrm{Fs}$

(e) $T = 150\,\mathrm{Fs}$

(f) $T = 200\,\mathrm{Fs}$

(g) $T = 250\,\mathrm{Fs}$

(h) $T = 300\,\mathrm{Fs}$

Figure 7.13: Plot of probability density on the lower surface for a MCTDH calculation with $M_x = M_z = 2$ and $k_0 = 20$.

(a) $T = 0\,\mathrm{Fs}$ (b) $T = 50\,\mathrm{Fs}$

(c) $T = 100\,\mathrm{Fs}$ (d) $T = 120\,\mathrm{Fs}$

(e) $T = 150\,\mathrm{Fs}$ (f) $T = 200\,\mathrm{Fs}$

(g) $T = 250\,\mathrm{Fs}$ (h) $T = 300\,\mathrm{Fs}$

Figure 7.14: Plot of probability density on the lower surface for a MCTDH calculation with $M_x = M_z = 3$ and $k_0 = 20$.

(a) $T = 0\,\mathrm{Fs}$ (b) $T = 50\,\mathrm{Fs}$

(c) $T = 100\,\mathrm{Fs}$ (d) $T = 120\,\mathrm{Fs}$

(e) $T = 150\,\mathrm{Fs}$ (f) $T = 200\,\mathrm{Fs}$

(g) $T = 250\,\mathrm{Fs}$ (h) $T = 300\,\mathrm{Fs}$

Figure 7.15: Plot of probability density on the lower surface for a MCTDH calculation with $M_x = M_z = 5$ and $k_0 = 20$.

(a) $T = 0\,\mathrm{Fs}$ (b) $T = 50\,\mathrm{Fs}$

(c) $T = 100\,\mathrm{Fs}$ (d) $T = 120\,\mathrm{Fs}$

(e) $T = 150\,\mathrm{Fs}$ (f) $T = 200\,\mathrm{Fs}$

(g) $T = 250\,\mathrm{Fs}$ (h) $T = 300\,\mathrm{Fs}$

Figure 7.16: Plot of probability density on the lower surface for a MCTDH calculation with $M_x = M_z = 7$ and $k_0 = 20$.

(a) $T = 0\,\mathrm{Fs}$ (b) $T = 50\,\mathrm{Fs}$

(c) $T = 100\,\mathrm{Fs}$ (d) $T = 120\,\mathrm{Fs}$

(e) $T = 150\,\mathrm{Fs}$ (f) $T = 200\,\mathrm{Fs}$

(g) $T = 250\,\mathrm{Fs}$ (h) $T = 300\,\mathrm{Fs}$

Figure 7.17: Plot of probability density on the lower surface for an "exact" calculation with $k_0 = 20$.

(a) $T = 80\,\mathrm{Fs}$ (b) $T = 90\,\mathrm{Fs}$

(c) $T = 100\,\mathrm{Fs}$ (d) $T = 110\,\mathrm{Fs}$

(e) $T = 120\,\mathrm{Fs}$ (f) $T = 130\,\mathrm{Fs}$

(g) $T = 140\,\mathrm{Fs}$ (h) $T = 150\,\mathrm{Fs}$

Figure 7.18: Plot of the probability density on the upper surface for an “exact” calculation with $k_0 = 20$.

8

Discussion and summary

In this part of the thesis we have formulated a general non-adiabatic extension of the MCTDH method and successfully applied it to respectively a one-dimensional model system and the two-dimensional system of H_2+Cu(100). Both of the numerical studies show that the generalized MCTDH scheme does indeed produce the exact solutions in the limit of many single-particle functions, as was expected from the formulation. However, the two studies also seem to reveal that the MCTDH method is most advantageously geared for the approximate limit of description, as compared to more direct methods like the split-operator approach. If this is in fact true, it is quite interesting to note that in the literature, the MCTDH method is generally referred to as an exact quantum approach. Whereas this is in principle correct, the best use of the method appears to be in the approximate limit, which, strictly speaking, puts this approach in another type of category. Many recent publications have applied the MCTDH scheme on multi-dimensional systems[59, 78], but very few (if any) report a comparison of the CPU times to the exact methods, often because the systems under consideration are so big (*e.g.* five-dimensional) that such direct calculations are simply not possible. In these cases the obvious question would naturally be, how accurate are the MCTDH calculations then ?

In the studies presented in this part of the thesis we have applied the generalized MCTDH scheme to fairly simple systems, at least in terms of dimensionality. The reason for this was of course that we wanted to test the performance on this approach against a direct "exact" method. However, one could surely argue that the systems studied so fare might not be large and complex enough to really exploit the advantages of the MCTDH approach. One of the distinct advantages of the MCTDH scheme is exactly connected to the large flexibility of the scheme to deal with complicated situations encountered in complex collision experiments. The scheme allows for the employed time-dependent basis-sets to be adjusted and fine tuned for exactly the numerical problem at hand. This we did not exploit to a full extent in the work presented here. The other distinct advantage of the MCTDH scheme is related to the fact that one avoids to compute multi-dimensional matrix elements, which in turn should give a favorable scaling of the numerical implementation. With only two dimensions it is reasonable to say that this advantageous feature of the MCTDH scheme has also not been exploited fully.

Thus, all in all it seems plausible that the somewhat frustrating picture outlined in this work will change as we move on to larger dimensionality. For the exact same reason I am presently working on the implementation of the generalized MCTDH scheme to a three-dimensional system. As was clearly demonstrated in the previous chapter the working equations are easily obtained from the general expressions derived in chapter 6, *cf.* eq. (6.19b)→(7.14) and eq. (6.25)→(7.15). The difficult part is rather related to the proper choice of the numerical representation (*i.e.* FBR) of the Hamiltonian, which in turn is closely related to the choice of coordinate representation for the reactive system. This problem was discussed in detail in section 2.1, and we pointed put the distinct advantage of the hyperspherical coordinates, primarily due to the evenhanded way the different arrangement channels are described in this coordinate system. Thus, my choose of coordinates for this three-dimensional study are a slightly modified version of the Johnson coordinates defined in subsection 2.1.3. In these hyperspherical coordinates the Hamiltonian operator for a general three particle system, A+B+C, with zero total angular momentum, read as[64]

$$\widehat{\mathbf{H}} = \widehat{\mathbf{H}}^0 + V = -\frac{2\hbar^2}{\mu\rho^2}\left(\frac{\partial^2}{\partial\theta^2} + \frac{1}{\sin^2\theta}\frac{\partial^2}{\partial\phi^2} + \frac{1}{\sin^2 2\theta} + \frac{1}{16}\right) + V(\phi,\theta,\rho) \tag{8.1}$$

where the hyper-angles are confined to the intervals $0 \leq \theta \leq \pi/2$ and $0 \leq \phi \leq 2\pi$. It should be clear from this expression that θ display singularities at both extremes of the domain of definition. Hence, I have recently worked on the construction of a new effective ad hoc basis-set in this coordinate, which by construction removes the singularities. Using a factorization method of Infeld and Hull[95] on the a differential equation first studied by Pöschl and Teller[96] I have been able to construct numerical exact representations of the θ-eigenfunctions of $\widehat{\mathbf{H}}^0$. Using this basis-set I hope in the near future to be able to produce some new and exciting results for a non-adiabatic three-dimensional application of the generalized MCTDH scheme.

As a closing remark for this part of the thesis we note that in both of the presented numerical studies we saw clear evidence of the formation of resonances states, leading to significantly prolonged propagation times. Several different methods have been proposed in the literature to deal with this problem in time-dependent dynamics. For instance Neuhauser and coworkers[97] have studied a scheme where the description of collisions affected by resonances is split into a direct scattering event and a contribution coming solely from the formation of the resonances. In short they, stop the propagation of the wave function at some time when the direct scattering is believed to be over, and the wave function at this time-step is next used as a guided input for a subsequent characterization of the resonances using the Lanczos recursion, mentioned in subsection 4.1.4, or the filter diagonalization method[98, 99], also developed by Neuhauser. However, it is the point of view of this thesis that the time-independent so-called complex coordinate methods are better suited for the pure description of molecular resonances. This is exactly the topic of the next part of this thesis.

Part III

Resonances by complex methods

9

Introduction

In this last part of the thesis I will discuss and present two studies of molecular resonances by complex methods. This work is based on two publications[3, 4] (see A.3 and A.4 in part IV for the abstracts) and large parts of especially chapter 10 and 11 are reproductions of these articles. However, additional figures and explanations will be found in these chapters, and extensive reference will be made to the first introductory part of this thesis. To the extend possible, the two studies are linked together, and consequently the observant reader will find that certain sections have been shuffled around to give a more coherent presentation. It should also be noted that the order in which the work is presented is not chronological. This is done because the first project by fare offers the best introduction in terms of simplicity of the model and formulation.

Throughout the rest of this chapter we shall try to answer some of the fundamental questions concerning characteristics, nature and existence of molecular resonances in quantum dynamics, which in turn leads up to two studies in chapter 10 and 11. Section 9.1 gives a brief description of resonances, and in section 9.2 we will give a motivation for the study of resonances. The foundation for the discussions in these two sections was given in section 1.2 in the first part of this thesis. Next section 9.3 explains the underlying quantum mechanisms leading to the formation of resonances, and finally section 9.3 mentions some of the most important methods used to locate resonances, and focus on the two complex methods which will also be explained in greater details in the subsequent chapters.

9.1 What are resonances and how are they characterized?

When colliding particles temporarily stick together to form complexes we have what is known as a "resonance state" in the time-independent picture[1]. This is a state of the system that has enough energy to break up into smaller parts as *e.g.* in indirect photodissociation. As such a resonance state can be viewed as "something" in between a bound state, where the particles stay together, and a continuum state with free particles. Thus, as a natural prelude to the explicit definition of a resonance state we shall first have to review the latter two situations.

As motivated in the introduction of chapter 1, and subsequently exemplified in section 1.2, quantum mechanics is all about solving the Schrödinger equation subject to boundary conditions to ensure that certain physical requirements are met. If we, for the sake of simplicity, consider a simple elastic collision, we can follow along the same lines as given in section 1.2, and write the asymptotic form of the partial wave function as (see eq. (1.29b))

$$\lim_{r\to\infty} \psi_\ell^{scatt}(kr) \propto S_\ell(k)e^{ikr} - e^{-ikr} \tag{9.1}$$

where $k^2 = 2\mu E/\hbar^2 > 0$ and the ratio between the incoming and outgoing components of the continuum wave function is given by the celebrated S-matrix, $S_\ell(k) \equiv e^{i2\eta_\ell}$. When dealing with bound state problems the physics requires that the solution is square integrable, *i.e.* the solutions are in the Hermitian domain of the Hamiltonian, and the energy is real negative. Hence, we can write the boundary condition as

$$\lim_{r\to\infty} \psi_\ell^{bound}(kr) \propto e^{-\kappa r} \tag{9.2}$$

where $\kappa > 0$. Comparing this expression to the general boundary condition given in eq. (9.1), it is easy to see that stationary states correspond to solutions to a scattering problem with a negative imaginary wave number, $k = -i\kappa$, at a node of the S-matrix, $S(k) = 0$. Resonances, on the other hand, are on physical grounds defined as wave functions with *pure outgoing* (Siegert state[101]) boundary conditions with a complex wave number

$$\lim_{r\to\infty} \psi_\ell^{res}(kr) \propto e^{ikr} = e^{i\kappa_0 r}e^{\kappa_1 r} \tag{9.3}$$

---

[1] Schinke[100] argues in his book "Photodissociation Dynamics" that strictly speaking the term resonance is reserved for the time-independent formulation. In the time-dependent approach "resonance" states are characterized by *recurrences* (*i.e.* damped periodic oscillations) in the autocorrelation function. However, in this thesis we will not make this distinction.

where $\kappa_0 > 0$ and $\kappa_1 > 0$, *i.e.* $k = \kappa_0 - i\kappa_1$. If we again compare this expression to eq. (9.1), we see that resonance states have $S_\ell(-k) = 0$ for complex k. Noting the simple relation[2] $S_\ell(k) = S_\ell(-k)^{-1}$, we arrive at the well known characteristics that resonance states are associated with poles of the S-matrix for complex values of the energy. In the next section we shall discuss this fundamental feature in more detail and elaborate on the consequences in terms of calculations and measurements. The explanation of the divergence property of the resonance wave function in eq. (9.3), ($|\psi_\ell^{res}(r \to \infty)|^2 = e^{2\kappa_1 r}, \kappa_1 > 0$), and a simple physical interpretation of the complex energy, emerge if we consider a stationary solution to the time-dependent Schrödinger equation. If $\psi(r)$ is a solution to the time-independent Schrödinger equation, satisfying eq. (9.3), the solution to the time-dependent problem reads as $\Psi_\ell^{res}(r,t) = \psi_\ell^{res}(r)\exp[-iEt/\hbar]$, where the energy is a complex number $E \equiv E_{res} - i\Gamma/2$. Consequently the probability density of the resonance state is not time-independent in contrast to a bound state, but rather it leaks in time as

$$\begin{aligned} |\Psi_\ell^{res}(r,t)|^2 &= |\psi_\ell^{res}(r)|^2 \exp[-i(E - E^*)t/\hbar] && (9.4a) \\ &= |\psi_\ell^{res}(r)|^2 \exp[-\Gamma t/\hbar] && (9.4b) \end{aligned}$$

and $\Gamma = 2\kappa_0\kappa_1\hbar^2/\mu > 0$ can now be identified as the rate constant or *width* of the exponentially decaying state. Noting that the lifetime is $\mathcal{T} = \hbar/\Gamma$, we conclude that the negative imaginary energy of a resonance is associated to the inverse *lifetime*, and the real part of the energy, $E_{res} = (\kappa_0^2 - \kappa_1^2)\hbar^2/(2\mu)$, is referred to as the *position* of the resonance. As noted by Moiseyev[103] the divergent property of eq. (9.3) is simply a consequence of the conservation law of the number of particles in coordinate and time space (*i.e.* $|\Psi_\ell^{res}(r \to \infty, t \to \infty)|^2$ should remain constant). Using this simple but nonetheless fundamental argument, it furthermore follow from eq. (9.4b) that the broader or shorter-lived a resonance is (*i.e.* for increasing value of Γ in eq. (9.4b)), the more divergent is the asymptotic part of the wave function, $\psi_\ell^{res}(r)$. We especially note that sharp (or long-lived) resonances have a very small asymptotic amplitude as compared to very broad resonances or continuum states. This is an important feature of quasi-bound states that we will refer to several times in the subsequent chapters.

Actually, decaying states, as defined in eq. (9.4b), were already introduced into quantum mechanics in 1928 by Gamow[104], and hence they are sometimes referred to as Gamow states in the literature. As a closing remark to this section I would like to quote Landau[105]: "Although decaying states may appear as just an academic

---

[2] This relation is easily shown by substituting $k \to -k$ in eq. (9.1) and recast it into a form comparable to the former[102].

exercise, they are probably more realistic than conventional quantum mechanics; if we wait long enough many (if not all) particles, nuclei and atoms do decay in time and thus must be described as a type of Gamow (ed. resonance) state."

9.2 Why are resonances so important to study?

The short answer to the question raised in the title of this section was already given in the previous part of this thesis: Resonances manifest itself as complicated structures in the reaction probabilities, and can in the time-dependent description of dynamics result in considerably prolonged propagation times. We actually saw clear examples of this in both the numerical studies presented in respectively chapter 6 and 7. Thus, as such it seems obvious that the ability to predict the exact location of resonances is of great importance to theoreticians in general. However, resonances are of course more then just an annoying complicating feature of a given dynamical system, it represents an interesting physical phenomenon, which often itself is enough reason to study such resonances.

To give a more comprehensive and elaborate answer to this question, however, we shall in this section show how the formal definition of a resonances state, given in the previous section, can easily be shown to lead to these complicating features. To do this, we start by recasting eq. (9.1) into a form which is more convenient for the discussion to follow

$$\lim_{r\to\infty} \psi_\ell^{scatt}(kr) \propto S_\ell(E)^{1/2}\left(S_\ell(E)^{1/2}e^{ikr} - S_\ell(E)^{-1/2}e^{-ikr}\right) \tag{9.5}$$

where $E = \frac{\hbar^2 k^2}{2\mu}$. As mentioned above a resonance state is defined as a pure outgoing Siegert state (see eq. (9.3)) and thus for $E_0 = E_{res} - i\Gamma/2$ it follows that $S_\ell(E_0)^{-1/2} = 0$. Using Taylor series, we can next expand $S_\ell(E)^{-1/2}$ to first order around its zero

$$\begin{aligned} S_\ell(E)^{-1/2} &\approx (E - E_0)\,\dot{S}_\ell^{-1/2}(E_0) && (9.6a)\\ S_\ell(E)^{1/2} &\approx (E - E_0^*)\,\dot{S}_\ell^{-1/2*}(E_0) && (9.6b)\end{aligned}$$

where $\dot{S}_\ell^{-1/2}(E_0) \equiv \frac{dS_\ell^{-1/2}}{dE}|_{E=E_0}$. To obtain eq. (9.6b) we have made used of the fact that the S-matrix is unitary, and further assumed E to be real. It then follows that in the neighborhood of a resonance the S-matrix approximately reads as

$$\begin{aligned} e^{2i\eta_\ell} &\equiv S_\ell(E) = \frac{S_\ell(E)^{1/2}}{S_\ell(E)^{-1/2}} \approx \frac{\dot{S}_\ell^{-1/2*}(E_0)}{\dot{S}_\ell^{-1/2}(E_0)}\,\frac{E - E_{res} - i\Gamma/2}{E - E_{res} + i\Gamma/2} && (9.7a)\\ &\equiv e^{2i\eta_\ell^{pot}}e^{2i\eta_\ell^{res}} && (9.7b)\end{aligned}$$

where we have defined a non-resonant (*i.e.* potential) and a resonant part of the phase-shift by

$$e^{2i\eta_\ell^{pot}} \equiv \frac{\dot{S}_\ell^{-1/2*}(E_0)}{\dot{S}_\ell^{-1/2}(E_0)} \tag{9.8a}$$

$$e^{2i\eta_\ell^{res}} = \frac{\cos\eta_\ell^{res} + i\sin\eta_\ell^{res}}{\cos\eta_\ell^{res} - i\sin\eta_\ell^{res}} \equiv \frac{E - E_{res} - i\Gamma/2}{E - E_{res} + i\Gamma/2} \tag{9.8b}$$

$$= 1 - i\frac{\Gamma}{E - E_{res} + i\Gamma/2} \tag{9.8c}$$

such that $\eta_\ell = \eta_\ell^{pot} + \eta_\ell^{res}$. It is clear from eq. (9.8c) that for $|E - E_{res}| >> \Gamma$ $\eta_\ell \to \eta_\ell^{pot}$, such that in energy regions far from the influence of a resonance, the phase-shift, η_ℓ is a smooth function of E, given by eq. (9.8a). From eq. (9.8b) and the Euler's identity $\tan\theta = (e^{i\theta} - e^{-i\theta})/(ie^{i\theta} + ie^{-i\theta})$, it follows that

$$\tan\eta_\ell^{res} = \frac{\Gamma}{2(E_{res} - E)} \tag{9.9}$$

such that the resonant part of the phase-shift must go through an odd multiple of $\pi/2$ as E traverses E_{res}. Finally, using eq. (1.33a), and the Euler's identity $\sin\theta = (e^{i\theta} - e^{-i\theta})/(2i)$, we obtain the following purely resonant contribution to the partial cross-section

$$\boxed{\sigma_\ell^{res} = \frac{4\pi}{k^2}(2\ell+1)\sin^2\eta_\ell^{res} = \frac{4\pi}{k^2}(2\ell+1)\frac{\Gamma^2/4}{(E_{res} - E)^2 + \Gamma^2/4} \qquad (9.10)}$$

which is the famous Breit-Wigner formula for a the resonance shape of the cross-section. From this equation it is clear that at $E = E_{res} \pm \Gamma/2$ the cross-section is equal to half its maximum value which exactly accounts for the name "resonance *width*" of Γ. In practice however this simple line shape is distorted by the interference from the background or potential phase-shift, η_ℓ^{pot}.

Thus, the existence of resonance states in many molecular reactions show up as complicated structures in the S-matrix or cross-sections, and as such constitutes an important physical phenomenon that must be taken into account when rationalizing anomalous behaviors in scattering data. Actually this point is beautifully illustrated in chapter 6 where we discovered a sharp (at first disturbing) peak in the reaction probability as a function of the collision energy, which as we shall soon show correspond to the formation of a resonance. However, the amount of work associated with the explicit location of the energy positions and life-times of the resonances have been (and to some extent still is) a serious problem to theoreticians. One way to efficiently characterize such resonances is through the use of so-called complex methods, as is the topic of the next two chapters.

9.3 How are resonances formed in quantum dynamics?

The formation of resonances owes to the existence of an attractive well in the interaction potential, and ion-molecule systems like H^++O_2 are good candidates for this[106]. Quantum mechanically, we distinguish between two different kinds of resonances owing to the underlying mechanisms. The simplest are the so-called *shape* or elastic resonances where the wave function is trapped in the well behind a barrier. As illustrated in figure 9.1 this could be the result of a non-adiabatic coupling between respectively an attractive and a repulsive diabatic potential energy surface, or it could simply be a centrifugal barrier (see second term in eq. (3.1b)). In chapter 6 we also found indications of a shape resonance in the model system of two strongly coupled repulsive diabatic surfaces, see figure 6.1. For energies near

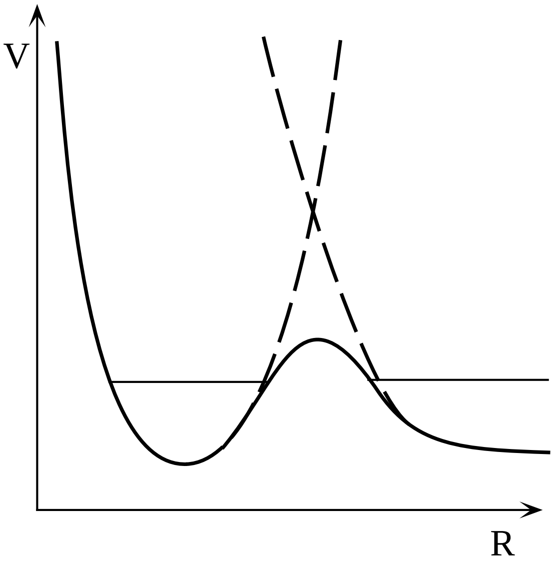

Figure 9.1: Shape resonances correspond to standing waves of the system that tunnel out through a barrier. The barrier is the result of a non-adiabatic coupling between the two diabatic surfaces (the dashed curves)

eigenenergies of the "binding" part of the Hamiltonian (*e.g.* the zero-order Hamiltonian in the absence of non-adiabatic coupling, see dashed curves in figure 9.1), the system forms standing waves in the well and leaks out through the barrier via a tunneling mechanism. Thus, shape resonances can occur in a simple one dimensional system.

Feshbach or inelastic resonances, on the other hand, are associated with energy transfer from translational motion to some internal degree of freedom. In figure 9.2, a continuum state is coupled to some bound state of the vibrational motion, and by this redistribution of the collision energy the system is trapped. Energy then flows back from the vibrational to the translational mode, and eventually enough energy is accumulated in the dissociative coordinate to enable the system to escape.

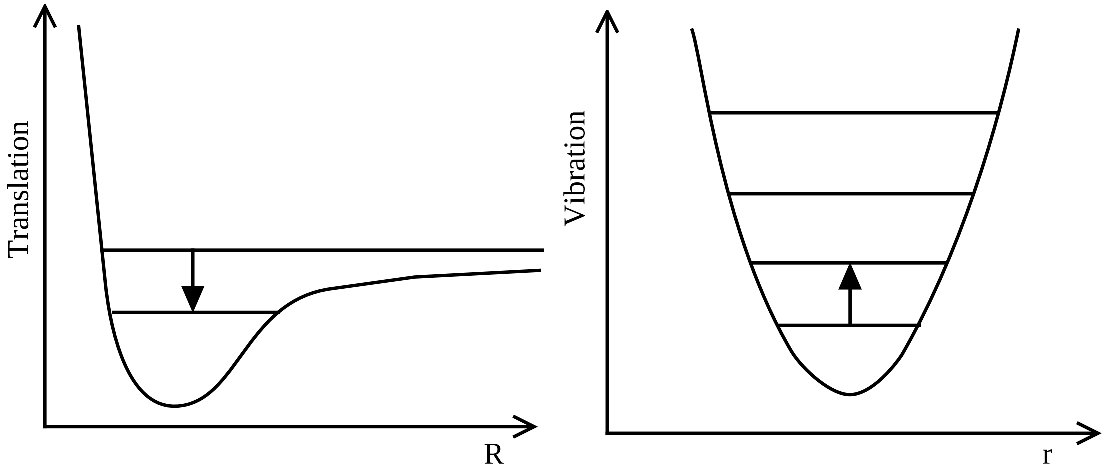

Figure 9.2: When continuum states in the translational motion couple to bound states of some internal degree of motion (*e.g.* vibration) Feshbach resonances are formed.

Thus, common to both types of mechanisms is that they lead to meta-stable states that are embedded in the continuum and *in resonance* with the discrete energy levels of the binding part of the system, which of course accounts for the name "resonance states". So, loosely speaking, ordinary continuum wave functions turn into bound-state-like wave functions in the vicinity of these "zero-order" energies, and the coupling to the dissociative part of the Hamiltonian broadens these discrete energy levels, such that the width (Γ) depend on the coupling strength between the two manifolds. Thus, in conclusion we note that the characteristic resonance structures observed in cross-sections, as described in section 9.2, are actually "fingerprints" of the underlying "binding" part of the system.

9.4 How can resonances be located?

Two important consequences follow immediately from the simple characterization of a resonance state given above in section 9.1. Since the energy must be real positive in any scattering experiment ($k^2 = 2\mu E/\hbar^2 > 0$), one can never have a system which is only decaying. Hence resonances are always accompanied by, often numerous discretized, continuum states. Furthermore, from a "methodical" point of view, the complex value of the resonance energy and the divergent property of $\psi_\ell^{res}(r)$ mean that we cannot obtain resonance states simply by solving the Hermitian Schrödinger equation subject to real boundary conditions. In other words the numerical methods developed for bound problems are not directly applicable to the treatment of resonance states. This is a complicating aspect in the theoretical study of resonances, and have led to many different numerical methods. In the following we briefly review some of the most popular time-independent methods used to locate resonances in quantum dynamics, and especially focus on two complex methods which form the basis of the work presented in this part of the thesis. As noted in the summary of the last part of this thesis time-dependent methods have also been applied successfully to the study of special situations of molecular resonances (see also reference [107, 108]), but it is the overall point of view of this thesis that the time-independent methods, to be discussed below, offer the most general approach to the location of resonances.

One "brute force" way to locate resonances is of course to solve the close-coupled (vibrational) equations (see eq. (3.10) or eq. (3.23)) with the Siegert state asymptotic boundary conditions given in eq. (9.3). Alternatively one can also solve the coupled equations subject to the general boundary condition given in eq. (9.1), and then look for poles or structures in the S-matrix[106] (*i.e.* rapid jumps of the resonance part of the phase shift through $\pi/2$ modulo π, see paragraph below eq. (9.8)). However both these direct approaches are very demanding in terms of computational time, as the calculation has to be repeated for many different collision energies. Especially if the system displays very sharp resonances (*i.e.* long-lived) one needs a very fine grid in the collision energy. Also the existence of short-lived resonances can give rise to problems when using these methods, since generally the exact position and width can be difficult to assign for very broad or overlapping resonance lines. Another method is the so-called stabilization method[109] where the system is placed in a box of slightly varying size. The resonance states are then found as the solutions to the $\mathcal{L}^2$ problem that are stable with respect to small variations of the box-size. This is a very easy scheme to implement, but it has not been very popular in terms of actual applications to real systems, due to often low accuracies of especially the calculated resonance widths. A way to overcome these problems more generally is to extend the quantum mechanics to non-Hermitian Hamiltonians, which leads us to what we shall refer to as the complex methods.

In the complex coordinate method[3] (CCM), the reaction or dissociative coordinate (*e.g.* R) in the total Hamiltonian is complex scaled, and the resulting non-Hermitian eigenvalue problem is solved using standard complex eigenvalue routines. Formally one encloses the system in a box ($\mathcal{L}^2$ method) and transforms the Hamiltonian, $\widehat{\mathbf{H}}(R)$, according to

$$\boxed{\widehat{\mathbf{H}}\left(R\right) \rightarrow \widehat{\mathbf{H}}\left(Re^{i\theta}\right) \equiv \widehat{\mathbf{H}}^{\theta} \qquad (9.11)}$$

The resonances then correspond to the complex eigenvalues, $\mathcal{E}_n = E_n - i\Gamma_n/2$, of $\widehat{\mathbf{H}}^{\theta}$ which are stable with respect to variation of the scaling-parameter θ, *i.e.*

$$\frac{\partial \mathcal{E}_n(\theta)}{\partial \theta} = 0 \Leftrightarrow \begin{cases} \frac{\partial E_n(\theta)}{\partial \theta} = 0 \\ \frac{\partial \Gamma_n(\theta)}{\partial \theta} = 0 \end{cases} \qquad (9.12)$$

This complex coordinate method is based on rigors mathematics (dilatation transformations) due to the work of Balslev[4] and Combes[110] and Simon[111, 112] in the early seventies. The relation between the resonance position, E_n, and width, Γ_n, and the scaling-parameter, θ_n, is given by the fundamental condition

$$\boxed{\tan(2\theta_n) = \frac{\Gamma_n}{2(E_n - E_{thres})} \qquad (9.13)}$$

which is the essence of the Balslev–Combes[110] theorem which forms the basis of CCM. In eq. (9.13) E_{thres} is the threshold energy below which the bound states

---

[3] In the physical chemistry literature this method also goes under different names like "complex scaling" and "complex coordinate rotation", but throughout this thesis we adopt the name "complex coordinate method". This is partly in loyalty to Nimrod Moiseyev, who has used this term consistently in his numerous publications (*e.g.* [103]) and whom I had the pleasure to have private communication with several times during my study.

[4] It so happens that Balslev was actually teaching mathematics at the University of Århus when I was a undergraduate, and I followed his lectures for a year. Ironically, ever since I started to study the CCM I have in vain tried to find someone how could explain to me the mathematical foundation of this method in detail. I have over time approached some of the experts in the application the CCM to molecular resonances, and it appears to me that the CCM is simply considered a "recipe".

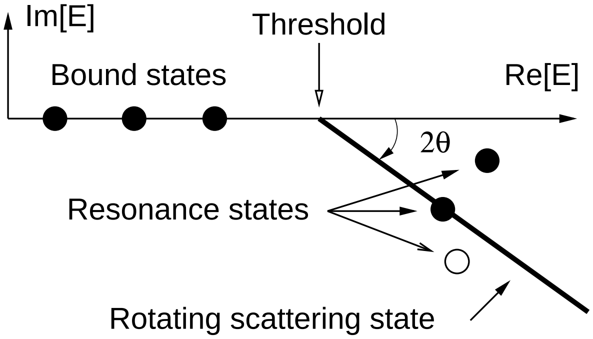

Figure 9.3: Schematic illustration of the eigenvalues of the complex-scaled Hamiltonian as they are gradually rotated into the complex energy plane. The filled dots represent revealed resonances, whereas the empty dots correspond to resonances not yet exposed due to a too low rotation angle θ (see text below eq. (9.13) for a description).

are located, and we note that all the parameters entering eq. (9.13) strictly belong to the same channel as E_{thres}. Next recalling the characteristics of the bound, resonance and scattering states, outlined in section 9.1, we can now give a schematic representation of the eigenvalues of the complex-scaled Hamiltonian as they are gradually rotated into the complex energy plane, see figure 9.3. Note that the bound states stays below the threshold on the real energy axis ($\Gamma_{bound} \equiv 0$), the resonance states correspond to stagnation-points which satisfy eq. (9.12) and (9.13) and the scattering states just continues to be rotated into the complex energy plane as θ increases. The computational advantage of this variational complex method is that it isolates, in principle, all the resonance states from the continuum states as stationary points in the complex energy plane of θ-trajectories, see figure 9.3. Also, as this is an $\mathcal{L}^2$ method it enables us to use numerical techniques developed for bound state problems. The CCM has been applied successfully to many different physical systems [113–116], but it should be clear from eq. (9.11), that the analytical complex continuation of the Hamiltonian can only be accomplished when one has an *analytical* expression for the potential energy function. In other words the CCM has for many years mainly been restricted to simple analytical model systems. However by using the identity

$$\underline{\underline{\mathrm{H}}}^{\theta}_{m,n} \equiv \int_R dR \left\{ \Phi_m(R)\, \widehat{\mathbf{H}}\left(e^{i\theta}R\right) \Phi_n(R) \right\} \tag{9.14a}$$

$$= e^{-i\theta} \int_{Re^{i\theta}} dR \left\{ \Phi_m\left(e^{-i\theta}R\right) \widehat{\mathbf{H}}(R)\, \Phi_n\left(e^{-i\theta}R\right) \right\} \tag{9.14b}$$

the complex scaling is shifted from the Hamiltonian to the (real) basis functions, $\Phi_m(R)$, which are in turn known analytically. This idea of "backward scaling" the basis functions as opposed to "forward scaling the Hamiltonian", forms the starting-point of the work to be presented in chapter 11. Here a new method is developed where matrix elements expressed in a multi-dimensional discrete variable representation (DVR) are backward scaled to give the equivalent of eq. (9.14b).

The other complex method, due to Jolicard and Austin[117], and here referred to as the optical potential method (OPM) , consist of adding a local optical potential in the asymptotic region of the potential energy function. This method is also an $\mathcal{L}^2$ method, and as discussed in section 1.1 the optical potential acts as an absorbing boundary removing flux from the system as it approaches the asymptotic region, and thereby preventing reflection and transmission from the artificial box boundaries. The central idea of the OPM is, that by varying the amplitude of the optical potential the system is slightly perturbed, and resonances show up as stable eigenfunctions of the non-Hermitian Hamiltonian just like in the CCM. Thus, the OPM also satisfy the variational condition, eq. (9.12), just now θ is an amplitude parameter in the optical potential. Naively one could say that this method resembles the stabilization method mentioned above, where the system is perturbed at the boundary. However it is important to emphasize that the OPM is an extension of quantum mechanics to the non-Hermitian domain of the Hamiltonian much like the CCM. Actually Rom, Lipkin and Moiseyev[118] have shown that by a specific choice of the local optical potential (a complex potential) the CCM can be shown to be identical to an optical potential method. In practice, however, the optical potential is often chosen as a simple negative imaginary potential (NIP) known from time dependent molecular dynamics[84–86]. Consequently, the OPM with an arbitrary optical potential may not always produce the correct positions and widths of the resonances (see discussion to come in section 10.2). This problem is closely related to the fact is that in principle the NIP should be perfectly absorbing in the whole energy range of interest, which can be a serious problem in practical calculations. Hence boundary effects created by the finite nature of the basis set can be significant, leading to unphysical perturbations of the system, which in turn shifts the actual position and width of the resonances. The CCM, on the other hand, is based on rigorous mathematics, and hence, by virtue of the Balslev–Combes[110] theorem, the complex scaling expressed in eq. (9.11) or eq. (9.14b) is "guaranteed" to give the correct resonances – of course within the approximation of a finite basis set. However, it should be stressed that the OPM has important advantages over the CCM. First, the overall numerical scheme is very simple, and we need not worry about the analytical nature of the potential energy term. Secondly, there exist good candidates in the literature for almost perfectly absorbing

NIP's [87, 119].

We close this chapter by outlining a simple correction procedure for the OPM proposed by Jolicard and Humbert[120]. They showed that for two successive calculations of the complex resonance energy, made for the two values Λ_1 and Λ_2 of the amplitude parameter in the NIP, a corrected energy is given by

$$\mathcal{E}_{res} = \mathcal{E}_{\Lambda_2} + \frac{\mathcal{E}_{\Lambda_1} - \mathcal{E}_{\Lambda_2}}{1 - \mathcal{E}'_{\Lambda_1}/\mathcal{E}'_{\Lambda_2}} \tag{9.15}$$

where $\mathcal{E}'_\Lambda = \partial\mathcal{E}/\partial\Lambda = \left\langle \Phi^\dagger_\Lambda \left| \partial V_{opt}/\partial\Lambda \right| \Phi_\Lambda \right\rangle$. The associated corrected resonance eigenfunction reads as

$$\Phi_{res} = \Phi_{\Lambda_2} + \frac{\Phi_{\Lambda_1} - \Phi_{\Lambda_2}}{1 - \mathcal{E}'_{\Lambda_1}/\mathcal{E}'_{\Lambda_2}} \tag{9.16}$$

This correction procedure is derived from the generalized complex Hellmann-Feynman, theorem mentioned in section 3.2 (eq. (3.29) with $\xi \to \theta$), which takes a very simple form for a resonance state since the analogous of eq. (9.12) is also satisfied in the OPM. We also note that recently [121] the Hellmann-Feynman theorem has been applied to the CCM, leading to an algebraic θ-equation which can be solved iteratively to give a correction to the rotation angle. However, the problem with these schemes is that since eq. (9.12) is only strictly satisfied for a resonance-state they do only produce meaningful corrections in the immediate neighborhood of such resonance states. Thus, for model potentials where the approximate resonance positions are often known in advance these correction procedures can be very useful, but in the general situation this is not always the case.

10

Resonances in $H^+ + O_2$ by the optical potential method

The objective of the work to be presented in this chapter is twofold: First we want to re-examine the resonances of the H^++O_2 system, employing a different method than the close-coupling approach previously used by Grimbert *et al.*[106]. The method of choice is the optical potential method (OPM), reviewed in the previous chapter, since this is a very easy scheme to implement. The second objective is to generally evaluate this method against the close-coupling approach, hoping to be able to set up a computational scheme which is more general and effective in the sense that it enables us to calculate and subsequently isolate all the resonances in one step.

Thus, this work reviews the OPM, summarizes some techniques and tools to isolate and verify the resonances, and subsequently reports calculations of resonance positions and widths for the electronically elastic H^++O_2 collision described in the framework of the Infinite-Order Sudden (IOS) approximation. The positions are shown to be in reasonable agreement with previous results obtained for the system solving the close-coupled equations[106]. However, we also observe very long-lived resonances that were not reported before.

The chapter is organized as follows. Section 10.1 presents the overall numerical scheme in which a negative imaginary potential is added to the asymptotic part of the electronic potential energy surface. In section 10.2 we present the numerical results obtained using this optical potential method and compare the resonance positions and widths with previous results for this system in the framework of the IOS approximation. Finally section 10.3 concludes and sums up the most important features of the optical potential method.

10.1 Method of calculation

In this section we present the overall numerical scheme for our implementation of the optical potential method outlined in section 9.4. The Infinite-Order Sudden approximation (IOS) and its limitations will not be explained in great detail, we instead refer to a review paper by Baer[41] and the references mentioned therein. The numerical scheme is formulated in terms of an optimized discrete variable representation (DVR) of the two dimensional wave function. Many of the numerical techniques and tools used in this implementation have already been discussed in detail in section 2.2, and we shall only briefly review the most important features of the DVR/FBR-schemes.

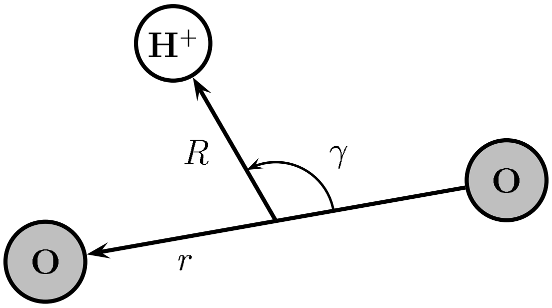

Figure 10.1: Definition of the translational coordinates R, the vibrational coordinate r and the fixed relative angle γ.

An important objective of the work presented in this chapter is to reproduce the positions and widths of the resonances in the H^++O_2 system calculated by Grimbert *et al.* [106]. Thus, we are going to make the same approximations for the collision, *i.e.* the study is carried out in the framework of the IOS approximation[41], where the relative angle γ is fixed to 45°, *cf.* figure 10.1. Ion-molecule systems usually differ significantly from atom-molecule systems because the potential is more attractive. Grimbert *et al.* [106] further argue that since the lifetimes of the resonances in H^++O_2, with the exception of two, are found to be small compared to the characteristic rotation time of an O_2 molecule (of the order of 10^{-11} s), the IOS approximation is justifiable. Thus, unless otherwise mentioned, the parametrical γ dependence is omitted throughout the rest of this chapter.

10.1.1 The IOS Hamiltonian

In the IOS approximation the Hamiltonian for the system under consideration reads as

$$\begin{aligned}\widehat{\mathbf{H}}(r,R) &= -\frac{\hbar^2}{2\mu_{tot}}\frac{\partial^2}{\partial R^2} - \frac{\hbar^2}{2\mu_{O_2}}\frac{\partial^2}{\partial r^2} + \frac{\hbar^2\ell(\ell+1)}{2\mu_{tot}R^2} + V(r,R) &\text{(10.1a)}\\ &\equiv \widehat{\mathbf{T}}_R + \frac{\hbar^2\ell(\ell+1)}{2\mu_{tot}R^2} + \widehat{\mathbf{h}}(r,R) &\text{(10.1b)}\end{aligned}$$

where ℓ is the relative orbital angular momentum and $\widehat{\mathbf{h}}(r,R) \equiv \widehat{\mathbf{T}}_r + V(r,R)$ is the O_2 Hamiltonian depending parametrically on R. The definition of the two Jacobi coordinates r and R is illustrated in figure 10.1. We further define the zero-order translational Hamiltonian

$$\widehat{\mathbf{H}}_0(R) \equiv \widehat{\mathbf{T}}_R + \frac{\hbar^2\ell(\ell+1)}{2\mu_{tot}R^2} + V_{eff}(R) \tag{10.2}$$

where the effective potential, $V_{eff}(R)$, is defined as the minimum of $V(r,R)$ with respect to the vibrational coordinate r. In the next two subsections we will define a complete direct product basis-set in r and R, which shall serve as the working basis-set when we later set up the non-Hermitian Hamiltonian, and subsequently diagonalize it. To obtain this optimized basis-set we shall first use truncation techniques like preconditioning in a zero-order Hamiltonian and successive adiabatic reduction (SAR) – all techniques that were discussed in section 2.2. The subsequent truncations will be done according to some *fictive* total translational energy (E_{tot}), and it is important to note that this collision energy does not explicitly enter the overall scheme for the optical potential method – only when we design the basis-set. This is exactly one of the advantages of the complex methods over the close-coupled approach, as pointed out in section 9.4. Thus, when E_{tot} is mentioned in the following subsections it should be interpreted as some sort of truncation parameter rather than an actual total translational energy.

10.1.2 Definition of FBR and DVR in the translational coordinate

In the translational coordinate R, we use a primitive FBR basis-set of particle-in-a-box (PIB) sin-functions. These basis functions are simple $\mathcal{L}^2$ functions that define a DVR basis-set in a very simple way, see subsection 2.2.5. We start by defining the box for the translational coordinate. As this coordinate is clearly not "bounded" we will have to provide the box parameters, R_{min} and R_{max}, by some means of guessing, based on the topology of the potential energy surface, $V_{eff}(R)$ in eq. (10.2), and subsequently test for convergence. It should be noted that the presence of long-range multi-polar interactions in ion-molecule systems, like H^++O_2, result in a much larger value of R_{max} than for the corresponding neutral atom-molecule system. Next, we shift the domain of R to go from zero to $R_{max} - R_{min}$ and define the size of the FBR and the associated DVR basis-set, by specifying the underlying grid. As mentioned in subsection 2.2.5, the PIB-DVR has an equidistant or uniform grid, and a simple classical analysis of the de Broglie wavelength gives a grid spacing of

$$\Delta R = \frac{\lambda_{min}}{2\eta} = \frac{\pi\hbar}{\eta\sqrt{2(E_{tot} - V_{min})\mu_{tot}}} \tag{10.3}$$

where η is a parameter larger than unity (typically 3-4). The primitive normalized FBR basis-set is thus defined as

$$\varphi_n(R) \equiv \sqrt{\frac{2}{R_{max}}}\sin\left(\frac{n\pi R}{R_{max}}\right), \text{where} \quad \begin{cases} n = 1, 2, \dots, N_R \\ N_R = \frac{R_{max}-R_{min}}{\Delta R} - 1 \\ R \in \,]0; R_{max} - R_{min}[\end{cases} \tag{10.4}$$

and as discussed in subsection 2.2.5, it is isomorphic to a DVR basis-set, $\{|\mathcal{R}'_p\rangle,\ p = 1, N_R\}$, *cf.* eq. (2.38). This DVR, and the underlying uniform grid, $\{R'_p,\ p = 1, N_R\}$, will constitute the "lowest-level" basis-set in the R coordinate, and we shall not give any further reference to the explicit FBR in eq. (10.4). It should be clear from the context that so far this working basis-set has not been optimized for the numerical problem at hand – or to use a DVR terminology – the grid points have not been chosen so as to reflect the physics of the problem. In other words we would like to have a truncated and optimized DVR grid that reflects the topology of the potential energy surface such that the grid is dense in regions where the de Broglie wavelength (*cf.* eq. (10.3)) is small and more sparse elsewhere. To obtain this we successively employ preconditioning, truncation and the HEG optimizing scheme, all presented in subsection 2.2.6. Using the basic property of the PIB-DVR (see eq. (2.40) and (2.41)) we first construct a set of eigenfunctions of the zero-order Hamiltonian defined in eq. (10.2)

$$\widehat{\mathbf{H}}_0|q\rangle = E^0_q|q\rangle, \quad |q\rangle = \sum_{p=1}^{N_R}\langle\mathcal{R}'_p|q\rangle|\mathcal{R}'_p\rangle \tag{10.5}$$

This basis-set, $\{|q\rangle,\ q = 1, N_R\}$, is then truncated according to a given collision energy E_{tot}. The resulting compact basis-set, $\{|q\rangle,\ q = 1, N_R^{HEG} < N_R\}$, is then used to construct a new HEG-DVR basis-set by diagonalizing the position "operator"

$$\widehat{\mathbf{R}}|\mathcal{R}_q\rangle = R_q|\mathcal{R}_q\rangle, \quad |\mathcal{R}_q\rangle = \sum_{p=1}^{N_R} \langle\mathcal{R}'_p|\mathcal{R}_q\rangle|\mathcal{R}'_p\rangle \tag{10.6}$$

This set of eigenvalue equations thus defines a compact DVR basis-set, $\{|\mathcal{R}_q\rangle,\ q = 1, N_R^{HEG}\}$, with the optimized grid points given as the eigenvalues. Note that the new HEG grid, $\{R_q,\ q = 1, N_R^{HEG}\}$, as opposed to the original PIB grid, $\{R_p,\ p = 1, N_R\}$, is not uniform. This optimized HEG-DVR basis-set will constitute the working basis-set in the coordinate R. As it is a DVR, the potential energy function is simply diagonal in this basis (eq. (2.40)), and the kinetic energy term is easily constructed by transforming back to the PIB-DVR (eq. (10.6)) and then using the analytical expression of the FBR (see eq. (2.41) and (2.42)).

10.1.3 Definition of FBR and DVR in the vibrational coordinate

For the vibrational coordinate r we also use a primitive FBR basis set of PIB sin-functions. Hence, we proceed in an analogous way to the previous section, except in this case the size of the r-box is determined from the fact that the system is bound in this degree of freedom. Thus, r_{min} and r_{max} are given as the classical turning points for the potential energy surface at the energy E_{tot}. Consequently eq. (10.3), eq. (10.4) and subsection 2.2.5 also apply after the substitution $R \to r$ is made, but it is important to emphasize that the constructed FBR/DVR scheme is of much smaller size than for the unbound R coordinate (*i.e.* $N_r < N_R^{HEG} < N_R$). To construct a compact basis-set in the vibrational coordinate we next employ the SAR scheme presented in subsection 2.2.8. Thus, in the PIB-DVR for r, we first setup a set of eigenvalue equations for the fixed R-Hamiltonian, $\widehat{\mathbf{h}}(r; R_q)$, defined in eq. (10.1b).

$$\widehat{\mathbf{h}}(r; R_q)|m, q\rangle = E_m(R_q)|m, q\rangle \tag{10.7}$$

This defines a set of *adiabatic* vibrational states in each of the HEG grid points obtained through eq. (10.6). For each HEG grid point, R_q, the local basis-set of the ray-eigenstates, $\{|m, q\rangle,\ m = 1, N_r\}$, is next contracted by keeping only those states for which the adiabatic energy, $E_m(R_q)$, is located below the threshold energy, $E_{tot}(v)$, corresponding to the energy in the lowest vibrationally *closed* channel H^++$O_2(v, X^3\Sigma_g^-)$. That is, at for each HEG grid point, R_q, we defined the size of the local adiabatic basis-set, N_r^q, such that $E_{N_r^q}(R_q) \leq E_{tot}(v) < E_{N_r^q+1}$. We can then combine this compact adiabatic basis-set with the HEG-DVR defined in eq. (10.6) by means of a direct product. Thus, we finally define the overall working basis-set in of both coordinates, r and R, as

$$|m, \mathcal{R}_q\rangle \equiv |m, q\rangle |\mathcal{R}_q\rangle \quad \text{where} \quad \begin{cases} m = 1, 2, \ldots, N_r^q \\ q = 1, 2, \ldots, N_R^{HEG} \end{cases} \tag{10.8}$$

10.1.4 The optical potential method

As mentioned in section 9.4 the OPM is essentially a non-Hermitian variational method in the amplitude parameter of a NIP added to the asymptotic part of the potential energy function. Many different kinds of NIP's have been proposed in the literature [84–86, 119], and we choose an exponential form whose absorbing properties have been investigated thoroughly by Vibók and Balint-Kurti[87]. Thus the NIP, $V_{opt}(R)$, reads as

$$V_{opt}\left(R\right) = \begin{cases} 0 & \text{for} \quad R_{min} \leq R \leq R_0 \\ -i\Lambda N \exp\left(-2\frac{R_{max}-R_0}{R-R_0}\right) & \text{for} \quad R_0 < R \leq R_{max} \end{cases} \tag{10.9}$$

where Λ is a premultiplier used to minimize the reflection and transmission from the potential and N is a normalization constant found numerically to be 13.22 [87]. For a given energy domain reference [87] provides optimized tabulated values for the parameter Λ and the range of definition, $\Delta R_{opt} \equiv R_{max} - R_{min}$. However in the present application of the optical potential to locate resonances, the premultiplier Λ is not a fixed parameter, but rather a *variational* amplitude parameter. Thus, we cannot simply follow the guidelines given in reference [87] to assign $\{\Lambda, \Delta R_{opt}\}$. Instead we have to use many different values of ΔR_{opt} to test for convergence. This clearly emphasizes yet another drawback of the OPM, as compared to the CCM; the added optical potential introduces new parameters into the numerical scheme. This usually implies a lot of additional convergence tests to determine these parameters.

The optical potential, eq. (10.9), is added to the total Hamiltonian, eq. (10.1a), and for different values of the parameter Λ, a matrix representation of this non-Hermitian Hamiltonian is then computed in the basis-set derived above, eq. (10.8). It is important to note that since the optical potential is only a function of R, and the complete basis-set is a DVR in this coordinate, the addition of the NIP just adds complex values of V_{opt} (at the HEG grid points) to the diagonal. Thus the DVR in the translational coordinate, makes the implementation of the optical potential method very easy. The computed complex symmetric matrix is next diagonalized for many different values of Λ, and for successive calculations in Λ

the produced complex eigenvalues are connected using a maximum-overlap scheme for the associated complex eigenvectors. Finally the Λ-trajectories are plotted in the complex energy plane with the real part (*i.e.* energy position) along the positive x-axis and the imaginary part (*i.e.* half width) along the negative y-axis (recall figure 9.3). A visual inspection of each trajectory next follows in order to determine which ones correspond to either a bound, continuum or resonance state. The bound states are not affected by the presence of the NIP placed in the asymptotic region, and hence they show up as coinciding dots on the real energy axis *below* the value of the threshold energy, *i.e.* the zero-order vibrational energy in the entrance channel. (Bound states have in principle an infinitely large lifetime corresponding to zero width, *i.e.* no imaginary energy component). The resonance and continuum states, on the other hand, are only found *above* this value of the threshold energy. The latter have amplitude in the whole coordinate space and hence they are very sensitive to small changes in the NIP. Consequently the continuum states correspond to trajectories which are continuously rotated into the negative imaginary energy plane as the amplitude parameter, Λ, increases. From the theory of resonances by complex methods (see eq. (9.12)) it follows that resonance, or quasi-bound states, are visually identified as stagnation points or cusps in the complex energy plane. However, it is very important to emphasize that these simple characteristics of the three different types of states are not generally sufficient as a guideline to isolate resonance states when using the optical potential method. The reason for this complicating aspect of the optical potential method is of course that this is an approximate method as pointed out in section 9.4. The presence of the NIP slightly perturbs the system in a non-physical way, thereby causing it to change its characteristic behavior under the complex scaling, *i.e.* variation of Λ. This means that sometimes continuum trajectories can behave as resonance trajectories and vice versa. Especially for large values of Λ, *i.e.* for large perturbations from the NIP, can one observe spurious behaviors of the complex trajectories. All in all this means that one has to be a little careful before a final identification of a resonance state can be made. In other words we need additional techniques or tools to verify the existence of a resonance after it has been isolated. We have come up with the following simple tests:

1. Perform a convergence test by slightly changing the remaining parameters entering the definition of the negative imaginary potential. We found it to be especially useful to repeat the calculations with different values of the domain of definition for the NIP. Trajectories corresponding to a real physical resonance will show very little effect on these changes in the domain of Λ where the quasi-bound states are formed. “Ghost-trajectories”, on the other hand, will not show the same invariance with respect to these variations, and

often one observes dramatic changes of the trajectory for all values of Λ. (See figure 10.4 and figure 10.5 in the next section for an illustration).

2. Alternatively one can graphically plot the probability density of the state calculated at the value of Λ where the stagnation point is observed. As pointed out in section 9.1 the divergent property of the asymptotic part of a resonance wave function increases with the width. Resonances will show a large amplitude in the interaction region (with vibrational excitation for Feshbach resonances) and a relatively small periodic amplitude in the entrance channel corresponding to the pure outgoing boundary condition mentioned in section 9.1 eq. (9.3). Continuum states, on the other hand, will display a relatively large amplitude in the asymptotic regions of the channel. For very sharp resonances it can actually be difficult to distinguish a resonance state from a bound state since it has almost negligible amplitude at the boundary. Thus, if one first filters off all the bound states by truncating the trajectories below the threshold energy this test can be useful – although a bit time consuming. This technique can of course also be used when applying the complex coordinate method to be discussed in the next chapter, although this is in principle an exact method, and should therefore not give rise to spurious behavior of the trajectories. (See figure 10.6 and figure 10.7 in the next section for an illustration).

3. Finally we also mention the the self-correcting scheme by Jolicard and Humbert[120], eq. (9.15), as a tool to verify resonances. First we note that this scheme only produces meaningful corrections to the resonance positions when the successive values of the variational parameters Λ_i are close to a resonance. Outside this domain of Λ, and for non-resonant states, eq. (9.15) gives "arbitrary" complex values, which makes the visual tracking of the new "chaotic" Λ-trajectories in the complex energy plane extremely difficult. This is of course not an artifact of the self-correcting scheme itself, but simply stems from the fact that it is based on the approximation in eq. (9.12) which is only satisfied in the immediate neighborhood of a resonance state. Thus, this scheme should only be used at the values of Λ where the stagnation point is observed, which makes it less attractive as a general tool for verifying a resonance state. However, we found it very useful as a tool to confirm and correct the exact positions of the resonances once a positive identification was made by either 1 or 2.

10.2 Numerical results

In all the reported calculations we have used the same collision conditions as Grimbert *et al.* [106], in order to compare with their results. Thus, a single value of the relative angle, $\gamma = 45^\circ$ in figure 10.1, and an orbital angular momentum value, $\ell = 0$ in eq. (10.1a), are considered. The latter implies that the barrier produced from the centrifugal term in eq. (10.1a) can be neglected, and consequently the system will only display *Feshbach* resonances under these circumstances. Further the collision energy is restricted to $E_{tot} < 0.2\,\text{eV}$ as measured from the $\mathrm{H}^+ + \mathrm{O}_2(v = 0, X^3\Sigma_g^-)$ dissociation threshold. As in reference [106] we are also going to disregard the charge transfer channel, $\mathrm{H} + \mathrm{O}_2^+\,(X^2\Pi_g)$, which leaves us with an electronically elastic collision problem. All in all this implies that only the $v = 0$ channel is open (vibrational elastic scattering). Thus the calculated Feshbach resonances are of the type

$$\left[\mathrm{HO}_2^+\right]^* \;\rightarrow\; \mathrm{H}^+ \;+\; \mathrm{O}_2\left(v = 0, X^3\Sigma_g^-\right) \tag{10.10}$$

The diabatic electronic potential energy surface correlating with $\mathrm{H}^+ + \mathrm{O}_2(X^3\Sigma_g^-)$ is that of Grimbert *et al.* [122]. Numerical values of the corresponding potential on the HEG and PIB grid, defined in section 10.1, are obtained by a two-dimensional spline interpolation in r and R, see figure 10.2. The box parameters in the two Jacobi coordinates are fixed to

$$R_{min} = 0.0\,\text{au} \qquad R_{max} = 20\,\text{au} \tag{10.11a}$$

$$r_{min} = 1.5\,\text{au} \qquad r_{max} = 2.9\,\text{au} \tag{10.11b}$$

Since no data points are available in the interval going from $R = 15\,\text{au}$ to $R = 30\,\text{au}$ we used the value of the potential at $R = 30\,\text{au}$ in this interval. This produces a slight discontinuity at $R = 15\,\text{au}$ of the order of 0.02 mHartree. However, this approximation is made in order to reserve some additional space for the domain of definition of the NIP. Perhaps a somewhat more disturbing feature is the cut-off of the surface of reference [122] at $r_{max} = 2.9\,\text{au}$, see figure 10.2. At this value of the vibrational coordinate (and $R \approx 2 - 3\,\text{au}$) the potential energy is far below the maximal collision energy of $7\,\text{mHartree} \approx 0.2\,\text{eV}$. Consequently the potential energy surface we use in the calculations has an infinite wall at $r = 2.9\,\text{au}$. In the close-coupled calculations by Grimbert *et al.* [106] this caused no problems since they used vibrational eigenstates of $\mathrm{O}_2(\mathrm{X}^3\Sigma_g^-)$ as the basis-set in the r coordinate. Thus they employed a vibronic *diabatic* basis-set which has negligible amplitude at $r_{max} = 2.9\,\text{au}$. However, as explained in subsection 10.1.3, eq. (10.7), we employ a vibronic *adiabatic* basis-set in r, which depend parametrically on the HEG grid points defined in subsection 10.1.2. As mentioned before this makes it possible to construct a very optimized and compact basis-set, *cf.* eq. (10.8), which so to speak follows the dynamics as the collision takes place. The problem, however, is that this adiabatic basis-set does not have the "built-in" boundary conditions that makes it ignore the presence of the infinite wall at large values of r. This is probably the most significant difference in the "physical setup" of the two calculations.

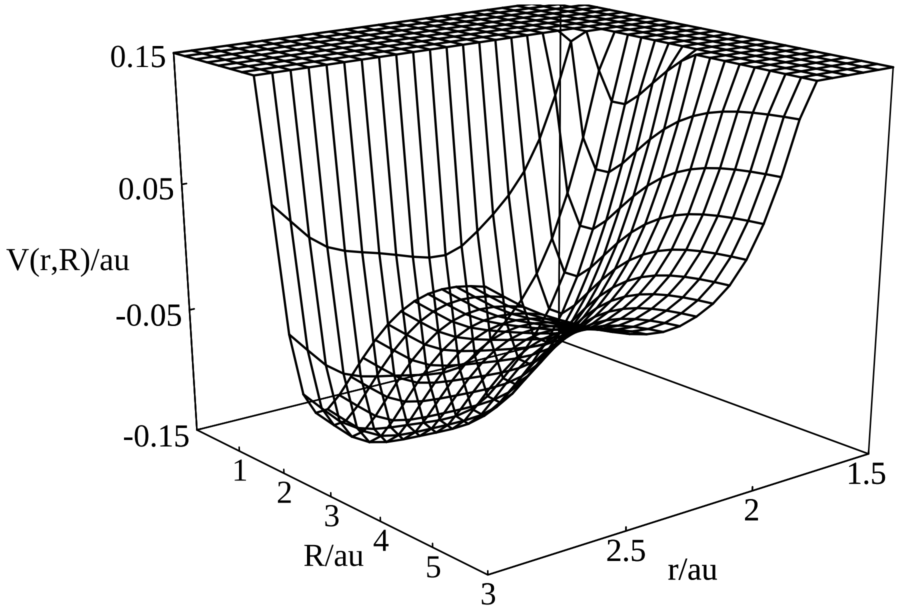

Figure 10.2: Plot of the spline interpolated electronically diabatic potential energy surface correlating with H^++$O_2(X^3\Sigma_g^-)$ [122]. The definition of the two Jacobi coordinates r and R are illustrated in figure 10.1 and the relative angle γ is fixed at 45°. The origin of energies is the vibronic zero-point channel energy. (Note also the cut-off of the surface for large values of r).

Using the numerical method explained in section 10.1 and the "physical setup" mentioned above we next performed calculations of resonances in the electronically elastic H^++$O_2(X^3\Sigma_g^-)$ collision. In these calculations we used 40 particle-in-a-box functions in r, and 350 in R. Using the HEG scheme the later basis-set was truncated to 100 DVR functions. The truncation of the adiabatic states in r resulted in 2 to 19 basis-functions depending on R. Thus, $N_r = 40$, $N_r^q = 2 - 19$, $N_R = 350$, and $N_R^{HEG} = 100$ in section 10.1, and the total size of the contracted direct product basis-set, defined in eq. (10.8), was in the order of 550. This was sufficient to obtain convergence for almost all of the resonances. The convergence was tested by employing the first of the techniques discussed in subsection 10.1.4. Thus, we performed successive calculations with 5 different values for the domain of definition for the NIP. R_{max} in eq. (10.9) was fixed as listed in eq. (10.11a) and R_0 was successively given values corresponding to $\Delta R_{opt} \equiv R_{max} - R_0 = 3, 4, 5, 6$

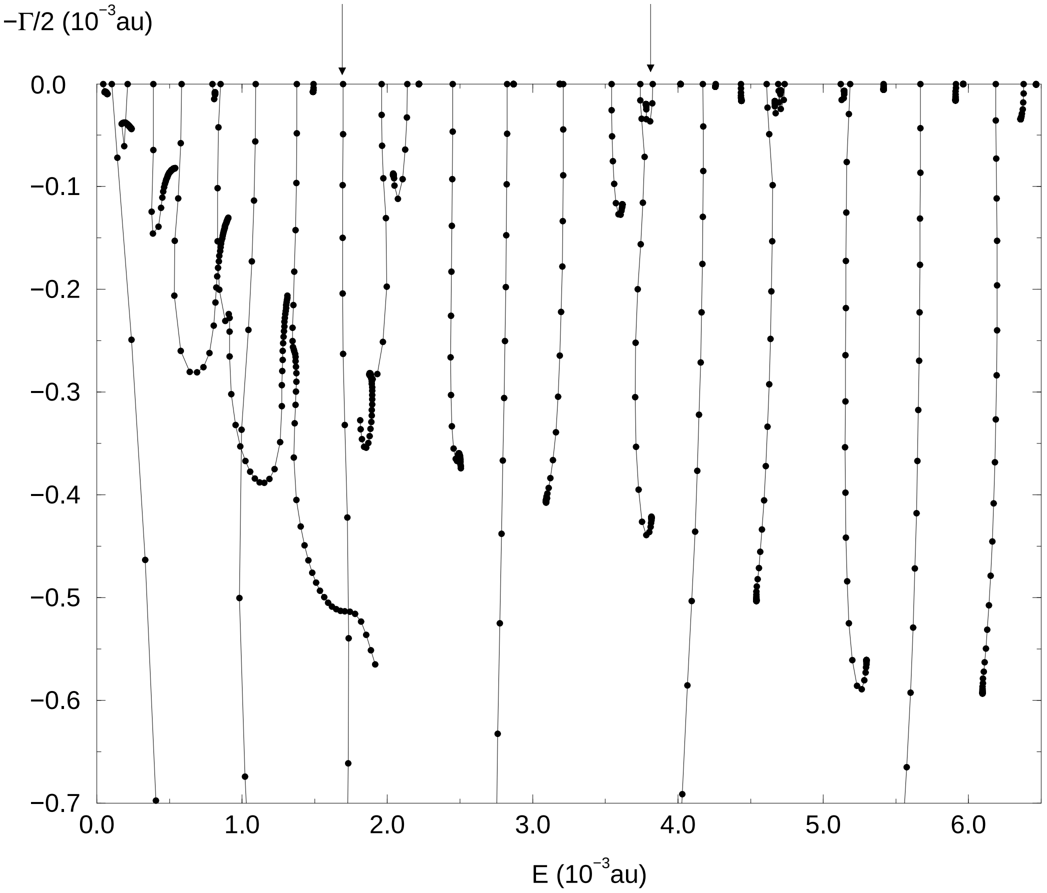

Figure 10.3: Plot of the all the Λ-trajectories. Note that the complex energy window shown in this plot does not include some of the broad resonances. Also, bound states are excluded as the energy axis is scaled relative to the threshold energy. The two arrows mark a typical continuum and resonance trajectory, respectively shown in figure 10.4 and 10.5.

and 7 au. For each calculation, corresponding to a fixed ΔR_{opt}, the variational Λ parameter in eq. (10.9) was changed from zero to 8×10^{-3} in 40 steps of 0.2×10^{-3}. This turned out to be sufficient to isolate all the resonances.

Figure 10.3 shows an overview-plot of all the Λ-trajectories in the complex energy plane, with ΔR_{opt} fixed to 7 au. In figure 10.4 and figure 10.5 we have plotted Λ-trajectories with different values of ΔR_{opt} corresponding to the two characteristic situations marked by the arrows in figure 10.3. The trajectories are plotted in the complex energy plane with the real part (*i.e.* energy position) along the positive x-axis and the imaginary part (*i.e.* half width) along the negative y-axis. Figure 10.4 shows an example of a typical continuum state which is very sensitive to small changes in the NIP. Note the spurious behavior of the trajectories with small values of ΔR_{opt}. They actually behave as a resonance state in the sense that they have stagnation points - although at different positions in the complex energy plane. However, this is not a "true resonance state", but rather a continuum state which is perturbed by an imperfect NIP. This is clearly seen from the trajectories obtained from calculations with a more absorbing or perfect NIP (*i.e.* $\Delta R_{opt} > 5\,\text{au}$) where the trajectories are continuously rotated into the negative imaginary energy plane as the amplitude parameter, Λ, increases. Thus, figure 10.4 clearly illustrates the need and importance of additional convergence/verification tests as discussed in subsection 10.1.4; with only one calculation (*e.g.* $\Delta R_{opt} = 3\,\text{au}$) one could erroneously confuse the continuum state in figure 10.4 with a "true resonance state" as shown in figure 10.5. In the latter case (figure 10.5) the trajectories show very small changes with variations of ΔR_{opt} which is exactly what characterizes a resonance state. A close-up of the trajectories actually shows that for Λ and ΔR_{opt} large enough, the calculated complex energies almost coincide. Thus, the true resonance state is only formed for specific values of *both* Λ and ΔR_{opt}. All the 5 trajectories in figure 10.5 show the characteristic behavior of a resonance state (*i.e.* a stagnation point), but only 3 of them actually correspond to a "true resonance". Again this emphasizes the importance of a convergence test; with only one calculation (*e.g.* $R_{opt} = 4\,\text{au}$) one would obtain incorrect values of the resonance position and width. The variation of R_{opt} corresponds to changing the energy domain in which the NIP is an almost perfect absorber.

Finally we show a three-dimensional plot of the probability density of the wave function for the two characteristic situations illustrated in figure 10.4 and 10.5. Figure 10.6 shows the divergent property of the continuum state in the asymptotic region of the configuration space (*cf.* eq. (9.3) with large κ_1). As we do not impose any selective boundary conditions on the wave functions in the $\mathcal{L}^2$ OPM, other than the absorbing one from the NIP, continuum states show up as extremely broad resonances in this formulation. The large amplitude in the entrance channel explains the dramatic changes observed in figure 10.4 as the NIP (*i.e.* perturbation) is varied. Figure 10.7 shows the resonance state with its characteristic shapes; large rapidly changing amplitude in the r-direction of the interaction region, corresponding to the vibrational excitation of a Feshbach resonance, and the small R-periodic amplitude in the asymptotic region of the channel, which corresponds to the purely outgoing boundary condition of a resonance (*cf.* eq. (9.3)) as discussed in section 9.1.

In table 10.1 we have listed the calculated energy positions and associated widths for resonances below a collision energy of 7×10^{-3} Hartree, which is the energy domain investigated by Grimbert *et al.* [106]. The table reports the results from

Table 10.1: Convergence of positions, E, and widths, Γ, for resonances in the H^++O_2 ($\ell = 0, \gamma = 45°$) collisional system, described in the IOS approximation and using the OPM described in section 9.4 and subsection 10.1.4. The table lists results from 5 different OPM calculations with $\Delta R_{opt} = 3, 4, 5, 6$ and 7 au arranged in the 5 pairs of columns. The results are reported in atomic units and relative to the zero-point vibrational energy ($3.508 \cdot 10^{-3}$ Hartree as measured from the bottom of the potential in the entrance channel, *cf.* figure 10.2). As an illustration to this table see figure 10.5 where the resonance state number 10 is plotted.

	$\Delta R_{opt} = 7\,\mathrm{au}$		$\Delta R_{opt} = 6\,\mathrm{au}$		$\Delta R_{opt} = 5\,\mathrm{au}$		$\Delta R_{opt} = 4\,\mathrm{au}$		$\Delta R_{opt} = 3\,\mathrm{au}$	
Nr.	E[b]	Γ[c]	E[b]	Γ[c]	E[b]	Γ[c]	E[b]	Γ[c]	E[b]	Γ[c]
1	0.814	1.8(−3)	0.814	1.8(−3)	0.813	1.6(−3)	0.815	2.0(−2)	0.815	2.0(−2)
2	1.489	1.5(−2)	1.489	1.5(−2)	1.489	1.5(−2)	1.490	1.6(−2)	1.489	1.4(−2)
3	2.042	1.8(−1)	2.042	1.8(−1)	2.042	1.8(−1)	—[a]	—[a]	—[a]	—[a]
4	2.215	4.0(−7)	2.215	4.0(−7)	2.215	4.0(−7)	2.215	4.0(−7)	2.215	4.0(−7)
5	2.492	7.2(−1)	2.492	7.4(−1)	—[a]	—[a]	—[a]	—[a]	—[a]	—[a]
6	2.869	2.8(−4)	2.869	2.8(−4)	2.869	2.8(−4)	2.869	2.8(−4)	2.869	2.8(−4)
7	3.092	8.2(−1)	3.092	8.2(−1)	3.064	8.0(−1)	3.110	7.0(−1)	—[a]	—[a]
8	3.186	1.3(−6)	3.186	1.3(−6)	3.186	1.3(−6)	3.186	1.3(−6)	3.186	1.3(−6)
9	3.616	2.4(−1)	3.616	2.4(−1)	3.616	2.4(−1)	3.615	2.2(−1)	—[a]	—[a]
10	3.780	4.0(−2)	3.780	4.0(−2)	3.780	4.0(−2)	3.780	4.0(−2)	3.780	4.0(−2)
11	3.818	8.4(−1)	3.817	8.4(−1)	3.824	8.6(−1)	—[a]	—[a]	—[a]	—[a]
12	4.017	2.4(−4)	4.017	2.4(−4)	4.017	2.4(−4)	4.017	2.4(−4)	4.017	2.6(−4)
13	4.256	5.4(−3)	4.256	5.4(−3)	4.256	5.4(−3)	4.256	5.4(−3)	4.256	5.4(−3)
14	4.436	3.2(−2)	4.436	3.2(−2)	4.436	3.2(−2)	4.436	3.2(−2)	4.436	3.2(−2)
15	4.665	3.4(−2)	4.665	3.4(−2)	4.665	3.4(−2)	4.665	3.4(−2)	4.665	3.4(−2)
16	4.707	1.3(−2)	4.707	1.3(−2)	4.707	1.3(−2)	4.707	1.3(−2)	4.707	1.3(−2)
17	5.144	1.3(−2)	5.144	1.3(−2)	5.144	1.3(−2)	5.144	1.3(−2)	5.144	1.3(−2)
18	5.416	1.1(−2)	5.416	1.1(−2)	5.416	1.1(−2)	5.416	1.1(−2)	5.416	1.1(−2)
19	5.910	3.2(−2)	5.910	3.2(−2)	5.910	3.2(−2)	5.910	3.2(−2)	5.910	3.2(−2)
20	5.965	1.3(−4)	5.965	1.3(−4)	5.965	1.3(−4)	5.965	1.3(−4)	5.965	1.3(−4)
21	6.096	1.2(−2)	6.095	1.2(−2)	6.094	1.2(−2)	6.082	1.2(−2)	—[a]	—[a]
22	6.358	6.8(−2)	6.358	6.8(−2)	6.358	6.8(−2)	6.358	6.8(−2)	6.358	6.8(−2)
23	6.464	1.6(−3)	6.464	1.6(−3)	6.464	1.6(−3)	6.464	1.6(−3)	6.464	1.6(−3)
24	6.660	4.6(−2)	6.660	4.6(−2)	6.660	4.6(−2)	6.660	4.6(−2)	6.660	4.6(−2)
25	6.856	7.4(−2)	6.856	6.6(−2)	6.856	6.2(−2)	6.856	6.0(−2)	6.856	6.0(−2)

[a] Difficult to assign, *i.e.* no clear stagnation-point was found for this particular choice of the optical potential.

[b] The positions of the resonances are listed in units of 10^{-3} Hartree.

[c] The width of the resonances are listed in units of 10^{-3} au. We have further used the short notation $(-x)$ for 10^{-x}, *i.e.* a value of *e.g.* 8.4(−1) correspond to a width of $8.4 \cdot 10^{-4}$au.

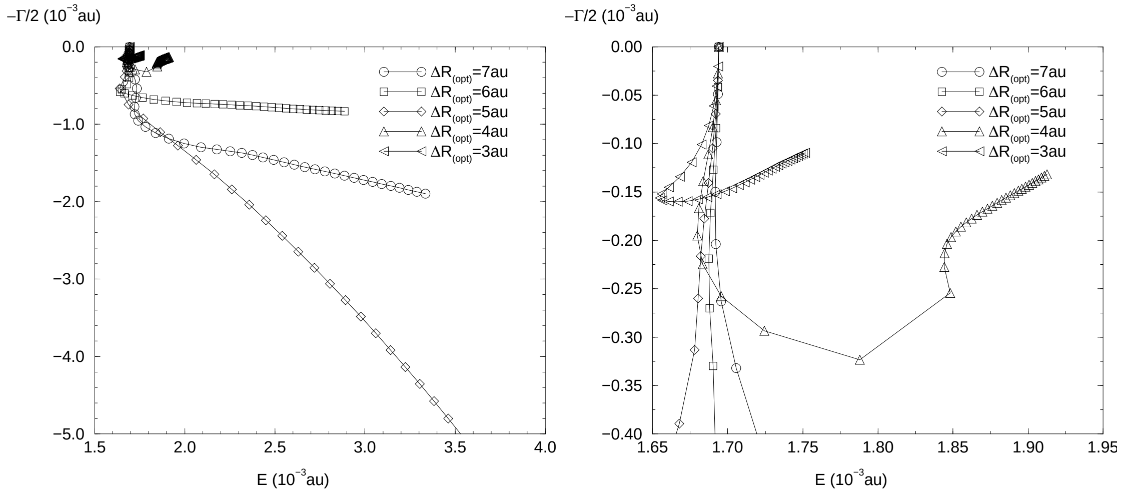

Figure 10.4: Full scale and close-up plots of complex energy trajectories for the continuum state marked by the left arrow in figure 10.3. The trajectories are obtained from calculations with 5 different values of $\Delta R_{opt} \equiv R_{max} - R_0$ in eq. (10.9), and each of these 5 trajectories are made up by 40 connected points corresponding to the different values of the variational Λ parameter entering eq. (10.9). For almost all values of Λ the trajectories are clearly very sensitive to the changes in the optical potential. Note the *different* stagnation points for the $R_{opt} = 3$ and 4 au trajectories in the right close-up plot. See also figure 10.6 for a 3D-plot of the amplitude of this continuum state.

5 different calculations corresponding to $\Delta R_{opt} = 3, 4, 5, 6$ and 7 au. It should be evident from this table that all the listed states are indeed resonances and not just "ghost-states", *i.e.* perturbed continuum states that merely behave as quasi-bound states (*cf.* figure 10.4). Actually, with the exception of resonance number 1,2,3,5,7,9,11,21 and 25, they all show complete invariance with respect to the changes in the NIP. However, of the sensitive resonances, some of them (*cf.* 3,5,7,9 and 11) even loose the characteristic stagnation point as ΔR_{opt} decreases, and thus start behaving as continuum states. A closer inspection of table 10.1 furthermore shows that these sensitive states are all broad (*i.e.* short-lived) resonances. The reason for this behavior is easily explained when we recall the very definition and characteristic of a resonance state discussed in the introduction of section 9.1 (*cf.* paragraphs below eq. (9.3) and eq. (9.4b)). The amplitude in the asymptotic region of the entrance channel increase rapidly with the width of the resonance, and consequently the range needed to absorb the wave functions associated with narrow resonances is much less than for the broad ones. This is clearly reflected in table 10.1. However, increasing ΔR_{opt} eventually also means extending the R-box, and the underlying grid size, which can be very costly in terms of computing time. Also, the NIP is in practice only perfect in a narrow energy-window, *i.e.* the NIP is

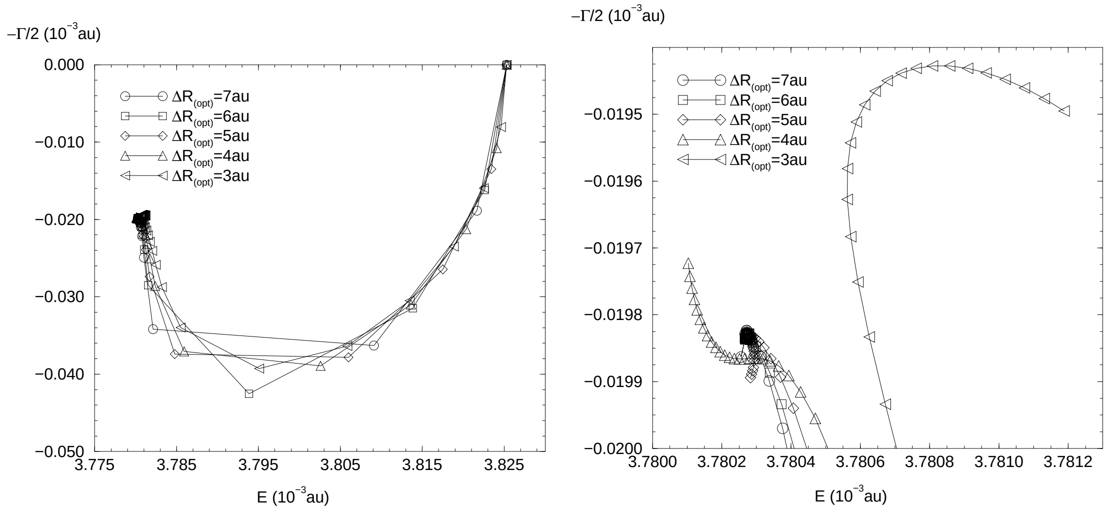

Figure 10.5: Full scale and close-up plots of complex energy trajectories for the resonance marked by the right arrow in figure 10.3, corresponding to resonance state number 10 in table 10.1 and table 10.2. The trajectories are obtained from calculations with 5 different values of $\Delta R_{opt} \equiv R_{max} - R_0$ in eq. (10.9), and each of the 5 trajectories are made up by 40 connected points corresponding to the different values of the variational Λ parameter entering eq. (10.9). For the last 20-30 values of Λ the trajectories are clearly very insensitive to the changes in the optical potential. Note the slight drifting of the stagnation points for the $R_{opt} = 3$ and 4 au trajectories in the right close-up plot caused by the imperfect NIP. See also figure 10.7 for a 3D-plot of the amplitude of this resonance state.

almost always accompanied by some reflections from the boundary. This generally leads to shifting of the true energy positions and widths, but we expect these perturbations from the NIP to be predominant for the broad resonances where the asymptotic amplitude is large. All in all we conclude that the optical potential method seems best suited to study sharp resonances.

Table 10.2 shows a comparison of the converted resonances listed in table 10.1 and earlier results obtained by Grimbert *et al.* [106] solving the close-coupled equations. The table shows 25 resonances, 18 of which correspond to the resonances located by Grimbert *et al.* For the large majority of the resonances, the positions are in acceptable agreement (*i.e.* $|\Delta E| < 0.15 \times 10^{-3}$ Hartree) with the previous calculations, but the widths are some times off by a factor as much as 10. It is however reassuring to see that there is a clear match in the variations of the widths in the two columns, but the deviations do not seem to follow any particular pattern. It is difficult to give a clear cut explanation for the deviations, but one could probably argue that we did not reproduce the exact collision conditions under which the study by Grimbert *et al.* was conducted. Resonances are widely known to be ex-

Table 10.2: Comparison of positions, E, widths, Γ, and lifetimes, $\mathcal{T}$, for resonances in the H^++O_2($\ell = 0, \gamma = 45°$) collisional system, described in the IOS approximation. The first three columns correspond to the converted results from table 10.1 obtained using the optical potential method. The last three columns correspond to previous results found by Grimbert *et al.* [106] solving the closed coupled set of equations. The results are reported in atomic units and relative to the zero-point vibrational energy ($3.508 \cdot 10^{-3}$ Hartree as measured from the bottom of the potential in the entrance channel, *cf.* figure 10.2).

	Optical potential method			Close-coupled equations[106]		
Nr.	E (10^{-3} au)	Γ (10^{-3} au)[c]	τ (s)[c]	E (10^{-3} au)	Γ (10^{-3} au)[c]	τ (s)[c]
1	0.81	1.8(−3)[b]	1.3(−11)[b]	0.80	1.4(−3)	1.7(−11)
2	1.49	1.5(−2)	1.6(−12)	1.49	5.8(−3)	4.1(−12)
3	2.04	1.8(−1)	1.3(−13)	1.85	1.2(−1)	1.9(−13)
4	2.22	4.0(−7)	6.0(−8)	—[a]	—[a]	—[a]
5	2.49[b]	7(−1)[b]	3(−14)[b]	2.36	8.6(−2)	2.8(−13)
6	2.87	2.8(−4)	8.6(−11)	—[a]	—[a]	—[a]
7	3.01	8.2(−1)[b]	2.9(−14)[b]	2.93	1.3(−2)	1.8(−12)
8	3.19	1.3(−6)	1.9(−8)	—[a]	—[a]	—[a]
9	3.62	2.4(−1)	1.0(−13)	3.72	1.9(−1)	1.3(−13)
10	3.78	4.0(−2)	6.0(−13)	3.89	1.5(−3)	1.7(−11)
11	3.82[b]	8.4(−1)[b]	2.9(−14)[b]	3.99	1.3(−1)	1.9(−13)
12	4.02	2.4(−4)	1.0(−10)	—[a]	—[a]	—[a]
13	4.26	5.4(−3)	4.5(−12)	—[a]	—[a]	—[a]
14	4.44	3.2(−2)	7.6(−13)	—[a]	—[a]	—[a]
15	4.67	3.4(−2)	7.1(−13)	4.55	4.8(−2)	5.0(−13)
16	4.71	1.3(−2)	1.9(−12)	5.08	7.5(−3)	3.2(−12)
17	5.14	1.3(−2)	1.9(−12)	5.21	4.1(−2)	6.0(−13)
18	5.42	1.1(−2)	2.2(−12)	5.58	1.4(−2)	1.7(−12)
19	5.91	3.2(−2)	7.6(−13)	5.87	6.8(−3)	3.5(−12)
20	5.97	1.3(−4)	1.9(−10)	—[a]	—[a]	—[a]
21	6.09	1.2(−2)	2.0(−12)	6.04	3.1(−2)	8.0(−13)
22	6.36	6.8(−2)	3.6(−13)	6.44	6.5(−2)	3.7(−13)
23	6.46	1.6(−3)	1.5(−11)	6.70	5.8(−3)	4.1(−12)
24	6.66	4.6(−2)	5.3(−13)	6.81	5.2(−2)	4.7(−13)
25	6.86	7(−2)[b]	3(−13)[b]	6.95	7.4(−2)	3.3(−13)

[a] No previous resonance reported in reference [106].

[b] Difficult to assign, see table 10.1.

[c] In this column we have used the short notation $(-x)$ for 10^{-x}.

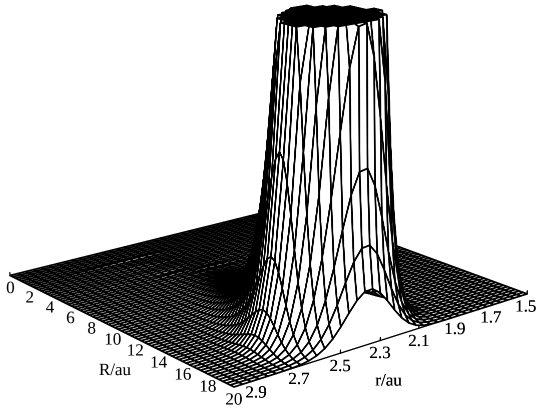

Figure 10.6: Plot of the probability density for the continuum state shown in figure 10.4. In this calculation ΔR_{opt} and Λ, entering eq. (10.9), were fixed at respectively 7 au and 4×10^{-3}, corresponding to the 20th point on the $\Delta R_{opt} = 7$ au trajectory in figure 10.4. Note the divergent property of the continuum wave function in the asymptotic region of the configuration space.

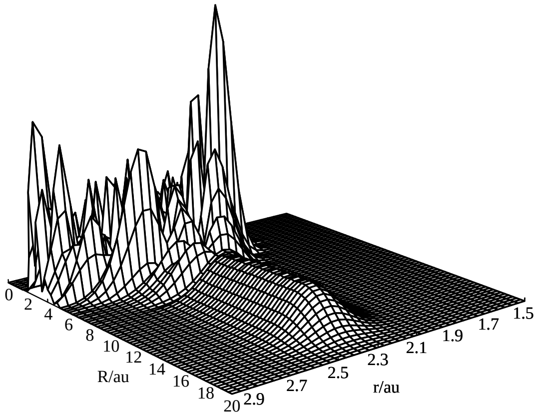

Figure 10.7: Plot of the probability density for the resonance state shown in figure 10.5, and listed in table 10.1 and table 10.2 as number 10. In this calculation ΔR_{opt} and Λ, entering eq. (10.9), were fixed at respectively 7 au and 4×10^{-3}, corresponding to the 20th point on the $\Delta R_{opt} = 7$ au trajectory in figure 10.5. Note that the characteristic resonance wave function has large amplitude in the interaction region of the coordinate space and a very small amplitude in the entrance channel.

tremely sensitive to the curvature of the potential energy surface, and the extension of the surface beyond 15 au might have influenced the calculations. However, as mentioned before, we believe that the most significant difference in the "physical setup" of the two calculations is related to the different basis-set approaches. In the optical potential calculations presented in this thesis we employed a vibronic *adiabatic* basis-set of the order of 500 whereas Grimbert *et al.* used 14 vibronic *diabatic* basis functions to solve the coupled equations. Apart from the obvious difference in the sizes of the employed basis-sets, which is definitely in favor of the present calculation, it should also be stressed that the underlying physical description of the collision differs in the two cases. The diabatic basis-set deals with the somewhat disturbing cut-off of the surface at $r_{max} = 2.9$ au (*cf.* figure 10.2) in an ad hoc way, whereas the adiabatic basis-set does not. Consequently the surface exhibits a wall in the presented calculations which was not present in the previous studies by Grimbert *et al.* This clearly makes the comparison difficult. Finally we note that disagreements between the two compared methods have been observed before in the literature; Monnerville *et al.* [123] exactly finds a disagreement for broad resonances in the one-dimensional study of predissociation of CO. They argue that this is primarily due to the fact that close-coupling approaches are generally not capable of correctly reproducing very broad resonances. The shape of the found resonances are not Lorentzian (*i.e.* simple asymmetric) which can give significant error-bars when assigning the resonance position and width. We can go along with this argument, but find it equally important to emphasize that the OPM also has problems in this limit as pointed out above.

Table 10.2 also shows 7 new resonances, 4 (*cf.* 4,6,8 and 12) of which being very long-lived (*i.e.* $\tau > 10^{-10}\,\mathrm{s}$). It is interesting to see that the only new relatively short-lived resonances (*cf.* 13,14 and 20) are located in the most dense parts of the spectra which is also where the largest deviations are found (*e.g.* 16). Thus it seems plausible that Grimbert *et al.* [106] overlooked or simply missed these resonances because they overlapped. The finding of the new very sharp resonances is not very surprising considering the fact that the close-coupling approach, used by Grimbert *et al.*, exactly has a problem isolating very sharp resonances unless the energy grid is equally very dense.

10.3 Conclusion

All the resonances found by Grimbert *et al.* [106] are confirmed, although the widths of some resonances are off by a factor of 10. In the previous section we have discussed some important issues that should provide arguments to explain the disagreement between the two approaches. We especially drew attention to the different basis-sets employed in the two calculations, and further pointed out that both methods show weaknesses in the limit of very broad resonances. Given these facts we find the agreement acceptable, but stress that it is difficult to make a final conclusive evaluation of the found resonances relative to the previous results. However, it is striking that we found 7 new resonances, 4 of which were very long-lived, $\mathcal{T} > 10^{-11}\,\mathrm{s}$. First of all, this clearly shows what we expected from the very beginning, namely that the method of close-coupled equations is not well suited to isolate sharp resonances, unless of course the energy grid is made very dense at the cost of computational time. We also note that the existence of these very long-lived resonances could well signify that the use of the IOS approximation, on this system, might be called in question. Grimbert *et al.* [106] argue that since they found only two resonances with lifetimes comparable to the characteristic rotation time of the O_2 molecule (of the order of $10^{-11}\,\mathrm{s}$), the IOS approximation was justifiable. Given the discovery of the new resonances we question this justification, but at the same time we acknowledge that this is by no means a definitive proof of the invalidity of the IOS approximation applied to the H^++O_2 system - it merely invalidates the way it has been justified in reference [106].

The present study also gives an examination of the optical potential method as an alternative to the close-coupled approach. We believe the OPM to be more accurate and general in the sense that it, in principle, isolates all the resonances in the complex energy plane in one step, *i.e.* we do not have to scan the real energy axis. The subsequent visual inspection of the complex trajectories is however rather tedious. This inconvenience of the OPM was further intensified by the present discovery of spurious behavior of the trajectories. This forced us to introduce additional techniques to isolate and verify the existence of a resonance state; we especially focused on the convergence tests where we made small variations in the domain of definition of the NIP, and plotted the probability density of the corresponding wave function. To "routinely" overcome these problems discovered with the isolation of resonances in the complex energy plane, we will have to employ the "exact" complex coordinate method, which will be the topic of the next chapter. However, as will be clarified in chapter 12 (see figure 12.2) – after the numerical CCM scheme has been established in chapter 11 – this approach, to the study of resonances on the particular surface used by Grimbert *et al.* [106], was not successful.

11

Numerical complex scaling

In this chapter we shall discuss in more details yet another approach to the calculation of molecular resonances which was briefly introduced in section 9.4 as the complex coordinate method (CCM). Especially we will present a new effective numerical scheme which for the first time allows for this exact method to be applied to a general dynamical system where no analytical expression is available for the potential energy surface.

At the very heart of the application of the complex coordinate method (CCM) for the calculation of resonances lies the problem of analytic continuation of a potential energy function,$V(x)$, into the complex coordinate plane, $x \to xe^{i\theta}$, [110, 111, 113, 114]. This requirement has mainly limited its use so far to analytic functions such as Coulomb, pairwise or LEPS potentials. In order to apply the method with arbitrary molecular potentials, such as those coming out of an *ab initio* calculation, one needs a systematic procedure. Different methods have been proposed, essentially based on the continuation of the potential matrix elements evaluated in some convenient basis-set[115, 116]. Amongst these latter methods, the identity[1]

$$\begin{aligned}\overline{V}_{ij} &= \int_x dx \varphi_i(x)\; V(xe^{i\theta})\; \varphi_j(x) && \text{(11.1a)}\\ &= e^{-i\theta}\int_{xe^{i\theta}} dx\varphi_i(xe^{-i\theta})\; V(x)\; \varphi_j(xe^{-i\theta}) && \text{(11.1b)}\end{aligned}$$

was first applied by Moiseyev and Corcoran[124] to the study of molecular resonances of H_2 and H_2^-. This equation relates the matrix elements $\overline{V}_{ij}$ of the

---

[1] Note that this is not a usual bra-ket matrix element (see footnote 5 on page 47), since the left basis function is not complex conjugated.

complex scaled potential $\overline{V}(x) \equiv V(xe^{i\theta})$ between *unscaled* basis functions $\{\varphi_i\}$ to those of the unscaled potential potential $V(x)$ between backward *scaled* basis functions $\{\widetilde{\varphi}_i(x) \equiv \varphi_i(xe^{-i\theta})\}$. It is based on the assumption that an exact molecular potential is dilation analytic. In the following, we will use a bar to denote forward scaling, such as $\overline{V}(x) \equiv V(xe^{i\theta})$, and a tilde for the backward scaling, as in $\widetilde{\varphi}_i(x) \equiv \varphi_i(xe^{-i\theta})$.

Eq. (11.1) is of central importance as it shifts the scaling from the potential to the basis functions $\{\varphi_i\}$ which are known *analytically.* This procedure was later successfully applied by Datta and Chu[125] to the rotational predissociation of Ar-N$_2$. In the same line, Ryabov and Moiseyev[126] recently proposed a method aimed at directly providing the complex scaled matrix elements of a real potential $V(x)$ determined by its values on a grid $\{x_p\}$. This procedure was successfully applied to the determination of the predissociation resonances of the three dimensional HCO and DCO radicals. Using a Discrete Variable Representation[23, 127, 128] (DVR) for the Jacobi angle α, they first computed the matrix elements of the complex scaled potential $V(Re^{i\theta}, r, \alpha_\gamma)$ at fixed values α_γ. (R corresponds here to the H-CO dissociation coordinate). By diagonalization of the resulting complex scaled Hamiltonian $H(Re^{i\theta}, r, \alpha_\gamma)$, they were able to obtain *prediagonalized* complex scaled ray-eigenstates $\{|\overline{\Phi}_m(\alpha_\gamma)\rangle\}$ in order to reduce the size of the overall basis set $\{|\overline{\Phi}_m(\alpha_\gamma)\rangle|\alpha_\gamma\rangle\}$.

In the new approach, presented in this chapter, we adopt a different point of view, and show how one can directly obtain the complex scaled matrix elements, starting only from *unscaled* ones:

$$\langle R_p|\langle\Phi_m(R_p)|H|\Phi_{m'}(R_{p'})\rangle|R_{p'}\rangle \tag{11.2a}$$

$$\Downarrow$$

$$\langle R_p|\langle\Phi_m(R_p)|\overline{H}|\Phi_{m'}(R_{p'})\rangle|R_{p'}\rangle \tag{11.2b}$$

The main difference with respect to Ryabov and Moiseyev's approach stems from the fact that ours is equivalent to a numerical continuation of multidimensional elements as shown by eq. (11.2). Also, it allows one to choose the dissociation coordinate as the discrete variable, which in turn allows for the construction of a very compact adiabatic basis-set by employing the SAR method presented in subsection 2.2.8. This is especially advantageous in the present context, as it has recently been shown[28] that the adiabatic energy curves provide a very good zero-order description of the resonances. Thus, our whole approach is still based on the identity relation given by eq. (11.1). We will furthermore demonstrate that such a numerical continuation can be performed for an arbitrary DVR.

The outline of this chapter is as follows. In section 11.1, we first show how one can numerically continue matrix elements $\langle R_p|V|R_{p'}\rangle$ expressed in a DVR, and give a one-dimensional example. This formulation is then used in section 11.2 in order to obtain numerically continued multidimensional matrix elements. The method is illustrated on a two dimensional model first introduced by Eastes and Marcus[129, 130]. Finally, section 11.3 concludes.

11.1 One dimensional formulation

We suppose that the system is to be described in terms of a DVR $\{|\mathcal{R}_p\rangle, p = 1, N\}$, related to an Finite Basis Representation (FBR) $\{\varphi_n(R), n = 1, N\}$ through the unitary transformation

$$|\mathcal{R}_p\rangle = \sum_{p=1}^{N} U_{pn}|\varphi_n\rangle \tag{11.3}$$

as described in detail in subsection 2.2.4. The goal of this section is to show how one can obtain the $\langle\mathcal{R}_p|\overline{V}|\mathcal{R}_{p'}\rangle$ matrix elements of the rotated potential $\overline{V} \equiv V(Re^{i\theta})$ from the real ones

$$\langle\mathcal{R}_p|V|\mathcal{R}_{p'}\rangle = V(R_p)\delta_{pp'} \tag{11.4}$$

We will first derive the formulation in the case of an arbitrary FBR-DVR scheme. The cases of both a uniform grid and an optimized grid will then be studied in more details later. As the kinetic energy term is analytical, its complex continuation is straightforward, and does not require any particular treatment. For example, in the case of $T_R = -\hbar^2/2\mu\ d^2/dR^2$, the complex scaled kinetic operator displays matrix elements given by

$$\begin{aligned}\langle\mathcal{R}_p|\overline{T}_R|\mathcal{R}_{p'}\rangle &= e^{-2i\theta}\langle\mathcal{R}_p|T_R|\mathcal{R}_{p'}\rangle && (11.5a)\\ &= e^{-2i\theta}\left[\underline{\underline{U}}\,\underline{\underline{T}}\,\underline{\underline{U}}^T\right]_{pp'} && (11.5b)\end{aligned}$$

where $\underline{\underline{T}}$ is the unscaled kinetic energy matrix expressed in the $\{\varphi_n\}$ basis set.

11.1.1 General formulation

Use of identity in eq. (11.1) allows us to write

$$(\mathcal{R}_p|\overline{V}|\mathcal{R}_{p'}) = e^{-i\theta}(\widetilde{\mathcal{R}}_p|V|\widetilde{\mathcal{R}}_{p'}) \tag{11.6}$$

where the $(\dots|\dots)$ notation means that the hermitian conjugation is not used (see the discussion on using the c-product rather than the scalar product in reference [103]). The backward rotated $|\widetilde{\mathcal{R}}_p\rangle$ vectors are naturally defined from eq. (11.3) as

$$|\widetilde{\mathcal{R}}_p\rangle = \sum_{n=1}^{N} U_{pn}|\widetilde{\varphi}_n\rangle \tag{11.7}$$

leading to the expression

$$(\mathcal{R}_p|\overline{V}|\mathcal{R}_{p'}) = e^{-i\theta}\sum_{nn'} U_{pn}(\widetilde{\varphi}_n|V|\widetilde{\varphi}_{n'})U_{p'n'} \tag{11.8}$$

Because we explicitly consider in this chapter the case where no analytic expression is available for the potential, the $(\widetilde{\varphi}_n|V|\widetilde{\varphi}'_n)$ integrals have to be performed numerically. The most convenient way to compute such integrals consists in using a related quadrature scheme (preferably of Gaussian accuracy, see subsection 2.2.3 and 2.2.4)

$$(\widetilde{\varphi}_n|V|\widetilde{\varphi}_{n'}) = \sum_{q}^{M} \widetilde{\varphi}_n(R_q)V(R_q)\mathcal{W}_q\widetilde{\varphi}_{n'}(R_q) \tag{11.9}$$

where R_q and $\mathcal{W}_q$ correspond respectively to the quadrature abscissae and weights. In this sum, if one uses for M the same value as the number N of basis functions φ_n, i.e. if the quadrature abscissae $\{R_q\}$ coincide with the DVR points $\{R_p\}$, then one would obtain erroneous matrix elements. The reason is that, as explained in subsection 2.2.3, the quadrature of eq. (11.9) would be exact for non-rotated functions φ_n only as long as the relation $n + n' + d^o[V] \leq 2M + 1$ is satisfied. One has thus to use a quadrature scheme, $\{R_q\}$, of dimension higher than that of the DVR $\{R_p\}$.

At this point, it might be useful to review some of the characteristic features of the DVR method, as presented in subsection 2.2.4. The basic relation, eq. (11.4), is a direct consequence of the definition of the $\{|\mathcal{R}_p\rangle\}$ DVR as the transform of the FBR $\{\varphi_n\}$ given by eq. (11.3). In fact, the $\langle\varphi_n|V|\varphi_{n'}\rangle$ matrix elements computed from the associated quadrature scheme

$$\langle\varphi_n|V|\varphi_{n'}\rangle = \sum_{p}^{N} U_{pn}V(R_p)U_{pn'} \tag{11.10}$$

are not exact for the same reason as discussed previously. However, by the use of the unitary transformation, they lead back to eq. (11.4). As we will show below, this is not the case for the analogous representation of eq. (11.9).

By using a higher order quadrature scheme $\{R_q\}$, one can thus achieve an exact evaluation of the $(\widetilde{\varphi}_n|V|\widetilde{\varphi}_{n'})$ matrix elements of eq. (11.9). Defining the rectangular complex matrix $\underline{\underline{\widetilde{U}}}$

$$\widetilde{U}_{qn} = (R_q|\widetilde{\varphi}_n) \tag{11.11}$$

eq. (11.9) can be recast into the equivalent DVR type expression

$$(\widetilde{\varphi}_n|V|\widetilde{\varphi}_{n'}) = \sum_q^M \widetilde{U}_{qn} V(R_q) \widetilde{U}_{qn'} \tag{11.12}$$

which with eq. (11.8) leads to the following relation for the $(\mathcal{R}_p|\overline{V}|\mathcal{R}_{p'})$ matrix

$$\boxed{(\mathcal{R}_p|\overline{V}|\mathcal{R}_{p'}) = e^{-i\theta} \left[\underline{\underline{U}} \cdot \underline{\underline{\widetilde{U}}} \cdot \underline{\underline{V}}^{(d)} \cdot \underline{\underline{\widetilde{U}}}^t \cdot \underline{\underline{U}}^t \right]_{pp'} \qquad (11.13)}$$

$\underline{\underline{V}}^{(d)}$ being the real diagonal matrix

$$V^{(d)}_{qq'} = V(R_q)\delta_{qq'} \tag{11.14}$$

But consequently, the $(\mathcal{R}_p|\overline{V}|\mathcal{R}_{p'})$ matrix elements as defined by eq. (11.8) are *no longer diagonal.* This departure from usual DVR properties causes no real problem in the formulation as will be shown in the next subsections. In the case of a one dimensional system, one can question the utility of such a DVR scheme as it does not lead to any advantage compared to a direct FBR formulation. Its actual interest will appear in section 11.2 when dealing with multidimensional systems.

11.1.2 One dimensional test case

As a first application of the above formulation, we consider the case of an equidistant grid

$$\{R_p \equiv p\,\Delta R\ ,\ p = 1, N\} \tag{11.15}$$

(A system can always be translated such that its domain of interest lies between 0 and $R_{max} = (N+1)\Delta R$). As described in subsection 2.2.5 the associated DVR $\{\mathcal{R}_p, p = 1, N\}$ is the conjugate representation of the sine basis set $\{\varphi_n, n = 1, N\}$[24, 131]

$$\varphi_n(R) = \sqrt{\frac{2}{(N+1)\Delta R}} \sin \frac{n\pi R}{(N+1)\Delta R} \tag{11.16}$$

eigenstates of the $[0, R_{max}]$ box. These two representations are related through the unitary transformation eq. (11.3) where

$$U_{pn} = \sqrt{\frac{2}{(N+1)}} \sin \frac{n\pi R_p}{(N+1)\Delta R} \tag{11.17}$$

In order to test our formulation, we present now a simple calculation aimed at determining the resonances of the model Hamiltonian

$$H = T + V = -\frac{1}{2}\frac{d^2}{dR^2} + (R^2 - 0.8)e^{-0.1R^2} + 0.8 \tag{11.18}$$

already studied by Moiseyev *et al.*[132] and Korsch *et al.*[133], see figure 11.1.

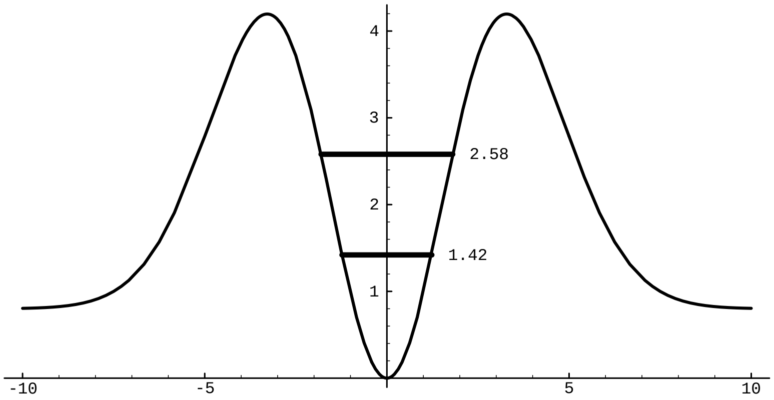

Figure 11.1: Plot of the one-dimensional model potential, previously studied by Moiseyev *et al.*[132] and Korsch*et al.*[133]. Note the two energy levels corresponding to the positions of the resonances listed in table 11.1.

This system displays a string of resonances, and in order to obtain the odd ones, one can restrict the domain of R to $[0, \infty[$, and use a basis set of functions $\{\varphi_n(R)\}$ which all satisfy the boundary condition $\varphi_n(0) = 0$, such as the PIB of eq. (11.16). In this study, we will focus on the lowest two odd resonances (*i.e.* $E^{(1)}_{res}$ and $E^{(3)}_{res}$), see figure 11.1 for an illustration.

Two series of calculations, presented in table 11.1, have been performed. In each case, the dimension N of the $\{\mathcal{R}_p\}$ DVR has been varied while the box size was kept at the value $R_{max} = 15$. In the first series, used as a reference and shown in column 1, we employed the *analytic* expression of the potential and defined the scaled Hamiltonian matrix elements in the DVR as

$$(\mathcal{R}_p|\overline{H}|\mathcal{R}_{p'}) = -\frac{1}{2}e^{-2i\theta}\langle\mathcal{R}_p|\frac{d^2}{dR^2}|\mathcal{R}_{p'}\rangle + V(R_p e^{i\theta})\delta_{pp'} \tag{11.19}$$

The next three columns display results obtained from a numerical continuation of the potential V by means of eq. (11.8) and (11.12), with

$$(R_q|\widetilde{\varphi}_n) = \sqrt{\frac{2}{M+1}} \sin \frac{n\pi R_q e^{-i\theta}}{R_{max}} \tag{11.20}$$

Column 2 in table 11.1 corresponds to using a quadrature grid $\{R_q\}$ twice as dense as the $\{|\mathcal{R}_p\rangle\}$ DVR, explicitly retaining in the calculation the *non diagonal* terms $(\mathcal{R}_p|\overline{V}|\mathcal{R}_{p'})$. Column 3 differs from column 2 in that these off diagonal terms were discarded in the calculation. Finally, column 4 also corresponds to retaining the non diagonal terms, but using a quadrature grid identical to that of the initial DVR.

Table 11.1: Results for the first two odd resonances of the one-dimensional Hamiltonian model, eq. (11.18). The first column corresponds to an analytic continuation of the potential, the following ones to a numerical continuation by a quadrature using M points. In column 3, a diagonal definition of the DVR was enforced.

Size N	Analytical continuation[a]	Numerical continuation[a] $M = 2N+1$	$M = 2N+1$[b]	$M = N$
18	$1.42 - i8.86(-6)$	$1.42 - i4.43(-5)$	−−−−−−−[c]	$1.42 - i5.77(-5)$
18	$2.60 - i1.83(-1)$	$2.53 - i1.98(-1)$	$2.65 - i0.61(-1)$	−−−−−−−[c]
24	$1.42 - i5.84(-4)$	$1.42 - i5.87(-4)$	$1.37 - i1.63(-3)$	$1.42 - i6.23(-4)$
24	$2.59 - i1.74(-1)$	$2.59 - i1.79(-1)$	$2.60 - i0.41(-1)$	$2.65 - i1.04(-1)$
29	$1.42 - i5.83(-4)$	$1.42 - i5.83(-4)$	$1.37 - i1.35(-3)$	$1.42 - i6.21(-4)$
29	$2.58 - i1.74(-1)$	$2.58 - i1.74(-1)$	$2.61 - i0.42(-1)$	$2.66 - i1.71(-1)$

[a] Below we have used the short notation $(-x)$ for 10^{-x}.

[b] In this column the results are listed from calculations where the off-diagonal elements of eq. (11.13) are ignored.

[c] Resonance position unassignable.

The main conclusion which emerges from these calculations is that the proposed numerical continuation scheme is able to reproduce the correct results, provided the off diagonal terms $(\mathcal{R}_p|\overline{V}|\mathcal{R}_{p'})$ are explicitly retained in the formulation. In fact, the $M = N$ calculations with these terms lead to better results than those using the dense quadrature grid ($M = 2N+1$), but a diagonal $\overline{V}$ definition. As will be shown in section 11.2, these off diagonal terms pose no problem and still allow one to use the DVR formulation in conjunction with an adiabatic reduction of the basis.

11.1.3 Optimization of the DVR scheme

As shown above, a sine-based DVR allows for an easy primary description of a complex scaled potential. This is equivalent to the very general role played by the plane wave basis set for time dependent wave packets, due to the underlying FFT scheme[134]. However, for a Morse potential, such as the one associated to the two-dimensional model studied in section11.2 (see eq. (11.40b)), it constitutes a poor representation in terms of efficiency. The reason is that the spacing between grid points is dictated by the maximum kinetic energy allowed, which corresponds to the bottom of the well. In the asymptotic region, where the de Broglie wavelength can be considerably larger, one could use in principle a much broader mesh size. This is exactly the problem addressed by the HEG method discussed in subsection 2.2.6. To repeat, Harris, Engerholm and Gwinn (HEG)[26] have showed that if $\{\varphi_n\}$ is some basis set, one can use the eigenvalues $\{R_p\}$ of the position matrix $\langle\varphi_n|\hat{R}|\varphi_{n'}\rangle$ in order to numerically evaluate the matrix elements of any function $f(R)$

$$\langle\varphi_n|f(R)|\varphi_{n'}\rangle = \sum_p U_{pn} f(R_p) U_{pn'} \tag{11.21}$$

where $\underline{\underline{U}}$ is the associated eigenvector matrix. It was later shown by Dickinson and Certain[27] that this method was equivalent to a quadrature scheme of Gaussian accuracy. The HEG method thus provides a way to define a numerical quadrature when no analytic expression is known for the eigenfunctions $\{\varphi_n\}$, or when it is too cumbersome to deal with.

Analyzed in terms of the DVR formulation, the HEG method allows for the definition of a DVR $\{|\mathcal{R}_p\rangle\}$, conjugate to the $\{\varphi_n\}$ FBR

$$|\mathcal{R}_p\rangle = \sum_n U_{pn}|\varphi_n\rangle \tag{11.22}$$

which satisfies the basic relation

$$f(R)|\mathcal{R}_p\rangle = f(R_p)|\mathcal{R}_p\rangle \tag{11.23}$$

This property was later used by Leforestier[135] and Echave and Clary[82] in order to define an adapted DVR to some zero-order Hamiltonian H^0, the eigenfunctions of which being precisely the $\{\varphi_n\}$ basis set as described in subsection 2.2.6.

The $(\mathcal{R}_p|V|\mathcal{R}_{p'})$ matrix elements appearing in the HEG formulation can be numerically continued by means of eq. (11.8) and (11.12), provided one can express the $(R_q|\widetilde{\varphi}_n)$ terms. This can be realized, for example, by first computing the $\{\varphi_n\}$

eigenstates of interest in the primary sine basis set $\{|S_m\rangle, m = 1, M\}$ conjugate to the dense $\{|R_q\rangle\}$ DVR :

$$|\varphi_n\rangle = \sum_m C_{mn}|S_m\rangle \tag{11.24}$$

(In order to carry on the HEG procedure, one has to truncate the $\{\varphi_n\}$ basis set, otherwise the HEG representation $\{|\mathcal{R}_p\rangle\}$ would be strictly identical to the primary DVR $\{|R_q\rangle\}$). The $(R_q|\widetilde{\varphi}_n)$ terms can then be expressed as

$$(R_q|\widetilde{\varphi}_n) = \sum_m C_{mn}(R_q|\widetilde{S}_m) \tag{11.25}$$

with

$$(R_q|\widetilde{\varphi}_m) = \sqrt{\frac{2}{M+1}}\sin\frac{m\pi R_q e^{-i\theta}}{R_{max}} \tag{11.26}$$

Similarly, the scaled kinetic matrix elements in the HEG DVR can be computed from those in the primitive sine $\{S_m\}$ basis set

$$(\mathcal{R}_p|\overline{T}_R|\mathcal{R}_{p'}) = \sum_{nn'} U_{pn}(\varphi_n|\overline{T}_R|\varphi_{n'})U_{p'n'} \tag{11.27a}$$

$$= e^{-2i\theta}\sum_{nmn'} U_{pn}C_{mn}(S_m|T_R|S_m)C_{mn'}U_{p'n'} \tag{11.27b}$$

11.1.4 Summary

With the use of eq. (11.12), eq. (11.6) can be cast into the DVR type expression

$$(\mathcal{R}_p|\overline{V}|\mathcal{R}_{p'}) = e^{-i\theta}(\widetilde{\mathcal{R}}_p|V|\widetilde{\mathcal{R}}_{p'}) \tag{11.28a}$$

$$= e^{-i\theta}\sum_q^M(\widetilde{\mathcal{R}}_p|R_q)(R_q|V|R_q)(R_q|\widetilde{\mathcal{R}}_{p'}) \tag{11.28b}$$

As discussed in subsection 11.1.1, the quadrature (involving the R_q points) is performed on a grid *denser* that the one $\{R_p\}$ of final interest. This equation shows that the complex scaled matrix elements in a DVR can be obtained from the unscaled elements computed in a related (denser) DVR. The method we developed in subsection 11.1.1 allowed us to compute the $(R_q|\widetilde{\mathcal{R}}_p)$ quantities by using some intermediate basis set $\{\varphi_n\}$

$$(R_q|\widetilde{\mathcal{R}}_p) = \sum_n U_{pn}(R_q|\widetilde{\varphi}_n) \tag{11.29}$$

in which the backward rotation can be carried out. In the case of an equidistant DVR $\{|\mathcal{R}_p\rangle\}$, the $\{\varphi_n\}$ correspond to sine functions. In the HEG case, the $\{\varphi_n\}$ correspond to numerical eigenstates of some zero order Hamiltonian H^0, and one has to perform one more step

$$(R_q|\widetilde{\mathcal{R}}_p) = \sum_{nm} U_{pn}C_{mn}(R_q|\widetilde{S}_m) \tag{11.30}$$

in order to reach the analytic sine basis set $\{S_m\}$.

11.2 Multidimensional formulation

As discussed in detail in subsection 2.2.8, Bačić and Light [127] have shown that a basis, supposed here to depend only on the two variables R and r for sake of clarity, can be very efficiently contracted using the SAR scheme. In the following we shall assume that the total Hamiltonian reads as

$$H = T_R + h \tag{11.31}$$

where $h = T_r + V(R,r)$ displays no differential operator with respect to R. The first step in the SAR scheme is to define an adiabatic basis $\{|\Phi_m(R_p)\rangle, m = 1, M_p\}$, as solutions to the fixed R Hamiltonian $h(R_p)$

$$h(R_p)|\Phi_m(R_p)\rangle = \mathcal{E}_m(R_p)|\Phi_m(R_p)\rangle \tag{11.32}$$

By using a DVR $\{|\mathcal{R}_p\rangle, p = 1, N\}$ for the R variable, one can contract the initial basis set into the new one $\{|\Phi_m(R_p)\rangle|\mathcal{R}_p\rangle \equiv |\Phi_m^{(p)}, \mathcal{R}_p\rangle\}$. (From now on, we will use the notation $|\Phi_m^{(p)}\rangle \equiv |\Phi_m(R_p)\rangle$). In this contracted basis set, the Hamiltonian operator H displays the following matrix elements

$$\langle \mathcal{R}_p, \Phi_m^{(p)}|H|\Phi_{m'}^{(p')}, \mathcal{R}_{p'}\rangle = \langle \mathcal{R}_p|T_R|\mathcal{R}_{p'}\rangle\langle \Phi_m^{(p)}|\Phi_{m'}^{(p')}\rangle + \mathcal{E}_m^{(p)}\delta_{mm'}\delta_{pp'} \tag{11.33}$$

Lipkin *et al.* [116] have used this SAR based formulation in order to reduce as much as possible the basis-set size prior to diagonalization of the complex scaled

Hamiltonian matrix. In the contracted basis set, the complex scaled Hamiltonian operator displays matrix elements given by

$$\langle \mathcal{R}_p, \Phi_m^{(p)} | \overline{H} | \Phi_{m'}^{(p')}, \mathcal{R}_{p'} \rangle = \langle \mathcal{R}_p | \overline{T}_R | \mathcal{R}_{p'} \rangle \langle \Phi_m^{(p)} | \Phi_{m'}^{(p')} \rangle + \langle \Phi_m^{(p)} | \overline{h}(R_p) | \Phi_{m'}^{(p')} \rangle \delta_{pp'} \tag{11.34}$$

This formulation explicitly relied on an analytical expression of the potential $V(R, r)$ entering h.

Recently, this approach was extended by Ryaboy and Moiseyev[126] to the case of a non dilation analytic potential. Analyzed in terms of the above two-dimensional formulation, their approach would consist in first computing a matrix representation of the complex scaled Hamiltonian, $h(\bar{r}, R_p)$, at fixed R, in a sine basis-set for r, r being the dissociation coordinate. The corresponding matrix elements were obtained by means of the identity relation, eq. (11.1), using backward scaled sine functions $\varphi_i(re^{-i\theta})$ and a quadrature rule. Diagonalization of the resulting matrix lead to complex scaled ray-eigenstates $\{|\bar{\Phi}_m(R_p)\rangle\}$, to be used as the basis set for the r variable. The overall basis set was then defined as $\{|\bar{\Phi}_m^{(p)}\rangle|\mathcal{R}_p\rangle\}$. The formulation we propose aims at obtaining the complex scaled matrix elements in terms of the *unscaled* ones as given by eq. (11.33). It will focus on the $\overline{h}$ term of eq. (11.34), as the kinetic energy operator, T_R, poses no problem, and can easily be treated as shown in section 11.1.

11.2.1 General formulation

Starting from the expression (see eq. (11.32))

$$h = \sum_m |\Phi_m(R)\rangle \mathcal{E}_m(R) \langle \Phi_m(R)| \tag{11.35}$$

one can write

$$\begin{aligned}
(\mathcal{R}_p|\overline{h}|\mathcal{R}_{p'}) &= e^{-i\theta}(\widetilde{\mathcal{R}}_p|h|\widetilde{\mathcal{R}}_{p'}) && \text{(11.36a)}\\
&= e^{-i\theta}\sum_m (\widetilde{\mathcal{R}}_p|\,\{|\Phi_m(R)\rangle\mathcal{E}_m(R)\langle\Phi_m(R)|\}\,|\widetilde{\mathcal{R}}_{p'}) && \text{(11.36b)}
\end{aligned}$$

In the this expression, the terms between brackets $\{\dots\}$ can be considered as a function of R. As discussed in subsection 11.1.1, one should evaluate the integral over R by using a quadrature scheme defined on a grid $\{R_q, q = 1, M\}$ denser than the DVR $\{\mathcal{R}_p, p = 1, N\}$ of interest. This can be realized by using twice the closure relation $1 = \sum_q^M |R_q\rangle\langle R_q|$, leading to the equivalent form

$$(\mathcal{R}_p|\overline{h}|\mathcal{R}_{p'}) = e^{-i\theta}\sum_{mq}(\widetilde{\mathcal{R}}_p|R_q)|\Phi_m^{(q)}\rangle\mathcal{E}_m^{(q)}|\Phi_m^{(q)}\rangle(R_q|\widetilde{\mathcal{R}}_{p'}) \tag{11.37}$$

One finally obtains for the matrix elements of $\overline{h}$ in the $\{|\Phi_m^{(p)}, \mathcal{R}_p\rangle\}$ basis-set as

$$\begin{aligned}(\mathcal{R}_p, \Phi_m^{(p)}|\overline{h}|\Phi_{m'}^{(p')}, \mathcal{R}_{p'}) = e^{-i\theta} \sum_{m"q} \Big\{ &(\widetilde{\mathcal{R}}_p|R_q)\langle\Phi_m^{(p)}|\Phi_{m"}^{(q)}\rangle \\ &\times \mathcal{E}_{m"}^{(q)}\langle\Phi_{m"}^{(q)}|\Phi_{m'}^{(p')}\rangle(R_q|\widetilde{\mathcal{R}}_{p'}) \Big\}\end{aligned} \tag{11.38}$$

This expression forms the central working equation in our method. Eq. (11.38) is quite general, and demonstrates that multidimensional matrix elements expressed in a contracted basis set can be numerically continued for complex scaling calculations. As emphasized before, the off diagonal terms of $\overline{h}$ have to be explicitly retained in the formulation. It should also be noted that the actual definition of the DVR chosen for the dissociation coordinate R only appears through the $(R_q|\widetilde{\mathcal{R}}_p)$ terms (see eq. (11.29) and (11.30)).

We shortly discuss now the computational cost of this formulation. The overlap terms $\langle\Phi_m^{(p)}|\Phi_{m"}^{(q)}\rangle$ appearing in eq. (11.38) are also required in the original formulation, associated to the kinetic operator matrix elements (see eq. (11.34)). As a consequence, they do not lead to any new calculation. The extra cost comes uniquely from the necessity to use a denser grid $\{R_q\}$ in order to perform the numerical continuation. This, in turn implies to perform the ray-eigenstate calculation on this dense grid associated to the adiabatic variable R. As will be shown in subsection 11.2.2, the computational effort typically increases by a factor of 1.5 due to this preconditioning step, when compared to the hypothetical case where an analytic expression of the potential is available.

11.2.2 Application to the Eastes-Marcus model

As a way to check the new formulation in a multidimensional case, we applied it to the well studied Eastes-Marcus model[129, 130]. It can be viewed as representing a dissociative collinear triatomic molecule

$$[\mathrm{ABC}]^* \rightarrow \mathrm{A} + \mathrm{BC}(v) \tag{11.39}$$

and consists in an harmonic oscillator (BC) coupled to a Morse potential (A-BC)

$$\begin{aligned}\widehat{\mathbf{H}} &= -\frac{1}{\mu}\frac{\partial^2}{\partial R^2} - \frac{\partial^2}{\partial r^2} + r^2 + V(R-r) && \text{(11.40a)}\\ V(x) &= D(\exp[-\alpha x] - 1)^2 - D && \text{(11.40b)}\\ \mu &= 0.2 \qquad \alpha = 0.05 \qquad D = 1.5 && \text{(11.40c)}\end{aligned}$$

A plot of the potential energy function in the Eastes-Marcus model, *cf.* eq. (11.40), is shown in figure 11.2.

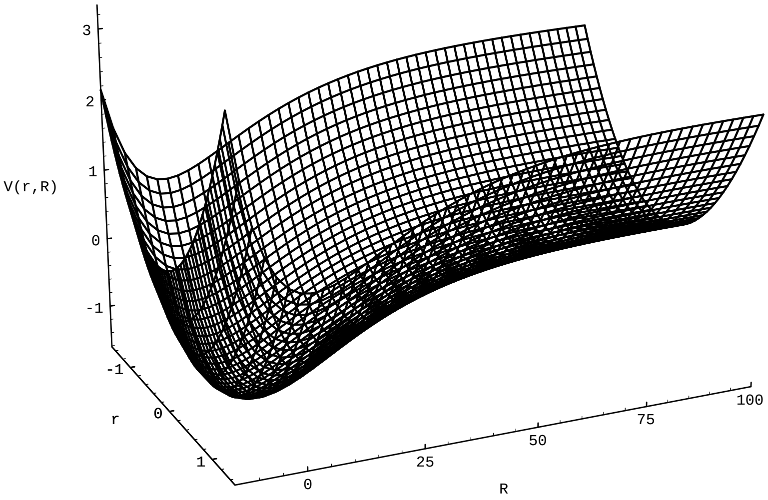

Figure 11.2: Plot of the two-dimensional model potential by Eastes-Marcus.

As a prelude to a zero-order description of the resonances we partition this Hamiltonian into the small perturbative term $\widehat{\mathbf{h}} = V(R-r) - V(R)$ and the zero-order Hamiltonian

$$\widehat{\mathbf{H}}^{(0)} = -\frac{1}{\mu}\frac{\partial^2}{\partial R^2} - \frac{\partial^2}{\partial r^2} + r^2 + V(R) \tag{11.41}$$

Thus, the zero-order eigenvalues are simply the sum of the harmonic BC oscillator eigenvalues, $2v+1$, and the Morse oscillator eigenvalues[136],*i.e.*

$$E^{(0)}_{v,n} = 2v + 1 - \alpha^2(a - n - 1/2)^2/\mu \tag{11.42}$$

where $a \equiv \sqrt{\mu D}/\alpha$, and $0 \le n < a - \frac{1}{2}$, which with the parameter in eq. (11.40c) implies that the Morse potential supports 10 bound states. In figure 11.3 and 11.4 we have shown illustrations of the formation of the two lowest resonances in the zero-order description of the Eastes-Marcus model, just outlined.

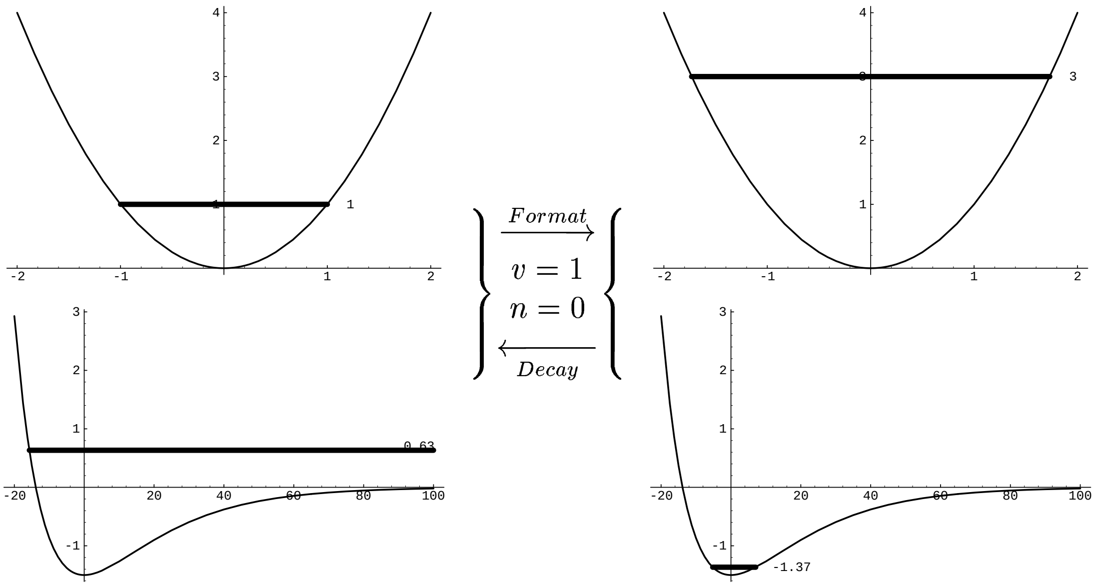

Figure 11.3: Zero-order illustration of the formation and decay of the first Feshbach resonance listed in table 11.2, *cf.* eq. (11.42) for $E^{(0)}_{1,0} = 1.63$. The left array of plots shows the initial situation with an excess energy in the translational degree of freedom and the ground vibrational level populated. The right array of plots shows the zero-order description of the resonance state where the ground state of the Morse potential and the first excited level of the harmonic oscillator is populated.

According to the SAR scheme by Bačić and Light[127], one first preconditions the basis set by computing the adiabatic solutions at fixed R_p values

$$\left\{-\frac{\partial^2}{\partial r^2} + D\left\{e^{-\alpha(R_p - r)} - 1\right\}^2 - D + r^2\right\}\Phi^{(p)}_m(r) = \mathcal{E}^{(p)}_m \Phi^{(p)}_m(r) \qquad (11.43)$$

This first step has been realized using a DVR $\{|r_i\rangle\}$ for the BC-oscillator

$$|\Phi^{(p)}_m\rangle = \sum_i C^{(p)}_{im}|r_i\rangle \qquad (11.44)$$

This procedure allows for a simplified calculation of the overlap terms $\langle\Phi^{(p)}_m|\Phi^{(q)}_{m'}\rangle$ entering eq. (11.38) as

$$\langle\Phi^{(p)}_m|\Phi^{(q)}_{m'}\rangle = \sum_i C^{(p)}_{im} C^{(q)}_{im'}. \qquad (11.45)$$

The final two-dimensional basis set reads as $\{|\Phi^{(p)}_m, R_p\rangle\}$, where $\{|R_p\rangle\}$ stands for the HEG representation. As discussed in subsection 2.2.6 and 11.1.3, it was obtained by diagonalizing the $\widehat{\mathbf{R}}$ operator in the truncated basis set of the eigenstates

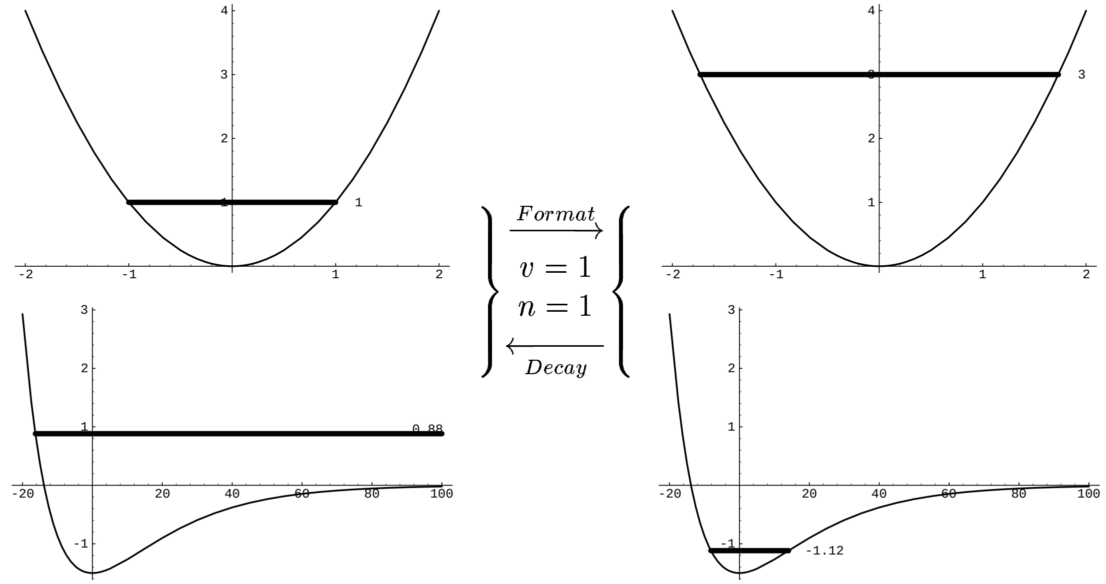

Figure 11.4: Zero-order illustration of the formation and decay of the second Feshbach resonance listed in table 11.2, *cf.* eq. (11.42) for $E^{(0)}_{1,1} = 1.88$. The left array of plots shows the initial situation with an excess energy in the translational degree of freedom and the ground vibrational level populated. The right array of plots shows the zero-order description of the resonance state where the first excited level of the Morse potential and the harmonic oscillator is populated.

$\{\phi_n(R)\}$ of the following Hamiltonian

$$\hat{h}^0 = -\frac{1}{\mu}\frac{\partial^2}{\partial R^2} + D\left\{e^{-\alpha R} - 1\right\}^2 - D. \tag{11.46}$$

We also made use of a uniform DVR $\{|R_q\rangle\}$, as the working basis set to express the eigenstates $\{\phi_n(R)\}$, as well as the dense DVR appearing in eq. (11.38).

We present in table 11.2 a comparison of the first two resonances as computed either by analytic or numerical continuation of the potential. While using always the same box size $(-20 \rightarrow 150)$ for R, different grid dimensions have been employed, corresponding to an increasing accuracy on the resonance widths. First, one can remark that the resonance positions are fully converged to a 6 digit accuracy in both sets of calculations. As could be expected, the widths obtained by analytic continuation converge first $(N = 40)$, but the results coming out of the numerical scheme display a relative error of only 5% for the same grid size. The important point is that by increasing the dimension of the scheme, the numerical results eventually converge onto the exact ones, as shown in the table. The accuracy needed in the calculations of molecular resonances will be further addressed below, in the next section.

Table 11.2: Comparison of the characteristics of the first two resonances of the Eastes-Marcus model, as obtained by either an analytic or numerical continuation of the potential. $M = 2N + 1$ denotes the size of the dense grid, where N is the size of the truncated HEG grid. A zero-order illustration of formation of these resonances are given in figure 11.3 and 11.4.

DVR size	$M = N$ Analytical continuation[a]	$M = 2N + 1$ Numerical continuation[a]
$N = 30$	$1.63901 - i2.2(-7)$	$1.63901 - i1.7(-7)$
$N = 30$	$1.88703 - i1.2(-6)$	$1.88703 - i6.9(-7)$
$N = 40$	$1.63901 - i2.0(-7)$	$1.63901 - i1.9(-7)$
$N = 40$	$1.88703 - i1.0(-6)$	$1.88703 - i9.7(-7)$
$N = 50$	$1.63901 - i2.0(-7)$	$1.63901 - i2.0(-7)$
$N = 50$	$1.88703 - i1.0(-6)$	$1.88703 - i9.8(-7)$
$N = 60$	$1.63901 - i2.0(-7)$	$1.63901 - i2.0(-7)$
$N = 60$	$1.88703 - i1.0(-6)$	$1.88703 - i1.0(-6)$

[a] Below we use the short notation $(-x)$ for 10^{-x}.

Finally figure 11.5 and 11.6 show plots of the complex energy trajectories for respectively the analytical and numerical continuation of the Hamiltonian, both employing 50 HEG grid points. First of all we note that both figures are in excellent agreement with the Balslev–Combes[110] theorem illustrated in figure 9.3. Secondly we note that with the exception of some of the continuum states the plots are completely identical as expected. The slight perturbation of some of the continuum trajectories in the numerical continuation, we believe is an artifact from the sine basis-set for large values of the rotation parameter θ. However, this is of no importance in the present context as we are only interested in the exact location of the bound and resonance states, and furthermore the continuum trajectories display the correct overall behavior.

11.3 Conclusion

We have presented a new procedure which allows one to numerically complex continue the matrix elements of any real Hamiltonian operator expressed in a Discrete Variable Representation. One thus avoids the need of a *global* analytical expression of the potential, and can use instead a piecewise one, such as the spline interpolation method. When applied to the multidimensional case, one can first

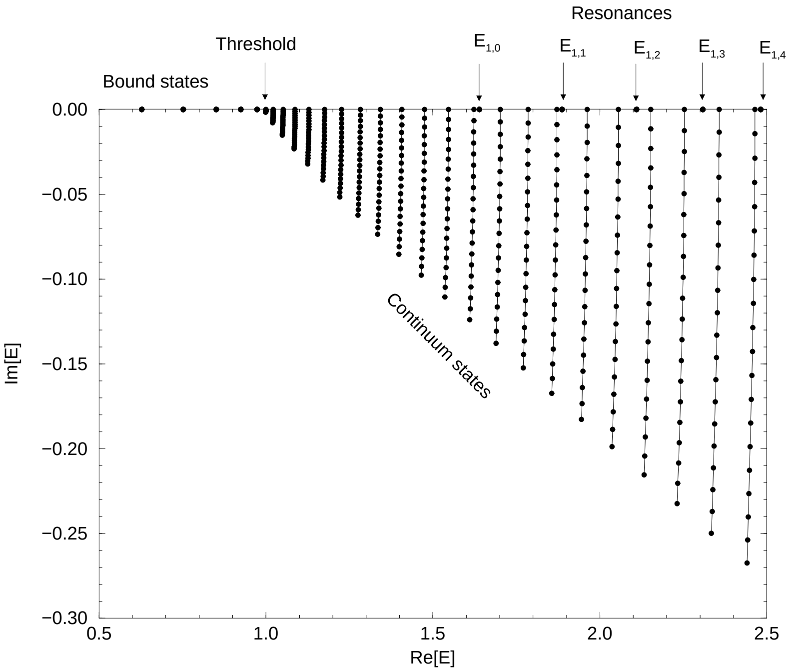

Figure 11.5: Plot of complex energy trajectories for the analytical continuation.

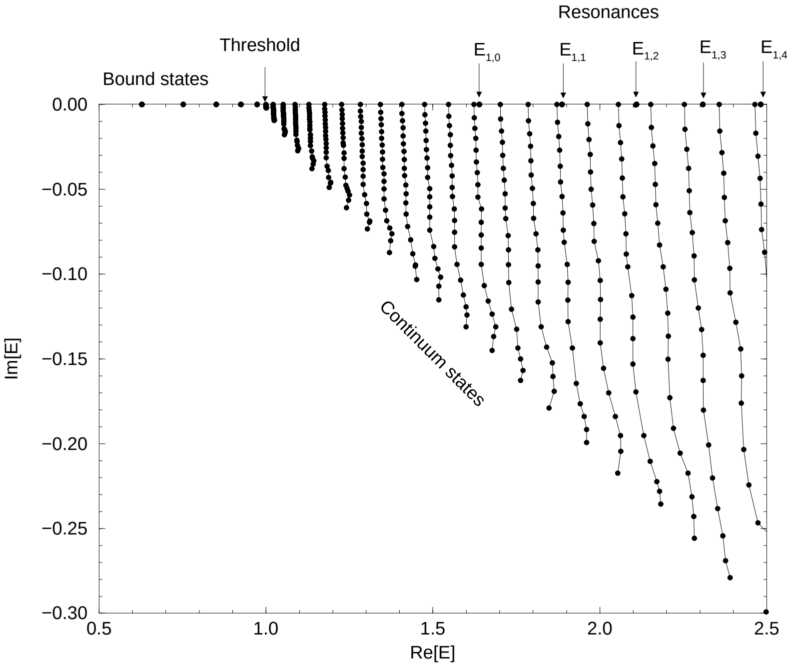

Figure 11.6: Plot of complex energy trajectories for the numerical continuation.

precondition the basis-set, using Bačić and Light SAR method[127] with the real potential, and then numerically continue the resulting matrix elements. It constitutes an extension of the method initially proposed by Moiseyev and Corcoran[124] to a multidimensional DVR type basis-set. Its interest stems from the fact that the SAR method produces an optimum contracted basis set in order to handle molecular systems. Also, it allows the dissociation coordinate to be treated by a grid adapted to the variation of the de Broglie wavelength, by means of the HEG method[26].

We now address the accuracy achieved by our numerical procedure on the Eastes-Marcus model. Considering the minimal basis set size ($N = 40$) which leads to converged results when using an analytical continuation of the potential, the resonance positions come out with a 6 digit accuracy through numerical continuation. However, the associated widths display a relative error of approximately 5%. We would first like to point out that in most cases, such a precision is amply sufficient for *numerical* molecular potentials, as those obtained from *ab initio* calculations. In fact, the intrinsic errors due to such potentials can be expected to overwhelm those associated to the numerical continuation procedure. A second point concerns the fact that this numerical scheme is well behaved. By increasing the number of points used, the results eventually converge onto the exact ones.

12

Discussion and summary

In this last part of the thesis we have studied resonances employing two different complex methods. In chapter 10 we successfully used the optical potential method (OPM), originating from Jolicard and Austin[117], for the calculation of resonances in the system of $H^{+}+O_2$ described in the framework of the Infinite-Order Sudden approximation. Next, in chapter 11 we presented a new numerical approach to the calculation of resonances using the exact complex coordinate method (CCM) on systems where no analytical expressions for the potential energy function exist. Subsequently we successfully tested this "numerical complex scaling of a discrete variable representation" on respectively a one and two-dimensional model system.

In these studies we found that both methods have their distinct pros and cons. The OPM was fairly easy to setup and implement using existing numerical techniques like the DVR, HEG and SAR schemes, discussed in detail in section 2.2. However, due to the approximate nature of this approach, which steams from the unphysical perturbations of the system caused by the imperfectness of the added optical potentials, tedious convergence tests seem unavoidable, where the different parameters entering the definition of this potential are varied. We also observed that these perturbations could lead to spurious complex energy trajectories, which behaved like resonances for certain values of the amplitude parameter, but actually tuned out to correspond to continuum states once the convergence test was performed. Thus, the biggest disadvantage of the OPM sums up in the fact that unless extensive convergence tests are performed one is not guaranteed to get the "correct" behavior of the energy trajectories, which in turn makes the visual inspection difficult.

This problem was not observed when employing the numerical complex coordinate method presented in chapter 11. This, of course, is due to the fact that the method is based on the mathematically rigors Balslev–Combes theorem[110] (*cf.*

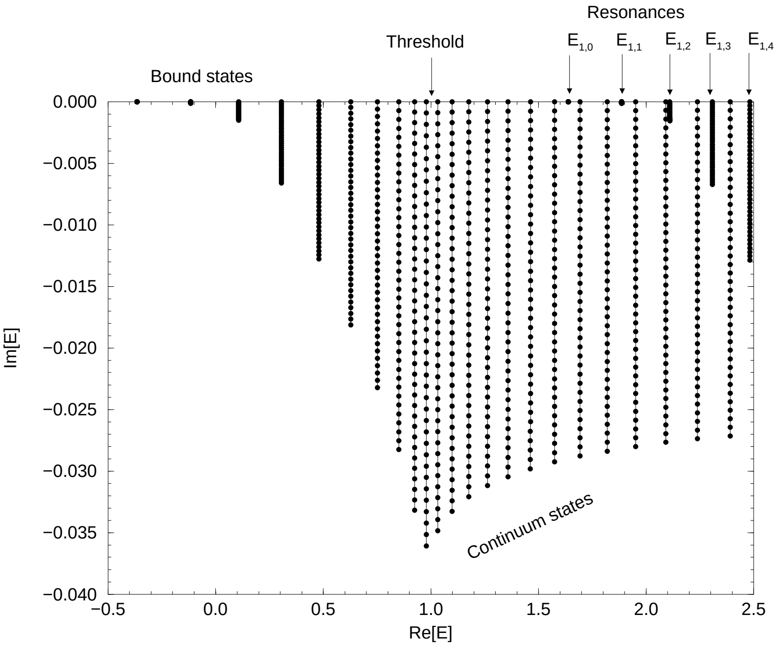

Figure 12.1: The optical potential method on the Eastes-Marcus model[129] studied in subsection 11.2.2.

eq. (9.13)). This point, I think, is clearly illustrated when figure 12.1, showing the results from a single OPM calculation[1] on the Eastes-Marcus model[129], studied in subsection 11.2.2, is compared to the corresponding figure 11.6 employing the numerical complex coordinate method. Figure 12.1 does clearly not display the "correct" behavior of the complex energy trajectories (*cf.* figure 9.3 and 11.5), as observed in figure 11.6. Some of the resonances and bound states behave as continuum trajectories, being constantly rotated into the negative imaginary energy plane, and the indication of the threshold energy has vanished. In fact the plot shows that the convergence is restricted to a narrow energy window around resonance $E_{1,0}$, corresponding the energy domain covered by the optical potential with the specific choice of the parameters in that calculation. However by change these potential parameters the energy window can be shifted to other domains of interest, leading to the correct width of other resonances. In contrast, the numerical complex coordinate method, presented in chapter 11, in principle covers the whole energy range in a single calculation, thereby making it more convenient.

However, the numerical complex coordinate method also has its drawbacks. First of all the numerical implementation is more involved, at least as compared to the

---

[1] For this calculation I used the same implementation of the OPM as used in the study of resonances in $H^+ + O_2$.

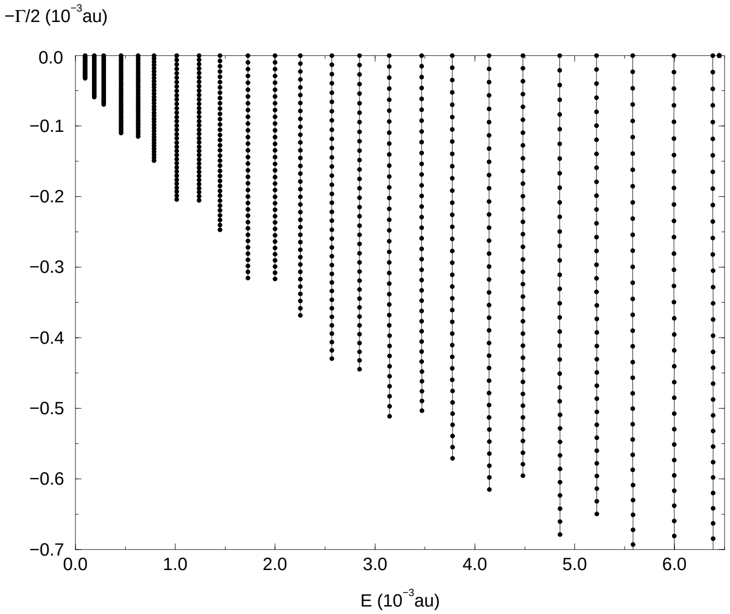

Figure 12.2: Numerical complex scaling on the system of H^++O_2 studied in chapter 10.

OPM. This is of course a minor detail, but in terms of popularity it could certainly play a role. Secondly it is more computationally demanding, due to the necessity to use a denser grid in order to perform the numerical continuation. However, two important points should be stressed in connection to this apparent computational disadvantage as compared to the OPM. As we do not need to perform any additional convergence tests in the complex coordinate method it is actually my experience that the extra CPU time makes up for the obligatory convergence tests in the OPM. Furthermore, as my supervisor use to put it, "there is no free meals in quantum dynamics", which of course in this context means that you don't go from an approximate description (the OPM) to an exact one (the CCM) without paying a price in terms for increased computational efforts. The fact that the CCM is in principle an exact method however also adds other "problem" to this method, namely the extreme sensitivity of the overall scheme to the nature of the system. This is clearly not an artifact of the CCM, but merely steams from the fact that the position of resonances are in general very sensitive to the curvature of the involved potential energy surfaces. Nevertheless I mention this as a limitation of the CCM for the following reason: When I first started to develop the method of numerical continuation, in corporation with Claude Leforestier, the motivation was actually to employ this exact method on the study of resonances in the H^++O_2 system. After the method had been thoroughly tested, as described in chapter 11, we were quite surprised and disappointed to discover that the method did not produce any resonances at all for the H^++O_2 system. This should be clear from figure 12.2 where a plot of the complex energy trajectories for a numerical complex scaling calculation on H^++O_2 is shown. The plot shows the correct behavior for the continuum trajectories, and the location of the threshold energy (*i.e.* the bound states), but no resonances are found. We are almost certain that the explanation for this should be found on the potential energy surface for this system. The problem with this potential, as was also noted in section 10.2, is the cut-off of the surface of reference [122] at $r_{max} = 2.9\,\text{au}$, see figure 10.2. This artifact of the potential is clearly transfered to the definition of the vibronic *adiabatic* basis-set, which is subsequently used in the numerical representation of the complex Hamiltonian. In the numerical continuation of matrix elements we exactly backward scale these perturbed basis functions, and it is very likely that the perturbation from the artifact of the surface is amplified by this complex rotation, thereby removing any traces of the resonance states. This would also explain way on the other hand the OPM does in fact work on this systems, as this method merely adds an extra (negative imaginary) potential to the asymptotic region of the Hamiltonian, leaving the basis-functions unscaled. Thus, not only do both methods have their distinct pros and cons, it also seems to be the case that situations may emerge where only one of the two can actually do the job, thereby making the methods complementary rather than competitive.

In this thesis we have only employed the two complex methods in up to two degrees of freedom, and the natural question would of course be to ask how the schemes are changed as one moves to larger dimensionality. In the present implementations of the two schemes we used standard complex eigenvalue routines for the diagonalization of the non-Hermitian Hamiltonians, but as more degrees of freedom are added to the system this will quickly turn out the be computationally impossible simply due to the exponential increase in the size of the involved matrices. As discussed in subsection 4.1.4 the Lanczos algorithm is a very powerful technique to selectively calculate eigenvalues of large matrices. However, a direct application of the Lanczos recursion scheme on the non-Hermitian Hamiltonian would generally lead to very slow convergence due to the fact that the Lanczos algorithm can be shown first to display the eigenvectors in the sparse part of the spectrum (*cf.* eq. (4.18)), whereas resonances are most often located in the dense part of the spectrum. The solution to this convergence problem is to first perform a *spectral inversion* of the complex Hamiltonian, by defining a new operator, derived from $\widehat{\mathbf{H}}$, which inverts (*i.e.* makes sparse) the desired dense spectrum in the eigenvalue domain of interest. Different operators can be used for such a filtered Lanczos algorithm, but the Green's function, $(E - \widehat{\mathbf{H}})^{-1}$ where E defined the energy window of interest, is probably the most popular choice. However, the use of the Green's function

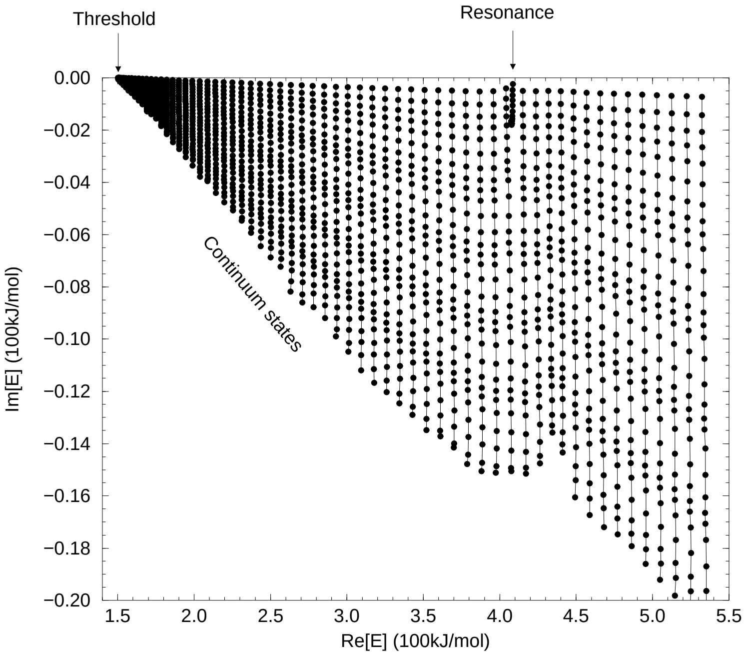

Figure 12.3: The numerical complex scaling on the model system studied in section 6.2.

raises another problem, namely how to compute it, without having to do a direct matrix inversion of $E - \underline{\underline{\text{H}}}$, which is clearly out of the question due to the large dimensionality if $\underline{\underline{\text{H}}}$. A very efficient way to compute the Green's function is to represent it by a recursive polynomial expansion, where knowledge is only needed for the action of the Hamiltonian operator on a state vector. We actually showed an example of this in subsection 4.1.3 where the evolution operator was represented by a Chebychev polynomial expansion. However, because the Hamiltonian is now non-Hermitian we cannot in general scale the spectrum of $\widehat{\mathbf{H}}$ to $[-1, 1]$ as is always the first step in a Chebychev expansion of an Hermitian operator (*cf.* eq. (4.10)). To my knowledge there now exist two different types of strategies to overcome this problem. The obvious one is to employ another type of polynomials which do not put the same restrictions on the eigenvalue spectrum of $\widehat{\mathbf{H}}$ as the Chebychev polynomials do. Thus, one can alternatively use Newton polynomials[137, 138] or so-called Faber polynomials[139]. If however one insist on employing a Chebychev expansion a very clever solution has recently been but forward by Mandelshtam and Taylor[140, 141], where instead for expanding the non-Hermitian Hamiltonian directly, one employs a modified Chebychev expansion scheme on the unscaled Hamiltonian, by incorporating the optical potential as a damping factor into the the recursion scheme itself. Hence, this approach is formally equivalent to the

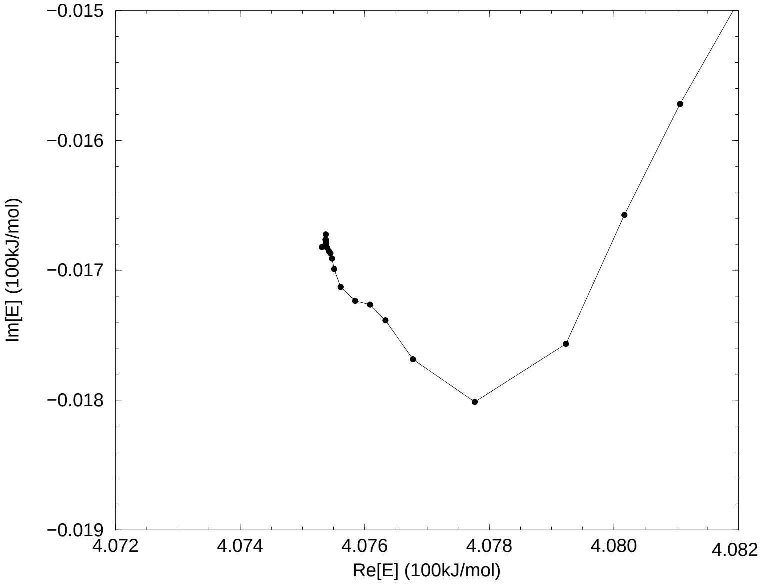

Figure 12.4: Closeup of the resonance shown in figure 12.3.

OPM, and cannot be used in the framework of the CCM.

Finally, I would like to very briefly point out the connection between the two parts for this thesis. As mentioned before we actually observed clear evidence for the formation of resonances in both of the numerical studies in part II. Thus, to emphasize this connection I have shown plots of the complex energy trajectories obtained from a numerical complex scaling of the model system studied in section 6.2. Figure 12.3 clearly shows that the system supports a single resonance in the energy domain investigated, and the closeup in figure 12.4 reveals the exact location of the resonance which is in excellent agreement with the peak observed in figure 6.2.

As a closing remark I would like to repeat what was stressed in the very beginning of this thesis. All of the work presented in this thesis is, in one or another way, based on the work of others, and neither me, nor my coworkers, can of course take the credit for the development of the MCTDH or complex-scaling methods. However, we have presented extensions and numerical reformulations which we believe have added extra values to these methods. Whether this is in fact true or not is naturally up to the scientific community to judge. Whatever the judgment might be, the overall motivation for the work presented in this thesis nicely summarize in the following motto

> Join those who seek the truth - but be on guard against those who claim that they have found it!

Part IV

Miscellaneous

A

Abstracts of publications

Below is a list of the abstracts for the publications on which large parts of this thesis is based. They are not listed in chronological order, but rather in the order of appearance in this thesis. Two of the papers (A.4 and A.1) have already published and a third (A.3) has been submitted to an international journal. The last paper (A.2) is still under development, and it is as yet undecided if it should be split into two separate publications. For the two published articles a small erratum is included, but we emphasize that most of the corrections are simple typographical mistakes (some of them actually introduced by the journal in the process of typesetting the paper), and non of the corrections change the results and conclusions made in these papers. Finally we also hope to publish the Gaussian MCTDH scheme described in section 5.2. However, as we (G. D. Billing and I) are still struggling with the numerical instabilities resulting from the employed non-orthogonal basis-set, this is still “work in progress”. Hence an abstract is not included below for this project.

A.1 Generalized MCTDH

Generalization of the Multi-Configuration Time-Dependent Hartree method to non-adiabatic systems.

Ken Museth and Gert Due Billing
Department of Chemistry (Lab. III), H.C.Ørsted Institute
University of Copenhagen, DK-2100 Copenhagen Ø, Denmark

Journal of Chemical Physics Vol. **105**, page 9191, 1996
Running title: Non-adiabatic systems in the MCTDH framework

We present a generalization of the MCTDH scheme, originally introduced by Meyer, Manthe and Cederbaum, Chem. Phys. Lett. **165**, 73 (1990), to a general non-adiabatic system. In the course of deriving the extended working equations a new compact notation is introduced. Subsequently the equations of motion are applied to a one-dimensional two-surface model system. Calculated energy-resolved transition probabilities for the model system, treated in the MCTDH framework, are shown to be in exact agreement with direct numerically "exact" calculations, using a Split-operator propagation scheme. Finally a comparison is made between the convergence and the consumed CPU-time for the two methods. The two numerical formulations of the scattering problem employ respectively a DVR and a FFT collocation scheme. The use of negative imaginary potentials to remove artificial boundary effects in the two schemes are also comment upon.

Erratum:

- ☞ In equation (5) $N_\kappa \rightarrow N$.
- ☞ Equation (9) should read as eq. (6.13).
- ☞ Equation (10) should read as eq. (6.14).
- ☞ The text between equation (18) and (19) should read as: "For the single-particle functions we are going to make the same assumption as previously make by Jäckle and Meyer (see eq. (14) and (17) in reference [75]). Thus,"
- ☞ Equation (13) should read as eq. (6.26c).
- ☞ Equation (A4) should read as eq. (6.21).

A.2 Two-dimensional non-adiabatic MCTDH

Non-Adiabatic study of H_2 on Cu(100) by the Multi-Configuration Time-Dependent Hartree method.

Ken Museth, Christian Laursen and Gert Due Billing
Department of Chemistry (Lab. III), H.C.Ørsted Institute
University of Copenhagen, DK-2100 Copenhagen Ø, Denmark

This paper is under preparation and will be submitted to the Journal of Chemical Physics shortly.

We present a non-adiabatic study of dissociation of H_2 on a Cu(100) surface using an extension of the multi-configuration time-dependent Hartree method recent proposed by Museth *et al.* in J. Chem. Phys. **105**, 9191 (1996). The calculations include the two lowest diabatic electronic surfaces, which are constructed from an EDIM-potential suggested by Truong *et al.*. In order to exploit the full advantages of the multi-configuration time-dependent Hartree formulation, these potential energy surfaces are approximated in a product representation of the involved coordinates. The dynamics is confined to a two-dimensional treatment for the reactive subsystem by quantizing the vibrational and the translational coordinates of the hydrogen molecule relative to the metallic surface. The non-diabatic formulation of the multi-configuration time-dependent Hartree method is tested against an "exact" time-dependent scheme employing the FFT transform method in the framework of a split-operator. From this comparison we show in this work that as the number of configurations are increased the multi-configuration time-dependent Hartree method results do indeed converge to the exact solution.

A.3 Resonances in H^++O_2 by the OPM

On the optical potential method as a generalized scheme to locate molecular resonances: Calculation of Feshbach resonances in the electronically elastic $H^+ + O_2(X^3\Sigma_g^-)$ collision.

Ken Museth
Department of Chemistry (Lab. III), H.C.Ørsted Institute
University of Copenhagen, DK-2100 Copenhagen Ø, Denmark

Claude Leforestier
Laboratoire Structure et Dynamique Moléculaires (UMR 5636), CC 014
Université des Sciences et Techniques du Languedoc
34095 Montpellier Cédex 05, France

Danielle Grimbert
Université de Cergy-Pontoise, 5 Mail Gay-Lussac
Neuville s/ Oise, 95031 Cergy-Pontoise Cédex, France

Victor Sidis Laboratorie des Collisions Atomiques et Moléculaires
Université Paris-Sud XI, 91405 Orsay Cédex, France

Submitted to the Journal of Chemical Physics May 1997
Running title: Resonances in the elastic H^++O_2 collision

The optical potential method is reviewed here with special emphasis on the available techniques used to isolate and verify molecular resonances. We next present calculations of Feshbach, resonances in the framework of the Infinite-Order Sudden approximation, of the electronically elastic $H^+ + O_2(X^3\Sigma_g^-)$ collision. In this approximation the relative angle between the oxygen molecule and the incoming proton is kept fixed thereby reducing the problem to a two dimensional one. The investigated energy domain of the resonances is below the channel energy for the first vibrational excitation (0.2 eV). The optical potential method, used to characterize the resonances, applies a negative imaginary potential (NIP) in the asymptotic region of the electronic potential energy surface. The positions and widths of the resonances are given as respectively the real and imaginary part of the stationary complex energies with respect to variations of the amplitude of the NIP. The overall numerical scheme is an optimized discrete variable representation of the complex integrals involved. The calculated resonances are finally compared to previous two dimensional calculations obtained by Grimbert *et al.*, Chem. Phys. Lett. **230**,(1994), p. 47-53.

A.4 Numerical complex scaling

On the direct complex scaling of matrix elements expressed in a discrete variable representation: Application to molecular resonances.

Ken Museth
Department of Chemistry (Lab. III), H.C.Ørsted Institute
University of Copenhagen, DK-2100 Copenhagen Ø, Denmark

Claude Leforestier
LSD SMS (UMR), CC 014
Université des Sciences et Techniques du Languedoc
34095 Montpellier Cédex 05(France)

Journal of Chemical Physics Vol. **104**, page 7008, 1996
Running title: Complex scaling of a DVR

We present an application of a method initially proposed by Moiseyev and Corcoran (Phys. Rev. **A20**, 814 (1978)) to a *direct* continuation of the matrix elements of a real Hamiltonian operator expressed in a contracted, Discrete Variable Representation type basis set. It is based on the identity which relates the matrix elements of a complex scaled potential between real basis set functions to those of the *unscaled* potential between backward scaled basis functions. The method is first applied to the study of the resonances of a one dimensional model by means of complex scaling. It is shown that the resulting matrix elements of the scaled potential are no longer diagonal in the DVR. This paradox is discussed and shown to be of no practical consequence in the formulation. The scheme is then extended to the direct complex scaling of a two dimensional Hamiltonian operator expressed in a contracted basis set built through the Successive Adiabatic Reduction method of Bačić and Light. Results show that, due to the use of a numerical continuation, slightly larger grids have to be used as compared to the case of an analytic continuation where the potential is available.

Erratum:

- ☞ In equation (3) the summation index should be changed to p.
- ☞ The caption for table 2 should also mention that $M \equiv 2N+1$ where M is the size of the dense grid, and N that of the truncated HEG grid, see table 11.2.

List of Figures

List of Tables

Bibliography

[1] K. Museth and G. D. Billing, J. Chem. Phys. **105**, 9191 (1996).

[2] K. Museth, C. Laursen, and G. D. Billing, J. Chem. Phys. (1997), to be submitted.

[3] K. Museth, C. Leforestier, and V. Sidis, J. Chem. Phys. (1997), submitted.

[4] K. Museth and C. Leforestier, J. Chem. Phys. **104**, 7008 (1996).

[5] A. H. Zewail, *Special issue of Chem. Phys.* (Elsevir Science, Amsterdam, 1996), Vol. 207.

[6] M. Abramowitz and I. A. Stegun, *Handbook of Mathematical Functions* (Dover Publications, New York, 1968).

[7] W. H. Miller, J. Chem. Phys. **50**, 407 (1969).

[8] R. A. Marcus, J. Chem. Phys. **45**, 4493 (1966).

[9] A. Kuppermann and G. C. Schatz, J. Chem. Phys. **62**, 2502 (1975).

[10] A. Kuppermann and G. C. Schatz, J. Chem. Phys. **65**, 4642 (1976).

[11] L. M. Delves, Nucl. Phys. **9**, 391 (1959).

[12] B. R. Johnson, J. Chem. Phys. **80**, 5051 (1980).

[13] B. R. Johnson, J. Chem. Phys. **79**, 1906 (1983).

[14] B. R. Johnson, J. Chem. Phys. **79**, 1916 (1983).

[15] F. T. Smith, J. Math. Phys. **3**, 735 (1962).

[16] P. R. Morse and H. Feshbach, in *Methods of Theoretical Physics* (McGraw-Hill, New York, 1953), pp. 1728–1734.

[17] D. R. Hartree, Proc. Camp. Phil. Soc. **24**, 111 (1928).

[18] E. A. Hylleraas, Z. Phys. **54**, 347 (1929).

[19] I. S. Gradshteyn and M. Ryzhik, *Table of Integrals, Series and Products* (Academic Press, London, 1965).

[20] D. Kosloff and R. Kosloff, J. Comput. Phys. **52**, 35 (1983).

[21] M. D. Feit and J. Fleck, J. Comput. Phys. **78**, 301 (1983).

[22] W. H. Press, B. P. Flannery, S. A. Teukolsky, and T. Vetterling, W, *Numerical Recipes* (Cambridge University Press, Cambridge, 1986).

[23] J. C. Light, I. P. Hamilton, and J. V. Lill, J. Chem. Phys. **82**, 1400 (1985).

[24] D. T. Colbert and H. W. Miller, J. Chem. Phys. **96**, 1982 (1992).

[25] Z. Bačić and J. C. Light, Annu. Rev. Phys. Chem. **40**, 469 (1989).

[26] D. O. Harris, G. G. Engerholm, and W. D. Gwinn, J. Chem. Phys. **43**, 1515 (1965).

[27] A. S. Dickinson and P. R. Certain, J. Chem. Phys. **49**, 4209 (1968).

[28] C. Leforestier, K. Yamashita, and N. Moiseyev, J. Chem. Phys. **103**, (1995).

[29] N. C. Blais *et al.*, Chem. Phys. Lett. **166**, 11 (1990).

[30] Y. M. Wu, B. Lepetit, and A. Kuppermann, Chem. Phys. Lett. **186**, 319 (1991).

[31] A. Kuppermann and Y. M. Wu, Chem. Phys. Lett. **205**, 517 (1993).

[32] Y. M. Wu and A. Kuppermann, Chem. Phys. Lett. **235**, 105 (1995).

[33] C. Zener, Proc. R. Soc. London Ser. A **137**, 696 (1932).

[34] L. D. Landau, Phys. Z. Sowjetunion **2**, 46 (1932).

[35] E. C. G. Stückelberg, Helv. Phys. Acta. **5**, 369 (1932).

[36] R. L. Kronig, *Band Spectra and Molecular Structure* (Cambridge University Press, New York, 1930).

[37] M. Baer, in *Theory of chemical reaction dynamics* (CRC Press, Boca Raton, Florida, 1985), Vol. 2, pp. 219–280.

[38] V. Sidis, Adv. Chem. Phys. **82**, 73 (1992).

[39] M. Born and J. R. Oppenheimer, Ann. Phys. **84**, 457 (1927).

[40] M. Born and K. Huang, *Dynamical Theory of Crystal Lattices* (U. P., Oxford, 1995).

[41] M. Baer, Adv. Chem. Phys. **82**, 187 (1992).

[42] R. Kosloff, *Dynamics of Molecules and Chemical reactions* (Marcel Dekker, New York, 1996), pp. 185–230.

[43] G. D. Billing, Int. Rev. Phys. Chem. **13**, 309 (1994).

[44] M. D. Feit, J. A. Fleck Jr., and A. Steiger, J. Comput. Phys. **47**, 412 (1982).

[45] A. D. Bandrauk and H. Shen, J. Chem. Phys. **99**, 1185 (1993).

[46] H. Tal-Ezer and R. Kosloff, J. Chem. Phys. **81**, 3967 (1984).

[47] R. Kosloff, Annu. Rev. Phys. Chem. **45**, 145 (1994).

[48] C. Lanczos, J. Res. Natl. Bur. Strand. **45**, 255 (1950).

[49] R. B. Gerber, V. Buch, and M. A. Ratner, J. Chem. Phys. **77**, 3022 (1982).

[50] R. Kosloff, A. Hammerlich, and M. A. Ratner, in *Proceedings of the 20th Jerusalem Symposium on Quantum Chemistry and Biochemistry*, edited by J. Jortner, A. Pullman, and B. Pullman (Reidel, Dordrecht, 1987).

[51] H. D. Meyer, U. Manthe, and L. S. Cederbaum, Chem. Phys. Lett. **165**, 73 (1990).

[52] N. Makri and W. H. Miller, J. Chem. Phys. **87**, 5781 (1987).

[53] E. J. Heller, J. Chem. Phys. **62**, 1544 (1975).

[54] P. A. M. Dirac, Proc. Cambridge Philos. Soc. **26**, 376 (1930).

[55] J. Kucar, H. D. Meyer, and L. S. Cederbaum, Chem. Phys. Lett. **140**, 525 (1987).

[56] S.-I. Swada, R. Heather, B. Jackson, and H. Metiu, J. Chem. Phys. **83**, 3009 (1985).

[57] F. Y. Hansen, N. E. Henriksen, and G. D. Billing, J. Chem. Phys. **90**, 3060 (1989).

[58] K. G. Kay, Chem. Phys. **137**, 165 (1989).

[59] U. Manthe, Seideman, and W. H. Miller, J. Chem. Phys. **99**, 10078 (1993).

[60] U. Manthe, Seideman, and W. H. Miller, J. Chem. Phys. **101**, 4759 (1994).

[61] D. H. Zhang and J. Z. H. Zhang, J. Chem. Phys. **99**, 5615 (1993).

[62] D. H. Zhang and J. Z. H. Zhang, J. Chem. Phys. **100**, 2697 (1994).

[63] D. H. Zhang and J. Z. H. Zhang, J. Chem. Phys. **101**, 1146 (1994).

[64] J. T. Muckerman, R. D. Gilbert, and G. D. Billing, J. Chem. Phys. **88**, 4779 (1988).

[65] G. D. Billing and J. T. Muckerman, J. Chem. Phys. **91**, 6830 (1989).

[66] N. Markovic and G. D. Billing, Chem. Phys. **173**, 385 (1993).

[67] N. Balakrishnan and G. D. Billing, Chem. Phys. **189**, 499 (1994).

[68] N. Balakrishnan and G. D. Billing, J. Chem. Phys. **104**, 4005 (1996).

[69] D. C. Clary, J. Chem. Phys. **95**, 7298 (1991).

[70] D. C. Clary, J. Chem. Phys. **96**, 3656 (1992).

[71] J. M. Bowman and D. Wang, J. Chem. Phys. **96**, 7852 (1992).

[72] J. Echave and D. C. Clary, J. Chem. Phys. **100**, 402 (1994).

[73] G. D. Billing, Mol. Phys. **89**, 355 (1996).

[74] U. Manthe, H. D. Meyer, and L. S. Cederbaum, J. Chem. Phys. **97**, 3199 (1992).

[75] A. Jäckle and H. D. Meyer, J. Chem. Phys. **102**, 5605 (1995).

[76] U. Manthe and A. D. Hammerich, Chem. Phys. Lett. **211**, 7 (1993).

[77] D. H. Audrey *et al.*, J. Chem. Phys. **101**, 5623 (1994).

[78] A. D. Hammerich *et al.*, J. Chem. Phys. **101**, 5623 (1994).

[79] J.-Y. Fang and H. Guo, J. Chem. Phys. **101**, 5831 (1994).

[80] J.-Y. Fang and H. Guo, Chem. Phys. Lett. **101**, 341 (1995).

[81] L. Liu, J. Y. Fang, and H. Guo, J. Chem. Phys. **102**, 2404 (1995).

[82] J. Echave and D. C. Clary, Chem. Phys. Lett. **190**, 225 (1992).

[83] G. Haase, M. Asscher, and R. Kosloff, J. Chem. Phys. **90**, 3346 (1989).

[84] C. Leforestier and R. Wyatt, J. Phys. Chem. **78**, 2334 (1983).

[85] R. Kosloff and D. Kosloff, J.Comput.Phys. **63**, 363 (1986).

[86] D. Neuhauser and M. Baer, J. Chem. Phys. **90**, 4351 (1989).

[87] A. Vibók and G. Balint-Kurti, J. Phys. Chem. **96**, 8712 (1992).

[88] N. Marković and G. D. Billing, J. Phys. Chem. **100**, 1085 (1994).

[89] G. D. Billing and K. Mikkelsen, *Introduction to Molecular Dynamics and Chemical Kinetics* (John Wiley and Sons, New York, 1996).

[90] T. N. Truong, M. I. Truhlar, and B. C. Garrett, J. Chem. Phys. **93**, 8227 (1989).

[91] M. S. Daw and M. I. Baskes, Phys. Rev. Letters **50**, 1285 (1983).

[92] G. Wiesenekker, G. J. Kroes, and E. J. Baerends, J. Chem. Phys. **104**, 7344 (1996).

[93] A. Jäckle and H. D. Meyer, J. Chem. Phys. **104**, 7974 (1996).

[94] E. Schmidt, Math. Ann. **163**, 433 (1906).

[95] I. Infeld and T. E. Hull, Rev. Mod. Phys. **23**, 21 (1951).

[96] G. Pöschl and E. Teller, Z. Phys. **83**, 143 (1933).

[97] D. Neuhauser, J. Chem. Phys. **95**, 4927 (1994).

[98] D. Neuhauser, J. Chem. Phys. **93**, 2611 (1990).

[99] D. Neuhauser, J. Chem. Phys. **100**, 5076 (1994).

[100] R. Schinke, *Photodissociation Dynamics* (Cambridge University Press, Cambridge, 1993).

[101] A. F. J. Siegert, Phys. Rep. **56**, 750 (1939).

[102] K. Smith, *The calculation of atomic collision processes* (John Wiley and Sons, University of Nabraska, 1971).

[103] N. Moiseyev, Isr. J. Chem. **31**, 311 (1991).

[104] G. Gamow, Z. Phys. **51**, 204 (1928).

[105] R. H. Landau, *Quantum Mechanics II* (John Wiley and Sons, New York, 1996).

[106] D. Grimbert, V. Sidis, and M. Sizun, Chem. Phys. Lett. **230**, 47 (1994).

[107] G. Jolicard and G. D. Billing, J. Chem. Phys. **97**, 997 (1992).

[108] N. Ben-Tal, N. Moiseyev, C. Leforestier, and R. Kosloff, J. Chem. Phys. **94**, 7311 (1991).

[109] A. U. Hazi and H. S. Taylor, Phys. Rev. A **1**, 1109 (1970).

[110] E. Balslev and J. M. Combes, Commun. Math. Phys. **22**, 280 (1971).

[111] B. Simon, Commun. Math. Phys. **27**, 1 (1972).

[112] B. Simon, Math.Phys. **97**, 247 (1973).

[113] B. R. Junker, Adv. At. Mol. Phys. **18**, 207 (1982).

[114] W. P. Reinhardt, Annu. Rev. Phys. Chem. **33**, 223 (1983).

[115] N. Lipkin, N. Moiseyev, and J. Katriel, Chem. Phys. Lett. **147**, 603 (1988).

[116] N. Lipkin, N. Moiseyev, and C. Leforestier, J. Chem. Phys. **98**, 1888 (1993).

[117] G. Jolicard and E. J. Austin, Chem. Phys. Lett. **21**, 106 (1985).

[118] N. Rom, N. Lipkin, and N. Moiseyev, Chem. Phys. **151**, 199 (1991).

[119] S. Brouard, D. Macias, and J. G. Muga, J. Phys. A **27**, L439 (1994).

[120] G. Jolicard and J. Humbert, Chem. Phys. **127**, 31 (1988).

[121] S. Adhikari and S. P. Bhattacharyya, Chem. Phys. Lett. **265**, 99 (1997).

[122] D. Grimbert, B. Lassier-Govers, and V. Sidis, Chem. Phys. **124**, 187 (1988).

[123] M. Monnerville and J. M. Robbe, J. Chem. Phys. **101**, 7580 (1994).

[124] N. Moiseyev and C. T. Corcoran, Phys. Rev. A **20**, 814 (1979).

[125] K. K. Datta and S.-I. Chu, Chem. Phys. Lett. **87**, 357 (1982).

[126] V. Ryaboy and N. Moiseyev, J. Chem. Phys. **103**, 4061 (1995).

[127] Z. Bačić and J. C. Light, J. Chem. Phys. **85**, 4594 (1986).

[128] Z. Bačić and J. C. Light, J. Chem. Phys. **87**, 4008 (1987).

[129] W. Eastes and R. Marcus, J. Chem. Phys. **59**, 4757 (1973).

[130] K. M. Christoffel and J. M. Bowman, J. Chem. Phys. **78**, 3952 (1983).

[131] C. Leforestier, J. Phys. Chem. **94**, 6388 (1991).

[132] N. Moiseyev, P. R. Certain, and F. Weinhold, Mol. Phys. **36**, 1613 (1978).

[133] H. J. Korsch, H. Laurent, and R. Möhlenkamp, Phys. Rev. A **26**, 1802 (1982).

[134] R. Kosloff, J. Phys. Chem. **92**, 2087 (1988).

[135] C. Leforestier, in 4^{th} *Topsoe Summer School on Time Dependent Methods in Quantum Mechanics* (G.D.Billing, Copenhagen, 1991).

[136] P. M. Morse, Phys. Rep. **34**, 57 (1929).

[137] S. M. Auerbach and C. Leforestier, Comput. Phys. Commun. **78**, 55 (1993).

[138] G. Ashkenazi, R. Kosloff, S. Ruhman, and H. Tal-Ezer, J. Chem. Phys. **103**, 10005 (1995).

[139] Y. Huang, D. J. Kouri, and D. Hoffman, J. Chem. Phys. **101**, 10493 (1994).

[140] V. A. Mandelshtam and H. S. Taylor, J. Chem. Phys. **102**, 7390 (1995).

[141] V. A. Mandelshtam, T. P. Grozdanov, and H. S. Taylor, J. Chem. Phys. **103**, 10074 (1995).